

Benchmarks and Examples for Thermo-Hydro-Mechanical/Chemical Processes in Porous Media

KOLDITZ, Olaf^{1,3}, GÖRKE, Uwe-Jens¹ & SHAO, Hua² (Eds)

Contributed (so far) by

ATTINGER, Sabine^{1,12}, BAUER, Sebastian⁶, BEYER, Christof⁶,
BLÖCHER, Guido⁸, BÖTTCHER, Norbert³, CACACE, Mauro⁸,
CENTLER, Florian¹, DELFS, Olaf-Jens¹, FISCHER, Thomas¹,
HESSEN, Jürgen², JIN, Shuang¹¹, KALBACHER Thomas¹,
KOSAKOWSKI, Georg⁷, KRUG, Stefanie², McDERMOTT, Chris⁵,
MUSUUZA, Jude¹², PARK, Chan-Hee^{1,9}, RADU, Florin¹
RINK, Karsten¹, SHAO, Haibing^{1,3}, SINGH, Ashok¹,
SUN, Feng^{1,3}, SUN, Yuanyuan^{1,3}, TARON Joshua¹,
THULLNER, Martin¹, WALTHER, Marc³, WANG, Wenqing¹,
WATANABE, Norihiro^{1,3}, WU, Yajie¹, XIE, Mingliang¹⁰,
XU, Wenjie^{2,3}, ZEHNER, Björn¹

¹Helmholtz Centre for Environmental Research (UFZ)

²Institute for Geosciences and Natural Resources (BGR)

³Technische Universität Dresden (TUD)

⁴Center for Applied Geosciences, University of Tübingen (ZAG)

⁵University of Edinburgh (UE), UK

⁶University of Kiel (CAU)

⁷Paul-Scherrer-Institute (PSI), Switzerland

⁸Helmholtz Centre Potsdam (GFZ) German Research Centre for Geosciences

⁹Korea Institute of Geoscience and Mineral Resources (KIGAM)

¹⁰Gesellschaft für Anlagen- und Reaktorsicherheit (GRS) mbH

¹¹Utrecht University (UU), NL

¹²Friedrich-Schiller-Universität Jena

July 26, 2011

Contents

1	Introduction	7
Part I - Theory and Numerics		13
2	Theory July 26, 2011	19
2.1	Continuum mechanics	20
2.2	Porous medium	30
2.3	Balance equations	36
2.4	Fluid properties	43
2.5	Mechanical properties	53
2.6	Porous medium properties	66
3	Numerical methods	72
3.1	Introduction	73
3.2	Object-orientation in finite element analysis	75
3.3	General finite element formulations	81
3.4	Element objects - ELE	83
Part II - Benchmarks for Single Processes		98
4	Heat transport	99
4.1	Linear heat conduction in a semi-infinite solid	101
4.2	Linear heat conduction in a finite solid	103
4.3	Radial heat conduction in a solid	105
4.4	Heat transport in a fracture	107
4.5	Heat transport in a porous medium	110

4.6	Heat transport in a fracture-matrix system	112
4.7	Heat transport in a fracture-matrix systems: 3D case study . . .	116
5	Groundwater flow	124
5.1	Fluid momentum	124
5.2	Groundwater flow in an anisotropic medium	125
5.3	Groundwater flow in a heterogeneous medium	126
5.4	Confined aquifer with constant channel source term	128
5.5	Theis' Problem	132
5.6	Unconfined aquifer	135
5.7	2D steady state flow in porous media with a discrete fracture .	137
6	Richards flow	141
6.1	Root water uptake in soils	141
7	Overland flow	142
7.1	One-dimensional surface flow	144
7.2	Surface flow on a tilted V-catchment	145
7.3	Infiltration excess (Horton) overland flow	146
8	Gas flow	149
8.1	Material functions	152
8.2	Element test	154
8.3	Verifications	155
8.4	Air flow example	159
9	Deformation processes	162
9.1	Elasticity	164
9.2	Elastoplasticity	183
9.3	Viscoplastic creep	191

10 Mass transport	203
10.1 Diffusion	204
10.2 Decay	208
10.3 Sorption	211
10.4 Sorption and decay	216
10.5 Matrix diffusion	219
10.6 Particle tracking	221
10.7 RWPT in fractures	232
10.8 ?Compositional gas flow	234
11 Coupled processes	236
Part III - Examples for Coupled Processes	237
12 Surface/subsurface flow	238
13 Density dependent flow	239
13.1 Theory	239
13.2 The Elder Problem	241
13.3 The Goswami Problem	243
13.4 The Schincariol Problem	248
14 Multiphase flow processes	250
14.1 Isothermal Two-Phase Flow	250
14.2 Non-Isothermal Two-Phase Flow	268
15 Consolidation (H^nM) processes	273
15.1 Single phase consolidation	273
15.2 Unsaturated (Richards) consolidation	283
15.3 Two-phase consolidation	292
15.4 Flow and mechanics in discrete fracture-matrix rock systems	299
15.5 Flow and mechanics in discrete fracture-matrix rock system (2 D)	303
15.6 Two-phase flow consolidation	307

16 Thermomechanics	308
16.1 Thermoelastic stress analysis in homogeneous material (3 D) . . .	309
16.2 Thermoelastic stress analysis in composite materials (3 D)	312
16.3 Thermoelastic deformation in a hollow cylinder	316
17 Reactive Transport	322
17.1 Calcite dissolution and precipitation (1D)	323
17.2 Cation Exchange (1D)	325
17.3 Serial and Parallel Reactions (1D)	328
17.4 Xylene degradation (1D)	331
17.5 TCE- and cis-DCE-degradation for zero valent iron surface (1D)	334
17.6 Sequential CHC degradation with isotope fractionation (1D) . .	336
17.7 Degradation Network (1D)	340
17.8 Degradation with double Monod kinetics (2D)	347
17.9 Clogging simulation (2D)	351
A Software engineering	356
B Data processing	359
C Geometric Modelling, Gridding and Visualization	363
D Parallel computing	371
Index	372
Bibliography	387

Chapter 1

Introduction

by Olaf Kolditz, Uwe Grke, Hua Shao and Wenqing Wang

Coupled process modelling has been already considered in the various engineering problems and geo-scientific applications as the computation method was introduced for problems of soil consolidation and dam construction, and oil/gas field exploration since early 1970. However, substantial progress in experimental and theoretical studies regarding the fully coupling effects of temperature, hydraulics, mechanics, as well as chemistry in fractured porous media was just made in the last two decades due mainly to demands from the performance and safety assessment of a high-level nuclear waste repository. Numerical methods and computer codes have been developed successfully within the international DECOVALEX project (1992 - 2011). Meanwhile a wider range of applications associated with THMC coupled problem such geothermal reservoir engineering, CO₂-storage, construction of underground opening etc. can be found in the different international conferences, e.g. GeoProc (www.mech.uwa.edu.au/research/geoproc), ComGeo (www.com-geo.org/).

For a long-term performance and safety assessment of a nuclear waste repository in deep geological formation, an important issue is the impact to guarantee the isolation of an underground repository. To answer this question, solute transport process under the coupled conditions involving mechanical stability, thermal loading from the high-level waste, and chemistry in the groundwater should be predicted numerically. Also, for the construction planning of such complex and implementation of experimental data gained from the in situ tests a multiple process coupled code is required.

In the course of the quick development of computer technology, complicated geoscientific and geotechnical problems can be analysed in a coupled manner using modern numerical codes. However, the understanding of the complicated coupled processes based on the experimental data available and implementation of the developed algorithm into the numerical codes are major challenge for the scientists, which require an interdisciplinary cooperation and interactive procedure.

Quality management is nowadays a standard tool for production and development to ensure a high quality of a produced result. A numerical code dealing with the coupled THMC process is highly complicated software product, since the different processes have different characteristic features, e.g. time and spatial scales, nonlinearities, and interaction degree etc.. To keep the high quality of the developed code, benchmark testing is therefore necessary, especially in case scientists from different disciplinary and different organisation are working on the same code. Therefore, code verification and validation of selected test case are documented during the code development, and finally a benchmarking book for code developer (DBB) is produced and quality ensured.

Scope of this book

The intention of this book is multifold and can be summarised as follow:

- Outline the theoretical background of THMC processes in porous media for applications in geotechnics and hydrology (Part I),
- Provide collected test cases which can be used for benchmarking the numerical code development for single (Part II) as well as coupled processes (Part III),
- Help to develop and set-up applications (www.opengeosys.net and connected OpenGeoSys development platform available through the internet, see also Appendix for more details)

Application areas

Geotechnics

The coupling phenomena of thermal (T), hydraulic (H), and mechanical (M) processes are important for the analysis of deep geosystems under high temperature, pressure and stress conditions. Application areas of THM coupled models are e.g. geothermal energy utilization, nuclear waste disposal, and carbon dioxide storage in the deep geological formation.

The following slides illustrate that the understanding of THM processes including chemical reactions (C process) is important to a large variety geotechnical and geothermal applications. The physical basics are exactly the same for these applications. Different is simply

- the geological environment and different rock types, i.e. crystalline rocks, volcanic rocks, sandstones, clay, bentonite, ...
 - the geofluids, i.e. water, brines, vapour, methane, carbon dioxide ...
 - the thermodynamic conditions, i.e. temperature, stress, pressure, salinity,
- ...

Fig. 1.0.1 shows the application area: nuclear waste disposal in deep geological formations. There are several concepts concerning host rock for the disposal of hazardous waste in deep geological media, i.e. crystalline, salt, sediment, and volcanic formations. Different concepts use different buffer systems as geotechnical barrier for the waste isolation, i.e. crushed salt, bentonite, and bentonite/sand mixture. THM/C coupled modelling is required for the long-term analysis of possible processes which might result in a release of contaminants from the repository [1]. In that case it is important to know, how long it will take until the contaminants can return into the biosphere.

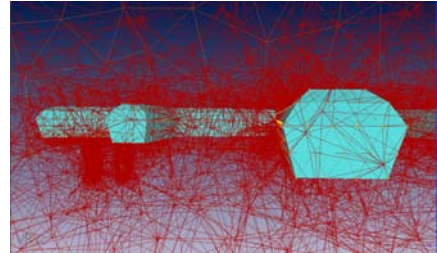


Figure 1.0.1: Tunnel system (Visualization by B. Zehner)

Fig. 1.0.2 illustrates the application area: Carbon Capture Storage (CCS). The idea is to capture the CO₂ from the power plants, liquefy it and inject it into the subsurface for long-term storage. Two basic concepts for appropriate geological systems are under proof now: depleted gas reservoirs and deep saline aquifers. After many years of operation many former gas reservoirs are depleted. These reservoirs are in an underpressurized status and can take up large volumes of fluids. Keeping the reservoir underpressurized and the impervious cap rocks are part of the storage concepts. THM/C modelling is required in order to calculate the possible fluid storage capacity and to better understand the highly coupled processes in the CO₂ injection area as well as their consequences for the storage concept [2].

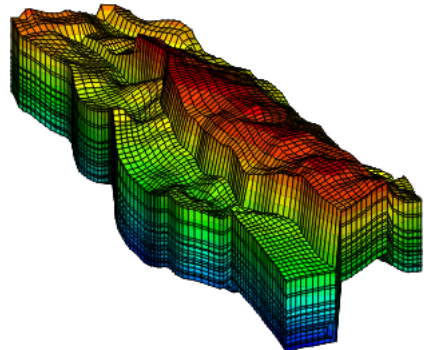


Figure 1.0.2: Subsurface reservoir for CO₂ storage

Fig. 1.0.3 depicts the application area: Geothermal energy, which is one of the alternative future energy resources under consideration. So-called shallow and deep geothermal systems are distinguished. Shallow systems are already commercially used e.g. for heating purposes. Deep geothermal reservoirs can be used for electric power production as high temperatures up to 200 C can be produced. THM/C modeling is required to design those geothermal power plants, e.g. in order to optimize production efficiency and reservoir lifetime. The significant cooling of the reservoir due to fluid reinjection gives raise to thermo-mechanical effects which needs to be controlled in order to avoid reservoir damage [3].

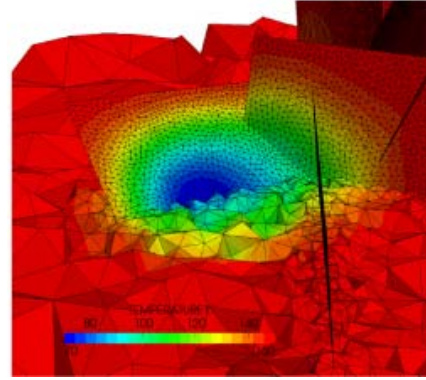


Figure 1.0.3: Simulated temperature field of water reinjection

Hydrology

The second application area for coupled process simulation is hydrology. River basins or catchments are also subject to THMC coupled processes, of course in a completely different range of thermodynamic conditions as deep geological systems. Hydrological processes are very complex to describe as they vary highly in time and in space. The evaluation of groundwater recharge is most important to a sustainable water resources management (so called safe yield). To this purpose, i.e. the understanding of small scale phenomena such as root / soil water interaction is of tremendous significance [4]. Typically groundwater models are used for management purposes particularly in semi-arid areas as the Jordan Valley in the Middle East [5].

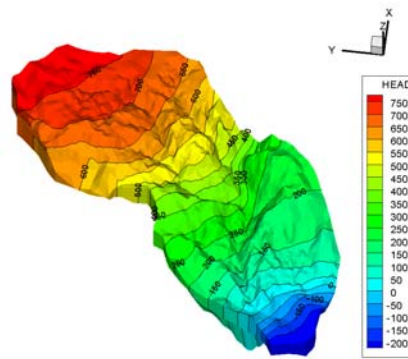


Figure 1.0.4: Groundwater model for the Wadi Kafrein catchment in Jordan

As water availability is an important issue in semi-arid and arid regions, groundwater quality is deteriorated in many urban areas of the world. Fig. 1.0.5 shows as an example a part of a groundwater quality model prepared for the Nankou basin in greater Beijing area. The idea of this modelling project is to identify possible sources for nitrate contamination originating from intense agriculture and fertilizer production [6]. Land use and climate changes will impact the availability and quality of water resources to a large degree in the future. The modelling should help to develop scenarios for improving the groundwater quality in the long term. Areas subject to large groundwater abstraction are also endangered to severe land subsidence.

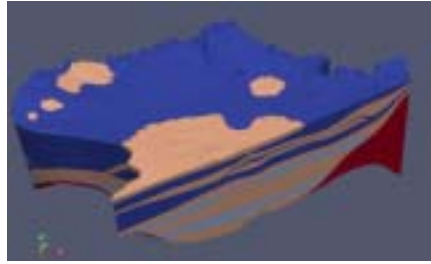


Figure 1.0.5: Nankou groundwater quality model [6]

1.0.1 Energy storage

A very recent research area for THMC modelling became energy storage. The economy and feasibility of renewable energy sources will depend on a large degree on efficient energy storage systems. Fig. 1.0.6 shows the numerical simulation of flow and heat distribution in a solid thermal energy storage block which will be used to store solar energy collected during days for use at nights (so called solar-thermics). The long term stability and efficiency of those energy storage devices can be optimized using THMC modelling (i.e. solving the inverse geothermal problem). In addition to thermal storage, thermo-chemical concepts are under development, i.e. storing thermal energy by triggering endothermic reactions and gaining thermal energy back on demand with the reverse reaction (exothermic).

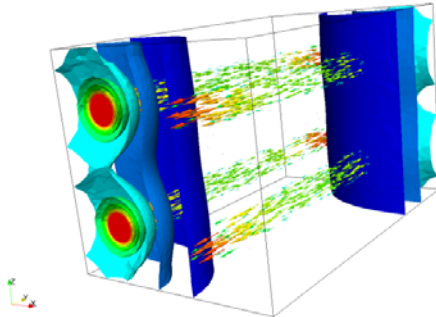


Figure 1.0.6: Optimizing energy storage concepts by modelling (OGS simulation by Wenqing Wang), [7]

Part I

Theory and Numerics

Symbols

Table 1.1: Latin symbols

Symbol	Meaning	Unit
c_p	Isobaric heat capacity	
c_v	Isochoric heat capacity	
C_4, C_{ijkl}	Consistent material tensor	
C	Concentration	kgm^{-3}
C_S	Sorbed concentration	$kgkg^{-1}$
d	Total (material) derivative	
$\mathbf{d} = \dot{\boldsymbol{\varepsilon}}$	Strain rate tensor	
\mathbf{D}	Hydrodynamic dispersion tensor	
e	Energy density	J/kg
\mathbf{e}_i	Cartesian base vectors, $i = 1, 2, 3$	
E	Youngs modulus	$1/Pa$
\mathbf{f}	Force density	
f	Phase distribution function	
$f(\rho, T)$	Helmholtz free energy	
\mathcal{F}	Resultant force	
\mathbf{g}	Gravity force	m/s^2
G	Shear modulus	
h	Piezometric (hydraulic head)	m
h	Specific enthalpy	
i	Internal energy density	$J kg^{-1}$
\mathbf{I}	Identity tensor	
\mathbf{j}	Flux density	
\mathbf{k}	Permeability tensor	m^2
K	Bulk modulus	
m	Mass density	kg/m^3
M	Mass	
n	Porosity	m^3/m^3
\mathbf{n}	Normal vector	
p	Pressure	Pa
p_c	Capillary pressure	Pa
\mathcal{P}	Material point	

Table 1.2: Latin symbols (cont.)

Symbol	Meaning	Unit
q	Source/sink term density	
Q	Source/sink term	
R	Gas constant	
s	Entropy	
S	Saturation	m^3/m^3
t	Time	s
\mathbf{t}	Traction (surface force density, Cauchy stress vector)	
T	Temperature	K
\mathbf{u}	Displacement vector	m
$\bar{\mathbf{u}}$	Displacement vector	m
\mathbf{x}	Position vector	m
x_1, x_2, x_3	Cartesian coordinates	m
\mathbf{X}	Reference position vector	m
v	Seepage velocity	m/s
\mathbf{v}	Velocity vector	$m s^{-1}$
v	Partial volume	m^3
V	Volume	m^3
V_m	Molare volume	
w	Darcy (filter) velocity	m/s
\mathbf{w}	Interface velocity vector	$m s^{-1}$

Table 1.3: Greek symbols

Symbol	Meaning	Unit
α	Phase indicator	
α_L	Longitudinal dispersivity	m
α_T	Transverse dispersivity	m
α_T	Thermal expansion coefficient	$1/K$
γ	Fluid phase indicator	
Γ	Model domain surface	
δ_{ij}	Kronecker symbol	
ϵ	Volume fraction	
ε	Strain tensor	
ε_d	Deviatoric strain tensor	
ε_v	Volumetric strain tensor	
η	Viscosity	
θ	Moisture content	m^3/m^3
λ	Pore size distribution index	
λ	Lamé constant	
λ	Thermal conductivity	
λ_c	Creep multiplier	
λ	Filtration coefficient	$m^{(}-1)$
μ	Dynamic viscosity	
μ	Lamé constant	
ν	Poisson ratio	
ρ	Material density	kg/m^3
σ	Cauchy stress tensor	
τ	Kirchhoff stress tensor	
ϕ	Individual constituent	
Φ	Flux vector	
Φ_c	Creep potential	
Φ_{pl}	Plastic potential	
χ	Effective stress parameter	
ψ	General intensive conservation quantity	
Ψ	General extensive conservation quantity	
ω	Gravimetric water content	
ω	Acentric factor	
Ω	Control volume, representative elementary volume (REV)	

ToDo

- Eqn or equation
- ψ or φ
- q or w (interface velocity)

Table 1.4: Math symbols

Symbol	Meaning	Unit
tr	Trace of ...	
$\nabla()$	Gradient operator	
$\nabla \cdot ()$	Divergence operator	
∂	Partial differential	
\otimes	Dyadic product	
A^T	Transpose of ...	
A_{ij}	Tensor components	
\dot{A}	Time derivative	s^{-1}
A_k	k component (e.g. chemical species)	
A'	Fluctuation of a quantity	
\bar{A}	Mean value of a quantity	
A^α		
A_{sw}	Swelling property	
A_{eff}	Effective property	
$A^{\alpha R}$	Material phase property	
A_r	Residual property	
A^w	Wetting property	
A^{nw}	Non-wetting property	
A_{el}	Elastic property	
A_{pl}	Plastic property	
A_0	Reference property	
A_{th}	Thermal property	
A_{ex}	Excess property	
A_c	Critical property (at critical point)	
\mathbf{A}	Vector	
\mathbf{A}	Tensor	

Chapter 2

Theory July 26, 2011

by Olaf Kolditz, Norbert Böttcher and Uwe-Jens Görke

Concerning the theoretical background of flow, transport, deformation, and reaction processes in porous media, there is a considerable amount of monographic literature available [8, 9, 10, 11, 12, 13, 14, 15]. The idea of this chapter is to provide a concise brief-as-possible description (compendium-like) of governing equations for thermo-hydro-mechanical / chemical [THM/C] processes in porous media. We will point to literature references rather than giving detailed derivations of the governing equations. This part is the theoretical basis for all benchmarks and examples upcoming in part II and III of this book. We will refer to this part in the examples sections where the working equations are briefly repeated. A list of symbols can be found in the Appendix.

From the mechanical point of view we consider non-isothermal flow of multiple fluid phases (compressible and incompressible fluids) in a deformable thermo-poro-elastic porous medium based on Biot's consolidation concept. A short introduction to continuum mechanics is given in section 2.1, followed by basic conservations principles (section 2.1.4) as well as an introduction to theory of porous medium (section 2.2). The followings steps are conducted to derive the general field equations:

- Macroscopic balance equations for mass, momentum and energy conservation of porous media (section 2.3),
- Constitutive relationships for non-isothermal multiphase flow and deformation processes in porous media, (sections 2.4 and 2.5),
- Applying the constitutive relationships and introducing physically based simplifications to the balance equations for the derivation of the general field equations. (parts II and III).

2.1 Continuum mechanics

The basic idea of continuum mechanics is that the evolution of a physical system is completely determined by conservation laws, i.e. basic properties such as mass, momentum, and energy are conserved during the considered process at all times. Any physical system can be completely determined by these conservation properties. In contrast, other quantities such as pressure or entropy do not obey conservation laws. The only additional information concerns the consistence of the material (e.g. fluids, solids, porous medium) in form of constitutive laws.

The concept of conservation means that the variation of a conservation quantity within a given control volume is due to the net effect of internal *sources* and of the amount of the quantity which is crossing the boundary surface of the considered volume - *fluxes*. Sources and fluxes are, in general, dependent of space-time coordinates as well as on mechanical and thermodynamic factors. Fluxes result from two contributions: first due to advective transport by fluid motion and second due to diffusion/dispersion processes. Diffusion is always present even when the fluid is at rest. Diffusion is the tendency towards equilibrium or homogeneity of a physical system.

The mechanical description of coupled thermo-hydro-mechanical (THM) processes in porous media is closely associated with the deformation of the solid phase, and the interaction of deformation and flow processes. Each solid material body (including the solid phase of a porous medium) can exhibit different kinds of motion (section 2.1.2):

- rigid body motion (translation or rotation of the body without changing its volume or shape), and
- deformation (local relative change of lengths and/or angles referred to neighboring particles, resulting in variations of the shape and/or volume of the material body under consideration).

Deformation processes of a porous medium interact with hydraulic processes of the coupled physical system particularly in the following way:

- effects on the stress state within the solid phase due to pore pressure evolution (with possible risk of rock failure), and
- variations of the pore size distribution due to the deformation of the solid skeleton, which affect the hydraulic properties, and thus, have an impact on the flow processes in the porous medium.

The analysis of deformation processes considered as mechanical response of the material body to the action of applied external forces is one of the objects of mechanics (micromechanics, continuum mechanics, CITATIONS). Porous media distinguish themselves by a sophisticated complex microstructure, whose

realistic simulation is extremely challenging, and from a practical point of view generally not efficient. Therefore, continuum mechanics (which is based on the assumption that matter is continuously distributed in space) provides the preferred approaches for the mathematical modeling of deformation processes in porous media. Appropriate models are not based on a physical characterization of the real microstructure, but consider their effects on the physical behavior in a phenomenological manner (section 2.2).

General statements of mechanics, which are independent of the specific material under consideration, refer to the kinematics of motion (shortly described in a following section) and the balance relations (section 2.3). By contrast, individual material dependent statements refer to the constitutive relations (section 2.5). Just both the balance relations as well as the constitutive relations constitute a mathematically closed system of equations to solve initial-boundary value problems of mechanics.

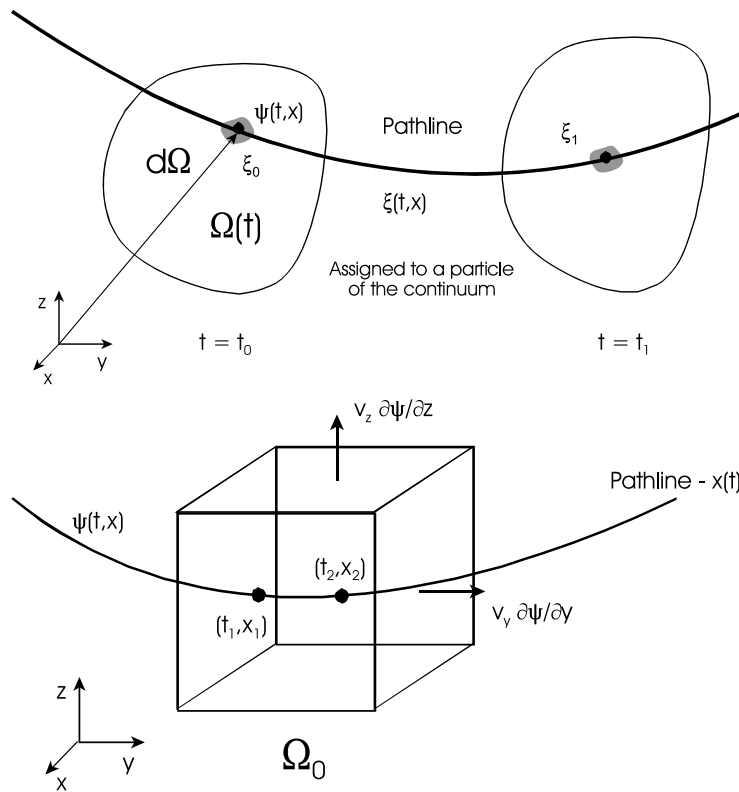


Figure 2.1.1: Two basic descriptions of motion - Langrangian (top) and Eulerian principles (bottom), adopted from [16]

2.1.1 Lagrangian and Eulerian principles

In the Lagrangian formulation we follow the quantity along a pathline, i.e. following particles (Fig. 2.1.1, top). In the Eulerian formulation of motion we consider variations of the quantity with respect to a fixed control volume at fixed places (Fig. 2.1.1, bottom).

A pathline is a curve along which a fixed particle of a continuum moves during a sequence of time. Pathline is Lagrangian concept of motion. A streamline is a curve along which a sequence of particles moves at a given time. By definition, the tangent to a streamline coincides with the velocity vector at that point. Streamline is Eulerian concept of motion. Note, for unsteady flow the streamline may vary from one instant to the next, whereas for steady flow streamlines remain unchanged with time. For steady motion both pathlines and streamlines coincide. Any particle will remain on a given streamline as time proceeds. Additional terms associated with kinematics of continua are the following (see also section 2.1.2).

2.1.2 Kinematics of continua

Kinematics analyzes the geometry of motion in general, and of deformation processes in particular. It is based on the assumption that a material (physical) body \mathcal{B} , which represents a set of elements \mathcal{P} called material points (aka: material elements, particles), at each moment of time can be uniquely defined with certain parts (usually different if motion occurs) of space. Assigning the material body particularly to its image in the three-dimensional Euclidean space of physical observations, the location of each material point at each time can be identified with the position vector $\mathbf{x}(t)$ in a physically well-founded manner. Consequently, the position vector can be represented by its Cartesian coordinates x_1, x_2, x_3 . In order to characterize the motion of a material body uniquely with respect to a reference state, the domain in space occupied by the material body at an arbitrarily selected time t_0 is of an emphasized significance. Usually in porous media mechanics, an appropriately chosen initial state of the solid skeleton is chosen as the reference state. The position vectors to define the positions of the material points at t_0 are denoted as \mathbf{X} .

One of the primary variables within the context of the numerical simulation of coupled THM processes is the displacement vector \mathbf{u} of the solid phase. The displacement vector is a commonly used kinematic variable to describe the motion (rigid body motion and/or deformation) of a solid material, and quantifies the change in the position of a given material point (cf. Fig. 2.1.2).

$$\mathbf{u}(\mathbf{X}, t) = \mathbf{x}(\mathbf{X}, t) - \mathbf{X} \quad (2.1)$$

In other words: the displacement vector connects the current position \mathbf{x} of a material point which under the impact of external forces has been moved, and was located at time t_0 at the position \mathbf{X} . As, in general, the displacement

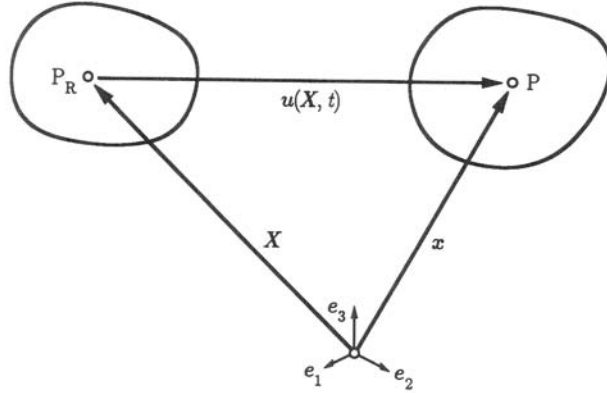


Figure 2.1.2: Definition of the displacement vector as the difference of the position vectors \mathbf{x} and \mathbf{X} of a material point (particle) of the body under consideration at various time t (current time) and t_0 [17]

vector will vary locally and temporally, $\mathbf{u}(\mathbf{X}, t) = \mathbf{u}(\mathbf{X}(\mathbf{x}, t), t) = \bar{\mathbf{u}}(\mathbf{x}, t) \equiv \mathbf{u}$ represents a vector field as function of space and time.

For the sake of the possible comparison of the response of material bodies, which are composed of different materials and/or have a different geometry, to the impact of external forces it is not reasonable to deal with the physically obvious variables displacement and force, but rather to introduce relative physical variables like strain and stress measures. Strain measures represent second-order kinematic tensor variables characterizing the local deformation processes, which deviate from the rigid body motion of a material body.

Based on the definition of the displacement gradient

$$\nabla \bar{\mathbf{u}}(\mathbf{x}, t) = \frac{\partial u_i}{\partial x_j} \mathbf{e}_i \otimes \mathbf{e}_j \quad (2.2)$$

with the orthonormal system of Cartesian base vectors \mathbf{e}_i ($i = 1, 2, 3$), the strain tensor $\boldsymbol{\varepsilon}(\mathbf{x}, t)$ in case of small (infinitesimal) deformations is established as the symmetric part of the displacement gradient.

$$\boldsymbol{\varepsilon}(\mathbf{x}, t) = \frac{1}{2} \left(\nabla \bar{\mathbf{u}}(\mathbf{x}, t) + (\nabla \bar{\mathbf{u}}(\mathbf{x}, t))^T \right) \quad (2.3)$$

The matrix of the coefficients of the strain tensor consists of so-called normal components

$$\varepsilon_{ii} = \frac{\partial u_i}{\partial x_i} \quad (2.4)$$

and shear components.

$$\varepsilon_{ij} = \frac{1}{2} \left(\frac{\partial u_i}{\partial x_j} + \frac{\partial u_j}{\partial x_i} \right) \quad (i \neq j) \quad (2.5)$$

For special cases it can be easily shown that normal strain is geometrically interpreted as elongation of material line elements (Fig. 2.1.3),

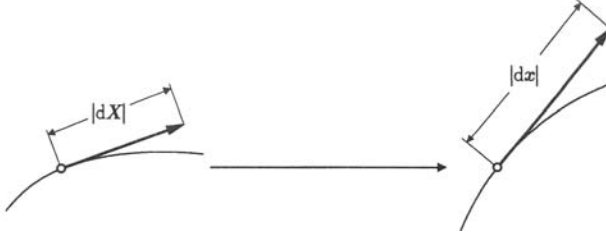


Figure 2.1.3: Extension (normal strain) of a material line element $d\mathbf{X} = |d\mathbf{X}|e$ [17]

and shear strain represents the change of the angle between two material line elements, which initially were perpendicular to each other (Fig. 2.1.4).

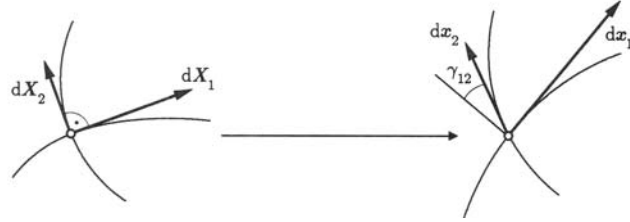


Figure 2.1.4: Shear (shear strain) of two material line elements $d\mathbf{X}_1 = |d\mathbf{X}_1|e_1$ and $d\mathbf{X}_2 = |d\mathbf{X}_2|e_2$, which are orthogonal in the undeformed state [17]

For the analysis of certain deformation processes it is reasonable to consider local volume changes and shape changes separately. Within this context, the strain tensor can be additively split into two parts: a volumetric ε_v and a so-called deviatoric (volume-preserving) ε_d one.

$$\boldsymbol{\varepsilon} = \boldsymbol{\varepsilon}_d + \boldsymbol{\varepsilon}_v \quad (2.6)$$

The individual partial strain tensors are defined as follows:

$$\boldsymbol{\varepsilon}_v = \frac{1}{3} \text{tr}(\boldsymbol{\varepsilon}) \mathbf{I} = \frac{1}{3} (\varepsilon_{11} + \varepsilon_{22} + \varepsilon_{33}) \mathbf{I} \quad (2.7)$$

$$\boldsymbol{\varepsilon}_d = \boldsymbol{\varepsilon} - \boldsymbol{\varepsilon}_v \quad (2.8)$$

Based on the definition

$$\mathbf{v}^s(\mathbf{x}, t) = \dot{\bar{\mathbf{u}}}(\mathbf{x}, t) \quad (2.9)$$

of the velocity of material points of the solid skeleton, the strain rate tensor

$$\dot{\boldsymbol{\varepsilon}}(\mathbf{x}, t) = \mathbf{d}(\mathbf{x}, t) = \frac{1}{2} \left(\nabla \mathbf{v}^s(\mathbf{x}, t) + (\nabla \mathbf{v}^s(\mathbf{x}, t))^T \right) \quad (2.10)$$

with its coefficients

$$d_{ij} = \frac{1}{2} \left(\frac{\partial v_i^s}{\partial x_j} + \frac{\partial v_j^s}{\partial x_i} \right) \quad (2.11)$$

can be defined, which is necessary for the investigation of deformation processes in case of rate-dependent material behavior.

In case of small strains, which was assumed here, the relation between the strain tensor and the displacement vector is a linear one (see section (2.3)). Considering large strains, the definition of appropriate strain measures requires more sophisticated reflections about the kinematics of motion. As a result, different strain tensors can be obtained representing non-linear functions of the displacement vector.

2.1.3 Stress Tensor

The momentum as well as the moment of momentum of a material body are affected by external forces acting on it, which represent the mechanical effect of the surroundings (cf. Fig. 2.1.5). Summarizing all local forces, the resultant force \mathcal{F} can be defined.

$$\mathcal{F} = \int_{\partial\mathcal{B}} \mathbf{t} da + \int_{\mathcal{B}} \mathbf{f} dm = \int_{\Gamma} \mathbf{t}(\mathbf{x}, t, \mathbf{n}) d\Gamma + \int_{\Omega} \mathbf{f}_v(\mathbf{x}, t) \varrho(\mathbf{x}, t) d\Omega \quad (2.12)$$

Generally, the material body under consideration bears forces distributed over its surface with the surface force density \mathbf{t} (traction, Cauchy stress vector), and forces distributed over the volume of the material body with the volume force density (mass distributed specific volume force) \mathbf{f}_v . As mentioned above, only gravity ϱg should be considered as specific volume force.

The traction vector $\mathbf{t}(\mathbf{x}, t, \mathbf{n})$ is considered to be a function of the location of its action on the surface, a function of time and of the normal vector, which characterizes the orientation of the surface element $d\Gamma$. Assuming a linear relation between the traction and the normal vector (Cauchy's theorem), the stress measure $\boldsymbol{\sigma}(\mathbf{x}, t)$ (Cauchy stress tensor) is defined as a link between surface traction and surface orientation.

$$\mathbf{t}(\mathbf{x}, t, \mathbf{n}) = \boldsymbol{\sigma}(\mathbf{x}, t) \mathbf{n} \quad \Rightarrow \quad \boldsymbol{\sigma} = \sigma_{ij} \mathbf{e}_i \otimes \mathbf{e}_j \quad (2.13)$$

Based on Cauchy's theorem, the differential surface force $d\mathbf{f}_0$ acting on a surface element can be obtained.

$$d\mathbf{f}_0 = \mathbf{t} d\Gamma = (\boldsymbol{\sigma} \mathbf{n}) d\Gamma = \boldsymbol{\sigma} (\mathbf{n} d\Gamma) = \boldsymbol{\sigma} d\Gamma \quad (2.14)$$

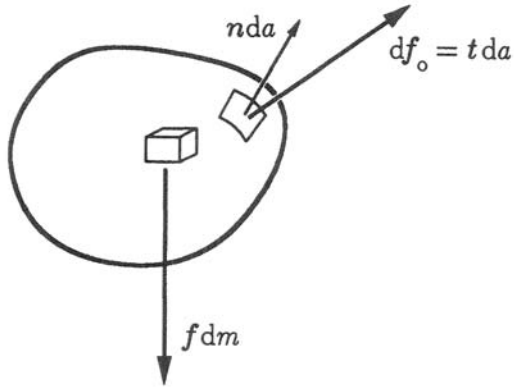


Figure 2.1.5: External volume and surface forces acting on infinitesimal geometrical elements of a material body [17]

For certain cases it is reasonable to use the so-called Kirchhoff stress tensor τ , a weighted Cauchy stress measure, instead of the Cauchy stress tensor itself.

$$\tau = \frac{\rho_0}{\varrho} \sigma \quad (2.15)$$

The second-order stress tensor characterizes the local internal load state referring to a material point of the body under consideration. Generally, it can be defined by three stress vectors acting on three faces of an infinitesimal tetrahedron, which are perpendicular to each other analyzing the equilibrium of forces for this domain. The coefficients of the resulting stress tensor are denoted by two indices – the first indicates the direction of the normal vector of the face under consideration, the second one the direction of the stress coefficient (see Fig. 2.1.6 for the three-dimensional case).

The sign convention, usually applied in continuum mechanics, implies positive stress coefficients coinciding with the directions of the axes of coordinates at faces with normal vectors also coinciding with the directions of the axes of coordinates. Consequently, tensile stress coefficients are positive, compressive stresses negative. Positive stress coefficients on opposite faces are oppositely directed (but of equal absolute value). The matrix of the coefficients of the (Kirchhoff) stress tensor is composed as follows:

$$\tau_{ij} = \begin{pmatrix} \tau_{xx} & \tau_{xy} & \tau_{xz} \\ \tau_{yx} & \tau_{yy} & \tau_{yz} \\ \tau_{zx} & \tau_{zy} & \tau_{zz} \end{pmatrix} \quad (2.16)$$

Analogous to the strain tensor, the coefficients τ_{xx} , τ_{yy} , τ_{zz} are called normal stresses, the coefficients τ_{ij} ($i \neq j$) shear stresses with $\tau_{ij} = \tau_{ji}$ (symmetry of the stress tensor, which results from the balance of moment of momentum).

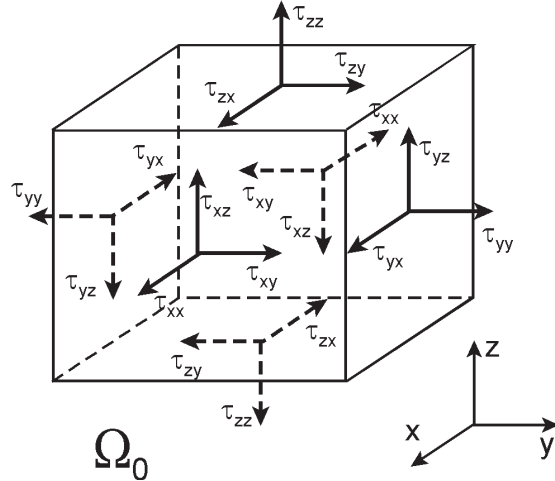


Figure 2.1.6: Coefficients of the stress tensor acting on a small hexahedral element [16]

In the special uniaxial stress case only at one face of a volume element a normal stress occurs, whereas all the other faces are stress-free. Consequently, the stress coefficient is calculated as the force acting on the face under consideration divided by its area.

2.1.4 Conservation principles

1

Based on the kinematical foundation (section 2.1.2) we formulate the general conservation principle of continuum mechanics for both Eulerian and Lagrangian points of view (section 2.1.1). The amount of a (conservation) quantity in a defined volume Ω is given by

$$\Psi = \int_{\Omega} \psi d\Omega(t) \quad (2.17)$$

where Ψ is an extensive conservation quantity (i.e. mass, momentum, energy) and ψ is the corresponding intensive conservation quantity such as mass density ρ , momentum density $\rho\mathbf{v}$ or energy density e (see Table 2.1).

The balance equations for mass, momentum and energy conservation can be derived based on two fundamental principles, i.e. Eulerian and Lagrangian

¹Truesduell

Table 2.1: Conservation quantities

Extensive quantity	Symbol	Intensive quantity	Symbol
Mass	M, M_k	Mass density	ρ, ρ_k
Linear momentum	\mathbf{m}	Linear momentum density	$\rho \mathbf{v}$
Energy	E	Energy density	$e = \rho i + \frac{1}{2} \rho v^2$

frameworks (e.g. [16]) Both conservation principles are related by two different forms of derivatives

$$\frac{d\psi}{dt} = \frac{\partial\psi}{\partial t} + \mathbf{v} \cdot \nabla\psi \quad (2.18)$$

the total (or material) d and partial derivatives ∂ , respectively. The general integral balance equation is given by

$$\frac{d}{dt} \int_{\Omega} \psi d\Omega = \int_{\Omega} \left(\frac{\partial\psi}{\partial t} + \nabla \cdot \Phi \right) d\Omega = \int_{\Omega} q^{\psi} d\Omega \quad (2.19)$$

where ψ is a general conservation quantity, Φ is the total flux of ψ , and Q is a source/sink term for ψ . The corresponding extensive and intensive conservation quantities are summarized in Tab. 2.1.

The total flux Φ^{ψ} of a quantity ψ is defined as

$$\Phi^{\psi} = \mathbf{v}^E \psi \quad (2.20)$$

where \mathbf{v}^E is a mean particle velocity. Physically Φ^{ψ} represents the quantity of ψ passing through a unit area of the continuum, colinear with \mathbf{v}^E , per unit time with respect to a fixed coordinate system, i.e. Eulerian point of view.

For the case of a multi-component continuum let \mathbf{v} denote the mass-weighted velocity describing a more ordered motion of the particles of a fluid element. The total flux can be written as

$$\Phi^{\psi} = \mathbf{v}^E \psi = \underbrace{\mathbf{v}\psi}_{\Phi_A^{\psi}} + \underbrace{(\mathbf{v}^E - \mathbf{v})\psi}_{\Phi_D^{\psi}} \quad (2.21)$$

and, therefore, decomposed into two parts: an advective flux Φ_A^{ψ} and a diffusive flux Φ_D^{ψ} relative to the mass-weighted velocity:

- Advective flux of quantity ψ

$$\Phi_A^{\psi} = \mathbf{v}\psi \quad (2.22)$$

- Diffusive flux of quantity ψ (Fick's law)

$$\Phi_D^\psi = -\alpha \nabla \psi \quad (2.23)$$

where α is a diffusivity coefficient. The negative sign indicates, that diffusive flux is positive in the direction of negative gradient.

If the conservation quantity is a vector (e.g. linear momentum) then the flux becomes a tensor and the source term a vector (e.g. body forces):

- Advection flux of vector quantity ψ

$$\Phi_A^\psi = \mathbf{v} : \psi = [v_x \ v_y \ v_z] \begin{bmatrix} \psi_x \\ \psi_y \\ \psi_z \end{bmatrix} = \begin{vmatrix} v_x \psi_x & v_x \psi_y & v_x \psi_z \\ v_y \psi_x & v_y \psi_y & v_y \psi_z \\ v_z \psi_x & v_z \psi_y & v_z \psi_z \end{vmatrix} \quad (2.24)$$

- Diffusive flux of vector quantity ψ

$$\Phi_D^\psi = -\rho \nabla : \psi = -\alpha \begin{vmatrix} \frac{\partial \psi_x}{\partial x} & \frac{\partial \psi_y}{\partial y} & \frac{\partial \psi_z}{\partial z} \\ \frac{\partial \psi_x}{\partial x} & \frac{\partial \psi_y}{\partial y} & \frac{\partial \psi_z}{\partial z} \\ \frac{\partial \psi_x}{\partial x} & \frac{\partial \psi_y}{\partial y} & \frac{\partial \psi_z}{\partial z} \end{vmatrix} \quad (2.25)$$

When substituting the flux definition into the general balance equation (2.19), we yield the so-called transport equation

$$\frac{d}{dt} \int_{\Omega} \psi \, d\Omega = \underbrace{\int_{\Omega} \frac{\partial \psi}{\partial t} \, d\Omega}_1 + \underbrace{\int_{\Omega} \nabla \cdot (\mathbf{v} \psi) \, d\Omega}_2 - \underbrace{\int_{\Omega} \nabla \cdot (\alpha \nabla \psi) \, d\Omega}_3 = \underbrace{\int_{\Omega} q^\psi \, d\Omega}_4 \quad (2.26)$$

with the followind terms:

1. Rate of increase of ψ within a fluid element
2. Net rate of ψ due to flux out of the fluid element
3. Rate of increase / decrease of ψ due to diffusion
4. Rate of increase / decrease of ψ due to sources

2.2 Porous medium

Soil or rock can be considered as a multiphase medium consisting of a solid phase (solid matrix) and of one or more fluid phases (gas and liquids), which occupy the void space (Fig. 2.2.8). Fluids are immiscible, if a sharp interface is maintained between them. In general, a phase is defined as a part of a continuum, which is characterized by distinct material properties and by a well-defined set of thermodynamic state variables. State variables describe the physical behaviour at all points of the phase. They must vary continuously within the considered phase of a continuum. Phases are separated from each other by surfaces referred to as interphase boundaries. Transport of components may occur within a phase and/or across interphase boundaries. Those interphasic exchange processes between adjacent phases can result from diffusive and/or advective mechanisms.

In fact, it is impossible to describe the complex geometry of the solid matrix and the topology of the void space at the microscopic level, i.e. the topology of the pore space will never be known in detail. As a consequence, boundary conditions for a mathematical model cannot be stated at this scale, since they are not known at the microscopic level. Moreover, it will be extremely difficult to measure values of state variables at each point within a phase in order to observe processes, to calibrate and to verify any model. Finally, the complete formulation and resolution of balance equations at the microscopic level is impossible and may not be reasonable. Therefore, it is necessary to transform the problem from a microscopic scale to a macroscopic level. Starting from the microscopic balance equations for extensive quantities (masses, momentum, energy), this procedure is the subject of the theory of the porous medium [8, 9, 10, 11, 12, 13, 14, 15]. The entire problem is rewritten in terms of averages of microscopic quantities, which have measurable values. The resulting macroscopic model is referred to as the continuum approach. This conceptual model implies that a real system is replaced by a number of overlapping continua representing the corresponding phases. It is assumed that each phase, occupying a certain part of the porous domain, is regarded as a continuum. These individual phases interact with each other at any place within the entire domain, because they are present at each point within the porous medium, i.e. all phases are completely mixed.

$$\Omega_0 = \sum_{\alpha} \Omega^{\alpha} \quad (2.27)$$

In addition to the porous medium approach, there exist different types of structural models for fractured rocks, which characterize the degree of inhomogeneity: the fractured medium and the fractured porous medium. The term fractured medium means that only the fractures are important for the considered process, so blocks surrounded by the fractures may be neglected in the model. The term fractured porous medium means that both fracture system and porous matrix are significant for the considered process. The domain of a fractured porous

medium consists of two subdomains, representing heterogeneities at different scales, i.e. the diameter of pores in the matrix and the characteristic length of fractures.

Appropriate averaging rules must be defined in order to realize the above described transformation from a microscopic to a macroscopic level. For this purpose, a well-defined sample size of an averaging volume must be found, which is referred to as the representative elementary volume (abbreviated REV). On the one hand, this averaging unit has to be sufficiently large, so that the influence of microscopic inhomogeneity on the values of averaged (macroscopic) quantities will vanish, i.e. they become independent of size, shape, and orientation of the REV. On the other hand, the REV must be small enough to reflect the macroscopic heterogeneity. In particular, the REV must be much smaller than the domain of interest, which may vary in size for a flow or a transport problem, respectively. From the mathematical point of view, the macroscopic (averaged) quantities must be continuous and differentiable functions (in space and in time), so that solutions of the governing differential balance equations can be determined. Finally, the continuum approach cannot be employed unless a common range of a REV can be selected for all material properties (e.g. porosity, permeability, dispersivity) as well as for all relevant state variables. This requirement is important with respect to the different conceptual models for fractured rock, which are introduced in the following.

2.2.1 Macroscopic Equations

In fact, it is impossible to describe the complex geometry of the solid matrix and the topology of the void space at the microscopic level, i.e. the topology of the pore space will never be known in detail. Therefore, a statistical approach is used for the derivation of balance equations at a macroscopic level. The physical property of a porous medium is decomposed in phase-related mean values $\bar{\psi}^\alpha$ and local fluctuations ψ'^α .

$$\psi^\alpha = \bar{\psi}^\alpha + \psi'^\alpha \quad (2.28)$$

An appropriate averaging volume is called the Representative Elementary Volume (REV) (Fig. 2.2.7).

Several averaging procedures can be defined [11]. As an example we consider volumetric averaging which is also denoted as the concept of volume fractions. The volumetric averaging operator is given by

$$\bar{\psi}^\alpha = \frac{1}{\epsilon^\alpha \Omega_0} \int_{\Omega_0} f^\alpha \psi^\alpha d\Omega \quad (2.29)$$

where α is the phase indicator, $\epsilon^\alpha = \Omega^\alpha / \Omega_0$ is the volumetric fraction of the α phase, Ω_0 is the averaging volume (corresponding to the representative elementary volume), $f^\alpha = 1/0$ (inside or outside α phase) is the phase distribution function.

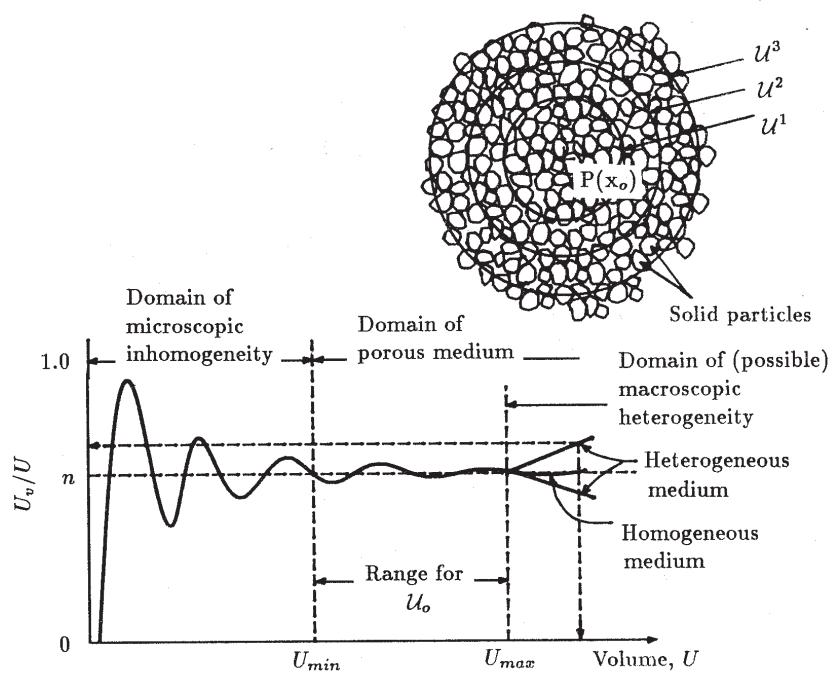


Figure 2.2.7: Definition of the representative elementary volume (REV) [11]

Due to the above definition the following averaging rules can be derived.

- Sum

$$\overline{\psi_1^\alpha + \psi_2^\alpha} = \overline{\psi_1^\alpha} + \overline{\psi_2^\alpha} \quad (2.30)$$

- Product

$$\overline{\psi_1^\alpha \psi_2^\alpha} = \overline{\psi_1^\alpha} \overline{\psi_2^\alpha} + \overline{\psi_1^\alpha} \overline{\psi_2^\alpha} \quad (2.31)$$

- Time derivative

$$\epsilon^\alpha \overline{\frac{\partial \psi^\alpha}{\partial t}} = \frac{\partial \epsilon^\alpha \overline{\psi^\alpha}}{\partial t} - \frac{1}{\Omega_0} \int_{S^{\alpha\beta}} \psi^\alpha \mathbf{w} \cdot d\mathbf{S} \quad (2.32)$$

- Spatial derivative

$$\epsilon^\alpha \overline{\nabla \psi^\alpha} = \nabla (\epsilon^\alpha \overline{\psi^\alpha}) + \frac{1}{\Omega_0} \int_{S^{\alpha\beta}} \psi^\alpha \cdot d\mathbf{S} \quad (2.33)$$

where \mathbf{w} is the velocity of the $\alpha\beta$ -phase interface.

To derive a phase related macroscopic balance equation, we have to average the balance equation in differential form for a certain phase (2.19). By use of the above averaging operators and rules the following general macroscopic balance equation can be obtained.

$$\begin{aligned} \frac{\partial \epsilon^\alpha \overline{\psi^\alpha}}{\partial t} &= -\nabla \cdot (\epsilon^\alpha \bar{\psi}^\alpha \mathbf{v}^\alpha + \epsilon^\alpha \overline{\psi'^\alpha} \mathbf{v}'^\alpha + \epsilon^\alpha \overline{\Phi_{\text{Diff}}^{\psi^\alpha}}) \\ &- \frac{1}{\Omega_0} \int_{S^{\alpha\beta}} \Phi_{\text{Diff}}^{\psi^\alpha} \cdot d\mathbf{S} - \frac{1}{\Omega_0} \int_{S^{\alpha\beta}} \psi^\alpha (\mathbf{v} - \mathbf{w}) \cdot d\mathbf{S} + q^{\psi^\alpha} \end{aligned} \quad (2.34)$$

with the dispersive flux

$$\Phi_{\text{Disp}}^{\psi^\alpha} = \epsilon^\alpha \overline{\psi'^\alpha} \mathbf{v}'^\alpha \quad (2.35)$$

2.2.2 Theory of Mixtures

The Theory of Mixtures as one of the basic approaches to model the complex behavior of porous media has been developed over decades (concerning basic assumptions see e.g. [18, 19]). As the Theory of Mixtures does not incorporate any information about the microscopic structure of the material², it has been combined with the Concept of Volume Fractions by e.g. [20, 21, 14, 22]. Within the context of this enhanced Theory of Mixtures (also known as Theory of Porous Media), all kinematical and physical quantities can be considered at the macroscale as local statistical averages of their values at the underlying microscale. Concerning a detailed overview about the history of the modeling of the behavior of multiphase multicomponent porous media, the reader is referred to e.g. [15]. Comprehensive studies about the theoretical foundation and numerical algorithms for the simulation of coupled problems of multiphase continua are given in e.g. [15, 23, 14] and the quotations therein.

The individual constituents φ^α of a porous material represent the phases of the overall aggregate or components within a phase. Below, $\alpha = s$ marks one immiscible solid phase (no sorption processes are considered), and $\alpha = \gamma$ denote several immiscible pore fluid phases. A porous medium, however, consists of multiple phases (fluids such as water, air and non-aqueous phase liquids (NAPLs) as well as solids). Moreover, these phases can contain several chemical components which can be dissolved in liquids or adsorbed to the solid phase (Fig. 2.2.8).

²Within the context of the Theory of Mixtures the ideal mixture of all constituents of a multiphase medium is postulated. Consequently, the realistic modeling of the mutual interactions of the constituents is difficult.



Figure 2.2.8: Conceptual approach of a porous medium model, adopted from [16]

Within the framework of the Concept of Volume Fractions, scalar variables like volume fractions and saturations are defined to describe the microstructure of a porous medium in a macroscopic manner neglecting the real topology and distribution of the pores. These variables serve as measures of local fractions of the individual constituents. The volume fractions n^α represent the ratio of the partial volume dv^α of a given constituent φ^α of a multiphase body with respect to the overall volume dv of a representative elementary volume (REV) of the control domain Ω under consideration. Consequently, based on the definitions of the overall volume of the control domain

$$V = \int_{\Omega} dv \quad (2.36)$$

and the corresponding partial volumes of the individual constituents

$$V^\alpha = \int_{\Omega} dv^\alpha \quad \text{with} \quad V = \sum_{\alpha} V^\alpha \quad (2.37)$$

the volume fractions

$$n^\alpha = \frac{dv^\alpha}{dv} \quad (2.38)$$

provide some information about the local volume distribution of the individual constituents.

$$V^\alpha = \int_{\Omega} dv^\alpha = \int_{\Omega} n^\alpha dv \quad (2.39)$$

One of the most characteristic media properties of a porous material is the porosity, the local amount of fluid volume fractions.

$$n = \sum_{\gamma} n^\gamma = 1 - n^s \quad (2.40)$$

Since, in general, the overall medium is completely filled with matter, from Eqn. (2.37) follows the saturation condition regarding the overall aggregate.

$$\sum_{\alpha} n^{\alpha} = 1 \quad (2.41)$$

If multiphase flow occurs, it is more convenient for various applications to use the (partial) fluid saturations S^{γ} instead of the volume fractions. These local functions are given by

$$S^{\gamma} = \frac{dv^{\gamma}}{dv - dv^s} = \frac{n^{\gamma}}{n} \quad (2.42)$$

obviously fulfilling the saturation condition regarding the pore content.

$$\sum_{\gamma} S^{\gamma} = 1 \quad (2.43)$$

Usually, constraint conditions addressing real physical effects are formulated to simplify complex mathematical and numerical models. Within the context of porous media, it is reasonable in most applications to assume the (material) incompressibility of constituents as a substantial constraint condition. The issue of (in)compressibility of a material is closely connected to the possible temporal evolution of its mass density.

Within the framework of the Concept of Volume Fractions, two different formulations of mass density related to the constituents of a porous medium are introduced. The so-called material (effective, realistic) density $\rho^{\alpha R}$ is defined as the ratio of the mass fraction dm^{α} of the given individual constituent φ^{α} with respect to its partial volume fraction.

$$\rho^{\alpha R} = \frac{dm^{\alpha}}{dv^{\alpha}} \quad (2.44)$$

In contrast, the so-called partial (global, bulk) density is given by the ratio of the mass fraction of the constituent under consideration with respect to the volume fraction of the overall aggregate.

$$\rho^{\alpha} = \frac{dm^{\alpha}}{dv} \quad (2.45)$$

Based on the definition of the volume fractions (2.38), the material and the partial densities are correlated to each other.

$$\rho^{\alpha} = n^{\alpha} \rho^{\alpha R} \quad (2.46)$$

If the volume fractions change with time under external loading, from Eqn. (2.46) follows that for an intrinsically incompressible individual constituent (constant material mass density) compressibility referred to the overall aggregate is observed.

$$\rho^{\alpha R} = \text{const} \Rightarrow \rho^{\alpha} \neq \text{const} \quad \text{as} \quad n^{\alpha} \neq \text{const} \quad (2.47)$$

Obviously, the mass density of the porous medium (homogenized overall aggregate) is defined as the sum of the partial densities of its constituents.

$$\rho = \sum_{\alpha} \rho^{\alpha} \quad (2.48)$$

The conceptual idea behind the formulations and relations presented above consists in the assumption that the mass fractions of all constituents of the multiphase medium are simultaneously present and statistically uniformly distributed over the entire control domain. Within this context, the material body under consideration is theoretically substituted by an aggregate completely and continuously filled by superimposed (overlapping) homogenized partial continua. In other words, all constituents of a porous medium are characterized as smeared substitute continua with reduced mass densities. Consequently, the motion and physics of the individual constituents as well as the overall aggregate can be specified by well-accepted phenomenological methods of continuum mechanics.

Describing the transport and deformation of the constituents of porous media within the framework of continuum mechanics it is assumed that the geometry of the control domain under consideration is characterized at each time by the solid skeleton, whereas the fluid pore content is able to flow across the boundary of the surface. This assumption serves as conceptual nucleus for the simulation of complex, coupled physical processes in multiphase porous media, particularly if a deformable solid skeleton is observed. Within this context, it proves to be reasonable not to model the absolute motion state of the pore content, but its motion relative to the motion of the solid phase, considering the porous medium as a local thermodynamic open system with the solid skeleton as volume under observation.

The macroscopic characterization of the physical processes considering the real microstructural situation in a statistically averaged manner is completely adequate for the most hydrological, geotechnological and biomechanical problems under consideration (cf. [24] and others).

2.3 Balance equations

We derive the balance equations for phase and component masses as well as for momentum and energy of a porous medium.

2.3.1 Phase mass balance

We consider the mass balance of individual phases of a porous medium. Neglecting mass exchange between the phases (no dissolution and sorption processes), the local mass balance for the individual constituent φ^{α} of the porous medium

is given by

$$\frac{d_\alpha \rho^\alpha}{dt} + \rho^\alpha \nabla \cdot \mathbf{v}^\alpha = \frac{\partial \rho^\alpha}{\partial t} + \nabla \cdot (\rho^\alpha \mathbf{v}^\alpha) = 0 \quad (2.49)$$

with the velocity \mathbf{v}^α of the constituent under consideration, and the usual divergence operator $\nabla \cdot ()$. From the velocity-displacement relation for the solid skeleton follows

$$\mathbf{v}^s = \dot{\mathbf{u}}^s \quad (2.50)$$

with the solid displacement vector \mathbf{u}^s . The derivative

$$\frac{d_\alpha A}{dt} = \frac{\partial A}{\partial t} + \mathbf{v}^\alpha \cdot \nabla A \quad (2.51)$$

with the usual gradient operator $\nabla()$ denotes the material time derivative of an arbitrary variable A with respect to the motion of a material point of the constituent φ^α (cf. equation (2.18)). It consists of a local (diffusive) part and a convective part associated with the velocity of the constituent.

As mentioned above, the transport processes of the fluid constituents of a porous medium are considered as their relative motion with respect to the motion of the deformable solid skeleton. Consequently, the relations between the material time derivatives (here, of an arbitrary variable A) with respect to the solid skeleton, and with respect to the individual fluid constituent φ^γ is of crucial interest in terms of a unified numerical characterization of the different processes.

$$\frac{d_\gamma A}{dt} = \frac{d_s A}{dt} + \mathbf{v}^{\gamma s} \cdot \nabla A \quad (2.52)$$

Here,

$$\mathbf{v}^{\gamma s} = \mathbf{v}^\gamma - \dot{\mathbf{u}}^s \quad (2.53)$$

is the so-called seepage velocity describing the fluid motions with respect to the deforming skeleton material.

According to the generalized formulation (2.49), considering equations (2.40) and (2.46), the local solid phase mass balance is given by

$$\frac{d_s [(1-n)\rho^{sR}]}{dt} + (1-n) \rho^{sR} \nabla \cdot \dot{\mathbf{u}}^s = 0 \quad (2.54)$$

Assuming material incompressibility of the solid phase, i.e. $d_s \rho^{sR}/dt = 0$ we derive the following expression for porosity changes.

$$\frac{d_s n}{dt} = (1-n) \nabla \cdot \dot{\mathbf{u}}^s = 0 \quad (2.55)$$

Following the same procedure, additionally considering Eqns. (2.42) and (2.52), the mass balance relations for the fluid constituents φ^γ can be defined with respect to the solid phase motion.

$$\frac{d_s (nS^\gamma \rho^{\gamma R})}{dt} + \nabla \cdot (nS^\gamma \rho^{\gamma R} \mathbf{v}^{\gamma s}) + nS^\gamma \rho^{\gamma R} \nabla \cdot \dot{\mathbf{u}}^s = 0 \quad (2.56)$$

Applying the solid phase mass balance (2.54), Eqn. (2.56) can be represented in a more detailed description.

$$\begin{aligned} nS^\gamma \frac{d_s \rho^{\gamma R}}{dt} + n\rho^{\gamma R} \frac{d_s S^\gamma}{dt} \\ + \nabla \cdot (\rho^\gamma \mathbf{w}^{\gamma s}) + S^\gamma \rho^{\gamma R} \nabla \cdot \dot{\mathbf{u}}^s = 0 \end{aligned} \quad (2.57)$$

Here

$$\mathbf{w}^{\gamma s} = nS^\gamma \mathbf{v}^{\gamma s} \quad (2.58)$$

is usually denoted as filter velocity of the motion of the pore fluid constituent φ^γ .

Rewriting equation (2.57) in terms of partial derivatives we yield

$$\begin{aligned} nS^\gamma \frac{\partial \rho^{\gamma R}}{\partial t} + nS^\gamma \mathbf{v}^{\gamma s} \cdot \nabla \rho^{\gamma R} + n\rho^{\gamma R} \frac{\partial S^\gamma}{\partial t} + n\rho^{\gamma R} \mathbf{v}^{\gamma s} \cdot \nabla S^\gamma \\ + \nabla \cdot (\rho^\gamma nS^\gamma \mathbf{v}^{\gamma s}) + S^\gamma \rho^{\gamma R} \nabla \cdot \dot{\mathbf{u}}^s = 0 \end{aligned} \quad (2.59)$$

Primary variables

The selection of primary variables matters and is ruled by our interest in non-isothermal and non-isobaric processes which promotes the choice of pressure p and temperature T as primary variables. The substitutions of phase density

$$d\rho^\alpha(p, T) = \frac{\partial \rho^\alpha}{\partial p} dp + \frac{\partial \rho^\alpha}{\partial T} dT \quad (2.60)$$

and phase saturation

$$dS^\alpha(p, T) = \frac{\partial S^\alpha}{\partial p} dp + \frac{\partial S^\alpha}{\partial T} dT \quad (2.61)$$

will result in formulations of the phase mass balance equations in terms of the selected primary variables.

2.3.2 Momentum balance

Dealing with flow in porous and fractured media we have to consider the mechanics of fluids in tubes and channels. The governing equation for flow of incompressible viscous fluids is the well-known Navier-Stokes equation

$$\underbrace{\frac{\partial \mathbf{v}}{\partial t} + (\mathbf{v} \cdot \nabla) \mathbf{v}}_{\text{inertial terms}} = \mathbf{g} - \frac{1}{\rho} \nabla p + \underbrace{\frac{\mu}{\rho} \nabla^2 \mathbf{v}}_{\text{viscous term}} \quad (2.62)$$

The Navier-Stokes equation can be integrated for laminar flow in straight, circular tubes when steady-state boundary conditions are applied. In this case

convective acceleration term ($\mathbf{v} \cdot \nabla \mathbf{v}$) becomes zero. This solution is called the Hagen-Poiseuille equation [25].

$$\Delta p = \frac{8\mu L}{\pi R^4} Q \quad (2.63)$$

where Q is the volumetric flow rate, which is velocity multiplied by tube cross-section area, L is tube length and R is tube radius. The linear relationship between pressure drop and flow rate Q breaks down if convective acceleration and/or transient effects become important. The first case is denoted **non-linear laminar flow**, when inertial effects become important, e.g. due to curvature of tubes or channels. The second case is related to **turbulent flow**, when flow pattern become transient due to velocity fluctuations.

Confusion between non-linear laminar flow and 'true' turbulent flow may arise from the fact that - concerning the relationship between pressure drop and the flow rate - inertia effects in laminar flow are expressed in the same fashion as in turbulent flows

$$\Delta p = AQ + BQ^2. \quad (2.64)$$

This means if inertia effects or turbulence effects become significant, the relationship between pressure drop and flow rate (2.63) is no longer linear. Therefore, we have to distinguish between three different flow regimes: linear laminar flow, non-linear laminar flow and 'true' turbulent flow. Equation (2.64) is known as the Forchheimer equation [26].

[27] found that the volume of fluid percolating through a sand column is proportional to the applied pressure difference

$$Q = qA = A \frac{k}{\mu} \frac{\Delta p}{L} \rightarrow \Delta p = \frac{L}{A} \frac{\mu}{k} Q. \quad (2.65)$$

Comparing the structure of equations (2.65) and (2.63), the analogy between porous media flow and tube flow becomes obvious. Both equations are characterized by linear relationships between pressure drop and flow rate.

Darcy's law can be derived from the Navier-Stokes equations. To this purpose a spatial averaging procedure over a representative elementary volume (REV) has to be conducted, where microscopic quantities are transformed into macroscopic ones [9]

$$\langle \psi \rangle = \frac{1}{\text{REV}} \int_{\text{REV}} \psi dV \quad (2.66)$$

where ψ is a local, microscopic quantity and $\langle \psi \rangle$ is a spatially averaged macroscopic quantity.³ For fractures the averaging procedure can be splitted into

³See also equation (2.29) for general definition of a mean value for a porous medium. Both notations $\bar{\psi}$ and $\langle \psi \rangle$ are common in literature.

two steps

$$\langle \psi \rangle = \frac{1}{2b \text{REA}} \int_{-b}^{+b} \int_{\text{REA}} \psi \, dx \, dA \quad (2.67)$$

where b is half fracture aperture and REA is a representative elementary area. In the following we deal with quantities which are averaged over fracture thickness and, therefore, are representative for a certain area of fracture surface.

Darcy's law is based essentially on the assumption that fluid motion is inertialess, i.e. inertial terms can be neglected with regard to viscous forces

$$0 = \langle \mathbf{g} \rangle - \frac{1}{\langle \rho \rangle} \nabla \langle p \rangle + \frac{\langle \mu \rangle}{\langle \rho \rangle} \nabla^2 \langle \mathbf{v} \rangle. \quad (2.68)$$

Brackets indicate macroscopic quantities. Thus Darcian flow is a special case of creeping flow for which viscous forces prevail over inertial forces. A central topic in porous medium theory is the determination of the viscous drag term. This leads to the concept of permeability for characterization of the hydromechanical properties of porous media [28]. Introducing permeability in the following manner

$$\nabla^2 \langle \mathbf{v} \rangle = -\mathbf{k}^{-1} \mathbf{w} \quad (2.69)$$

where k is the permeability of the porous medium and \mathbf{v} is the Darcy or seepage velocity, which are macroscopic quantities by definition. Substituting this expression into equation (2.68) we obtain

$$0 = \mathbf{g} - \frac{1}{\langle \rho \rangle} \nabla \langle p \rangle - \frac{\langle \mu \rangle}{\langle \rho \rangle} \mathbf{k}^{-1} \mathbf{w}. \quad (2.70)$$

Rearranging the terms, we yield the usual form of Darcy's law. We omit the averaging brackets in the following to keep the notation briefly

$$\mathbf{w} = -\frac{\mathbf{k}}{\mu} (\nabla p - \rho \mathbf{g}). \quad (2.71)$$

We emphasize that quantities in the above Darcy equation are macroscopic ones related to a certain REV of a porous medium, whereas quantities in the Navier-Stokes equation (2.62) have local meaning.

Darcy's law has been accepted as fundamental relationship for porous medium hydraulics. However, its validity is restricted to a certain range of geometric and physical conditions. Deviations from linearity between seepage velocity and pressure drop are denoted as non-Darcian flow. Geometric issues are concerned with pore and fracture geometry.

As described above we used the analogy to flow in straight tubes for explanation of hydromechanical processes in porous media. Tube bundles model is one

approach to hydromechanics of porous media. However in real geologic materials pores are curved, have varying cross-sections, may be sealed, and suffer from dead-end effects. Rock fractures are characterized by rough surfaces. Physical causes underlying non-linear effects can be high flow rates, molecular effects, ionic effects and non-Newtonian behavior of the fluid itself [29].

Darcy's law

For linear momentum conservation in porous media we assume, in general, that inertial forces can be neglected (i.e. $d\mathbf{v}/dt \approx 0$) and body forces are gravity at all. Assuming furthermore that internal fluid friction is small in comparison to friction on the fluid-solid interface and that turbulence effects can be neglected we obtain the Darcy law for each fluid phase γ in multiphase flow (cf. equation (2.58)).

$$\mathbf{w}^{\gamma s} = nS^\gamma(\mathbf{v}^\gamma - \mathbf{v}^s) = -nS^\gamma \left(\frac{k_{\text{rel}}^\gamma \mathbf{k}}{\mu^\gamma} (\nabla p^\gamma - \rho^\gamma \mathbf{g}) \right) \quad (2.72)$$

Non-isothermal consolidation

Deformation processes in porous media are described by the momentum balance equation in terms of the total Cauchy's stress tensor $\boldsymbol{\sigma}$, which is additively decomposed into several partial stresses according to different physical events. The specific local overall linear momentum balance equation is given as follows:

$$\begin{aligned} \nabla \cdot \left[\boldsymbol{\sigma}_{\text{eff}} & - \sum_\gamma (\chi(S^\gamma) p^\gamma) \mathbf{I} - \boldsymbol{\sigma}_{\text{sw}} \right. \\ & \left. - \alpha_T \Delta T \left(\frac{\mathbf{C}}{4} : \mathbf{I} \right) \right] + \rho \mathbf{g} = \mathbf{0} \end{aligned} \quad (2.73)$$

The representation of the stress decomposition (2.73) is based on a modified effective stress law presented in [30], where $\boldsymbol{\sigma}_{\text{eff}}$ is the macroscopic effective stress tensor, χ is the saturation dependent effective stress parameter of Bishop's type [31], $\boldsymbol{\sigma}_{\text{sw}}$ denotes the swelling stress, α is the thermal expansion coefficient, \mathbf{I} represents the second-order identity tensor, $\frac{\mathbf{C}}{4}$ is the fourth-order elastic material tensor, which will be discussed later, and \mathbf{g} is the gravity vector.

2.3.3 Energy balance

Heat transport

The equation of energy conservation is derived from the first law of thermodynamics which states that the variation of total energy of a system is due to the work of acting forces and heat transmitted to the system.

The total energy per unit mass e specific energy) can be defined as the sum of internal (thermal) energy i and specific kinetic energy $v^2/2$. Internal energy is due to molecular movement. Gravitation is considered as an energy source term, i.e. a body force which does work on the fluid element as it moves through the gravity field. The conservation quantity for energy balance is total energy density

$$\psi^e = \rho e = \rho(i + v^2/2) \quad (2.74)$$

Using mass and momentum conservation we can derive the following balance equation for the internal energy.

$$\rho \frac{di}{dt} = \rho q^i - \nabla \cdot \mathbf{j}_{\text{th}} + \sigma \cdot \nabla \mathbf{v} \quad (2.75)$$

where q^i is the internal energy (heat) source, \mathbf{j}_{th} is the diffusive heat flux. Applying the chain to the left hand side of the above equation yields

$$\rho \frac{di}{dt} = \rho \frac{dcT}{dt} = \rho c \frac{dT}{dt} + \rho T \frac{dc}{dt} \quad (2.76)$$

as well as the definition of the material derivative

$$\frac{dT}{dt} = \frac{\partial T}{\partial t} + \mathbf{v} \cdot \nabla T \quad (2.77)$$

we obtain the heat energy balance equation

$$\rho c \frac{\partial T}{\partial t} + \rho c \mathbf{v} \cdot \nabla T - \nabla \cdot \lambda \nabla T + \rho T \frac{dc}{dt} - \sigma \cdot \nabla \mathbf{v} = \rho q_{\text{th}} \quad (2.78)$$

Porous medium

The heat balance equation for the porous medium consisting of several solid and fluid phases is given by

$$\left(\sum_{\alpha} \epsilon^{\alpha} c^{\alpha} \rho^{\alpha} \right) \frac{\partial T}{\partial t} + \nabla \cdot \left(\left(\sum_{\gamma} n S^{\gamma} \rho^{\gamma} c^{\gamma} \mathbf{v}^{\gamma} \right) T - \left(\sum_{\alpha} \epsilon^{\alpha} \lambda^{\alpha} \right) \nabla T \right) = \sum_{\alpha} \epsilon^{\alpha} \rho^{\alpha} q_{\text{th}} + \left(\sum_{\gamma} n S^{\gamma} \mathbf{v}^{\gamma} \right) \cdot \nabla \sigma \quad (2.79)$$

where α is all phases and γ is fluid phases, respectively.

Most important is the assumption of local thermodynamic equilibrium, meaning that all phase temperatures are equal and , therefore, phase contributions can be superposed. The phase change terms cancel out with the addition of the individual phases.

2.4 Fluid properties

The above balance equations derived from first principles (section 2.3) are "material-less", i.e. they are valid for any kind of material. Constitutive relationships are necessary to close the balance equations as well as to specify the properties for fluid flow, heat transfer and mechanical stress/deformation of the specific material under consideration. For determination of material properties laboratory tests have to be conducted. A number of material properties can not be determined directly. This must be done by back analysis using inverse modeling. We organized the description of material properties in two sections: Fluid and mechanical properties (2.5) for THM/C processes in porous media.

As we have to deal with a large variety of geotechnical and hydrological applications (section 1) we allow the most complex case for fluid properties including phase changes. We consider very general equations of state (EOS) such as Redlich-Kwong [32], Peng-Robinson [33] equations as well as the fundamental Helmholtz free energy equation (2.90).

Fig. 2.4.9 shows as an example the phase diagram in case of CO_2 as working fluid. If we are interested in different fluids (e.g. CH_4 , H_2O , and N_2) Tab. 2.2 gives an overview about the corresponding fluid property correlations.

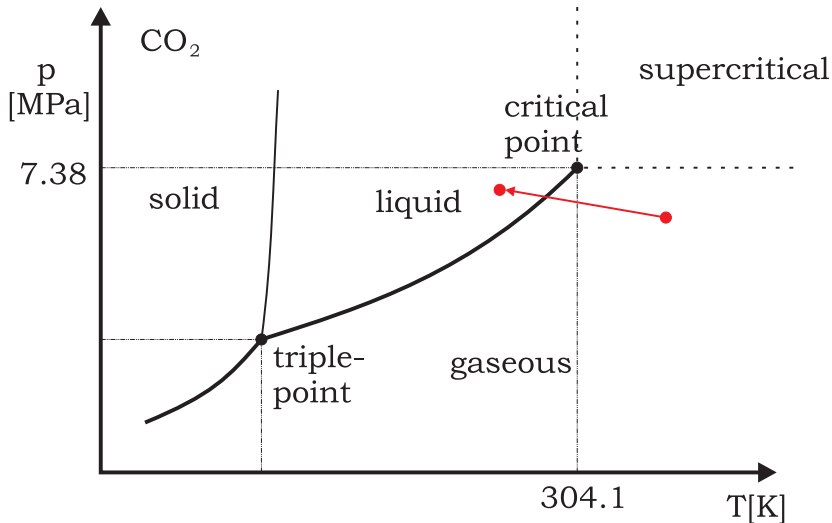


Figure 2.4.9: Phase diagram of carbon dioxide. The two extreme conditions ($[400]\text{K}$ at $[6.5]\text{MPa}$ and $[300]\text{K}$ at $[7]\text{MPa}$) are crossing a phase boundary of CO_2 , so a phase change from hot gas to liquid state will be forced.

Table 2.2: References for fluid properties of CH₄, CO₂, H₂O, and N₂

Fluid	Specifier	Density	Viscosity
Methane CH ₄	CH4-RK	[32]	Friend, 1989 [34]
	CH4-PR	[33]	
	CH4-HE	[35]	
Carbon dioxide CO ₂	CO2-RK	[32]	Fenghour, 1998 [36]
	CO2-PR	[33]	
	CO2-HE	[37]	
Water H ₂ O	H2O-RK	[32]	IAPWS, 1998 [38]
	H2O-PR	[33]	
	H2O-HE	[39]	
Nitrogen N ₂	N2-RK	[32]	Stephan, 1987 [40]
	N2-PR	[33]	
	N2-HE	[41]	

2.4.1 Density

In subsurface oil and gas reservoirs, properties of gases and liquids strongly depend from environmental pressure and temperature conditions. Equations of state (EOS) may be used to describe the relationship of volume, pressure and temperature of a real fluid. The knowledge of a fluids volume or its density is essential to estimate further thermodynamic properties. The first EOS for real gases, which was based on the ideal gas law, was presented by Johannes Diderik van der Waals in 1873 [42]. In 1910 he received the Nobel prize for the development of the equation

$$p = \frac{RT}{V_m - b} - \frac{a}{V_m^2} \quad (2.80)$$

where p is the pressure, R is the gas constant, T is the temperature, V_m is the molare volume and a and b are correcting parameters.

Redlich-Kwong equation of state (RKEOS) The equation of Redlich and Kwong from 1949 (2.81) represents just a little improvement of the van der Waals equation [32]. It is given as

$$p = \frac{RT}{V_m - b} - \frac{a}{T^{0.5} V_m (V_m + b)}. \quad (2.81)$$

The results are satisfactory only for temperatures above the critical point (see Tab. 2.3).

Table 2.3: Fluid properties used in equations of state, where ω is the acentric factor, T_c and p_c are temperature und pressure at the critical point and R ist the gas constant.

Fluid	ω [-]	T_c [K]	p_c [MPa]	R [J/kg/K]
Carbon dioxide	0.239	304.13	7.38	188.9
Ethane	0.099	305.32	4.87	276.5
Methane	0.011	190.56	4.60	518.3
Water	0.344	647.10	22.06	461.5

Equation (2.81) can be recasted as a cubic equation in terms of volume

$$V_m^3 - \frac{RT}{p} V_m^2 - \left(\frac{RTb}{p} - \frac{a}{T^{0.5}p} + b^2 \right) V_m - \frac{ab}{T^{0.5}p} = 0. \quad (2.82)$$

This equation yields to one or three real roots depending on the number of phases in the system. In the two-phase region, the largest positive root represents the molar volume of the gas phase while the smallest root corresponds to the volume of the liquid phase. The correcting terms a and b are given as

$$a = 0.4275 \frac{R^2 T_c^{2.5}}{p_c} \quad (2.83)$$

and

$$b = 0.0866 \frac{RT_c}{p_c} \quad (2.84)$$

where T_c and p_c are Temperature and pressure at the critical point (see Tab. 2.3). Figs. 2.4.10 and 2.4.11 show the results of the RKEOS for several substances at four different temperatures in comparison to other equations of state.

Peng-Robinson equation of state (PREOS) D. Y. Peng and D. B. Robinson presented an improvement of the RKEOS in 1975 [33]. The proposed equation is also a two-constant van der Waals-Type equation and combines simplicity and accuracy. The PREOS is very simple to solve and gives satisfying results within the whole fluid redion of a gas. It is given in the form

$$p = \frac{RT}{V_m - b} - \frac{a(T_c) \cdot \alpha(T_r, \omega)}{V_m^2 + 2 \cdot bV_m - b^2} \quad (2.85)$$

where a and b are correcting terms. They can be derived by

$$a(T_c) = 0.45724 \frac{R^2 T_c^2}{p_c} \quad (2.86)$$

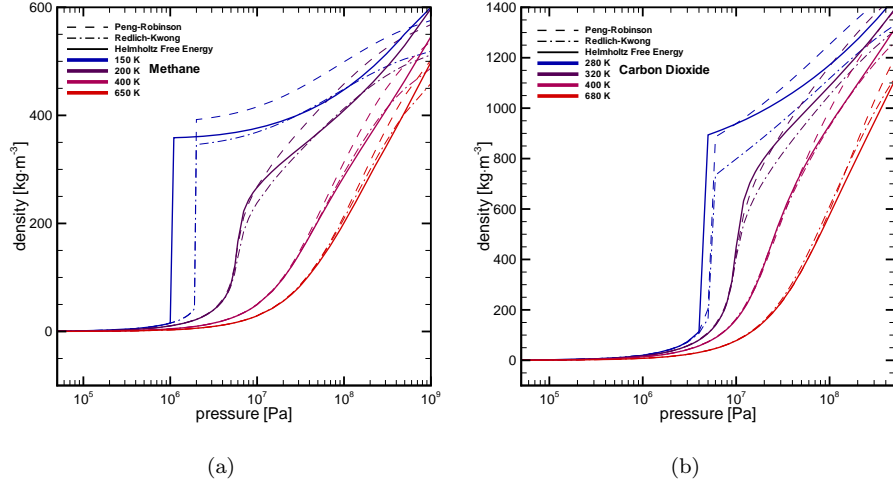


Figure 2.4.10: Density of CH_4 (a) and CO_2 (b) derived by different EOS. There stand — for the HELMHOLTZ Free Energy, - - - for the PREOS and - - - - for the RKEOS. The colours refer to different temperatures (blue - [280]K, violet - [320]K, pink - [400]K, red - [680]K).

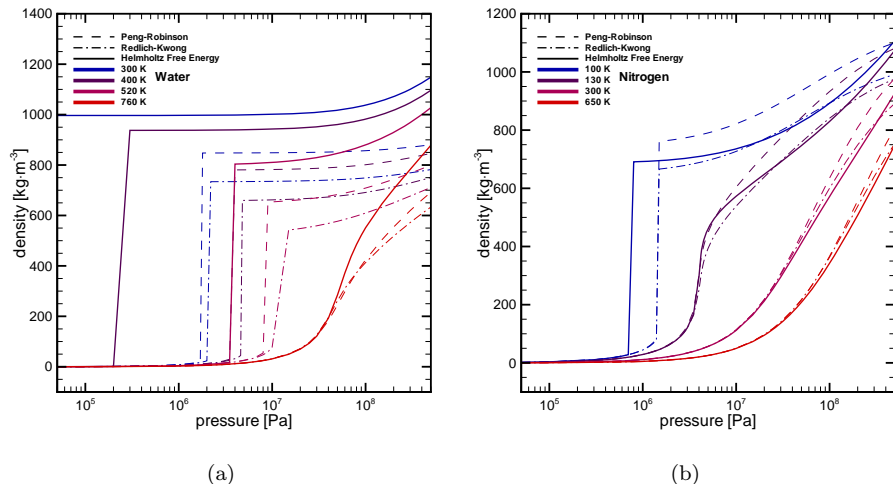


Figure 2.4.11: Density of H_2O (a) and N_2 (b) derived by different EOS. There stand — for the HELMHOLTZ Free Energy, - - - for the PREOS and - · - for the RKEOS. The colours refer to different temperatures (blue - [280]K, violet - [320]K, pink - [400]K, red - [680]K).

and

$$b(T_c) = 0.07780 \frac{RT_c}{p_c} \quad (2.87)$$

for the particular fluids under specification of pressure and temperature at the critical point. Parameter $\alpha(T_r, \omega)$ is a dimensionless function of reduced temperature T_r and acentric factor ω . It is given as

$$\alpha = (1 + (0.37464 + 1.54226\omega - 0.26992\omega^2)(1 - T_r^{0.5}))^2 \quad (2.88)$$

for $\omega \leq 0.49$ and

$$\alpha = (1 + (0.379642 + (1.48503 - (1.164423 - 1.016666\omega)\omega)\omega)(1 - T_r^{0.5}))^2 \quad (2.89)$$

for $\omega > 0.49$. Tab. 2.3 shows acentric factors and critical parameters for different real gases. The resulting density distribution of the PREOS is shown in Figs. 2.4.10 and 2.4.11 at four different temperatures.

Fundamental equations For highly precise results it is necessary to adapt fundamental equations based on the free energy. The HELMHOLTZ free energy is given as

$$\frac{f(\rho, T)}{RT} = \phi(\delta, \tau) = \phi^o(\delta, \tau) + \phi^r(\delta, \tau) \quad (2.90)$$

in dependence from density ρ and temperature T in its dimensionless form. These dimensionless parts are given as the terms $\delta = \rho/\rho_c$ and $\tau = T_c/T$, whereas ρ_c and T_c are density and temperature at the critical point (see Tab. 2.3). The HELMHOLTZ free energy provides relations between density, temperature and all thermodynamic properties of a fluid, which are expressed in the parameter ϕ^o as the ideal gas part and ϕ^r as the residual part. For their derivatives in the short forms like ϕ_δ^r , $\phi_{\delta\delta}^r$, ϕ_τ^r , $\phi_{\tau\tau}^r$, $\phi_{\delta\tau}^r$, ϕ_τ^o , $\phi_{\tau\tau}^o$ it is referred to [37].

Several authors used the approach of HELMHOLTZ free energy to develop EOS for different substances, e.g.:

- Span & Wagner [37], [43], [41] for carbon dioxide and for nitrogen,
- Pruss & Wagner [44], [39] for water,
- Bücker & Wagner [45] for ethane and
- Setzmann & Wagner [35] for methane.

The fundamental equation (2.90) according to Wagner et al. ([37],[44],[45], and [35]) is one of the most precise EOS at present. The equation and its derivatives can be used to describe all thermodynamic properties of a pure substance depending on density and temperature. So it is necessary to solve the relationship between density, pressure and temperature iteratively, as (2.91) shows

$$\frac{p(\delta, \tau)}{\rho RT} = 1 + \delta \frac{\partial \phi^r}{\partial \delta}. \quad (2.91)$$

For water, the equation became international standard for the IAPWS⁴ since

⁴International Association for the Properties of Water and Steam

1995. Certainly, the equation is complicated to solve and requires long computing time. Therefore, several codes it is possible to choose between an iterative solving algorithm and an interpolation of density values out of a database.

The semi-empirical fundamental equation (2.90) has to be fitted to measurement data by computer algorithms for each substance. Depending on the fluid, there are up to 200 adjusting coefficients to ensure a very accurate fit to the real gas behaviour. For each substance, equation (2.90) has separate ranges of validity, which are shown in Tab. 2.4.

Table 2.4: Ranges of validity of the free HELMHOLTZ equation (2.90) for several fluids valid from the melting point up to the indicated values.

Fluid	T [K]	p [MPa]	Reference
Carbon dioxide	216	1100	[37], [43]
Nitrogen	1000	2200	[41]
Ethane	520	30	[45]
Methane	625	1000	[35]
Water	1273	1000	[44], [39]

2.4.2 Enthalpy

The specific enthalpy h is the whole amount of energy of a fluid. It consists of the internal energy and the volume changing work. It can be expressed by deviations of the free HELMHOLTZ energy as

$$\frac{h(\delta, \tau)}{RT} = 1 + \tau (\phi_\tau^o + \phi_\tau^r) + \delta \phi_\delta^r. \quad (2.92)$$

2.4.3 Entropy

The entropy s represents which plenty of the energy of a system is potentially available to do work and which plenty of it is potentially defined as heat. In classical thermodynamics, the validity for the entropy is the thermodynamical system in equilibrium. The following equation is given for the entropy:

$$\frac{s(\delta, \tau)}{R} = \tau (\phi_\tau^o + \phi_\tau^r) - \phi^o - \phi^r. \quad (2.93)$$

2.4.4 Heat capacity

The specific heat capacity of a fluid is defined as the amount of heat which is needed to increase the temperature of a fluid of [1]kg by [1]K. In thermodynamics, it is distinguished between a heat capacity at constant pressure, the

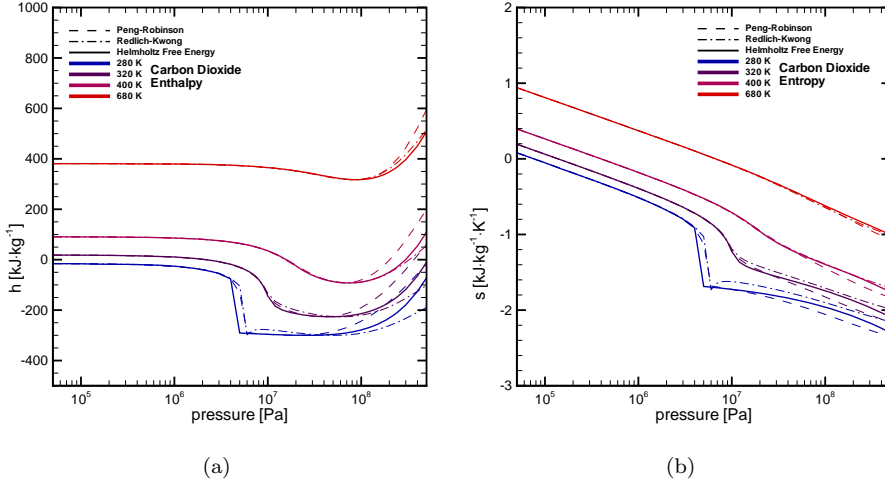


Figure 2.4.12: Enthalpy (a) and entropy (b) of CO₂ based on different EOS. There stand — for the HELMHOLTZ Free Energy, - - - for the PREOS and - · - for the RKEOS. The colours refer to different temperatures (blue - [280]K, violet - [320]K, pink - [400]K, red - [680]K).

isobaric heat capacity, and a heat capacity at constant volume, the isochoric heat capacity. Both can be expressed in terms of free HELMHOLTZ energy, like the following equations show:

isobaric heat capacity

$$\frac{c_p(\delta, \tau)}{R} = -\tau^2 (\phi_{\tau\tau}^o + \phi_{\tau\tau}^r) + \frac{(1 + \delta\phi_\delta^r - \delta\tau\phi_\delta^r)^2}{(1 + 2\delta\phi_\delta^r + \delta^2\phi_{\delta\delta}^r)} \quad (2.94)$$

isochoric heat capacity

$$\frac{c_v(\delta, \tau)}{R} = -\tau^2 (\phi_{\tau\tau}^o + \phi_{\tau\tau}^r). \quad (2.95)$$

Due to the high number of adjusting coefficients, the properties based on the HELMHOLTZ free energy may be seen as very accurate. On the other hand, the iterative solution of (2.91) takes long computing times, so for long-term simulations or for simulations with a high number of elements, it would be better to use the van der Waals-type equations of Redlich-Kwong or Peng-Robinson. These cubic equations are easy to solve and lead to results very fast. Figs. 2.4.12 and 2.4.13 illustrate, in which range of temperature and pressure those simple EOS may be used. Here, thermodynamical properties of carbon dioxide based

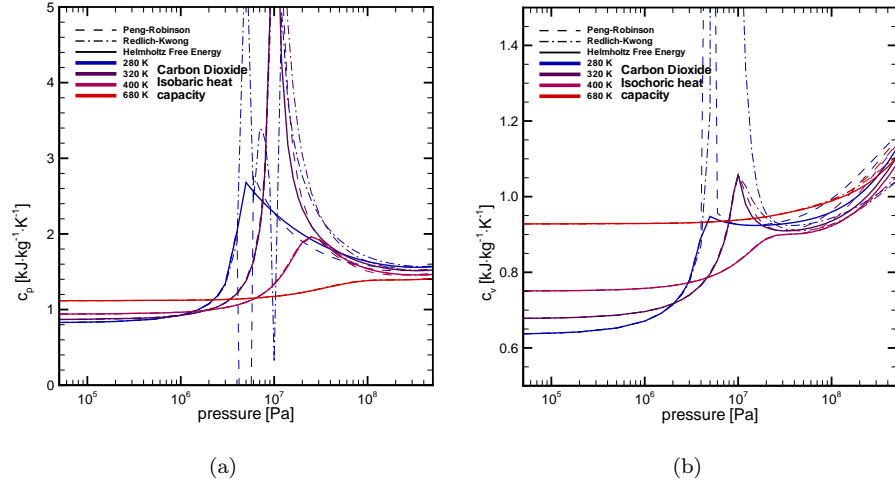


Figure 2.4.13: Isobaric heat capacity (a) and isochoric heat capacity (b) of CO_2 based on different EOS. There stand — for the HELMHOLTZ Free Energy, - - - for the PREOS and - - - - for the RKEOS. The colours refer to different temperatures (blue - [280]K, violet - [320]K, pink - [400]K, red - [680]K).

on temperature and density are shown calculated by different EOS. In general, if temperature rises while pressure is declining, the behaviour of a fluid approaches to that of the ideal gas and the cubic equations of state give suitable results. For instance, the resulting entropy and enthalpy values of carbon dioxide at low pressures and high temperatures are identical, regardless of the density model they are based on (see Fig. 2.4.12(a) and 2.4.12(b)). In the liquid and the dense supercritical region, the results based on different EOS diverge increasingly.

In addition, in the vicinity of the saturation curve, the results based on the van der Waals-type EOS may show large variations compared to the fundamental equation based curves (HELMHOLTZ free energy). Particularly, this becomes apparent from Figs. 2.4.13(a) and 2.4.13(b), where the heat capacities of CO_2 are given. The heat capacities at [400]K and [680]K (in the supercritical region of CO_2 , where no phase boundary exists) are identical, independent from according density model. Within the two-phase region at [280]K and [320]K, a strong deviation at the phase boundary can be seen.

For water, the cubic EOS are not suitable. Water is a high critical fluid, so its properties are too complex to be described by simple approaches. As we can see in Fig. 2.4.11(a), the RKEOS, as well as the PREOS give viable results only at pressures below [1]MPa and at high temperatures. Therefore it is recommended to use the fundamental equation of the HELMHOLTZ free energy to estimate the density of water.

2.4.5 Viscosity

Many authors developed correlation equations for viscosity η of fluids at a density ρ and a temperature T . Those correlation equations may be composed of two or three terms, like

$$\eta(\rho, T) = \eta_0(T) + \eta_{ex}(\rho, T) \quad (2.96)$$

or

$$\eta(\rho, T) = \eta_0(T) + \Delta\eta(\rho, T) + \Delta\eta_c(\rho, T). \quad (2.97)$$

In the two-term form, the viscosity correlation consists of a zero-density limit viscosity $\eta_0(T)$ at a temperature T , and an excess contribution viscosity $\eta_{ex}(\rho, T)$ at a density ρ and a temperature T . This type of correlation function is used (among others) by FRIEND et al. [34] or STEPHAN et al. [40]. The formulation can be enhanced by a term describing the viscosity in the immediate vicinity of the critical point, $\Delta\eta(\rho, T)$ (2.97), as described in FENGHOUR et al. [36] or HUBER et al. [38]. An overview about the used viscosity correlations for several substances is given in Tab. 2.5. To show an example, Fig. 2.4.14(a) portrays the resulting viscosities for carbon dioxide based on densities of different EOS.

Table 2.5: Ranges of T and p validity for viscosity correlations for several substances.

Fluid	T [K]	p [MPa]	Reference
Carbon dioxide	200–1500	≤ 300	[36]
Nitrogen	70–1100	≤ 100	[40]
Ethane	90–625	≤ 30	[46]
Methane	91–600	≤ 100	[34]
Water	273–1173	≤ 100	[38]

2.4.6 Thermal conductivity

Similar to the correlations between viscosity and T and p , the thermal conductivity λ can be expressed by an equation consisting of the following three parts (see [47]): A conductivity in the limit of zero-density $\lambda^0(0, T)$, where only two-body interaction occurs, a term $\Delta_c\lambda(\rho, T)$ which enhances the property function in the critical region of the fluid, and finally $\Delta\lambda(\rho, T)$ which represents the contribution of all other effects to the thermal conductivity at elevated densities including many-body collisions, molecular-velocity correlations and collisional transfer. This equation is

$$\lambda(\rho, T) = \lambda^0(T) + \Delta\lambda(\rho) + \Delta_c\lambda(\rho, T). \quad (2.98)$$

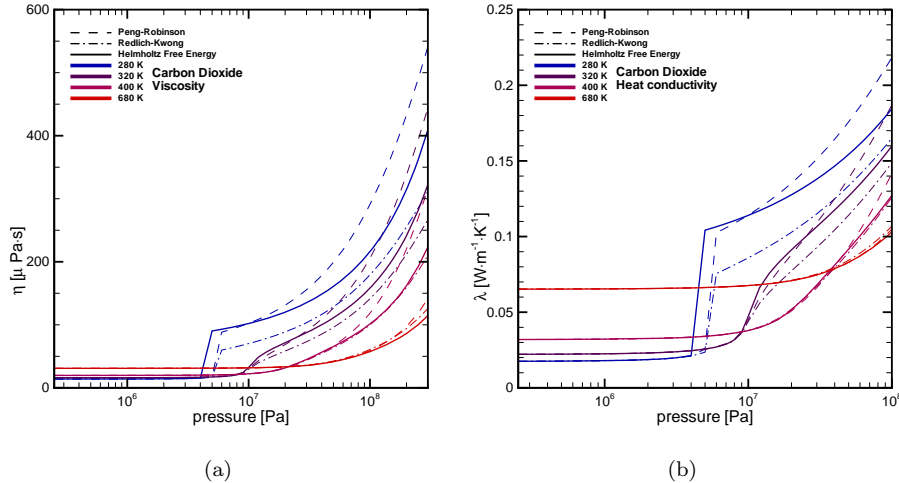


Figure 2.4.14: Viscosity (a) and thermal conductivity (b) of CO₂ based on different EOS. There stand — for the HELMHOLTZ Free Energy, - - - for the PREOS and - · - for the RKEOS. The colours refer to different temperatures (blue - [280]K, violet - [320]K, pink - [400]K, red - [680]K).

Fig. 2.4.14(b) shows the thermal conductivity of carbon dioxide at four temperatures based on different EOS. In Tab. 2.6 the ranges for the validity of T and p concerning thermal conductivity correlations for several substances are shown.

Table 2.6: Ranges of T and p validity for thermal conductivity correlations for several substances.

Fluid	T [K]	p [MPa]	Reference
Carbon dioxide	200–1000	≤ 100	[36]
Nitrogen	70–1100	≤ 100	[40]
Ethane	≤ 600	≤ 70	[48]
Methane	≤ 200	≤ 600	[48]
Water	≤ 800	≤ 100	[49]

2.5 Mechanical properties

Constitutive equations (i.e. constitutive relations, material laws) are relations between measures of deformation (e.g. strain tensor) and internal force density functions (stress tensor) resulting from the action of external forces. Usually, they are not laws of nature but represent mathematical models intended to characterize the typical material behavior based on physically reasonable assumptions (particularly consistent with the thermodynamic balance relations) and mathematically correct approaches.

2.5.1 Effective stress principle

Following the statements given in section 2.3.2 the total Cauchy's stress tensor in porous media is decomposed in partial stresses referring to the participating phases (note the sign convention of positive fluid phase pressure p^γ , but negative compressive normal stress for the solid phase).

$$\boldsymbol{\sigma} = (1 - n) \boldsymbol{\sigma}^s - n \left(\sum_{\gamma} S^{\gamma} p^{\gamma} \right) \mathbf{I} \quad (2.99)$$

Considering the effective stress principle, relation (2.99) can be modified defining the effective solid stress $\boldsymbol{\sigma}_{eff}^s$ as well as the overall fluid pressure p^{γ}

$$\begin{aligned} \boldsymbol{\sigma} &= (1 - n) \left[\boldsymbol{\sigma}^s + \left(\sum_{\gamma} S^{\gamma} p^{\gamma} \right) \mathbf{I} \right] - \left(\sum_{\gamma} S^{\gamma} p^{\gamma} \right) \mathbf{I} \\ &= \boldsymbol{\sigma}_{eff}^s - \left(\sum_{\gamma} S^{\gamma} p^{\gamma} \right) \mathbf{I} \end{aligned} \quad (2.100)$$

The effective solid stress is the total solid stress reduced by the excess pore liquid pressure, but referred to the domain of the overall porous medium. Consequently, its absolute value is lower than the intrinsic stress of the solid skeleton. Constitutive relations for the solid phase of porous media combine the solid skeleton deformation (in terms of the strain tensor) with the effective solid stress. Selected models are presented in the next paragraphs. As they are equally valid for single-phase solid materials as well as for the solid phase of porous media, the special notation of the effective stress tensor will be omitted without loss of generality.

Based on the stress decomposition (2.100), the equilibrium condition for the porous medium becomes

$$\rho \mathbf{g} + \nabla \cdot \boldsymbol{\sigma}_{eff}^s - \left(\sum_{\gamma} S^{\gamma} p^{\gamma} \right) \mathbf{I} = \mathbf{0} \quad (2.101)$$

2.5.2 Material classes

Usually laboratory tests are performed on specimens to investigate the mechanical behavior. Within this context, similar stress-strain curves can be caused by different physical effects, e.g. a nonlinear stress-strain curve does not necessarily suggest inelastic material behavior. For the sake of clarity, it is possible to introduce a classification of materials based on some essential distinctly identifiable material phenomena. For instance, comparatively simple experiments can be performed to investigate if the stress-strain curves are rate-dependent, and if hysteresis phenomena occur indicating dissipative effects.



Figure 2.5.15: Experimentally observed rate-independent solid material behavior. Cyclic uniaxial stress-strain curves [17]: elasticity (left) and elastoplasticity (right)

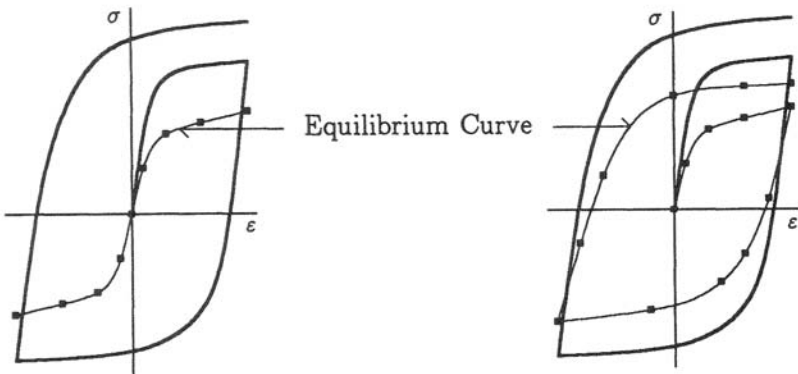


Figure 2.5.16: Experimentally observed rate-dependent solid material behavior. Cyclic uniaxial stress-strain curves [17]: viscoelasticity (left) and viscoplasticity (right)

Based on these assumptions the observable material behavior can be divided into four different basic classes:

- rate-independent without hysteresis,
- rate-independent with hysteresis,
- rate-dependent without hysteresis, and
- rate-dependent with hysteresis.

Figs. 2.5.15 and 2.5.16 schematically show typical cyclic stress-strain curves for these material classes. The equilibrium curves, presented in Figs. 2.5.16 can be observed as a result of relaxation experiments.

According to the experimental observations, there are four classes of mathematical models matching the material classes defined above:

- the theory of elasticity describes rate-independent material behavior without hysteresis,
- the theory of (elasto)plasticity describes rate-independent material behavior with hysteresis,
- the theory of viscoelasticity describes rate-dependent material behavior without hysteresis, and
- the theory of viscoplasticity describes rate-dependent material behavior with hysteresis.

Physically significant constitutive relations in the uniaxial case can be defined for the four classes of material theories based on so-called rheological models. These complex models consist of a simple networks of individual rheological elements (cf. Fig. 2.5.17), like

- elastic springs, which correspond to the linear stress-strain relation

$$\sigma = k \varepsilon \quad (2.102)$$

with the spring constant k representing the proportionality factor,

- viscous dashpots, which represent Newtonian viscous substances, and obey a linear relation between stress and strain rate

$$\sigma = \eta \dot{\varepsilon} \quad (2.103)$$

with the proportionality factor η characterizing the viscosity, and

- Coulomb friction elements, resisting any motion until a threshold stress σ^* is reached, whereas behind the threshold irreversible deformations occur

$$\varepsilon = \begin{cases} 0, & \text{if } \sigma < \sigma^* \\ \varepsilon(t), & \text{if } \sigma \geq \sigma^* \end{cases} \quad (2.104)$$

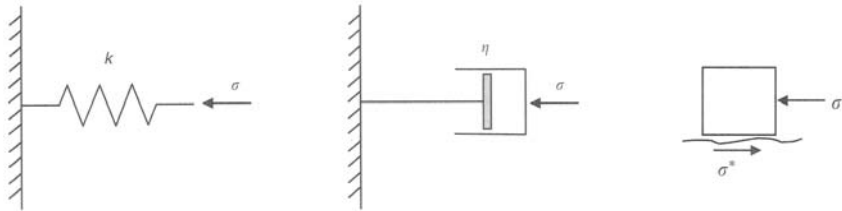


Figure 2.5.17: Mathematical modeling of solid material behavior. Basic individual elements of rheological models [50]: spring element (left), dashpot element (middle) and frictional element (right)

Differential equations, which are defined based on an appropriate composition of rheological models are only in a few special cases suitable to describe material response to external loading observed in reality. They can rather serve for marking the physical significance of mathematical models within the context of material theories. In Figs. 2.5.18 and 2.5.19 typical rheological models are presented, which characterize the material behavior of the four material classes defined above.



Figure 2.5.18: Mathematical modeling of rate-independent solid material behavior. Cyclic uniaxial stress-strain curves [17]: elasticity (spring element – left) and elastoplasticity (spring and frictional elements – right)

In Tab. 2.7 some typical technical as well as natural (including geological) materials are assigned to the generalized material classes considering their material behavior, which can be observed for characteristic application cases. Generally, the classification of the material behavior depends on the real loading regime (e.g. small or large strains), environmental conditions (e.g. temperature), and the time scale of the physical processes under consideration. Changing one or more of these conditions one and the same material can demonstrate different mechanical behavior. Basically, no materials are actually purely elastic over a wide range of stresses, temperature, and time. Otherwise, developing and using complex constitutive models, which include all observable phenomena is not advisable for practical reasons. Constitutive relations, rather, should represent idealized and simplified models according to the most dominating conditions appearing in the practical applications under consideration.



Figure 2.5.19: Mathematical modeling of rate-dependent solid material behavior. Cyclic uniaxial stress-strain curves [17]: viscoelasticity (spring and dashpot elements – left) and viscoplasticity (spring, dashpot, and frictional elements – right)

Table 2.7: Generalized classes of solid material behavior, and selected, typical representatives

Material class	Technical/natural material	Geomaterial
elasticity	metals at small strains, ceramics, bone, most other materials at small strains	igneous rocks (e.g. granite), hard sedimentary rocks (e.g. sandstone)
elastoplasticity	metals at large strains	most soils, soft sedimentary rocks (e.g. tuff)
viscoelasticity	rubber, glass, soft biological tissues	rock salt (halite)
viscoplasticity	polymers (plastics), wood, bitumen, metals at high temperature	clay soils, clay stone

2.5.3 Elasticity

In a micromechanical point of view, elasticity is predominantly caused by the evolution of interatomic forces in response to the impact of external forces. It can be observed for crystalline substances (where the atoms are established in regular structures) as well as for amorphous materials (where the atoms compose irregular structures), and is characterized by reversibility of the deformation processes and the absence of any hysteresis. Furthermore, it is assumed that the current stress state is uniquely defined by the current strain state, and does not depend on the strain history. Consequently, within the context of the constitutive model, the stress tensor is a function of the strain tensor, but it does not depend on the strain rate.

The isothermal isotropic linear elastic material model

$$\boldsymbol{\sigma} = 2\mu \boldsymbol{\varepsilon} + \lambda \text{tr}(\boldsymbol{\varepsilon}) \mathbf{I} \quad (2.105)$$

known as generalized Hooke's law is the simplest of all constitutive models for solid material behavior. Instead of the so-called Lamé constants μ and λ , Hooke's law is often represented in terms of other material parameters like the Young's modulus (i.e. elastic modulus, coefficient of elasticity, modulus of elasticity et al.) E , the Poisson's ratio ν , the shear modulus G , and the bulk modulus K . Some useful relations between these parameters are as follows:

$$\begin{aligned} E &= \mu \frac{2\mu + 3\lambda}{\mu + \lambda}, & \nu &= \frac{\lambda}{2(\mu + \lambda)} \\ \mu &= \frac{E}{2(1 + \nu)}, & \lambda &= \frac{\nu E}{(1 + \nu)(1 - 2\nu)} \\ G &= \frac{E}{2(1 + \nu)} = \mu \\ K &= \frac{E}{3(1 - 2\nu)} = \frac{(\mu + \lambda)(2\mu + 3\lambda)}{3} \end{aligned}$$

Thus, the coefficients of the consistent material matrix $d\boldsymbol{\sigma}/d\boldsymbol{\varepsilon}$, which is required for the numerical simulation of mechanical material behavior can be represented in case of linear elasticity straightforward.

$$\mathbf{C}_4 \equiv C_{ijkl} = \frac{d\sigma_{ij}}{d\varepsilon_{kl}} = 2\mu \delta_{ik} \delta_{jl} + \lambda \delta_{ij} \delta_{kl} \quad (2.106)$$

If a coupling of mechanical and thermal processes occur (non-isothermal mechanical processes), in addition to the strain caused by the impact of external forces a volumetric thermal strain can be observed, which usually is linearly related to the temperature difference.

$$\boldsymbol{\varepsilon}_{\text{th}} = \alpha_T (T - T_0) \mathbf{I} \quad (2.107)$$

Here, α_T denotes the linear thermal expansion coefficient, and T_0 the initial temperature. In small strain solid mechanics it is common practice to consider additive decompositions of the overall strain tensor into several constitutive parts according to the observed physical phenomena. Considering thermoelastic material behavior, the overall strain tensor consists of an elastic part and a thermal part.

$$\boldsymbol{\varepsilon} = \boldsymbol{\varepsilon}_{\text{el}} + \boldsymbol{\varepsilon}_{\text{th}} \quad (2.108)$$

As Hooke's law (2.105) has to be perceived as a constitutive model, which assigns the local stress state to local elastic strains, a non-isothermal generalization can be defined easily.

$$\boldsymbol{\sigma} = 2\mu \boldsymbol{\varepsilon}_{\text{el}} + \lambda \text{tr}(\boldsymbol{\varepsilon}_{\text{el}}) \mathbf{I} = 2\mu \boldsymbol{\varepsilon} + \lambda \text{tr}(\boldsymbol{\varepsilon}) \mathbf{I} - (2\mu + 3\lambda) \boldsymbol{\varepsilon}_{\text{th}} \quad (2.109)$$

A conclusion drawn from Hooke's law of linear elasticity is the specific representation of the equilibrium condition for a thermo-poro-elastic porous medium in case of small strains.

$$\nabla \cdot \left(\boldsymbol{\sigma}_{\text{eff}}(\boldsymbol{\varepsilon}) - \left(\sum_{\gamma} S^{\gamma} p^{\gamma} \right) \mathbf{I} - \frac{2\mu + 3\lambda}{3} \alpha_T (T - T_0) \mathbf{I} \right) = \rho \mathbf{g} \quad (2.110)$$

Although no materials are actually linearly elastic over a wide range of stresses, elastic constitutive models are often quite useful and accurate in many practical applications, e.g. in rock mechanics. The elastic material parameters given in Tab. 2.8 for selected soils and rocks show the large variation of material parameters, which is typical for geomaterials.

Table 2.8: Elastic material parameters for selected geomaterials

Material	Young's modulus [GPa]	Poisson's ratio
Sand	0.03...0.6	0.10...0.40
Clay	0.03...0.3	0.12...0.40
Clay stone	3...11	0.10...0.27
Salt rock	12...42	0.09...0.49
Sandstone	4...19	0.12...0.20
Granite	17...56	0.11...0.27
Basalt	31...97	0.19...0.30
Limestone	13...53	0.11...0.40

2.5.4 Elastoplasticity

The phenomenon of plastic yielding can be mainly observed in crystalline solid materials. It is associated with the motion of defects (so-called dislocations, discontinuities) of the regular atomic structure during deformation. Elastoplastic material behavior is characterized by elastic material response at the beginning of the deformation process. If a critical stress (the so-called yield stress) is reached, plastic flow occurs, whereas elastic material behavior can be observed again at the beginning of each unloading phase of a cyclic loading process.

In case of elastic-perfectly plastic material behavior, the stresses remain unchanged during plastic flow keeping the yield stress value. Usually, real materials show elastoplastic material behavior with hardening effects, which are distinguished by an increase of stresses during plastic flow with much lower slope of the stress-strain curve compared to the elastic phases of the entire deformation process. Elastoplastic material behavior with negligible elastic share is called rigid plasticity (see Fig. 2.5.20).

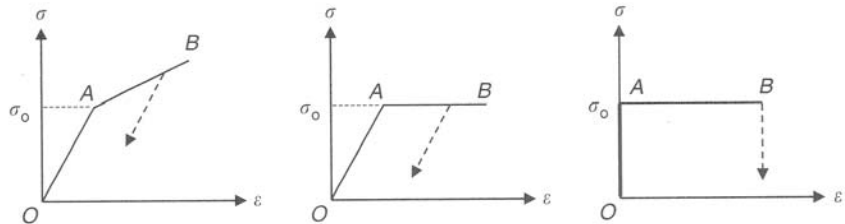


Figure 2.5.20: Schematic representation of material behavior exhibiting plastic yielding [50]: elastic-plastic with strain hardening (left), elastic-perfectly plastic (middle), and rigid-perfectly plastic (right)

During plastic flow a certain fraction of the strain energy is transformed into thermal energy or stored as internal energy due to a remodeling of the microstructure. Therefore, analyzing cyclic elastoplastic processes rate-independent hysteresees can be observed. Additionally, plastic deformation processes prove themselves to be irreversible.

In terms of the mathematical modeling of elastoplasticity no explicit stress-strain relation can be defined (no biunique relationship between these quantities exists) due to the hysteresis effects. Instead, a mathematically ascertainable functional relation can be created between the stress rate and the elastic strain rate.

$$\dot{\sigma} = C \dot{\varepsilon}_{\text{el}} \quad (2.111)$$

As shown in the case of thermoelasticity, the overall strain tensor can be additively split into two constitutive parts: an elastic one ε_{el} and the partial plastic

strain tensor $\boldsymbol{\varepsilon}_{\text{pl}}$.

$$\dot{\boldsymbol{\varepsilon}} = \dot{\boldsymbol{\varepsilon}}_{\text{el}} + \dot{\boldsymbol{\varepsilon}}_{\text{pl}} \quad (2.112)$$

Usually, the plastic yielding is mathematically characterized based on appropriately defined so-called yield conditions $\Phi_{\text{pl}}(\boldsymbol{\sigma})$ (i.e. flow condition, yield criterion). A yield condition is a relationship among the coefficients of the stress tensor separating the elastic domain in the stress space (which represents the area inside the yield condition) from the region of plastic yielding. Within this context, the plastic strain rate tensor is defined as follows:

$$\dot{\boldsymbol{\varepsilon}}_{\text{pl}} = \lambda_{\text{pl}} \frac{\partial \Phi_{\text{pl}}(\boldsymbol{\sigma})}{\partial \boldsymbol{\sigma}} \quad (2.113)$$

with the so-called plastic multiplier λ_{pl} . Consequently, the constitutive relation (2.111) can be reformulated.

$$\dot{\boldsymbol{\sigma}} = C \left(\dot{\boldsymbol{\varepsilon}} - \lambda_{\text{pl}} \frac{\partial \Phi_{\text{pl}}(\boldsymbol{\sigma})}{\partial \boldsymbol{\sigma}} \right) \quad (2.114)$$

It is generally accepted that plastic yielding is accompanied by incompressible (volume-preserving) deformation processes. Thus, yield conditions are usually defined in terms of the deviatoric stress tensor.

$$\boldsymbol{\sigma}_d = \boldsymbol{\sigma} - \frac{1}{3} \text{tr}(\boldsymbol{\sigma}) \mathbf{I} \quad (2.115)$$

One of the most widely-used and simplest models is known as von Mises yield condition

$$\Phi_{\text{pl}}(\boldsymbol{\sigma}) = \sqrt{\frac{3}{2} \boldsymbol{\sigma}_d \cdot \boldsymbol{\sigma}_d} - \sigma_0 = 0 \quad (2.116)$$

with the initial yield stress σ_0 and the second invariant of the stress deviator.

$$\boldsymbol{\sigma}_d \cdot \boldsymbol{\sigma}_d = (\boldsymbol{\sigma}_d)_{ij} (\boldsymbol{\sigma}_d)_{ij} = (\boldsymbol{\sigma})_{ij} (\boldsymbol{\sigma})_{ij} - \frac{1}{3} (\sigma_{ij} \delta_{ij})^2 \quad (2.117)$$

A generalization of the von Mises yield condition is the Drucker-Prager model with the material parameters a and b .

$$\Phi_{\text{pl}}(\boldsymbol{\sigma}) = \sqrt{\frac{2}{3} \boldsymbol{\sigma}_d \cdot \boldsymbol{\sigma}_d - b \text{tr}(\boldsymbol{\sigma})} - a = 0 \quad (2.118)$$

Within the context of the analysis of geomaterials, elastic-plastic material models play a certain role particularly for soils, whereas their relevance in rock mechanics for subsurface studies is rather minor due to the hardly observable cyclic processes.

2.5.5 Viscoelasticity

Viscoelasticity is a typical material property of amorphous substances, particularly polymeric materials. If a wide variety of individual macromolecular chains exhibit elastic material behavior under external loading, networks of macromolecular chains are characterized by internal friction causing rate-dependent effects. Additionally, during mechanical loading, a certain part of strain energy transforms into heat, which is responsible for the existence of hysteresis effects. Relaxation (decrease of stress values at constant strain after instantaneous loading) and retardation (creep – increase of strain values at constant stress after instantaneous loading) are typical mechanical phenomena for viscoelastic materials. Both, relaxation and creep, tend towards asymptotic values, which represent the equilibrium elastic state. In the equilibrium state of viscoelastic materials (at sufficiently small loading rates) no hysteresis occurs. As well no hysteresis is observed at very high loading rates. In this case, the viscoelastic material behavior can be approximated by elastic models using instantaneous parameters.

In contrast to elastoplastic materials, viscoelastic dissipative hysteresis effects are not necessarily accompanied by irreversible deformation processes. A certain heat supply and/or a sufficiently long recovery period can reestablish the shape of a viscoelastic body after mechanical loading.

There exists a wide variety of viscoelastic material models in terms of integral equations or differential relations. A large number of them represent the generalization and modification of uniaxial approaches, which are based on more or less complex rheological models. The simplest viscoelastic rheological models consist of one spring and one dashpot element, respectively (see Fig. 2.5.21).

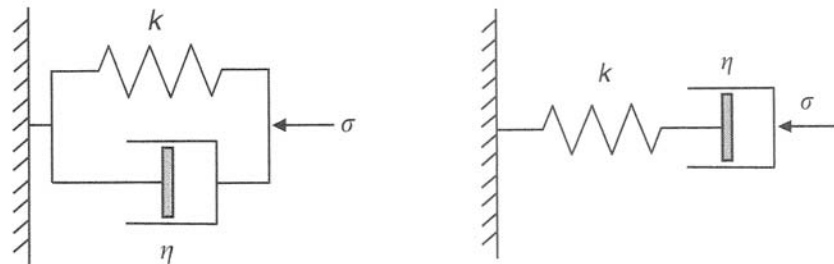


Figure 2.5.21: Mathematical modeling of reversible rate-dependent solid material behavior. Different combinations of a spring element with a dashpot element [50]: Kelvin-Voigt model (left) and Maxwell model (right)

The parallel connection of the spring and the dashpot elements is known as Kelvin-Voigt model. It is characterized by equal displacements (and therefore equal strain values) in both of the individual elements, whereas the stress value of the model will be the sum of the stresses in the spring and the dashpot. The constitutive behavior of the Kelvin-Voigt model is described by a differential equation.

$$\sigma = k \varepsilon + \eta \dot{\varepsilon} \quad (2.119)$$

If a stress σ_0 is instantaneously applied to a Kelvin-Voigt model, which is held constant thereafter, the solution of the differential equation (2.119) is given as follows:

$$\varepsilon = \frac{\sigma_0}{k} \left[1 - e^{-kt/\eta} \right] \quad (2.120)$$

which indicates that the strain increases asymptotically to its steady-state (elastic) value σ_0/k . Thus, the Kelvin-Voigt model represents the typical strain retardation, but neglecting any instantaneous strain.

The series connection of the spring and the dashpot elements is known as Maxwell model. Within this context, equal stress values occur in both of the individual elements, whereas the total displacement (and therefore the strain) of the model will be the sum of the displacements in the spring and the dashpot. The constitutive behavior of the Maxwell model can again be described by a differential equation.

$$\dot{\varepsilon} = \frac{1}{\eta} \sigma + \frac{1}{k} \dot{\sigma} \quad (2.121)$$

Applying an instantaneous stress, a Maxwell element exhibits an instantaneous elastic response characterized by the spring constant k , and a long-term viscous response specified by the viscosity η . If the Maxwell substance is subjected to an instantaneous jump in strain with the amplitude ε_0 , which is held constant thereafter, the differential equation (2.121) can be solved closely. The solution

$$\sigma = k \varepsilon_0 e^{-kt/\eta} \quad (2.122)$$

indicates a stress decrease (relaxation) at constant (non-zero) strain, whereas in case of the Maxwell model the stress relaxes to zero, simulating the behavior of a viscoelastic fluid.

2.5.6 Viscoplasticity

Viscoplasticity is the most general material class, and the constitutive theories of viscoplasticity must be defined, on principle, to model all macroscopically observable phenomena of material behavior. The viscoplastic material class combines elements of all the other classes presented above. Micromechanical phenomena causing viscoplastic material behavior are exceptionally complex.

Here, we will focus only on one typical effect of viscoplastic material behavior particularly relevant for geomaterials – creep processes. Although in both cases

characterizing the strain evolution at constant stress, viscoplastic creep differs from the viscoelastic creep (retardation) mentioned above, because no asymptotical strain value will be reached in the viscoplastic case. A typical viscoplastic creep curve is shown in Fig. 2.5.22.

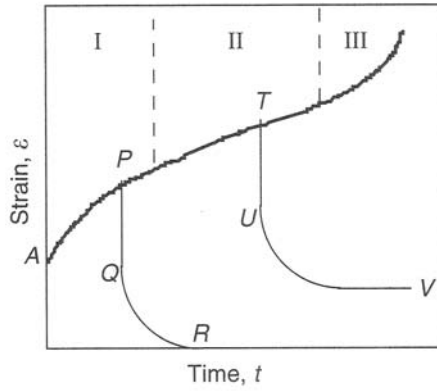


Figure 2.5.22: Schematical representation of a viscoplastic creep curve showing the three typical periods: primary, secondary, and tertiary creep [50]. The three periods are indicated by the Roman numerals I, II and III, the point A indicates the instantaneous elastic strain

For the viscoplastic creep behavior, generally, three typical periods can be observed. Whereas at all creep periods strain increases without reaching any asymptotical value, they differ in the strain rate. The first period, called primary creep, is characterized by a decreasing creep rate (transient creep), while for the second creep period, called secondary creep, a constant strain rate is observed (stationary creep, steady-state creep). The period of more or less constant strain rate is followed by the tertiary creep with ever-increasing strain rate, eventually causing mechanical failure of the structure under consideration. The total reduction of the applied stresses results in a strain relaxation. Unloading in the primary creep period is characterized by a complete strain relaxation (similar to viscoelastic behavior). However, if stress is removed during the secondary creep period, residual strains remain (effect of plasticity).

Comparable to theory of elastoplasticity, as starting point for the constitutive modeling of viscoplastic stress-strain states serves the functional relation between the stress rate and the elastic strain rate (2.111). The overall strain tensor is additively decomposed into several constitutive parts: apart from the partial elastic and plastic strain tensors a creep strain tensor is introduced $\dot{\epsilon}_c$.

$$\dot{\epsilon} = \dot{\epsilon}_{el} + \dot{\epsilon}_{pl} + \dot{\epsilon}_c \quad (2.123)$$

Similar to the plastic potential (yield condition), the creep behavior is mathematically characterized based on appropriately defined creep potentials $\Phi_c(\sigma)$

representing, again, relationships among the coefficients of the stress tensor. Consequently, the creep strain rate tensor is defined as follows:

$$\dot{\varepsilon}_c = \lambda_c \frac{\partial \Phi_c(\sigma)}{\partial \sigma} \quad (2.124)$$

with the so-called creep multiplier λ_c . Consequently, the constitutive relation (2.111) can be reformulated.

$$\dot{\sigma} = C \left(\dot{\varepsilon} - \lambda_{pl} \frac{\partial \Phi_{pl}(\sigma)}{\partial \sigma} - \lambda_c \frac{\partial \Phi_c(\sigma)}{\partial \sigma} \right) \quad (2.125)$$

In geomechanics, the long-term rock behavior during the stationary creep period is the main focus of interest. One widely-used creep potential characterizing secondary creep is the so-called Norton's model

$$\Phi_c(\sigma) = \frac{\alpha}{n+1} \left(\sqrt{\frac{3}{2} \sigma_d \cdot \cdot \sigma_d} \right)^{n+1} \quad (2.126)$$

with the material parameters α and n .

All of the constitutive models mentioned above are idealized approximations of the actual material behavior. The presented models are relatively simple, and allow to gain a first insight into the material theory of deformable solid substances. Some other aspects, which are relevant for rock mechanics analyzing material behavior could not be considered here, and are subject of further studies, like:

- Rate-dependent deformation processes in porous media are caused by the pore pressure diffusion through the solid skeleton at a finite rate, and intrinsic viscous properties of the matrix material. A separated experimental observation of these effects is quite challenging with according consequences to the constitutive modeling.
- Certain geomaterials show a layered structure (e.g. shale, sandstone). Consequently, material properties of these substances depend on the direction of the impact of external forces (known as anisotropic material behavior), which has to be considered in constitutive relations.
- Damage and failure of rocks play an important role in real geoprocesses, and require an individual consideration.
- The analysis of wave propagation (dynamic phenomena) in geomaterials is relevant for all kinds of seismic activities or seismic analyses.
- The design of appropriate lab tests is essential for the fundamental characterization of the material behavior, and the calibration of constitutive models.

2.6 Porous medium properties

We have considered the properties of fluid (section 2.4) and solid phases (section 2.5), respectively. Many of the properties of a porous medium can be determined based on the assumption of the local thermodynamic equilibrium allowing a superposition of phase related characteristics - except of the hydraulic properties for multiphase flow, which are discussed in this section in more detail. We restart with the different definitions of saturation.

2.6.1 Saturation

Saturation of a fluid phase γ is defined as the volumetric fraction ϵ^γ related to the sum of all fluid phases volumetric fractions.

$$S^\gamma = \frac{\epsilon^\gamma}{\sum_\gamma \epsilon^\gamma} \quad (2.127)$$

The sum of saturations of all fluid phases must be equal to unity (section 2.2.2). Effective saturation is defined as [51]

$$S_{\text{eff}}^\gamma = \frac{S^\gamma - S_r^\gamma}{1 - S_r^\gamma} \quad (2.128)$$

Moisture content (volumetric water content) is defined as the product of porosity and saturation.

$$\theta^\gamma = nS^\gamma \quad (2.129)$$

Gravimetric water content is defined as

$$\omega^\gamma = nS^\gamma \frac{\rho_d^s}{\rho^\gamma} \quad (2.130)$$

Applying the chain rule, we can express saturation changes in following way.

$$dS^\gamma = \frac{dS^\gamma}{dp^\gamma} dp^\gamma \quad (2.131)$$

The capillary pressure-saturation functions as well as the relations between relative permeability and saturation are substantial constitutive equations required for multiphase flow. Within this context, usually algebraic expressions are fit to the corresponding experimentally observed curves. Among the widely-used of these algebraic expressions are the Brooks-Corey [52] and van Genuchten [53] relations. If both are realized within the scientific software code developed by the authors, the numerical results presented in this paper are based on Brooks-Corey's approach.

2.6.2 Capillary pressure and relative permeability

As a consequence of interfacial tension a discontinuity in fluid pressure exists across the interface that separates two immiscible fluids. The partial pressure difference between two phases is denoted as capillary pressure, which is a function of saturation.

$$p_c^{\alpha\beta} = p^\beta - p^\alpha = f(S^\alpha) \quad (2.132)$$

In general, capillary pressure is the difference between partial pressures of non-wetting and wetting phases.

$$p_c = p^{nw} - p^w = f(S^w) \quad (2.133)$$

Capillary pressure is always positive: $p_c > 0, \forall S$. It is often assumed that air is at a constant atmospheric pressure taken as zero $p^g = 0$. This means, the macroscopic pressure of water in the unsaturated zone is always negative due to suction. Capillary pressure must be measured for given soils and pairs of fluids. In general, these experiments are conducted for equilibrium conditions with no fluid in motion. Various authors have proposed analytical functions for capillary pressure - saturation - relationships.

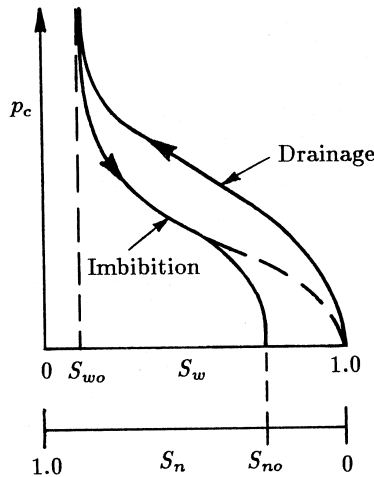


Figure 2.6.23: Capillary hysteresis [8], with $S_w = S^w$, $S_{w0} = S_r^w$, $S_n = S^{nw}$, $S_{n0} = S_r^{nw}$

The capillary pressure/saturation relationships differ for drainage and rewetting (imbibition) [54]. This phenomenon is called hysteresis (Fig. 2.6.23). Reasons for capillary pressure hysteresis are: (i) varying pore shape (ink-bottle effect), (ii) contact angle hysteresis (raindrop effect), (iii) entrapment of non-wetting fluids, (iv) swelling and shrinking of solid grains.

To introduce the concept of relative permeability we recall the Darcy law for flow of multiple fluid phases through porous media, equation (2.72). Fig. 2.6.24 shows an example of relative permeabilities for both wetting and non-wetting phases.

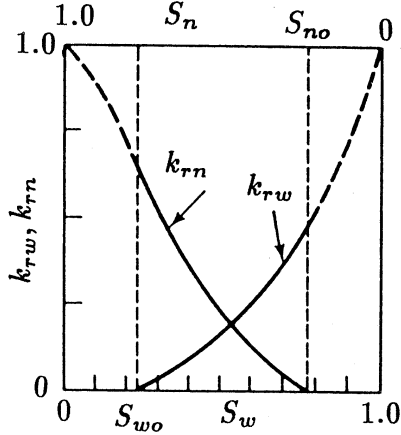


Figure 2.6.24: Relative permeability functions [8] with $S_w = S^w$, $S_{w0} = S_r^w$, $S_n = S^{nw}$, $S_{n0} = S_r^{nw}$, $k_{rn} = k^{nw}$, $k_{rw} = k^w$

We consider some of the most used models after van Genuchten, Haverkamp, Brooks-Corey.

van Genuchten model [53]

The definitions of effective saturation, capillary pressure and relative permeability for the van Genuchten model are as follows

$$S_{\text{eff}} = \frac{S^w - S_r^w}{1 - S_r^w} = (1 + (\alpha p_c)^n)^m \quad , \quad p_c > 0 \quad (2.134)$$

$$p_c = \begin{cases} 0 & S^w > S_{\max}^w \\ \frac{p_c^w g}{\alpha} (S_{\text{eff}}^{-1/m} - 1)^{1/n} & S_r^w < S^w < S_{\max}^w \\ p_{c\max} & S^w < S_r^w \end{cases} \quad (2.135)$$

with

$$m = 1 - \frac{1}{n} \quad (2.136)$$

$$k_{\text{rel}}(h) = \frac{1 - (\alpha h)^{n-2} [1 + (\alpha h)^n]^{-m}}{[1 + (\alpha h)^n]^{2m}} \quad (2.137)$$

Figs. 2.6.25 and 2.6.26 show the capillary pressure and relative permeability functions corresponding to the parameters given in Tab. 2.9, respectively.

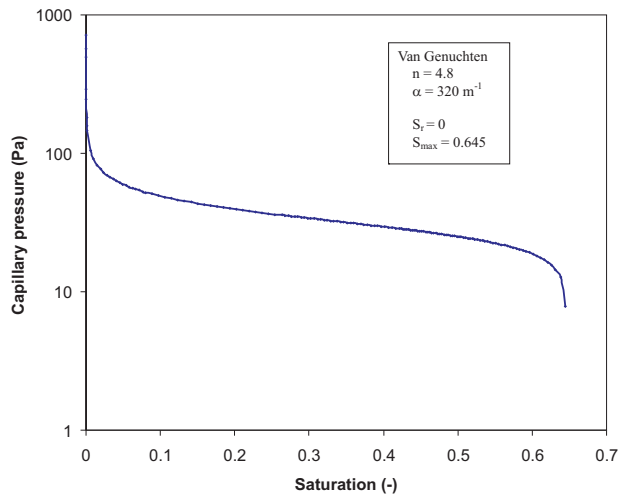


Figure 2.6.25: Capillary pressure / saturation relationship (Tuebingen experiment 2005)

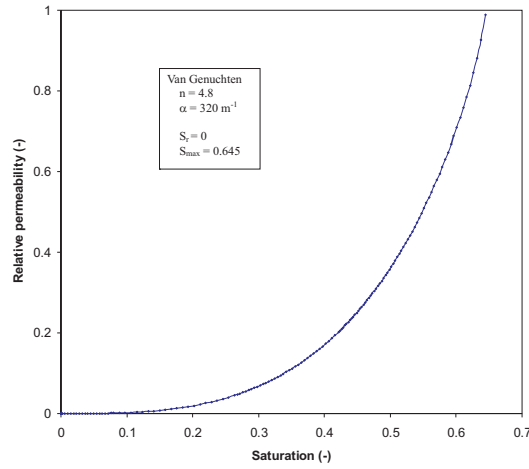


Figure 2.6.26: Relative permeability / saturation relationship (Tuebingen experiment 2005)

Table 2.9: Model parameter

S_r^w	residual water saturation	0	
S_{max}^w	maximal water saturation	0.645	
n	vG parameter	4.8	
α	vG coefficient	320	$[m^{-1}]$

Haverkamp model [55]

The formulas for the Haverkamp model are given in terms of pressure head $h = p^w/g\rho^w$ and moisture content $\theta = nS^w$. The definitions of effective saturation, capillary pressure and relative permeability for the Haverkamp model are as follows

$$\theta = \frac{\alpha(\theta_s - \theta_r)}{\alpha + |h|^\beta} + \theta_r \quad (2.138)$$

$$h = \left(-\frac{\alpha}{\theta}(\theta - \theta_s + \theta_r) \right)^{1/\beta} \quad (2.139)$$

$$\mathbf{k}_{\text{rel}}(h) = K_s \frac{A}{A + |h|^\beta} \quad (2.140)$$

Table 2.10: Model parameter

θ	volumetric water (moisture) content		$[cm^3/cm^3]$
θ_r	residual volumetric water content	0.075	$[cm^3/cm^3]$
θ_s	saturated volumetric water content	0.287	$[cm^3/cm^3]$
$h(\theta)$	soil water pressure head relative to the atmosphere		$[cm]$
α		1.611×10^6	$[Pa^{-1}]$
β		3.96	

Fig. 2.6.27 shows the capillary pressure saturation function corresponding to the parameters given in Tab. 2.10.

Brooks & Corey model [51]

The Brooks-Corey equations relating the saturation to the capillary pressure are

$$p^c = p^D S_{\text{eff}}^{-(1/\lambda)} \quad \text{for} \quad p^c \geq p^D \quad (2.141)$$

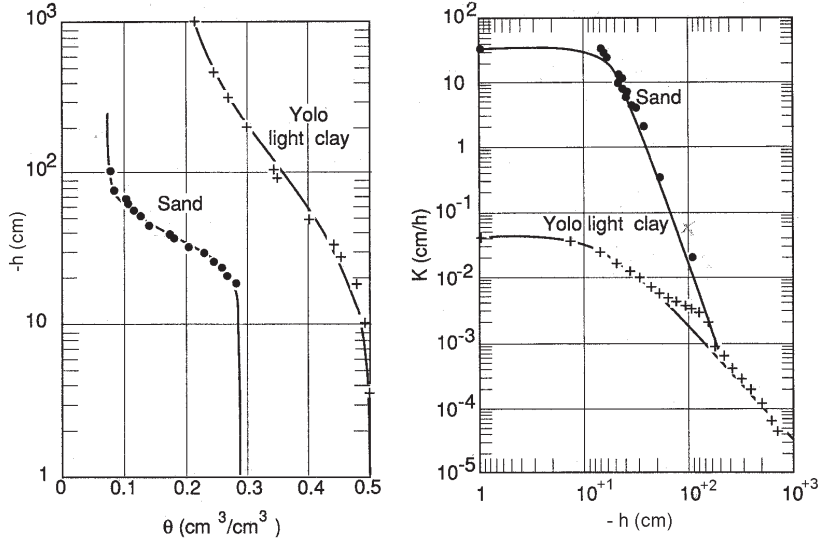


Figure 2.6.27: Hydraulic properties of unsaturated soil [55]

where p^D is usually known as entry pressure, λ is a pore-size distribution index. S_{eff} is a normalized wetting fluid saturation. For the case of CO_2 as wetting fluid into a saline aquifer it is defined as

$$S_{\text{eff}} = \frac{S^l - S_{\text{res}}^l}{1 - S_{\text{res}}^l - S_{\text{res}}^{\text{CO}_2}} \quad (2.142)$$

where S_{res}^l is the wetting phase residual or irreducible saturation, and $S_{\text{res}}^{\text{CO}_2}$ is the nonwetting phase residual saturation. The constitutive parameters p^D , λ , S_{res}^l and $S_{\text{res}}^{\text{CO}_2}$ are identified by fitting Eq. (2.141) to experimental data. Within this context, the entry pressure is to be understood as the minimum pressure that the nonwetting fluid must have to enter the largest pores. The relations between the relative permeability and the saturation are given by

$$k_{\text{rel}}^l = (S_{\text{eff}})^{(2+3\lambda)/\lambda} \quad (2.143)$$

$$k_{\text{rel}}^{\text{CO}_2} = (1 - S_{\text{eff}})^2 \left(1 - (S_{\text{eff}})^{(2+\lambda)/\lambda}\right) \quad (2.144)$$

Chapter 3

Numerical methods

by Wenqing Wang, Chan-Hee Park, Norihiro Watanabe and Olaf Kolditz

The design, implementation and application of a concept for object-orientated in finite element analysis of multi-field problems is presented in this paper. The basic idea of this concept is that the underlying governing equations of porous media mechanics can be classified into different types of partial differential equations (PDEs). In principle, equal types of PDEs for diverse physical problems differ only in material coefficients. Local element matrices and vectors arising from the finite element discretization of the PDEs are categorized into several types, regardless of which physical problem they belong to (i.e. fluid flow, mass and heat transport or deformation processes). Element (ELE) objects are introduced to carry out the local assembly of the algebraic equations. The object-orientation includes a strict encapsulation of geometrical (GEO), topological (MSH), process-related (FEM) data and methods of element objects. Geometric entities of an element such as nodes, edges, faces and neighbors are abstracted into corresponding geometric element objects (ELE-GEO). The relationships among these geometric entities form the topology of element meshes (ELE-MSH). Finite element objects (ELE-FEM) are presented for the local element calculations, in which each classification type of the matrices and vectors is computed by a unique function. These element functions are able to deal with different element types (lines, triangles, quadrilaterals, tetrahedra, prisms, hexhedra) by automatically choosing the related element interpolation functions. For each process of a multi-field problem, only a single instance of the finite element object is required. The element objects provide a flexible coding environment for multi-field problems with different element types. Here, the C++ implementations of the objects are given and described in detail. The efficiency of the new element objects is demonstrated by several test cases dealing with thermo-hydro-mechanical (THM) coupled problems for geotechnical applications.

3.1 Introduction

The numerical analysis of complex multi-field problems is an important issue for many engineering problems. A representative example is nuclear waste disposal. Nuclear waste repositories are constructed in deep geologic underground. Normally, the radioactive waste will generate heat for a long period of time with temperatures over 100°C. Possibly, ground water flow may be developed and gas will be produced due to the heating of the ground water. The coupling of thermal and hydraulic processes can cause mechanical damage in the near field of the host rock mass. To assess the safety of the underground repositories, the problem needs to be addressed as a thermo-hydro-mechanical (THM) coupled problem [56, 57, 58, 59, 60, 61, 62]. Although some commercial tools are already available, there is a tremendous demand in the development of fully coupled THM codes. Existing concepts couple obtainable codes which are specialized to hydraulic, mechanic or deformation problems. The coupling is then realized by data exchange between these codes. This procedure causes

a rigorous restriction of the modeling of coupling phenomena. In this work we present a finite element class which can deal with thermal, hydraulic as well as mechanic problems.

For the programming paradigms, there are two alternatives for finite element code design and development, i.e. procedure-oriented or object-oriented. The former does not encapsulate data and methods manipulating the data together, the latter does encapsulate data and methods and provides regulated communication between data and methods to perform tasks [63, 64]. The object oriented paradigm mboxcapaculates data abstract with its capabilities of data encapsulation, polymorphism and inheritance. Therefore, it provides us a easy way to develop and to maintain a code. This is a reason why more and more researchers are attracted to shift from using procedure oriented to OOP paradigm in numerical analysis. Other reasons for its popularity is that software of increasing complexity has to be developed by permanently increasing programmer teams. OOP has significant advantages by allowing rapid software development through mboxcapsulation, inheritance and polymorph of data and methods. The advantages of object-oriented programming for the development of engineering software was described in detail by [65].

Although the fundamentals of object-orientated programming (OOP) were established in the 1960s, it remains a very important concept to face challenges in scientific computation, such as the solution of coupled multi-field problems. One of the first applications of the object-oriented paradigm to finite element analysis was published in 1990 [66], where essential components of finite element methods such as elements, nodes and materials were abstracted into classes. More efforts have been made by [67, 68, 69, 70, 71, 72, 73] in order to demonstrated the advantages of OOP over the procedure oriented programming. Moreover, the applications to many different physical problems have been investigated, such as linear stress analysis [69, 70, 71], hypersonic shock waves [74], structural dynamics [75], 2D Mises plasticity [76], linear static problems [77, 78], electro-magnetics [79], solidification process [80], heat transfer as well as topological buildup [81]. A process-oriented approach for the solution of multi-field problems in porous media is presented in [82, 61]. Numerical objects for algebraic calculations in finite element analysis have been developed by [83, 84, 85]. mboxcapaculatesIn order to provide an automatic coding environment for finite element analysis, a symbolic code development concept is presented for the weak forms arising from the partial differential equations [86, 87, 88, 89].

Object design is the fundamental step in object-oriented programming. The utilization of OOP to finite element analysis is mainly focused on three aspects: (1) pre/post processing such as mesh generation and graphical user interface, (2) linear algebra and (3) finite element methods. In all these aspects, the core object is the element object. The design of element objects is associated with other objects corresponding to material properties, numerical methods, local geometry and topology of element etc. Specific material objects are described in the most of references cited above.

In this part we present the design, implementation and application of object-orientation in finite element analysis for multi-physics problems. The development of a universal object for local finite element calculation and assembly is able to cope with different kinds of physical problems (i.e. different types of partial differential equations) and is, in particular, designed for strongly coupled problems. Additionally, object-orientation is used in description of mesh topology for the global assembly of system equations. The description of the programming semantics of these objects is given in C++. All the developments of this work are conducted within the framework of the scientific software project OGS [90]. The the OO-FEM concept is verified by numerous test cases dealing with thermo-hydro-mechanical (THM) coupled problems in geotechnical as well as hydrological applications (Parts II and III of this book.)

3.2 Object-orientation in finite element analysis

Almost all numerical methods eventually have to deal with the solution of algebraic equation systems. The basic algorithms for the discretization of partial differential equations (PDEs) resulting from the initial-boundary-value-problems (IBVPs) of continuum mechanics can be generalized in principle as follows: time discretization, calculation of problem-specific node (finite difference method - FDM), element (finite element method - FEM), volume (finite volume method - FVM) contributions, incorporating initial and boundary conditions, assembling and solving the resulting equation system. For non-linear problems iteration schemes, such as Picard or Newton methods, have to be used.

The general solution algorithm for the finite element method is given in Table 3.1.

1. Domain mboxdiscretization (i.e. mesh generation): Creation of individual geometric elements (e.g. triangles, tetrahedra) and their topological relationships (mesh topology).
 2. Local element assembly: Depending on PDE type (section 3.3) all element matrices and vectors have to be computed. The element integration requires geometric operations such as interpolation with shape functions, calculation of inverse Jacobians and determinants. Additionally material functions have to be computed in Gauss points. Material functions can depend on field variables.
 - Geometric element operations (shape functions, Jacobian),
 - Material parameter calculation at Gauss points,
 3. Global assembly of the algebraic equation $\mathbf{Ax} = \mathbf{b}$: The local element entries are assembled into the global system matrix \mathbf{A} and global RHS vector \mathbf{b} . The equations systems is established after mboxincorporating boundary conditions and source/sink terms.
 - Assembly of system matrix \mathbf{A} (including incorporation of boundary conditions),
 - Assembly of RHS vector \mathbf{b} (including incorporation of source/sink terms),
 4. Solving the system equations,
 5. Iterative methods to handle non-linearities,
 6. Iterative methods to handle couplings (partitioned and monolithic schemes).
-

Table 3.1: General solution procedure of the finite element method

The implementation of the general solution algorithm for multi-field IBVPs according to Table 3.1 is illustrated in Fig. 3.2.1. The time loop represents time discretization. Within the time loop, specified physical processes (e.g. flow, transport, deformation) are solved using the finite element method (left box). The solution procedure of each process is unique (middle box). The basic part is the calculation and assembly of element contribution (right box).

Based on above described general solution algorithm for multi-field IBVPs, the fundamental concept of object-orientation in finite element analysis is the generalization of

- Process (PCS) types (section 3.2.1),
- Equation (PDE) types (section 3.2.2),
- Element (ELE) types (section 3.2.3).

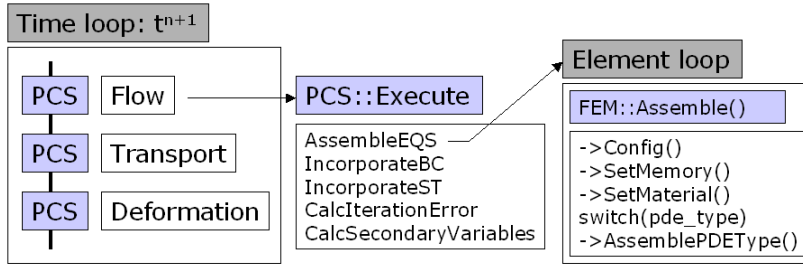


Figure 3.2.1: Implementation of solution algorithm

3.2.1 Process (PCS) types

The central idea behind object-orientation of processes is that the basic steps of the solution procedure: calculation of element contributions, assembly of equation system (including treatment of boundary conditions and source terms), solution of the equations system, linearization methods and calculation of secondary variables, are independent of the specific problem (e.g. flow, transport, deformation processes) [82, 90]. The process (PCS) class provides basic methods in order to solve a PDE in a very general way. The central part of the PCS object is the member function `PCS::Execute()` (Fig. 3.2.1, middle box) conducting these basic steps. Specific properties of the mechanical problem, such as PDE type, primary and secondary variables and material functions, are assigned during process configuration (member function `PCS::Config()`). In order to configure PCS instances we take advantage of polymorphism.

Fig. 3.2.2 illustrates the object-orientation of PCS types for the solution of IBVPs. The PCS object was designed to manage the complete solution algorithm in order to build the global equation system (EQS). In fact, the PCS object 'only' administrates references to geometric (GEO) objects (points, polylines, surfaces, volumes); MSH objects (mesh nodes, elements and mesh topology), node-related data such as initial (IC) and boundary (BC) conditions as well as source terms (ST); material data of porous media (fluid (MFP), solid (MSP), medium (MMP) and chemical (MCP) properties); parameters of the different numerical methods (NUM). PCS instances have 'only' pointers to the related objects as members. `mboxObjects` IC, BC and ST have pointers to object GEO to specify geometrical entities, which are managed by PCS to find element nodes on them. The values in IC and BC and ST are assigned to element nodes found be their GEO members. Object GEO also play a key role in the pre/post-process of the data of the finite element method.

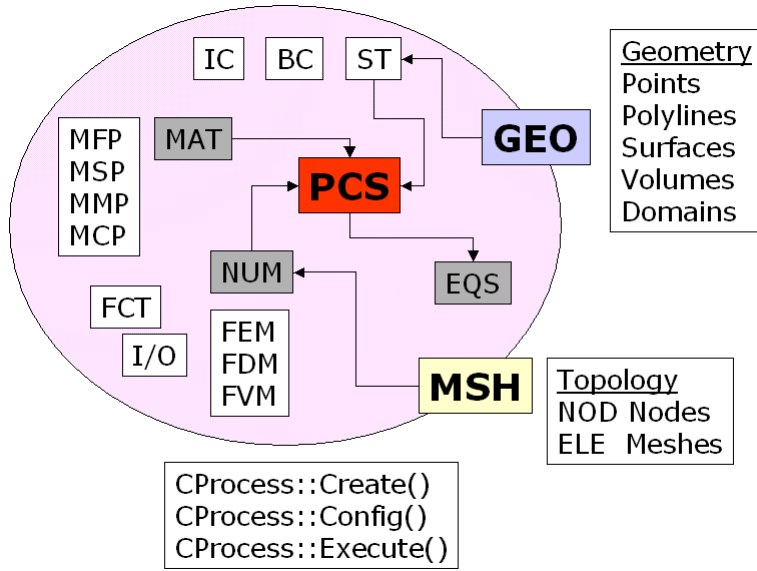


Figure 3.2.2: Structure of the process (PCS) object

3.2.2 PDE types

IBVPs in porous media mechanics, such as fluid flow, mass and heat transport, deformation can be categorized into elliptic, parabolic, hyperbolic or mixed equation types.

As an example to explain the generalization of PDE types, we illustrate the treatment of Laplace terms, which appear in flow, transport as well as deformation processes. In Fig. 3.2.3 the evaluation of finite element matrices for Laplace terms, i.e. $\mathbb{D}\partial^2/\partial x^2$ is given, where \mathbb{D} is a problem-specific material tensor. The special part of diffusion terms is the calculation of second order space derivatives. The second line of the equation in Fig. 3.2.3 represents the numerical integration of matrix being transformed into reference coordinates. From the view point of object-orientation we are faced with the following operations: tensor coordinate transformation (\mathbf{T}), Jacobian (\mathbf{J}), integration (\int) and computation of material properties (\mathbb{D} , e.g. diffusivity, conductivity tensor). The latter is the only problem-specific.

$$\mathbf{K}_e = \int_{\Omega_e} \nabla \mathbf{N} \mathbb{D} (\nabla \mathbf{N})^T d\Omega \quad (3.1)$$

$$= \sum_{gp=1}^{no_gp} \int_{\Omega_r} w_{gp} [\nabla \mathbf{N} \mathbb{D} (\nabla \mathbf{N})^T \det \mathbf{J}] |_{gp} d\Omega \quad (3.2)$$

```

void CFiniteElement::CalcLaplace()
{
    // Loop over Gauss points
    for (gp = 0; gp < no_gp; gp++)
    {
        GaussData();           // Integration points and weights
        Jacobian();            // det J, J-1
        GradShapefct();        // ∇N
        LaplaceMATFunction();  // Material parameters, D
        for (i=0; i<nnodes; i++) // Loop over element nodes
            for (j = 0; j < nnodes; j++)
            {
                if(j>i) continue; // Symmetry
                for (k = 0; k < ele_dim; k++)
                    for(l=0; l<ele_dim; l++)
                        (*Laplace)(i,j) += fkt * dshapefct[k*nnodes+i]
                                         * mat[ele_dim*k+l]
                                         * dshapefct[l*nnodes+j];
            }
    }
}

```

Figure 3.2.3: Finite element Laplace matrix and implementation

```

void CFiniteElementPCS::LaplaceMATFunction()
{
    // Calculate conductivity tensor D for Laplacian
    switch(PcsType){
        case L: // Liquid flow
        case U: // Unconfined flow
        case G: // Gas flow
        case T: // Two-phase flow
        case C: // Componental flow
        case H: // Heat transport
        case M: // Mass transport
        case O: // Overland flow
        case R: // Richard flow
    }
}

```

Figure 3.2.4: Implementation of process dependent material functions

Fig. 3.2.3 shows the implementation of the Laplace term calculation, in which Ω_r is the domain by the reference element. The `CalcLaplace()` member function of the finite element class works for different processes with different material functions (Fig. 3.2.4) and geometric element types. A short description is given

in the table below.

Code	Description
gp	Gauss integration points
GaussData()	Calculation of Gauss weights
Jacobian()	Calculation of Jacobian determinant and inverse
GradShapeFunction()	Calculation of shape function derivatives
LaplaceMATFunction()	Calculation of material coefficients
(*Laplace)(i,j)	Finite element matrix

3.2.3 Element (ELE) types

The basic concept we apply is that: element data, such as geometrical and topological properties, as well as operations of elements, such as element matrix calculations and treatment of boundary conditions, can be generalized.

The element object is the fundamental entity in both PDE and element types. In Fig. 3.2.5 the structure of the element object is illustrated. The element has two kinds of properties connected geometry and PDE types.

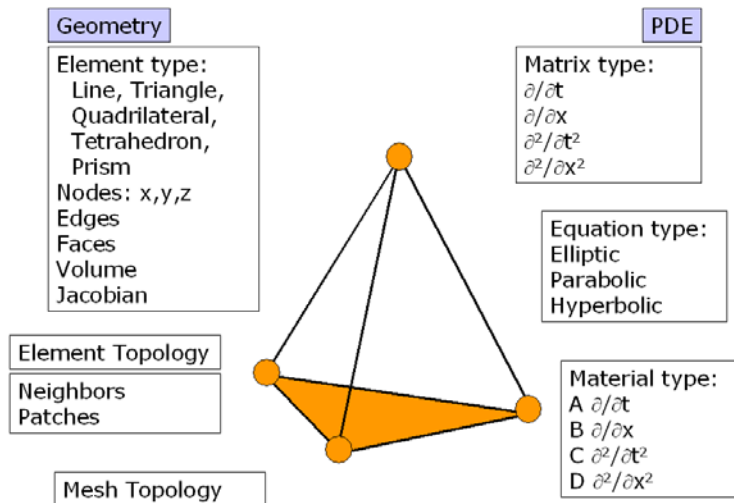


Figure 3.2.5: Structure of element object

Element geometry includes the geometric type (line, triangle, quad, tetrahedron, prism, hexahedron), node coordinates, edges, faces and volume. Coordinate transformation functionalities are considered as geometric element properties. Element topology is defined by element neighbor relationships. Patch properties are available for finite volume approaches and flux calculations. The elements form the mesh topology. Different geometric element types can be combined (Fig. 3.2.5) together to establish a mesh. Additionally, elements can be assigned to different meshes.

Depending on PDE type (elliptic, parabolic, hyperbolic, mixed), different first or second order differential terms have to be evaluated ($\partial/\partial t, \partial/\partial x, \partial^2/\partial t^2, \partial^2/\partial x^2$). These differential terms are categorized in corresponding FE matrix types (see section 3.3), mass matrix, Laplacian matrix, tangential matrix and coupling matrices. An obvious advantage of this element concept is that, depending on the geometric element type, interpolations (shape functions) and derivations as well as tensor operations and Gaussian integrations are conducted automatically in a correct way (see section 3.4.2). For material tensor properties in 1D, 2D or 3D ($\mathbf{A}, \mathbf{B}, \mathbf{C}, \mathbf{D}(\mathbf{x})$ in Fig. 3.2.5), the correct matrix multiplications are conducted automatically. Material functions ($A, B, C, D(u)$ in Fig. 3.2.5) are evaluated accordingly at corresponding Gaussian points of the selected element.

For the sake of object-orientation for numerical methods a so-called process (PCS) object was designed, implemented ([82], section 3.2.1) and successfully applied to different numerical methods (FEM: [61], FDM: [91], FVM: [92]).

3.3 General finite element formulations

The method of weighted residuals is applied to derive the weak formulation of the balance equations given in section 2.3.

Assume $\mathcal{V}^n \subset H_\Gamma^1(\Omega)^n$ is the test function space. For all $w \in \mathcal{V}^1$, we have the weak form of the mass balance equation (2.59) as

$$\int_{\Omega} \left(nS^\gamma \frac{\partial \rho^{\gamma R}}{\partial t} + nS^\gamma \mathbf{v}^{\gamma s} \cdot \nabla \rho^{\gamma R} + n\rho^{\gamma R} \frac{\partial S^\gamma}{\partial t} + n\rho^{\gamma R} \mathbf{v}^{\gamma s} \cdot \nabla S^\gamma + \nabla \cdot (\rho^\gamma nS^\gamma \mathbf{v}^{\gamma s}) + S^\gamma \rho^{\gamma R} \nabla \cdot \dot{\mathbf{u}}^s - q^\gamma \right) w \, d\Omega = 0$$

Applying integration by parts, divergence terms can be rewritten as

$$\int_{\Omega} \nabla \cdot \mathbf{A} \omega \, d\Omega = \int_{\Omega} \mathbf{A} \cdot \nabla \omega \, d\Omega + \int_{\Gamma} \mathbf{A} \cdot \mathbf{n} \omega \, d\Gamma \quad (3.3)$$

Under the same assumption, the weak form of heat balance equation (2.79) can be obtained as

$$\int_{\Omega} \sum_{\gamma} (\varepsilon^\alpha \rho^\alpha c_p^\alpha) \frac{\partial T}{\partial t} w \, d\Omega - \int_{\Omega} \mathbf{j}_{\text{th}} \cdot \nabla \omega \, d\Omega + \int_{\Gamma} \mathbf{j}_{\text{th}} \cdot \mathbf{n} \omega \, d\Gamma - \int_{\Omega} Q_{\text{T}}^\gamma w \, d\Omega = 0 \quad (3.4)$$

Taking account of nonlinearity, the weak form of the momentum balance equation (2.73) must be fulfilled throughout the load history, i.e.,

$$\int_{\Omega} \frac{1}{2} (\boldsymbol{\sigma}_{\text{eff}} - \sum_{\gamma} S^\gamma p^\gamma \mathbf{I}) : (\nabla \mathbf{w} + (\nabla \mathbf{w})^T) \, d\Omega - \int_{\Omega} \mathbf{w}^T \cdot \rho \mathbf{g} \, d\Omega - \int_{\Gamma} \mathbf{w}^T \cdot \mathbf{t} \, d\Gamma = 0 \quad (3.5)$$

for all $\mathbf{w} \in \mathcal{V}^n$, $n = 2, 3$. In principle, vector form of stress and strain tensor (cf. section 2.5) are used to developing the system equation of the discretized form of (3.5). Under this form, the constitutive law for the effective stress tensor can be expressed as

$$\boldsymbol{\sigma}_{\text{eff}} = \mathbf{C} \boldsymbol{\varepsilon}$$

with the corresponding strain-displacement relationship

$$\boldsymbol{\varepsilon} = \mathcal{L} \mathbf{u}^s$$

where \mathcal{L} is an differential operator.

$$\mathcal{L} = \begin{pmatrix} \partial/\partial x & 0 & 0 \\ 0 & \partial/\partial y & 0 \\ 0 & 0 & \partial/\partial z \\ \partial/\partial y & \partial/\partial x & 0 \\ 0 & \partial/\partial z & \partial/\partial y \\ \partial/\partial z & 0 & \partial/\partial x \end{pmatrix} \quad (3.6)$$

We use the Galerkin finite element method to solve the weak forms of balance equations above. All variables are approximated by admissible finite element functions in the Taylor-Hood finite element space, i.e, low order interpolation $\mathbf{N}_1 \in \mathbb{R}^n$ for pressure and temperature variables and high order interpolation $\mathbf{N}_2 \in \mathbb{R}^n$ for displacement, respectively. As a result of the finite element discretization of the weak forms (3.3), (3.4) and (3.5), we obtain local matrices and vectors for the global system equations [16]. Element matrices and vectors can be classified into following types (Table 3.2)

Type	Name	Equations
$\int_{\Omega} \mathbf{N}_1^T \mathcal{M} \mathbf{N}_1 d\Omega$	Mass matrix	(3.3),(3.4)
$\int_{\Omega} (\mathbf{N}_1)^T \mathcal{M} \nabla \mathbf{N}_1 d\Omega$	Advection matrix	(3.4)
$\int_{\Omega} (\nabla \mathbf{N}_1)^T \mathcal{M} \nabla \mathbf{N}_1 d\Omega$	Laplace matrix	(3.3),(3.4)
$\int_{\Omega} \mathbf{B}^T \mathcal{M} \mathbf{B} d\Omega$	Tangential matrix	(3.5)
$\int_{\Omega} \mathcal{M} \mathbf{B}^T \mathbf{m} \mathbf{N}_1 d\Omega$	Displacement coupling matrix	(3.3)
$\int_{\Omega} \mathcal{M} \mathbf{N}_1^T \mathbf{m}^T \mathbf{B} d\Omega$	Pressure coupling matrix	(3.5)
$\int_{\Omega} Q \mathbf{N}_1 d\Omega, \int_{\Omega} Q \mathbf{N}_2 d\Omega$	Source term vector	(3.3),(3.4),(3.5)
$\int_{\Gamma} q \mathbf{N}^T d\Gamma$	Neumann vector	(3.3),(3.4),(3.5)

Table 3.2: Matrix and vector types

where \mathcal{M} are a process-specific material functions, $\mathbf{B} = \mathcal{L} \mathbf{N}_2$ is so called strain-displacement matrix, $\mathbf{m} = (1, 1, 1, 0, 0, 0)^T$ is mapping vector. Based on this classification of matrix and vector types the finite element object is designed (section 3.4.2).

3.4 Element objects - ELE

In this section, the details of the implementation of the element objects are described. The relationship of element objects is shown in Fig. 3.4.6. For the simulation of each process in a coupled problem or each single problem, only an instance of mesh object (ELE-MSH) and an instance of finite element object are required. Geometric element object (ELE-GEO) manufacture the foundation of this concept (section 3.4.1). Meshes (ELE-MSH) are formed based from geometric element entities (section 3.4.4). Finite element object (ELE-FEM) basically compute the finite element matrices for different PDE types and geometric element types automatically using the corresponding shape functions (section 3.4.2). ELE-PCS object assemble the equation systems for the problem type, i.e. THM coupled ELE-PCS object problems for porous media (section 3.4.3). In box To this purpose, objects ELE-PCS and ELE-FEM and have a pointer member pointing to each other. When an instance of ELE-PCS object for a process in a coupled problem or a single problem is constructed, an instance of ELE-FEM object is created accordingly. During the construction of the instance of ELE-FEM object, the degree of freedom of the problem is initialized by the type the ELE-PCS instance, i.e. the specific problem. This means only one instance of ELE-PCS and one instance of ELE-FEM have to be created for each process in a coupled problems or for each single problem. Moreover, ELE-FEM has a pointer member pointing to interpolation function. This member is initialized by the messages from the instance of ELE-PCS and each instance of ELE-GEO for each finite element during the local assembly. Such initialization guarantees that interpolation function and its derivatives are set properly for each geometric element for a process or a problem.

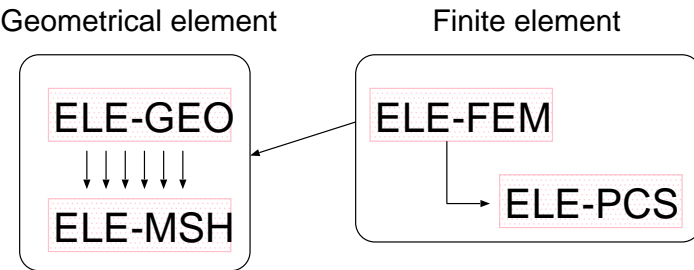


Figure 3.4.6: Relationship of element objects

In general, messages of the type of a process a problem and the type element determines the pointers to the corresponding interpolation function and its derivatives of an instance of ELE-FEM. An instance of ELE-FEM has a pointer to ELE-GEO as a member too. When local assembly comes to an element, or an instance of ELE-GEO, the ELE-FEM instance have the ELE-GEO pointer point to the element and initialized its numerical methods such as interpolation, Gauss integration accordingly. This is very helpful for the finite element analy-

sis of consolidation in porous media, in which, the Talyor-Hood finite element spaces, i.e. linear interpolation for flow process and quadratic interpolation for deformation process, is required for stability reason[56]. In default, the order of interpolation of each element is linear and the nodes of an element are its geometrical vertices. If the high order interpolation is required by a process or a problem, additional nodes are created for each instance of ELE-FEM during the construction of the mesh. The idea of this concept is, that specific process-related information are introduced as late as possible to keep the software concept as flexible as possible.

3.4.1 Geometric element object – ELE-GEO

As described in section 3.2, the first step of finite element analysis is the domain discretization. As a result we obtain element meshes. Hereafter, we refer to a mesh element as the geometric element object **ELE-GEO**. The intrinsic properties of a geometric element object are: nodes, edges, faces, volume and neighbors (Fig. 3.4.7). Neighbor relationships connect geometric element objects within a mesh and, therefore, represent topological properties.

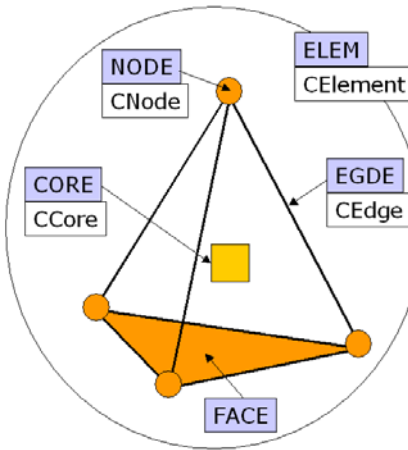


Figure 3.4.7: Mesh element

We design the following element property classes to encapsulate all geometric and topological element information.

- **CCore** for CORE object,
- **CNode** for NODE object,
- **CEdge** for EDGE object,

- `CElem` for `ELEM` object.

Faces and neighbors belong to `ELEM` object. Indeed, edges could be also assigned to the `ELEM` object. However, we consider an edge as an individual entity for two reasons. First, some numerical methods, such as mixed finite elements, require edges as a basic geometric property as nodes for the Galerkin FEM. Second, edges are frequently used as basic properties in automatic generation. As `NODE`, `EDGE` and `ELEM` objects share common data and methods, we abstract these into the `CCore` class as a base class.

```
class CCore
{
protected: // Properties
    long index; // global element index
    char position; // position indicator
    bool status; // status in usage
    int order; // order of interpolation
public: // Methods
    // Set members
    void SetIndex(const long index) {index = index;}
    void SetPosition(const char BC_type) {boundary = BC_type;}
    void SetStatus(const bool status) {status = status;}
    void SetOrder(const int order) {order = order;}
    // Get members
    long GetIndex() const {return index;}
    char GetPosition() const {return position;}
    bool GetStatus() const {return status;}
    int GetOrder() const {return order;}
    // Construction
    CCore(const int id); // constructor
    virtual ~CCore(); // destructor
    // Operators
    virtual void operator = (const CCore & g) {}
    virtual bool operator == (const CCore & g) {return false;}
    // Output
    virtual void output(ostream& os=cout) const {};
};
```

Figure 3.4.8: `CCore` implementation for basic geometric element properties and methods

Core object - CORE - geometric element base class

Common data of a geometric element are: global element index; position indicator within the whole domain, which indicates whether the geometric element is inside the domain or on the domain surface; status flag, which indicates whether this element is marked for some usage. Assign = as well as identity operators == are virtually defined. The C++ implementation of the `CCore` base class is given in Fig. 3.4.9.

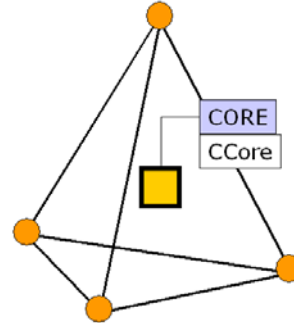


Figure 3.4.9: Core of mesh element

`mboxMember char position` is used to determine the location of the geometrical entity within a domain, e.g. it is inside the domain or on the boundary of the domain.

Classes `CNode`, `CEdge` and `CElem` are directly derived from the base class `CCore`. Assign = as well as the identity operator == are overloaded in these objects. With such overloading operators, passing data of an class instance, A, to another class instance, B, can be simply realized with the instruction `A=B`. Whether two instances are identical can be checked by the instruction `if(A==B)`.

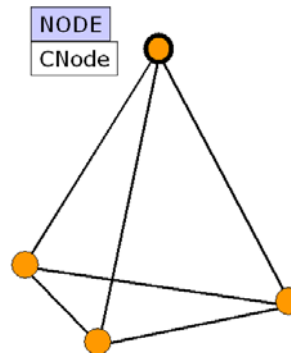


Figure 3.4.10: Node of element object

Node object - NODE

The node object (**NODE**) is derived from the **CCore** class. In addition, the **CNode** class provides the geometrical position of an element in real space, i.e. the coordinates of element nodes (Fig. 3.4.10).

```
class CNode:public CCore
{
    private: // Members
        double coordinate[3];
        Vector<long> ConnectedElements;
        mboxVector<long> ConnectedNodes;
    public:
        // Construction
        Node(const int Index, const double x,
              const double y, const double z=0.0);
        Node() {}
        ~Node() {ConnectedElements.resize(0); ConnectedNodes.resize(0);}
        // Operators
        void operator = (const Node& n);
        bool operator == (const Node & n);
        // Set members
        void SetX(const double argX) { coordinate[0] = argX; }
        void SetY(const double argY) { coordinate[1] = argY; }
        void SetZ(const double argZ) { coordinate[2] = argZ; }
        void SetCoordinates(const double* argCoord);
        // Get members
        double GetX() const {return coordinate[0];}
        double GetY() const {return coordinate[1];}
        double GetZ() const {return coordinate[2];}
        int GetNumberOfConnectedElements() const {return
            ConnectedElements.size(); }
        mboxint GetNumberOfConnectedNodes() const {return
            ConnectedNodes.size(); }
        // Output
        void Write(ostream& os=cout) const;
    private: // Class relations
        friend class CEdge;
        friend class CElem;
};
```

Figure 3.4.11: CNode implementation

Mesh elements having this node in common are determined immediately after mesh data is generated. Elements sharing this node are stored in vector **ConnectedElements**. This node-element relationship is very important information of the mesh topology. It is required e.g. for extrapolation of Gauss point values to node values or for projecting element properties to nodes. Using the **ConnectedElements** vector, the calculation of mesh topology can be enormously accelerated. **mboxFor** extrapolation of gauss point values to nodes, we only need to know the size of the vector, i.e. how many element connected to the nodes. Since extrapolation takes place in element-wise, node values are accumulated

from the contribution of its connected elements, we have to average the accumulated node value by dividing it with the number of connected elements after extrapolation is finished. Member vector `ConnectedNodes` stores indices of all nodes of connected elements and it used together with the degree of freedom of the preocess/problem to store indices of all nodes of connected elements and it can be used together with the degree of freedom of the preocess/problem to create the sparse matrix of the system equations.to create the sparse matrix of the system equations. The memory of `ConnectedNodes` is released as soon as the sparse matrix is created. Classes `CEdge` and `CElem` are set as friend classes of `CNode` so that they can access to `CNode` private members directly. The C++ implementation of class `CNode` is given in Fig. 3.4.11.

Instances of `NODE` object are stored in a global vector:

```
vector<CNode*>node_vector.
```

Edge object - EDGE

The edge object (`EDGE`) is derived from the `CCore` class. Edges are used to build up the frame of a geometric element object (Fig. 3.4.12). It is sufficient to use two nodes to form a geometric edge. However, for higher order finite elements, more points are required along an edge. Therefore, we use a vector of `CNode` pointers as class member for edge nodes (see Fig. 3.4.12). In case of quadratic finite elements, the first two nodes are element corner nodes and the last one is the middle point of this edge.

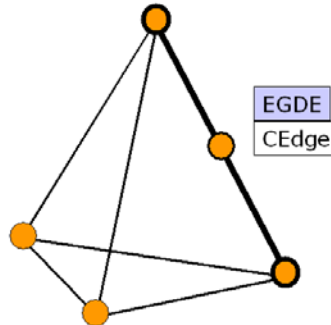


Figure 3.4.12: Edge of mesh element

The C++ implementation of the `CEdge` class is given in Fig. 3.4.13.

`Vector` is a "clone" of the standard C++ vector template, as `template Vector<class V> class V` with less memory consuming but sufficient and efficient functionality of vector algebraic calculation.

For node based finite elements (i.e. linear interpolation), edges are only used to the compute topological mesh structure mboxand to process Dirichlet boundary

conditions and source terms. For instance, if a Dirichlet boundary condition of a PDE is assigned by a polyline, edges of elements on the polyline will be found and the Gauss integration will be performed on these edges to produce node values of nodes of these edges. They are not needed to be stored for the later computations anymore. On the other hand, mixed finite elements or higher order finite elements require edges through all computations. In this case we save all edges of a mesh in a standard C++ vector: `vector<CEdge*>edges_vector`.

```
class CEdge:public CCore
{
    private: // Members
        vec<CNode* > nodes_of_edges;
    public: // Member functions
        // Construction
        Edge(const int Index, bool quadr=false);
        ~Edge();
        // Operators
        void operator = (CEdge& edg);
        bool operator == (CEdge& edg);
        // Member access
        void SetNodes( vec<CNode* >& Nodes)
        { for(int i=0; i<(int)Nodes.Size(); i++)  Nodes[i] = nodes_of_edges[i]; }
        void SetNodes( vec<CNode* >& Nodes) const { Nodes = nodes_of_edges; }
        // Output
        void Write(ostream& osm=cout) const;
    private: // Class relations
        Vector<CNode* > nodes_of_edges;
        friend class CElem;
};
```

Figure 3.4.13: CEdge implementation

```
class CEElement:public CCore
{
    private: // Members
        // ID
        CElem* owner;
        int ele_type; // Element type
        // Geometrical properties
        int dim; // dimension of element
        double volume; // element volume
        // Topological properties
        int nnodes; // number of element corner nodes
        int nnodesHQ; // number of element nodes for quadratic interpolation
        Vector<CNode* > nodes;
        int nedges; // number of edges
        Vector<CEdge* > edges;
        int nffaces; // number of faces
        // Mesh topology
        int sub_domain;
        Vector<CElem* > neighbors;
        Vector<CElem* > sons;
        Vector<long> nodes_index;
}
```

Figure 3.4.14: CElem implementation

Element object - ELEM

The element object (**ELEM**) is also derived from the **CCore** class. **ELEM** represents an individual element of a mesh. Node and edge objects are employed to construct the element object. An abstract mesh element object is designed for different geometric element types, i.e. lines, triangles, quadrilaterals, tetrahedra, triangle based prisms, hexahedra (Table 3.3, Fig. 3.4.15). These geometric element types are defined by an ID, i.e, integer number represent element type. The C++ implementation of **class CElem** is given in Fig. 3.4.14.

Basic members of the element object are identification, geometrical as well as topological properties and mesh relationships. Element ID (index) is inherited from the **CORE** object. Dimension and volume are basic geometric members. Depending on the geometric type of an element (**ele_type**), the following geometrical and topological properties are specified:

Table 3.3: Basic topology information of an geometrical element

Geometric type	ele_type	nnodes	nnodesHQ	nfaces	nedges
Line	1	2	3		
Quadrilateral	2	4	9	4	4
Hexahedron	3	8	20	6	12
Triangle	4	3	6	3	3
Tetrahedron	5	4	10	4	6
Prism	6	6	15	5	9

Element nodes and edges are kept in the following two member vectors

```
Vector<CNode*> nodes;
```

and

```
Vector<CEdge*> edges;
```

3.4.2 Finite element object – ELE-FEM

In this section we present the design of the finite element object, i.e. properties and methods, which are required to conduct the finite element analysis. In particular, we discuss the implementation of steps 2 and 3 described in Table 3.1, i.e., local element assembly and global assembly of system equation.

According to the principles of object-oriented programming, we encapsulate common data and functionalities of finite elements into a base class. There are two general tasks of the finite element object. First, local finite element calculations and, second, contributions of the element to the global equation system.

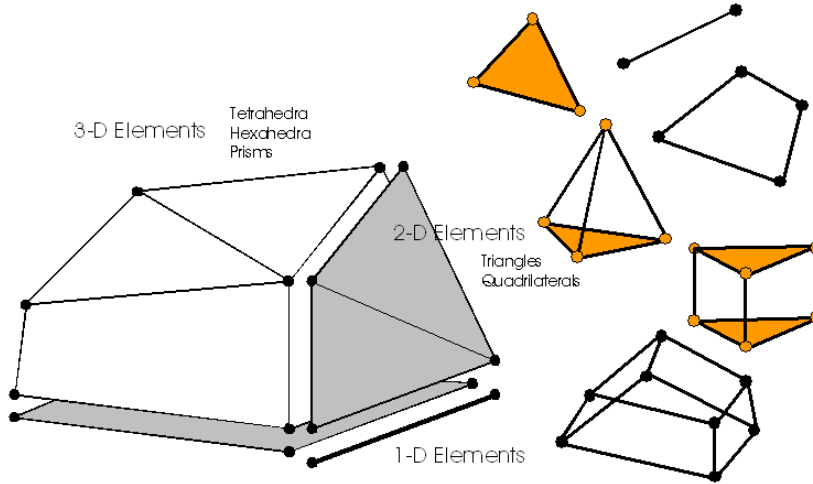


Figure 3.4.15: Geometric elements types

Afterwards, we derive specific finite element objects for different problem types (i.e. PDE types) in the framework of THM porous media mechanics (see Fig. 3.2.5).

Finite element base class: Local element calculations require the selection of specific interpolation functions as well as their derivatives at integration points corresponding to different element types. Therefore, element interpolation functions are regarded as basic items of the finite element object. These interpolation functions have two arguments: first, values of shape functions or the derivative of shape functions; second, reference points, e.g. Gauss points. Therefore, for each kind of geometric element type, we have four functions associated with element interpolation as

```
void ShapeFunctionXXXX(double*,double*);  
void ShapeFunctionHQXXXX(double*,double*);  
void GradShapeFunctionXXXX(double*,double*);  
void GradShapeFunctionHQXXXX(double*,double*);
```

where XXXX is specifying the different geometric element types. `ShapeFunction-XXXX` provides linear interpolation functions N_1 , whereas `ShapeFunctionHQXXXX` gives quadratic interpolation functions N_2 , mentioned in section 3.3. `GradShape-FunctionXXXX` and `GradShapeFunctionHQXXXX` offer the derivatives of the corresponding interpolation functions N_1 and N_2 , respectively. Interpolation functions for all kinds of element types are declared as global functions. The function pointer `void (*VoidFuncDXCDX)(double*,double*)` is defined to point to the

addresses of the global interpolation functions. The C++ implementation of the finite element base class **CElement** is given in Fig. 3.4.16.

```

class CFiniteElement {
protected: // Member data
    CElem* m_ele_geo; // Instance of geometric element
    int order; // Order of shape functions
    int n_gauss_points; // Number of Gauss points
    int n_gauss; // Number of sample points for Gauss integration
    mutable double unit[4]; // Local element coordinates
    double* Jacobian; // Jacobian matrix
    double* invJacobian; // Inverse Jacobian matrix
    double* shape_fct; // Linear shape function values at Gauss points
    double* shape_fct_HQ; // Quadratic shape function values at Gauss points
    double* d_shape_fct; // Linear shape function derivative values at Gauss points
    double* d_shape_fct_HQ; // Quadratic shape function derivative values at
                           // Gauss points
public: // Member functions
    CFiniteElement(const int order=1);
    virtual ~CFiniteElement();
    virtual void Config(CElem* m_ele_geo);
    virtual void ConfigNumerics(const int type);
    double GetGaussData(const int gp,int& gp_r,int& gp_s,int& gp_t)
    virtual void ComputeShapeFct(const int order);
    virtual void ComputeGradShapeFct(const int order);
    virtual double ComputeJacobian(const int order);
    virtual void RealCoordinates(double*xyz);
    virtual void RefCoordinates(double*xyz);
    virtual void LocalAssembly();
    virtual void FaceIntegration();
protected: // Member functions
    VoidFuncDXCDX ShapeFunction; // Prototype for linear shape functions
    VoidFuncDXCDX ShapeFunctionHQ; // Prototype for quadratic shape functions
    VoidFuncDXCDX GradShapeFunction; // Prototype for linear shape function derivatives
    VoidFuncDXCDX GradShapeFunctionHQ; // Prototype for quadratic shape
                                       // function derivatives
}

```

Figure 3.4.16: Finite element base class

Member variable, **m_ele_geo**, is a pointer to the corresponding geometric element object **CElem**, which links the finite element object to geometry. When the local assembly takes place for an element, the instance of this element is obtained by finite element object with its member function, **void Config(CElem m_ele_geo)**. With this, the finite element object has all geometrical and topological properties such as geometric type, coordinate nodes, neighbors for local element calculation.

Different weak forms arise from the different governing equations of flow problem, heat transport problem and mechanical problem (eqn. (3.3), (3.4) and (3.5)). This requires different element level computations for the specific problem. Since root finite element object provides the basic numerical functionality, we can use this object directly for the benefit of the polymorphism mechanism of object oriented programming.

3.4.3 Process related finite element objects – ELE-PCS

Only at this stage (last part of element object concept) we introduce process-related data. The element object `CFiniteElementPCS` should work for all processes: fluid flow, heat transport, deformation and reaction processes regardless of PDE type and type of unknown field functions (scalar or vector quantities).

The finite element object ELE-PCS has two tasks: First, calculation of element matrices, which are formed by shape functions ($\mathbf{N}_1, \nabla \mathbf{N}_1$) and process-specific material properties (MAT objects) (Step 2 in Table 3.1). Second, provide local element contributions to the global equation system: $A_{ij}x_i = b_j$, where i, j are global node indices (Step 3 in Table 3.1).

The C++ implementation of the process-related finite element object ELE-PCS is given in Fig. 3.4.17.

- **ELE-FEM relation:** Process related instances are derived from the finite element base class `CFiniteElement`. Therefore, they inherit all necessary geometric and topological data from ELE-GEO, ELE-FEM, and ELE-MSH objects.
- **PCS relation:** Process related finite element objects need a reference to the related PCS instance, which is conducted by the ELE-PCS class constructor.
- **MAT relations:** References to all MAT objects, i.e. `CFluidProperties*` `m_mfp`, `CSolidProperties*` `m_msp` and `CMediumProperties*` `m_mmp`, are used to get the required material parameters of the specified process(`CProcess*` `m_pcs`). Member function `SetMaterial()` prepares the references to process-specific material properties to accelerate later computations. This insures that the ELE-FEM objects works properly for all THM processes, i.e. fluid flow, heat transport and deformation.
- **Local assembly - Element matrices:** Based on geometric and finite element base data (ELE-FEM relation) and the references to material data (PCS-MAT relation) the process-specific element matrices can be calculated now (`CalcXXXXMatrix()`). Member functions are used to calculate the material coefficients in the Gauss integration points (`CalcXXXXMatrixCoefficients()`). They are defined as `inline` types to improve the computation efficiency. Local element matrices and vectors are stored in the corresponding symmetric/unsymmetric matrix and vector constructs.
- **Global assembly - Equation system:** The global assembly is conducted by the `Assemble()` function. It updates the individual element contributions in the equation system, i.e. global left-hand-side (LHS) matrix (A_{ij}) and global right-hand-side (RHS) vector (b_j). To this purpose the assembly functions needs the relations between local element node and global mesh node numbers, which is provided by the ELE-MSH topology (section 3.4.4). `Assemble()` functions are available for different PDE types.

How the `Assemble()` is implemented for a parabolic PDE is shown in Fig. 3.4.18.

```

class CFiniteElementPCS::public CFiniteElement {
private: // Member data
    // PCS relation
    CProcess* m_pcs;
    // MAT relations
    CFluidProperties* m_mfp;
    CSolidProperties* m_mfp;
    CMediumProperties* m_mmp;
    // Element matrices
    SymMatrix* MassMatrix;
    SymMatrix* LaplaceMatrix;
    SymMatrix* PressureCouplingMatrix;
    Matrixx* AdvectionMatrix;
    Matrixx* StrainMatrix;
    Matrixx* StrainCouplingMatrix;
    ...
    Matrixx* LHSMatrix;
    Vec* RHSVector;
public: // Member functions
    // Construction
    CFiniteElementPCS(CProcess* m_pcs);
    ~CFiniteElementPCS();
    // MAT functions
    void SetMaterial();
    inline void CalcMassMatrixCoefficient();
    inline void CalcAdvectionMatrixCoefficient();
    inline void CalcLaplaceMatrixCoefficient();
    inline void CalcStrainMatrixCoefficient();
    inline void CalcStrainCouplingMatrixCoefficient();
    inline void CalcPressureCouplingMatrixCoefficient();
    // Element matrices
    inline double InterpolateGPValues(double*); // Interpolation at Gauss points
    void SetMemory();
    void CalcMassMatrix();
    void CalcLumpedMassMatrix();
    void CalcAdvectionMatrix();
    void CalcLaplaceMatrix();
    void CalcStrainMatrix();
    void CalcStrainCouplingMatrix();
    void CalcPressureCouplingMatrix();
    void CalcGravityVector();
    void LocalAssembly(); // LHS element contribution
    ...
    // Element contribution to global equation system
    void GlobalAssembly(); // LHS matrix contribution
}

```

Figure 3.4.17: Process related finite element class

```

void CFiniteElementPCS::AssembleParabolicPDEType()
{
    // MAT relations
    SetMaterial();
    // Calculation and assembly of element matrices
    CalcMassMatrix();
    CalcLaplaceMatrix();
    CalcStrainCouplingMatrix();
    // Calculation and assembly of RHS vector
    CalcRHSVector();
}

```

Figure 3.4.18: Linear element assemble function

3.4.4 Element-Mesh relations – ELE-MSH

From Fig. 3.4.6 it can be seen, that element-mesh relations have multiple functions in the element concept, e.g.

- ELE-GEO relation: mesh topology, neighbor relationships of geometric elements, element connectivity, incorporation of boundary conditions,
- ELE-FEM relation: coordinate transformation between local element and global coordinates,
- ELE-PCS relation: local element nodes and node index in the global equation system, material domains.

ELE-GEO relation

Apart from the individual/intrinsic element properties, the ELEM object contains information about mesh topology, i.e. how this element is emplaced in the element mesh. For instance, the (`sub_domain`) index indicates the part of the domain to which this element belongs. This number is used e.g. to distinguish elements in different areas of the domain with different material properties. Neighbor relationships of geometric elements are important topological properties of an element mesh. Neighbors of an element are all those elements adjacent to the faces of the element. Since the definition of ELEM object provides necessary functionality of different geometric element types, we use pointers to ELEM object itself to recode neighbors as

```
Vector<CElem*> neighbors;
```

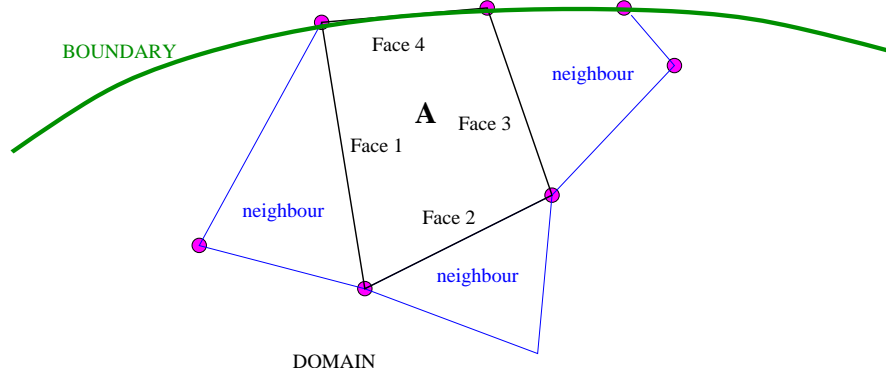


Figure 3.4.19: Definition of element neighbors

As an example Fig. 3.4.19 illustrates the arrangement of neighbor relationships in 2D space, in which quadrilateral element A has three neighbor elements adjacent to its faces (i.e. edges in 2D) 1, 2 and 3. Neighbors 1 and 2 are triangle elements, while neighbor 3 is a quadrilateral element. Face 4 is on the domain boundary, which is not shared by any other element. Vector member, **neighbors**, is initialized with size of 4 and assigned during mesh construction. The first three entries are assigned with pointers to neighbors 1, 2 and 3. The last entry of the vector is filled with a pointer to a surface (Face 4), which is an instance of ELEM object configured for a line element. The boundary type position of this instance is set as 'B'. The coding of the element neighboring process is given below:

```

neighbors[0] = (CElem*) Neighbour1;
neighbors[1] = (CElem*) Neighbour2;
neighbors[2] = (CElem*) Neighbour3;
neighbors[3] = (CElem*) Face4;
Face4->position = 'B'; // on domain boundary
Face4->owner = this; // this element

```

The above neighbor vector is a member of element, i.e., ELEM, object.

ELE-FEM relation

The ELE-FEM association concerns coordinate transformation between local element and global coordinates. Depending on the geometric and numerical type of a finite element, related shape functions and their derivatives are available (section 3.4.2). Jacobian calculations are another typical ELE-FEM methods.

ELE-PCS relation

Subdomain properties of element are used to describe heterogeneity, i.e. local variation of material properties for different problems. Element neighbor relationships are essential data for constructing the mesh and determine the propagation orientation of discontinuities in failure analysis (section ??). Moreover, the proposed element concept allows the assignment of different processes (PCS objects) and meshes (MSH objects).

- sparse objects (Wang 2009)
- parallelization (Wang et al. 2009)
- XFEM (Watanabe 2010)

Part II

Benchmarks for Single Processes

Chapter 4

Heat transport

by Norbert Bttcher, Guido Blcher, Mauro Cacace, Olaf Kolditz

In the first benchmark chapter we consider heat transport in a porous medium described by the heat balance equation (2.79). With the following assumptions:

- Constant material properties,
- Neglecting viscous dissipation effects,
- Local thermal equilibrium, $c\rho = \sum_{\alpha} c^{\alpha} \rho^{\alpha}$, $\lambda = \sum_{\alpha} \lambda^{\alpha}$

we obtain the **linear heat transport** equation

$$c\rho \frac{\partial T}{\partial t} + c\rho \mathbf{v} \cdot \nabla T - \nabla \cdot (\lambda \nabla T) = q_{\text{th}}, \quad (4.1)$$

where c is specific heat capacity, ρ is density, T is temperature, \mathbf{v} is advection velocity and λ is thermal conductivity.

Conduction takes place when a temperature gradient in a solid or a stationary fluid medium occurs. It runs into the direction of decreasing temperature. The thermal conductivity is defined in order to quantify the ease with which a particular medium conducts heat. Against it, convection is caused by moving fluids of different temperatures.

The equation for the heat conduction is

$$\frac{\partial T}{\partial t} = \nabla \cdot (\alpha \nabla T), \quad (4.2)$$

where $\alpha = \lambda/c\rho$ is the heat diffusivity constant.

Temperature changes cause a change of fluid density and viscosity which influences again the behaviour of the fluid while flowing through a porous medium and therefore the velocity of heat transport by groundwater flow. The dependence of density on temperature changes is regarded by using the relation given in (4.3)

$$\rho(T) = \rho_0 \cdot (1 + \beta_T (T - T_0)). \quad (4.3)$$

Here ρ_0 represents the initial density, T the temperature, T_0 the initial temperature and β_T is the thermal expansion coefficient assumed to be a material constant. A more comprehensive description of thermal material behavior of fluids and solids is given in sections 2.4 and 2.5, respectively. Temperature dependent material behavior results in **non-linear heat transport** which are discussed in the coupled processes part of this book.

We consider the following series of benchmarks for heat transport with slightly increasing complexity.

- Linear heat conduction in a semi-infinte domain (4.1)
- Linear heat conduction in a finite domain (4.2)
- Radial heat conduction in a solid (4.2.3)
- Heat transport in a fracture (4.4)
- Heat transport in a porous medium (4.5)
- Heat transport in a fracture-matrix system (4.6)

At the end of the chapter we present an application example dealing with:

- Heat transport in a 3D fracture-matrix system (section 4.7)

4.1 Linear heat conduction in a semi-infinite solid

4.1.1 Definition

We consider a 1D half-domain which is unlimited extended in one coordinate direction ($z \rightarrow \infty$).

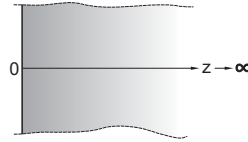


Figure 4.1.1: Model domain

4.1.2 Solution

Analytical solution

The analytical solution for the 1D linear heat conduction equation (4.2) is

$$T(x, t) = T_0 \operatorname{erfc} \left(\frac{x}{\sqrt{4\alpha t}} \right), \quad (4.4)$$

where T_0 is the initial temperature. The boundary conditions are $T(z = 0) = 1$ and $T(z \rightarrow \infty) = 0$.

The material properties for this model setup are given in Tab. 4.1.

Table 4.1: Solid phase material properties

Symbol	Parameter	Value	Unit
ρ	Density	2500	$\text{kg}\cdot\text{m}^{-3}$
c	Heat capacity	1000	$\text{J}\cdot\text{kg}^{-1}\cdot\text{K}^{-1}$
λ	Thermal conductivity	3.2	$\text{W}\cdot\text{m}^{-1}\cdot\text{K}^{-1}$

Using these values, the heat diffusivity constant is $\alpha = \lambda/c\rho = 1.28 \cdot 10^{-6} \text{m}^2/\text{s}$.

Numerical solution

The numerical model consists of 60 line elements connected by 61 nodes along the z-axis (figure 4.1.2). The distances of the nodes Δz is one meter. At $z = [0]\text{m}$ there is a constant temperature boundary condition.

The *Neumann* stability criteria has to be restrained so that the temperature gradient can not be inverted by diffusive fluxes. Using (4.5) the best time step can be estimated by

$$\text{Ne} = \frac{\alpha \Delta t}{(\Delta z)^2} \leq \frac{1}{2}. \quad (4.5)$$

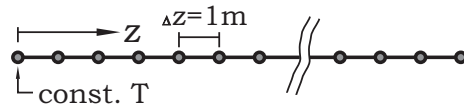


Figure 4.1.2: Spatial discretisation of the numerical model

With $\Delta z = [1]\text{m}$ and $\alpha = [1.28 \cdot 10^{-6}]\text{m}^2/\text{s}$ the outcome for the timestep is $\Delta t \leq [390625]\text{s}$ or 4.5 days, respectively.

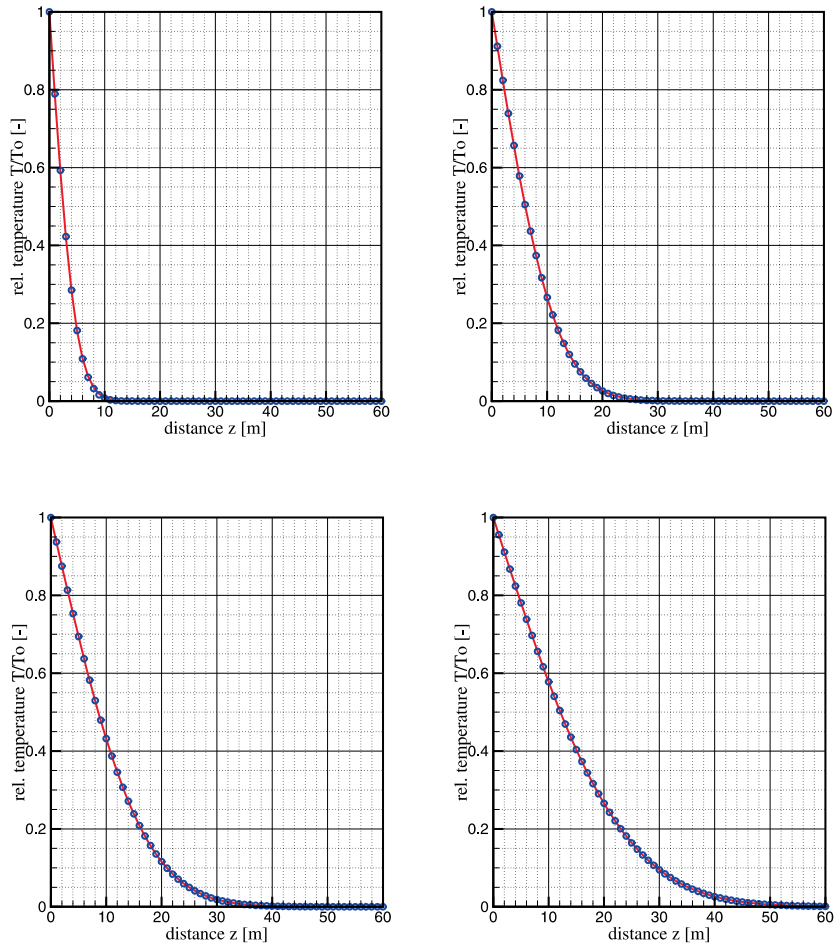


Figure 4.1.3: Temperature distribution along the z-axis after 2 months, 1 year, 2 years and 4 years (from top left to down right).

4.1.3 Results

Figures 4.1.3 show the comparison of the solution of (4.4) and the numerical simulation results. It is demonstrated the temperature distribution along the model domain after 2 months, 1 year, 2 years and 4 years.

4.2 Linear heat conduction in a finite solid

4.2.1 Definition

In the first example (section 4.1) there was a domain limited only by one side with a constant temperature at the boundary. The following problem shows the profile of a homogeneous and isotropic wall with a constant heat flow q_{th} on the left and a constant temperature T_L on the right boundary (Fig. 4.2.4). We consider diffusive heat transport on a two-side bounded domain.

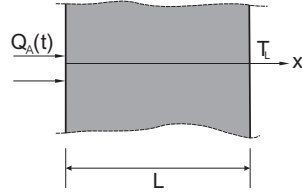


Figure 4.2.4: Heat conduction through a wall

4.2.2 Solution

Analytical solution

A solution for this problem can be found by solving the heat conduction equation (4.2) using Fourier's method (see [93]).

$$\begin{aligned} T(x, t) = & T_L + \frac{q_{\text{th}}}{\lambda}(L - x) \\ & + \sum_{n=1}^{\infty} -\frac{8L}{(2n-1)^2\pi^2} \frac{q_{\text{th}}}{\lambda} \cos \frac{(2n-1)\pi x}{2L} e^{-\frac{(2n-1)^2\pi^2}{4L^2}\alpha t} \end{aligned} \quad (4.6)$$

with T_L is the initial temperature, Q_A is the constant heat source, λ is the thermal conductivity and α is the heat diffusivity constant.

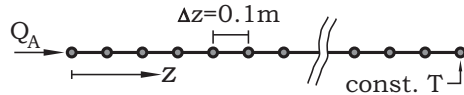


Figure 4.2.5: Boundary conditions and discretisation for the numerical model

Numerical solution

The numerical model consists of 40 line elements and 41 nodes along the x -axis (Fig. 4.2.5). The step size Δz is set to $[0.1]m$. On the left boundary a constant source term is set. The right side obtains a constant temperature condition. Tab. 4.2 shows the values of the used material properties. The heat diffusivity constant is $\alpha = [3.1 \cdot 10^{-6}]m^2/s$.

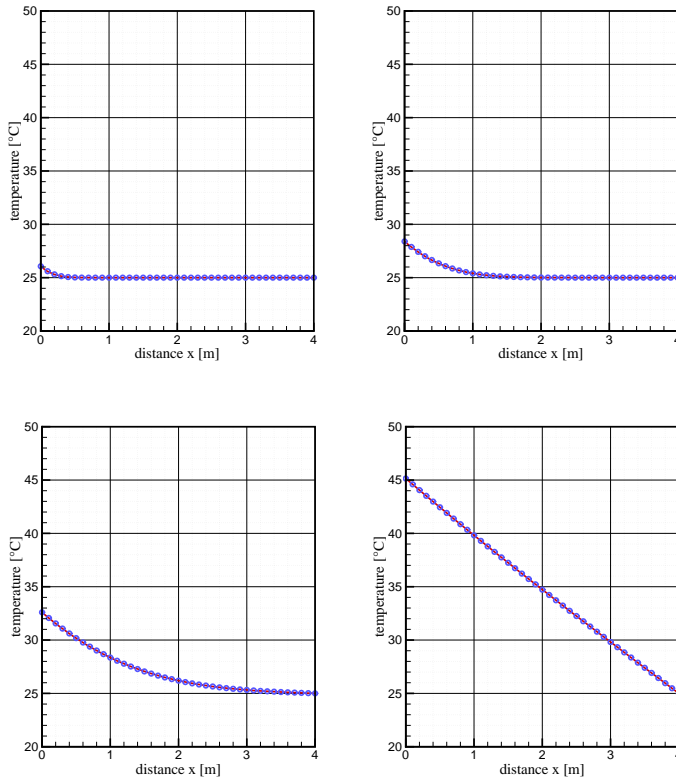


Figure 4.2.6: Temperature distribution along the wall profile after 10.000, 100.000, 500.000 and 5.000.000 seconds (from top left to down right).

4.2.3 Results

The comparison of analytical and numerical solution is presented in Fig. 4.2.6. It shows the distribution of the temperature along the profile of the wall. Due to the thickness of the wall, the heat transport takes very long, after 5×10^6 seconds (≈ 58 days) the temperature distribution becomes steady-state.

Table 4.2: Material properties.

Symbol	Parameter	Value	Unit
q_{th}	Heat source	[30]	$\text{W} \cdot \text{m}^{-2}$
T_L	Initial temperature	[25]	$^{\circ}\text{C}$
L	Wall thickness	[4]	m
ρ	Density of the solid	[2000]	$\text{kg} \cdot \text{m}^{-3}$
c	Heat capacity	[900]	$\text{J} \cdot \text{kg}^{-1} \cdot \text{K}^{-1}$
λ	Thermal conductivity	[5.5]	$\text{W} \cdot \text{m}^{-1} \cdot \text{K}^{-1}$

4.3 Radial heat conduction in a solid

4.3.1 Definition

A slice with a hole in its centre, that means a 2D annulus, which consists of a solid of a constant temperature is exposed to a higher temperature at the surface of its hole. The aim of this calculation is to simulate the heat transfer through a homogeneous solid by the use of an axisymmetric model. Fig. 4.3.7 shows a sketch of the calculation area assuming a homogeneous solid, a constant temperature in the whole body at the beginning and a heating of the slice at the inner surface of the hole .

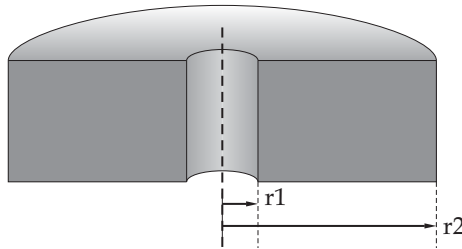


Figure 4.3.7: Radial heat conduction

The inner radius R_1 of the axisymmetric model is [1]m and the outer radius R_2 is [5]m. The numerical model consists of 40 elements and 41 nodes. The initial temperature in the whole area is [25] $^{\circ}\text{C}$. At the right boundary of the numerical model a thermal boundary condition is set with a constant value of [25] $^{\circ}\text{C}$. At the left boundary a source term for heat flux of $q_{\text{th}} = [30]\text{W/m}^2$ is defined. Thereby the continuous heating of the solid is simulated. The used parameters of the solid are listed in Tab. 4.3. The simulation of 5000 time steps with a constant time step length of [1000]s is done.

Table 4.3: Model parameters

Symbol	Parameter	Value	Unit
ρ^s	Density of the solid	[2.0]	$t \cdot m^{-3}$
c^s	Heat capacity	[900]	$J \cdot kg^{-1} \cdot K^{-1}$
λ^s	Thermal conductivity	[5.5]	$W \cdot m^{-1} \cdot K^{-1}$
q_{th}	Heat flux	30	W/m^2
R_1, R_2	Inner and outer radius	1,5	m
T_0, T_2	Initial and boundary temperatures	25,25	K

4.3.2 Solution

For the heating of the annulus with the inner radius R_1 and the outer radius R_2 the following analytical solution for temperature in dependency on the radius r exists. The parameters are according to Tab. 4.3.

$$T(r) = \frac{R_1 q}{\kappa} \ln \left(\frac{R_2}{r} \right) + T_0. \quad (4.7)$$

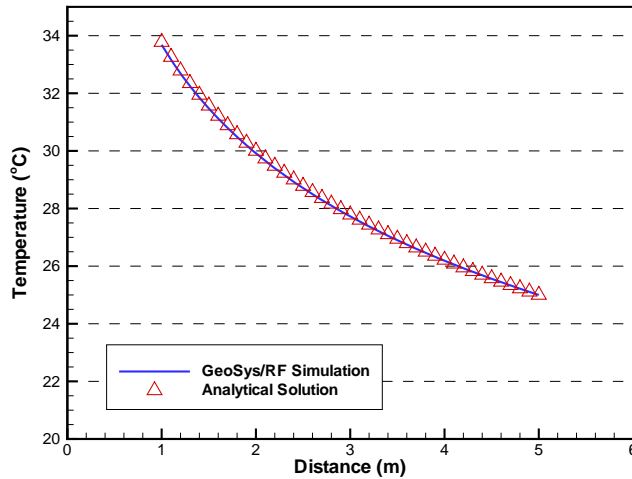


Figure 4.3.8: Temperature distribution along the radial distance

4.3.3 Results

The results of the analytical equation for the temperature distribution over the model length are compared to those of the numerical simulation. Fig. 4.3.8 shows the temperature distribution over the radius of the annulus. Obviously, with the axisymmetric numerical simulation generates comprehensible results that agree well with the analytical solution.

4.4 Heat transport in a fracture

4.4.1 Definition

This problem shows 1D heat transport by advection and diffusion in a [100]m long fracture. The fracture is fully saturated with water, flowing with constant velocity. There is no rock matrix around the fracture considered which could store heat (this will be examined in the next example). Fig. 4.4.9 depicts the model set-up.

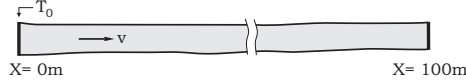


Figure 4.4.9: A fully saturated fracture with flowing water and a constant temperature at the left border

The fracture is described as a porous medium with [100]\% porosity, so that no solid material influences the heat transport process. The properties of the fluid are in Tab. 4.4.

Table 4.4: Model parameters

Symbol	Parameter	Value	Unit
ρ^l	Density of water	[1000]	$kg \cdot m^{-3}$
c^l	Heat capacity of water	[4000]	$J \cdot kg^{-1} \cdot K^{-1}$
λ^l	Thermal conductivity of water	[0.6]	$W \cdot m^{-1} \cdot K^{-1}$
v	Water velocity	3×10^{-7}	m/s
L	Fracture length	100	m

These values cause a diffusivity constant for water of $\alpha = [1.5 \cdot 10^{-7}] m^2/s$. The groundwater velocity in the fracture is $v = [3.0 \cdot 10^{-7}] m/s$.

4.4.2 Solution

For 1D-advection/diffusive transport, an analytical solution is given by Ogata & Banks [94] as

$$T(x, t) = \frac{T_0}{2} \left(\operatorname{erfc} \frac{x - v_x \cdot t}{\sqrt{4\alpha t}} + e^{\frac{v_x \cdot x}{\alpha}} \operatorname{erfc} \frac{x + v_x \cdot t}{\sqrt{4\alpha t}} \right), \quad (4.8)$$

where T_0 is the constant temperature at $x = 0$, v is the groundwater velocity and α is the heat diffusivity coefficient of water. More information can be found e.g. in [93],[95].

The mesh for the numerical model consists of 501 nodes combining 500 line elements. The distance between the nodes is $\Delta x = [0.2]m$. The boundary conditions applied are as follows:

- Left border:
 - constant source term (liquid flow) with $Q = [3.0 \cdot 10^{-7}]m^3/s$
 - constant temperature with $T = [1]^\circ C$
- Right border:
 - constant pressure with $P = [100]kPa$
- Initial conditions:
 - pressure with $P = [100]kPa$ for whole domain
 - temperature $T = [0]^\circ C$ for whole domain
- Time step:
 - $\Delta t = [133]s$

With the given parameters, the NEUMANN criteria (4.5) results on $\text{Ne} = 0.5$ which guarantees the numerical stability of the diffusion part of the transport process. The *Courant* criteria, given by

$$C = \frac{v_x \cdot \Delta t}{\Delta x} \leq 1 \quad (4.9)$$

is equal to $C = 0.2$.

4.4.3 Results

In Fig. 4.4.10 the comparison of analytical and numerical solution is plotted. The figure shows the temperature breakthrough curve at the end of the fracture at $x = [100]m$. The numerical results show an acceptable agreement to the analytical solution. In a further step, the diffusion part of the heat transport process was avoided by minimizing the thermal conductivity of the fluid. Fig. 4.4.11 shows the breakthrough curve for only advective heat transport.

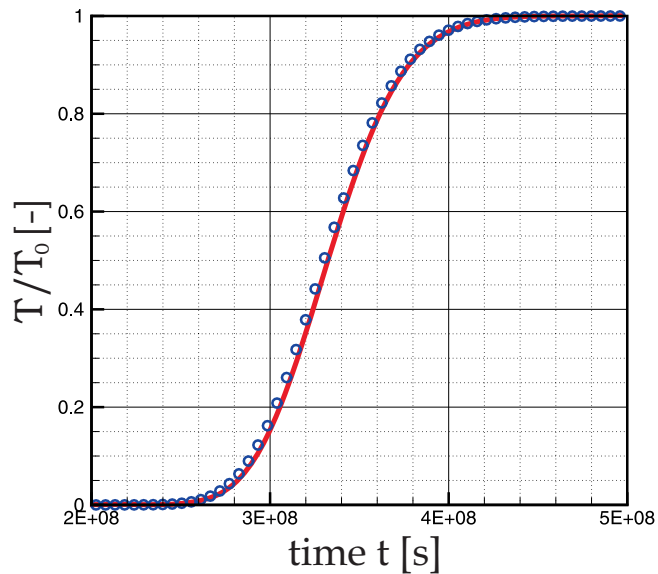


Figure 4.4.10: Temperature breakthrough curve at the point $x = [100]m$.

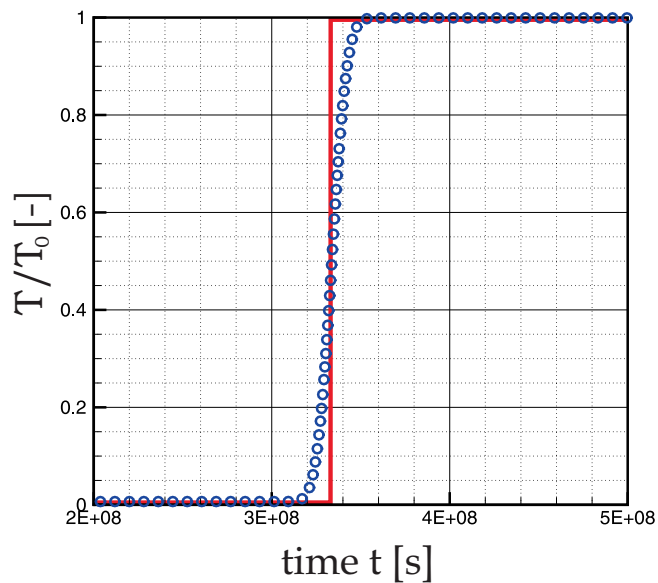


Figure 4.4.11: Temperature breakthrough curve when diffusion is neglected
(shows numerical diffusion)

4.5 Heat transport in a porous medium

4.5.1 Definition

In addition to the previous example (section 4.4) now we consider heat transport in a two-phase homogeneous porous medium consisting of a solid and liquid phase, i.e. a 1D test example for groundwater flow and simultaneous heat transport in an aquifer. The aim of the numerical simulation is also to determine the effect of varying density value with temperature changes.

4.5.2 Solution

For the 1-dimensional calculation the calculation area is simplified as a line of a length of [5.2]m. The calculation model includes 25 elements and 26 nodes. The initial pressure in the whole area is [100]kPa and the initial temperature [300]K. As boundary condition a constant pressure of [101]kPa is given at the left boundary and of [100]kPa at the right boundary. A constant temperature of [400]K is set at the left boundary. The used soil parameters are listed in Tab. 4.5. The fluid density is decreasing with increasing temperature. The viscosity, capacity and conductivity of water are set to constant values. The fluid parameters also can be found in Tab. 4.5.

Table 4.5: Used soil and fluid parameters.

Symbol	Parameter	Value	Unit
<i>Soil parameters</i>			
ϕ	Porosity	0.01	-
k	Permeability	$[1.0 \cdot 10^{-11}]$	m^2
ρ^s	Density	[2850]	$kg \cdot m^{-3}$
c^s	Heat capacity	[1000]	$J \cdot kg^{-1} \cdot K^{-1}$
λ^s	Heat conductivity	[3.2]	$W \cdot m^{-1} \cdot K^{-1}$
<i>Fluid parameters</i>			
ρ_0^f	Initial density	[1000]	$kg \cdot m^{-3}$
η	Viscosity	[0.001]	$N \cdot s \cdot m^{-2}$
c^f	Heat capacity	[4000]	$J \cdot kg^{-1} \cdot K^{-1}$
λ^f	Heat conductivity	[0.6]	$W \cdot m^{-1} \cdot K^{-1}$

In order to find out whether the consideration of varying water density with temperature changes is possible, one simulation run is done with a constant density of [1000]kg/m³, which is the initial water density before heating, and one run with a constant density of [900]kg/m³, the density after the heating

process. The temperature results for a heat transport with varying density have to be in between both temperature envelopes.

4.5.3 Results

The curve for temperature evolution, which is shown in Fig. 4.5.12 for the right boundary (node 26), shows the expected characteristics. Therefore it can be stated, that the consideration of temperature dependent fluid density is possible.

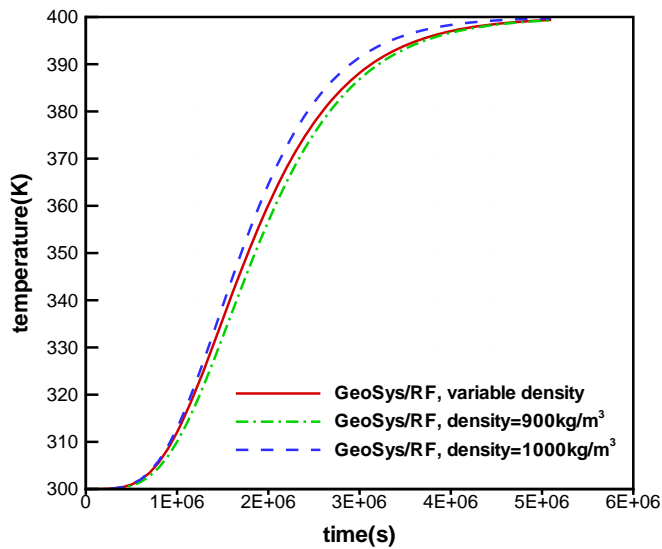


Figure 4.5.12: Temperature evolution with constant and variable fluid densities.

4.6 Heat transport in a fracture-matrix system

4.6.1 Definition

Based on the example for heat transport in a fluid filled fracture (section 4.4), this problem is extended by heat diffusion through a rock matrix orthogonal to the fracture (Fig. 4.6.13).

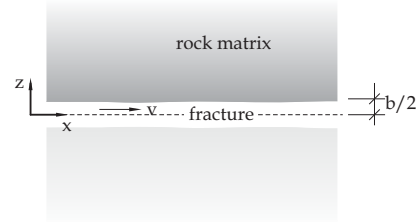


Figure 4.6.13: Heat transport in a fracture-matrix system

The model and material parameters for fracture and rock matrix, respectively, are given in Tab. 4.6.

Table 4.6: Model parameters for the LAUWERIER-problem.

Symbol	Parameter	Value	Unit
<i>spatial discretisation</i>			
L	fracture length	[50]	m
W	matrix width	[63.25]	m
Δx	step size X	[2]	m
Δz	step size Z	[0.1265]	m
$b/2$	half of fracture width	[$1.0 \cdot 10^{-3}$]	m
v_x	groundwater velocity	[$1.0 \cdot 10^{-4}$]	m/s
<i>temporal discretisation</i>			
Δt	time step length	[$2.0 \cdot 10^5$]	s
	number of timesteps	2500	
	total time	[$5.0 \cdot 10^8$]	s
<i>material properties – solid</i>			
λ	thermal conductivity	[1]	$W \cdot m^{-1} \cdot K^{-1}$
c	heat capacity	[1000]	$J \cdot kg^{-1} \cdot K^{-1}$
ρ	density	[2500]	$kg \cdot m^{-3}$
<i>material properties – fluid</i>			
c	heat capacity	[4000]	$J \cdot kg^{-1} \cdot K^{-1}$
ρ	density	[1000]	$kg \cdot m^{-3}$

4.6.2 Solution

For this problem an analytical solution was derived by LAUWERIER (1955) (see [95]) with following assumptions:

- in the fracture, heat is transported only by advection,
- in the rock matrix, heat transport takes place by diffusion (only along the z-axis).

The LAUWERIER solution is given by

$$T_D = \begin{cases} 0, & t_D < x_D \\ \operatorname{erfc} \left\{ \frac{\beta}{\sqrt{\alpha(t_D - x_D)}} \left[x_D + \frac{1}{2\beta} (z_D - \frac{1}{2}) \right] \right\}, & t_D > x_D, z_D \geq \frac{1}{2} \end{cases} \quad (4.10)$$

with the following dimensionless parameters:

$$t_D = \frac{v_x}{b} t, \quad x_D = \frac{x}{b}, \quad z_D = \frac{z}{b}, \quad \alpha = \frac{\lambda^s}{c^s \rho^s} \frac{1}{bv_x}, \quad \beta = \frac{\lambda^s}{c^l \rho^l} \frac{1}{bv_x} \quad (4.11)$$

where b is the fracture width, λ is the thermal conductivity, c is the heat capacity, ρ is the density and the suffixes s and f denote the solid (rock) and liquid (water) phases, respectively.

The numerical LAUWERIER model is formed as a coupling of advective 1D heat transport in x-direction and diffusive 1D heat transport in z-direction. This means, that nodes in the rock matrix are not influenced by their left or right neighbors. The matrix elements are connected to the fracture elements orthogonally. Fig. 4.6.14 shows a schematical description of the model setup. Because of the symmetry, the numerical model calculates just the domain above the x-axis.

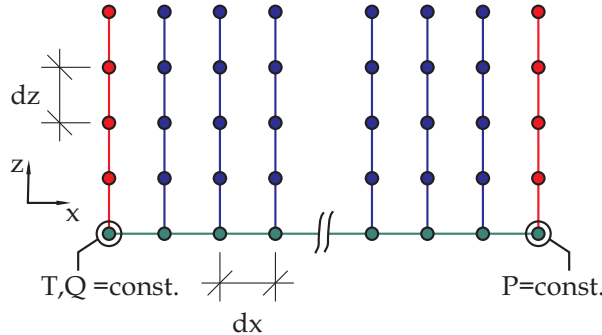


Figure 4.6.14: Alignment of the grid for the numerical model.

Fig. 4.6.15 shows the positions of observation points which were chosen to evaluate the numerical model by the comparison with analytical solutions.

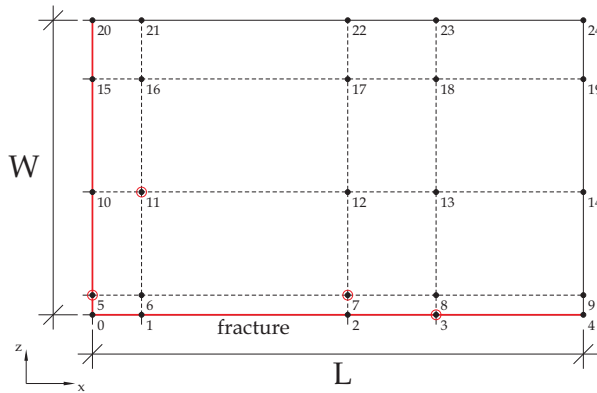


Figure 4.6.15: Positions of observation points for temperature breakthrough curves.

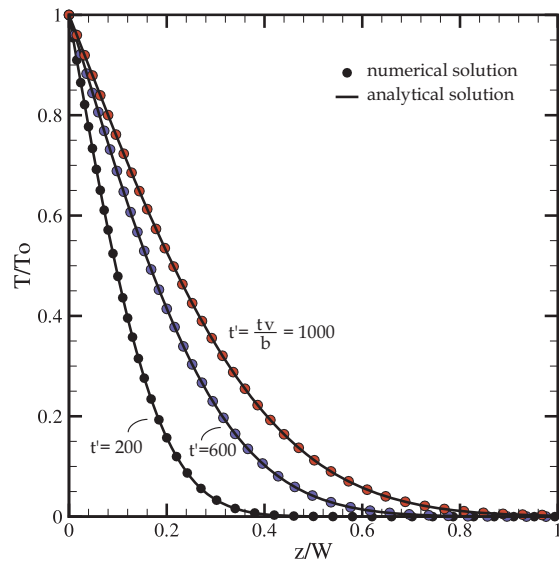


Figure 4.6.16: Temperature distribution orthogonal to the fracture at $x = 0$ at three different times.

4.6.3 Results

The quality of the numerical results can be shown by temperature distribution curves for several times in the rock matrix. Fig. 4.6.16 shows the temperature profiles for $x = [0]m$ at three moments t' . The numerical solution has a very good agreement to the analytical results. Temperature profiles along the fracture at $z = [0]m$ are plotted in Fig. 4.6.17.

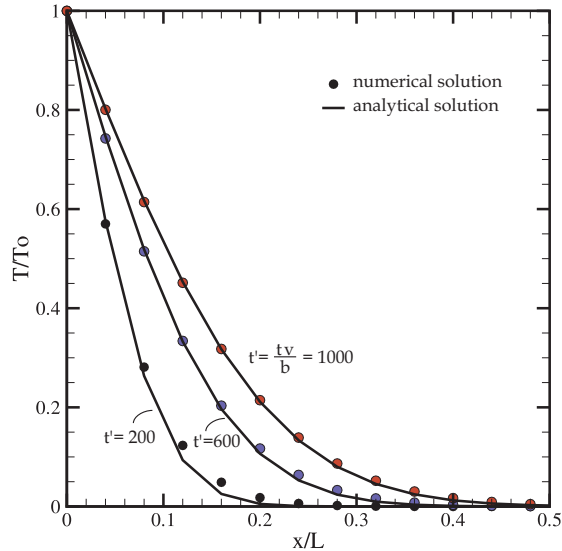


Figure 4.6.17: Temperature distribution along the fracture at three different times.

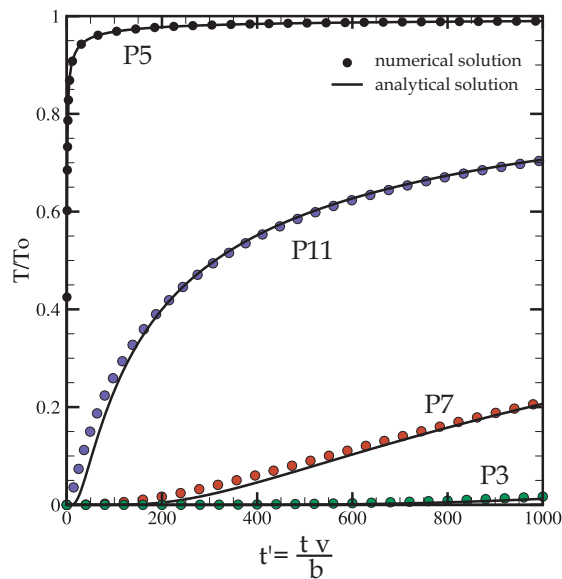


Figure 4.6.18: Temperature breakthrough curves at certain points in the rock matrix.

For long simulation times ($t' = 1000; t' = 600$) both solutions fits very well together. For short simulation times, the numerical solution differ slightly from the analytical results. This discrepancy for short simulation times can be examined in Fig. 4.6.18, where temperature breakthrough curves for certain points (see Fig. 4.6.15) is plotted.

4.7 Heat transport in a fracture-matrix systems: 3D case study

As a last example for linear heat transport we introduce an applied case study for a 3D fracture-matrix system.

4.7.1 Geology

The following problem deals with simulating fluid flow and heat transport in a 3 dimensional heterogeneous faulted geological system.

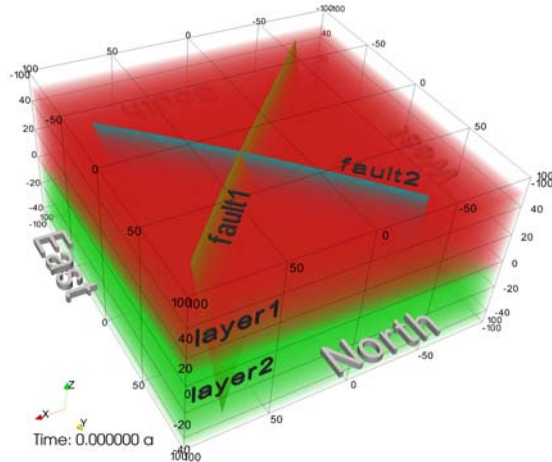


Figure 4.7.19: Sample model consisting of two geological layers cut by a system of two crossing faults.

The model volume consists of two sub-horizontal geological layers, including two dipping faults (Figure 4.7.19). The horizontal north-south and east-west extensions are 200 m, resulting in a horizontal model area of $40,000 \text{ m}^2$. The two geological layers are vertically bordered by three curved surfaces. The elevation of top, middle and bottom surface is $55 \text{ m} \pm 5\text{m}$, $0 \text{ m} \pm 7\text{m}$ and $-45 \text{ m} \pm 5\text{m}$, respectively. Therefore, an average thickness of 55 m for layer 1 and 45 m for layer 2 is established (Table 4.7).

Table 4.7: Geometrical attributes of the geological layers and faults.

property	unit	layer1	layer2
average thickness t	[m]	55	45
		fault1	fault2
dip direction	[°]	316.7	225
dip	[°]	80.6	63.2
length l	[m]	233.5	183.8

Both faults are penetrating the two geological layers. Fault 1 has a length of 233 m and is striking North-East, with dip coordinates of 316.7°; 80.6°. Fault 2 has a length of 184 m and is oriented perpendicular to fault 1, having dip coordinates of 225°; 63.2° (Table 4.7).

4.7.2 Initial and boundary conditions

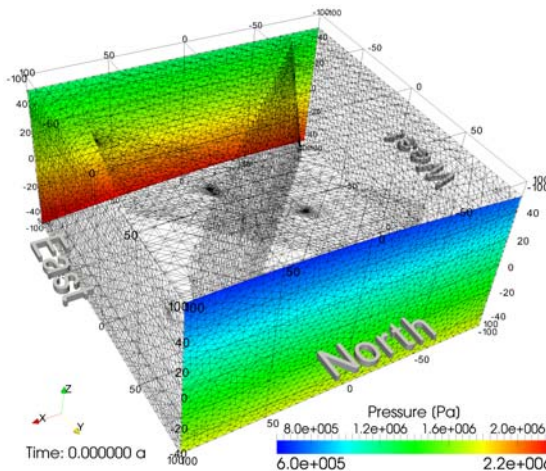


Figure 4.7.20: Pressure boundary condition of the sample model

During the simulation, a general flow field from the South to the North is generated. Dirichlet (or first-type) boundary conditions for pressure are set along the southern and northern boundaries (Figure 4.7.20). According to the definition of hydrostatic pressure, the pressure at the southern border is constant at $p(x, y = -100 \text{ m}, z) = \rho g z + 1.75 \cdot 10^6 \text{ Pa}$ and at the northern border at $p(x, y = 100 \text{ m}, z) = \rho g z + 1.25 \cdot 10^6 \text{ Pa}$ (Figure 4.7.20), where ρ [1000 kg/m³], g [9.81 m/s²] and z denotes the fluid density, gravitational acceleration and height of liquid column, respectively. An average hydraulic gradient $\nabla h = 5 \cdot 10^5 \text{ Pa} / 200$

$m = 0.25$ from the South to the North is provided. For the remaining domain, a pressure value of $1.75 \cdot 10^6$ Pa is initialized.

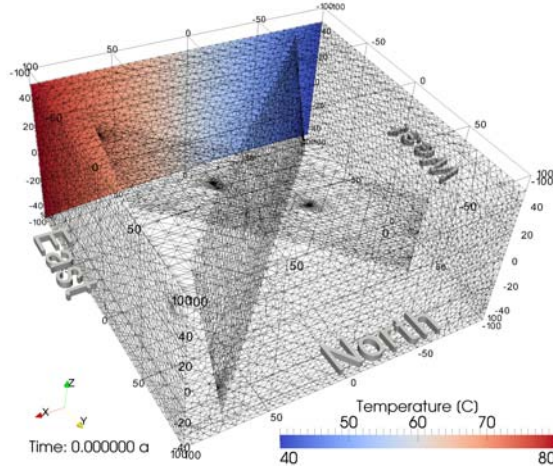


Figure 4.7.21: Temperature boundary conditions of the sample model.

To generate an inflow of hot and cold water from the southern border, Dirichlet boundary conditions for temperature are applied too (Figure 4.7.21). Along the southern border, temperature increases from 40°C to 80°C , in going from West to the East resulting in a temperature profile of $T(x, y = -100 \text{ m}, z) = 0.2^\circ\text{C}/\text{m} * x + 60^\circ\text{C}$ (Figure 4.7.21). For the remaining domain, the initial temperature is set to 60°C .

4.7.3 Parameters

Table 4.8 shows the hydraulic properties of the two geological layers.

Table 4.8: Porous medium properties of geological layers.

property	unit	layer1	layer2
porosity ϕ	[\cdot]	0.15	0.08
storage β	[$1/\text{Pa}$]	$7 \cdot 10^{-10}$	$7 \cdot 10^{-10}$
permeability k	[m^2]	$2 \cdot 10^{-14}$	10^{-14}

To assure a variation of the hydraulic properties, the upper geological layer was modeled twice as conductive as the lower layer. The permeability k of layer 1 is set to $2 \cdot 10^{-14} \text{ m}^2$ and the porosity ϕ to 0.15. For layer 2 the permeability k is set to 10^{-14} m^2 and the porosity ϕ to 0.08. The storage of both layers is

derived from the bulk compressibility β [1/Pa] of the rock and the embedded fluid. Assuming fissured rocks, the storage is set to $7 \cdot 10^{-10}$ 1/Pa.

In table 4.9 the relevant parameters for the system of the two faults are listed.

Table 4.9: Medium properties of faults.

property	unit	fault1	fault2
aperture a	[m]	.05	.05
porosity ϕ	[−]	1	1
storage β	[1/Pa]	$4.6 \cdot 10^{-10}$	$4.6 \cdot 10^{-10}$
permeability k	[m ²]	10^{-8}	$5 \cdot 10^{-9}$

The permeability of fault 1 is set to 10^{-8} m and that of fault 2 to $5 \cdot 10^{-9}$ m². The fault transmissivity is defined as the product of the fault permeability k and aperture a . To ensure a high contrast between fault transmissivity and matrix conductivity, the aperture of both faults is set to 0.05 m. To provide free fluid flow in the faults, a porosity value of 1.0 is chosen. The storage in the faults is due to the fluid compressibility only and $\beta = 4.6 \cdot 10^{-10}$ 1/Pa is assigned.

The simulation time is set to 145 years in order to observe in the simulation the major changes characterizing the temperature field.

4.7.4 Results

After approximately one month a steady state for pressure and velocity field is achieved (Figure 4.7.22).

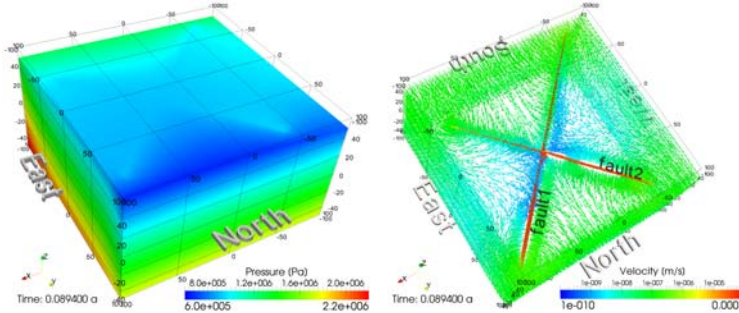


Figure 4.7.22: Simulated steady pressure (4.7.22a) and velocity field (4.7.22b) achieved after approx. 1 month.

Due to the fact that the implemented faults do not cut the southern and northern borders of the model, matrix flow is predominant in these areas. Accordingly,

the highest pressure gradients are observed at the northern and southern borders of the model (Figure 4.7.22a). In proximity to the cutting faults, the isobars (surfaces of constant pressure) are sub-horizontal due to high flow rates within the faults. Maximum Darcy velocities of $v = 10^{-4}$ m/s can be observed inside the faults (Figure 4.7.22b). Despite low pressure gradients, high flow rates occur in the fault planes. High values of fluid velocity are the result of the relative high transmissivity of the faults with respects to the surrounding domain.

Figure 4.7.22b shows the stationary flow field. As described above, highest flow velocities can be observed in the fault planes. The applied pressure boundary conditions force a regional flow field from the South to the North. The average velocity at the southern and northern regions is 10^{-7} m/s, with maximum inflow to the faults from the South. In the rest of the domain, outflow from the faults into the rock matrix is pronounced. In the central part of the model, faults act as the predominant flow paths. In contrast, low velocities (less than 10^{-8} m/s) characterize the eastern and western boundaries. An additional important fact is that at the southern edge of fault 1 and fault 2, backward flow from the North to the South occurs. Pressure equalisation within the faults results in higher matrix pressure at this area. This causes drainage of the rock matrix by the fault system.

Figure 4.7.23a-4.7.23d shows the 45°C , 55°C , 65°C and 75°C contours at four different time stages.

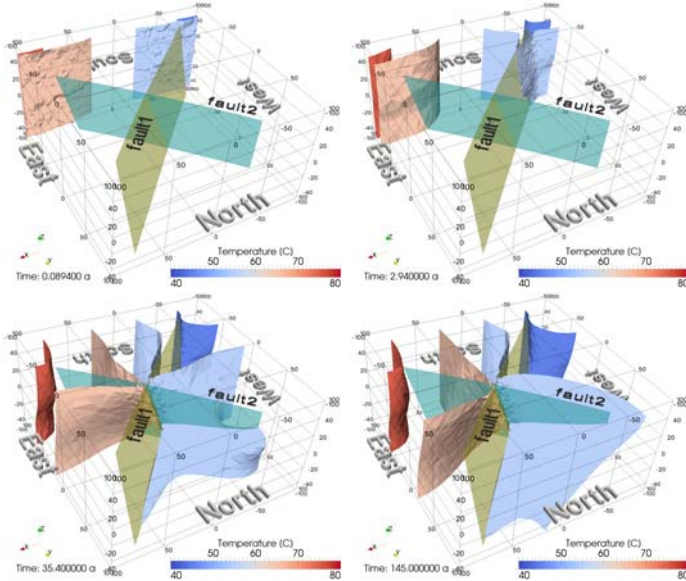


Figure 4.7.23: Temperature contour plots (45°C , 55°C , 65°C and 75°C isosurfaces) at four different time stages.

Before stationary field conditions for pressure and velocity are reached, conductive heat transfer does not affect the initial temperature field significantly (Figure 4.7.23a). After achieving the stationary pressure and velocity field, convective heat transfer (advection plus diffusion) becomes predominant. The cold water front ($T = 55^\circ\text{C}$) enters fault 1 after approx. 4 months (Figure 4.7.23b). Due to the geometry of fault 1 with respects to the southern boundary of the domain, cold water enters fault 1 in the upper part. After 35 years, (Figure 4.7.23c) cold water from fault 1 and hot water from fault 2 are mixed at the fault intersection. The final temperature field (Figure 4.7.23d) shows an average temperature of $T = 55^\circ\text{C}$ in the northern part which is less than the mean initial temperature of 60°C . The depression from the mean value is caused because fault 1 is more conductive than fault 2, which drives higher amounts of cold water into the system.

For a detailed observation of the pressure, velocity and temperature evolution inside the two faults, three observation points were set (Figure 4.7.24a).

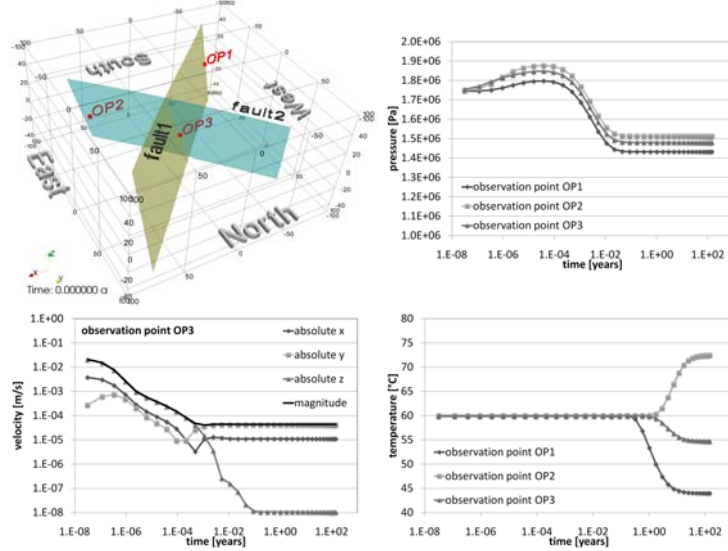


Figure 4.7.24: Location of three observation points within the fault faces (4.7.24a); Simulated pressure (4.7.24b) and temperature (4.7.24d) values at these observation points and simulated velocity components (4.7.24c) at observation point 3.

After starting the simulation the pressure increases at all observation points (Figure 4.7.24b). As shown for observation point 3 (Figure 4.7.24c), the initial magnitude of the velocity is due to vertical flow only. The observed downward flow is forced by the initial pressure conditions in combination with the chosen pressure boundary. Therefore, an initial increase of fluid pressure is observed.

After 1 month, a stationary pressure and velocity field is reached, as indicated by the horizontal lines in Figure 4.7.24b-4.7.24c.

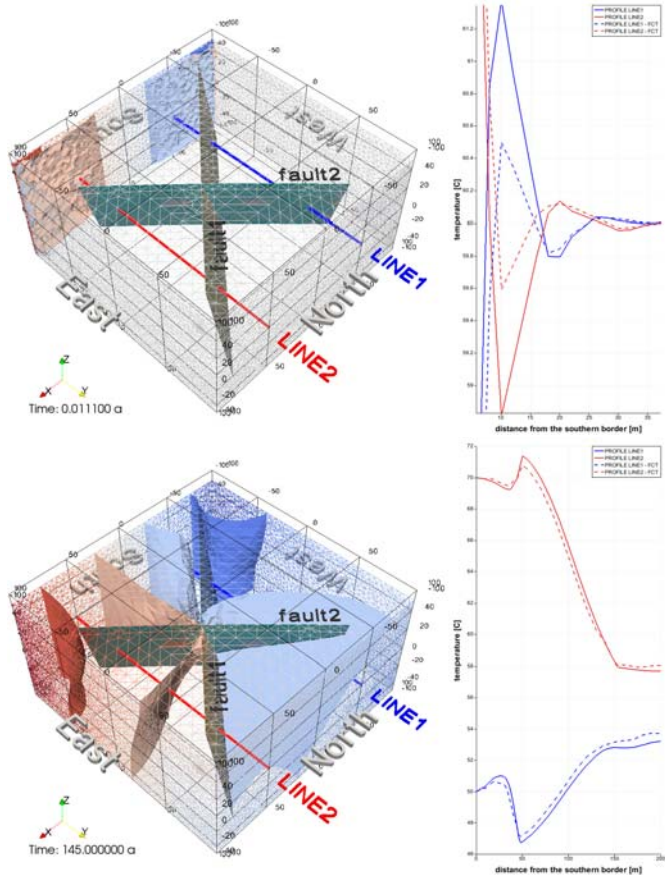


Figure 4.7.25: Simulated temperature along two lines at the beginning (4.7.25a) and at the final simulation time (4.7.25b) with and without flux corrected transport FCT.

The vertical component of velocity decreases over time from $3 \cdot 10^{-2}$ m/s to 10^{-8} m/s, and the horizontal flow from the South to the North with velocities between 10^{-5} m/s and 10^{-4} m/s becomes dominant. The cold water reaches the fault system at the edge of fault 1 (Figure 4.7.24d) after approx. 4 month. After an additional 17 months, cooling at observation point 3 begins. At the same time, hot water reaches fault 2 first. Due to the lower transmissivity of fault 2, the hot water reaches the intersection point after 10 years, and cooling at observation point 3 stops. Higher amounts of cold water enter the fault intersection (observation point 3) from the more conductive fault 1, causing temperature to decrease to 55°C. This corroborates the observation of the temperature field for

the total domain.

In a second run, the same problem described above has been numerically solved using the Flux Corrected Transport (FCT) scheme as implemented in Norihiro's branch of OpenGeoSys version 5. Figure 4.7.25 illustrates the differences regarding numerical oscillations in solving for the transport field with (dashed lines) and without (solid lines) FCT method. Figure 4.7.25a and Figure 4.7.25b show the calculated temperature profiles along the general flow field for two different stages in the simulation. As shown in Figure 4.7.25a, the FCT method seems to reduce the amplitudes of numerical oscillations by a maximum factor of three at the beginning of the simulation. The OGS benchmark files can be found in the subdirectory 2units2faults/FCT.

Chapter 5

Groundwater flow

by Feng Sun and Norihiro Watanabe

5.1 Fluid momentum

by Chan-Hee Park

5.2 Groundwater flow in an anisotropic medium

5.2.1 Definition

The aim of this example is to simulate the stationary groundwater flow in an anisotropic porous medium. In order to consider the permeability anisotropy, a 2-D numerical model is built which contains a higher permeability in the vertical direction than that in the horizontal direction. The aquifer is assumed saturated and stationary.

For the two-dimensional simulation, the cube consisting of a porous medium is simplified as a square with an area of 1 m². The calculation model includes 736 triangular elements and 409 nodes. At the lower left corner of the model a constant pressure of 1000 Pa is specified along two polylines of the length of 0.3 m (Fig. 5.2.1). At the top and the right borders the pressures are set to 0 in order to create the pressure gradient. As the porous medium is assumed to be anisotropic, which influences the groundwater flow, the values for the permeabilities are equal to 1.0×10^{-15} m² in x-direction and 1.0×10^{-14} m² in y-direction. Other property of the anisotropic media is shown in Table. 5.1.

Table 5.1: The parameters defined in the anisotropic media.

Symbol	Parameter	Value	Unit
n	porosity	0.2	–
κ_x	permeability	1.0×10^{-15}	m ²
κ_y	permeability	1.0×10^{-14}	m ²

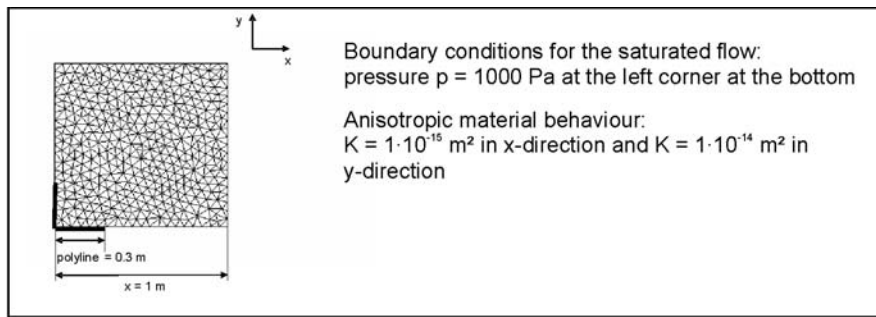


Figure 5.2.1: Calculation model (2-D) of the anisotropic media.

5.2.2 Evaluation method

This test example is not made up to introduce a new process, but it shows the possibility for the OGS user to give a specific permeability for each direction.

Therefore, the interpretation of OGS results comprises merely the comparison between pressure distributions due to the anisotropic permeability that were simulated by the use of RockFlow (RF) and OGS. This comparison is possible because both versions are developed separately concerning anisotropy of soils.

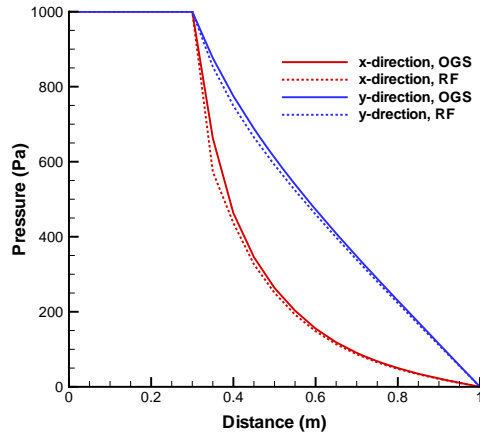


Figure 5.2.2: Pressure distribution caused by anisotropic saturated flow.

5.2.3 Results

In Fig. 5.2.2 the horizontal and vertical pressure distributions of an anisotropic groundwater flow model which is developed using the program code RF are depicted next to those calculated from the above described anisotropic model with OGS. While presuming an anisotropic medium, an inhomogeneous pressure field is developing because the groundwater is not able to spread out uniformly. This can be recognized at the different curve gradients in x- and y-direction. There are slight differences between the curve characteristics of the RF and OGS simulation results. These differences are due to different element types (square in the RF model) and the resulting different x- or y-coordinates. Therefore, the pressure distributions obtained by the simulation with OGS are evaluated to be correct.

5.3 Groundwater flow in a heterogeneous medium

5.3.1 Definition (2-D)

The aim of this example is to simulate the stationary groundwater flow in an isotropic and heterogeneous porous medium. In order to consider the heterogeneity,

neous of hydraulic conductivity, a 2-D numerical model is built. The heterogeneous distribution of hydraulic conductivity is shown in Fig. 5.3.3. The aquifer is assumed isotropic, heterogeneous, saturated and stationary.

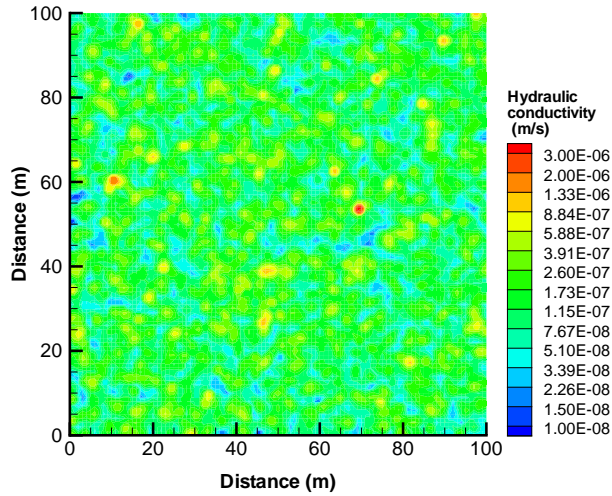


Figure 5.3.3: Calculation model (2-D): heterogeneous hydraulic conductivity distribution.

For the two-dimensional simulation, the cube consisting of a porous medium is simplified as a square with an area of 10000 m^2 . The calculation model includes 10000 quad elements and 10201 nodes. At the left boundary a constant head of 10 m and the right boundary a constant head of 9 m are specified in order to create a pressure gradient.

5.3.2 Results (2-D)

As shown in figure 5.3.4, the head distribution of the groundwater flow in a heterogeneous medium is depicted complying with the distribution of the hydraulic conductivity.

5.3.3 Definition (3-D)

For the three-dimensional simulation, the aquifer is defined as a $100 \text{ m} \times 100 \text{ m} \times 50 \text{ m}$ cuboid. The calculation model includes 60025 hex elements and 65000 nodes. A constant head of 10 m at the left surface and a constant head of 9 m at the right surface are specified in order to create a pressure gradient. The heterogeneous distribution of hydraulic conductivity is shown in Fig. 5.3.5.

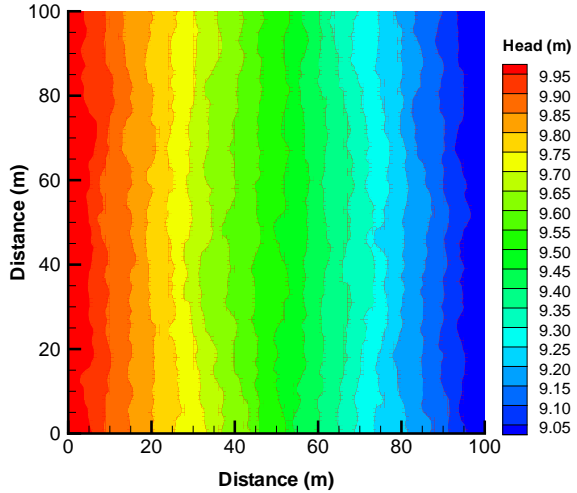


Figure 5.3.4: Head distribution in response to isotropic and heterogeneous medium.

5.3.4 Results (3-D)

As shown in figure 5.3.6, the 3-D head distribution of the groundwater flow in a heterogeneous medium is depicted in response to the distribution of the hydraulic conductivity.

5.4 Confined aquifer with constant channel source term

5.4.1 Definition

This example deals with an aquifer which is subject to a constant recharge line source. The channel is assumed to be independent of the groundwater head and not affected by the water loss or the exchange flux. Therefore, the source term represents a steady and uniform channel located above the aquifer. The cross-section of the channel is rectangular (Fig. 5.4.7).

The integrated recharge flow that provides the link between the channel and the groundwater is defined by Eq. 5.1 [96].

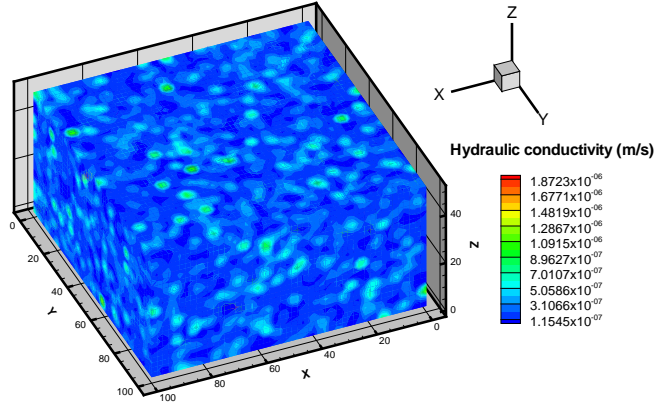


Figure 5.3.5: Calculation model (3-D): heterogeneous hydraulic conductivity distribution.

$$q^{ex} = \begin{cases} -K_{\Lambda}P \frac{(h_r - h_g)}{a} & h_g > (z_r - a) \\ -K_{\Lambda}P \frac{(h_r - (z_r - a))}{a} & h_g \leq (z_r - a) \end{cases} \quad (5.1)$$

where K_{Λ} is the channel bed conductivity, B is the channel width, a is the channel bed thickness, and h_r is the channel flow head, h_g is the groundwater table. The wetted perimeter $P = 2(h_r - z_r) + B$ for rectangular channel where z_r is the height of the top of the channel bed.

In this benchmark, the aquifer size is $20 \text{ m} \times 10 \text{ m}$ with the source term at the left boundary (See Fig. 5.4.10). The initial groundwater head is 0 m. The channel source term is the boundary condition at one side, at the opposite boundary the head is fixed with 0 m. At the remaining boundaries no-flow is imposed.

For the spatial discretization either 24×12 quadrants or hexahedra are used as well prisms which are generated by cutting the hexahedra into two parts. The hexahedra or prism height is 1 m. The time step is 1 minute. Simulation parameters for the aquifer and the channel source term are given in Table. 5.2.

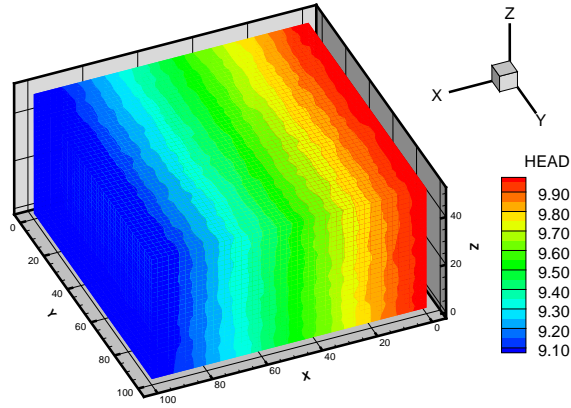


Figure 5.3.6: Head distribution in response to isotropic and heterogeneous medium (3-D).

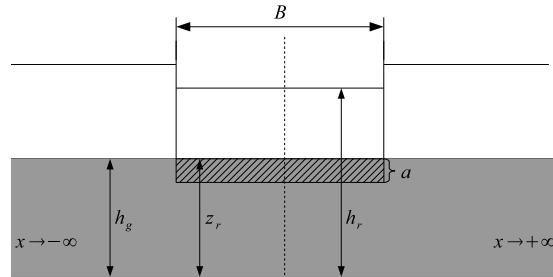


Figure 5.4.7: The illustration of the cross section of the channel/groundwater.

Table 5.2: Parameters for channel source term examples.

Symbol	Parameter	Value	Unit
Aquifer			
S	Storage	0.2	—
μ	Viscosity	1.0×10^{-3}	$Pa \cdot s$
K	Conductivity	1.0×10^{-3}	m/s
L	Thickness	25	m
Channel source term			
h_r	Channel water surface	3	m
z_r	Bed top location	0	m
a	Bottom sediment thickness	0.3	m
B	Channel width	34	m
K_A	Bed conductivity	1.0×10^{-6}	m/s

A constant recharge value of $4.0 \times 10^{-4} m^2/s$ is obtained from Eq. 5.1 when the properties of the channel are defined as those values in Table. 5.2. Because this problem is symmetric for uniform and isotropic conditions in the aquifer and only half of the domain is taken into account. Therefore, the constant Neuman boundary condition is assigned with the half of the recharge value ($2.0 \times 10^{-4} m^2/s$).

5.4.2 Solution

R. E. Glover [97] presented an analytical solution for a constant line source in an infinite aquifer domain in 1978, which gives the groundwater head at any point of the source line by the following equation,

$$h = q^{ex} \sqrt{\frac{\mu t}{\pi \rho g \kappa L S_y}} \quad (5.2)$$

where q^{ex} is the recharge rate [L^2/T], L is the saturated thickness of the aquifer [L], κ is the permeability of the aquifer [L^2/T], S_y is the specific yield of the aquifer [-], t is the time [T].

5.4.3 Results

Comparison of simulation results and analytical solution is given in Fig. 5.4.8 for quadrants and in Fig. 5.4.9 for hexahedra.

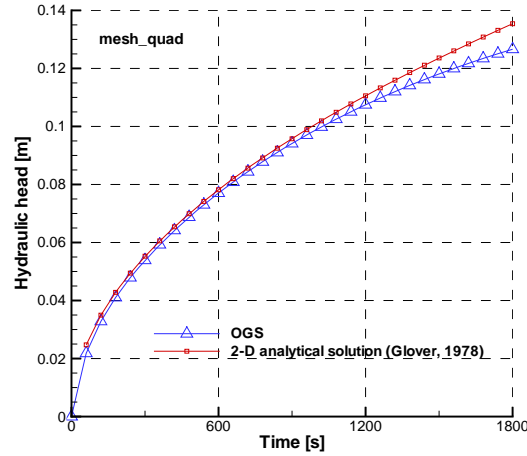


Figure 5.4.8: Results with quadratic elements and analytical solution for confined aquifer below uniform and steady channel.

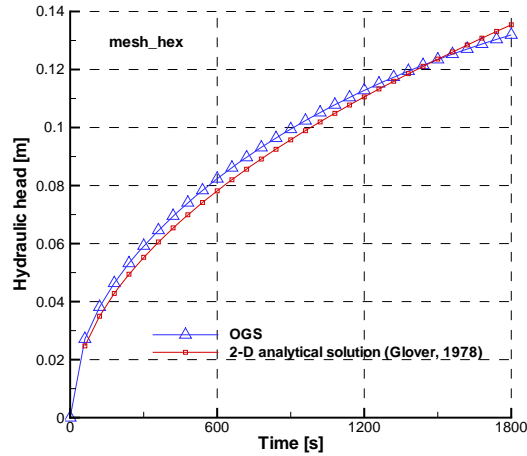


Figure 5.4.9: Results with hexahedral elements compared with the analytical solution for confined aquifer below uniform and steady channel.

The small differences between Fig. 5.4.8 and Fig. 5.4.9 are mainly caused by the channel source term. In the model with hexahedral elements, the channel source term is defined as a line source at the left-top boundary of the domain (Fig. 5.4.10).

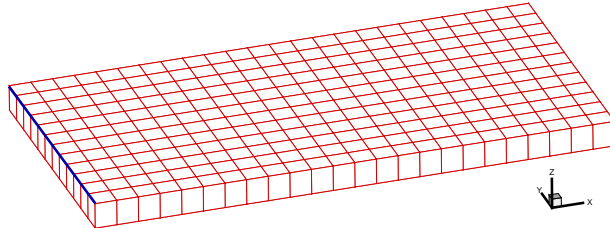


Figure 5.4.10: Computational domain and source term location.

5.5 Theis' Problem

5.5.1 Definition

Theis' problem examines the transient lowering of the water table induced by a pumping well. Theis' fundamental insight was to recognize that Darcy's law

is analogous to the law of the heat flow by conduction, i.e., hydraulic pressure being analogous to temperature, pressure-gradient to thermal gradient. The assumptions required by the Theis solution are:

- the aquifer is homogeneous, isotropic, confined, infinite in radial extent,
- the aquifer has uniform thickness, horizontal piezometric surface
- the well is fully penetrating the entire aquifer thickness,
- the well storage effects can be neglect,
- the well has a constant pumping rate,
- no other wells or long term changes in regional water levels.

5.5.2 Solution

The analytical solution of the drawdown as a function of time and distance is expressed by Eq. 5.3:

$$h_0 - h(t, x, y) = \frac{Q}{4\pi T} W(u) \quad (5.3)$$

$$u = \frac{(x^2 + y^2)S}{4Tt} \quad (5.4)$$

where h_0 is the constant initial hydraulic head [L], Q is the constant discharge rate [$L^3 T^{-1}$], T is the aquifer transmissivity [$L^2 T^{-1}$], t is time [T], x, y is the coordinate at any point [L], S is the aquifer storage [–]. $W(u)$ is the well function defined by an infinite series for confined aquifer as

$$W(u) = \int_u^{+\infty} \frac{e^{-u}}{u} du = -\gamma - \ln u + \sum_{k=1}^{\infty} \frac{(-1)^{k+1} u^k}{k \cdot k!} \quad (5.5)$$

where $\gamma \approx 0.5772$ is the Euler-Mascheroni constant. For practical purposes, the simplest approximation of $W(u)$ was proposed as $W(u) = -0.5772 - \ln u$ for $u < 0.05$. Other more exact approximations of the well function were summarized by R. Srivastava and A. Guzman-Guzman [98].

The parameters and initial & boundary conditions are defined in Table 5.3.

5.5.3 Results

Fig. 5.5.11 shows the comparison of analytically and numerically calculated drawdown of hydraulic head versus time at the distance of 9.639 m from the well.

Table 5.3: The parameters defined in 1-D Theis' problem.

Symbol	Parameter	Value	Unit
$h(0, r)$	Initial conditions	0	m
Q	Well pumping rate	1.2233×10^3	m^3/d
$h(t, 304.8)$	Boundary conditions	0	m
K	Hydraulic conductivity	9.2903×10^{-4}	m/s
S	Storage coefficient	0.0010	-
r	0.3048	Wellbore radius	m

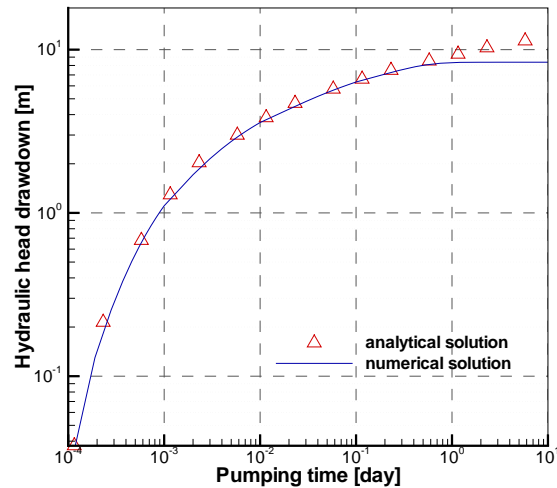


Figure 5.5.11: Calculated drawdowns at a distance of 9.639 m from the well.

5.5.4 2-D application

The 2-D application is solved in the following situation (Table. 5.4).

The aquifer horizontal domain size is 1000 m \times 750 m with the pumping well at the location coordinate (500, 375). The discretization of space is 10 m \times 10 m grid. The simulation time is 151.2 seconds and the time step is 1.036 seconds. The initial head is 20 m in the whole domain and the boundary condition is 0 m drawdown at the left and right boundaries. There is no flux through the top and bottom boundaries. The cone of depression induced by the pumping well at the end of the simulation is plotted in Fig. 5.5.12.

Table 5.4: The parameters defined in 2-D Theis' problem.

Symbol	Parameter	Value	Unit
Q	Discharge rate	1000	m^3/d
S	Specific storage	1.0×10^{-5}	$1/m$
T	Transmissivity	1000	m^2/d
B	Thickness of aquifer	20	m

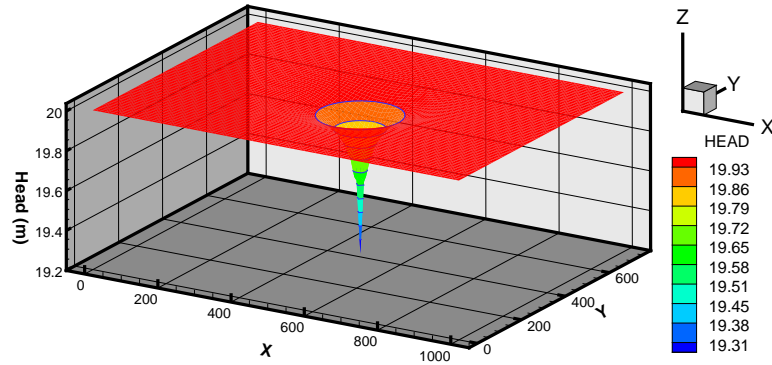


Figure 5.5.12: Cone of depression at the end of the simulation.

5.6 Unconfined aquifer

5.6.1 Definition

In this example the aquifer consists of a small strip with the size of $100 \text{ m} \times 2 \text{ m}$ (see Fig. 5.6.13). At both ends the head is fixed and constant recharge is imposed on the whole domain which leads to steady state flow. This setting allows the comparison with an analytical solution. Initial groundwater head is 0 m. At one end of the strip the head is 1 m at the other 5 m. At the top a source term is $1.0 \times 10^{-8} \text{ m/s}$ and at the remaining parts no-flow is imposed. For the spatial discretization 100 equal quadrants and 410 triangles or prisms are used. In the later case, the three-dimensional unconfined groundwater equation is solved with elements adapting to the water height. One time step with the size of 100 s is used. The specific storage $S_s = 0 \text{ m}^{-1}$ or specific yield $S_y = 0$ and a hydraulic conductivity K of $9.9 \times 10^{-6} \text{ m/s}$ are used.

5.6.2 Analytical solution

In an unconfined aquifer, the saturated thickness is defined as the vertical distance between the water table surface and the aquifer base. If the aquifer base is at the zero datum, then the unconfined saturated thickness (b) is equal to the head (h). With the Dupuit assumption (or Dupuit-Forcheimer assumption), where it is assumed that heads do not vary in the vertical direction (i.e., $\frac{\partial h}{\partial z} = 0$), a horizontal water balance is only applied to a long vertical column with area ($\delta x \delta y$) extending from the aquifer base to the unsaturated surface. For this vertical column, applying Darcy's law and mass balance expression, the groundwater flow equation for unconfined aquifer can be obtained:

$$S_y \frac{\partial h}{\partial t} = \nabla \cdot (kh\nabla h) + N \quad (5.6)$$

where N is the source term [L/T], represents the addition of water in the vertical direction, S_y is the specific yield of the aquifer [-], k is the hydraulic conductivity [L/T].

The unconfined groundwater flow equation is non-linear partial differential equation, for steady-state flow, it may be linearized by expressing the PDE in terms of the squared head:

$$\nabla \cdot (k\nabla h^2) = -2N \quad (5.7)$$

and for the homogeneous aquifers, Eq. 5.7 becomes

$$\nabla^2 \nabla h^2 = -\frac{2N}{k} \quad (5.8)$$

Eq. 5.8 can be solved by the standard integration method for linear PDEs. For the definition of the unconfined aquifer above, the analytical solution is expressed by the following equation.

$$h = \sqrt{-0.001x^2 - 0.14x + 25} \quad (5.9)$$

5.6.3 Results

Comparison of simulation results with prisms and analytical solution is shown in Fig. 5.6.13.

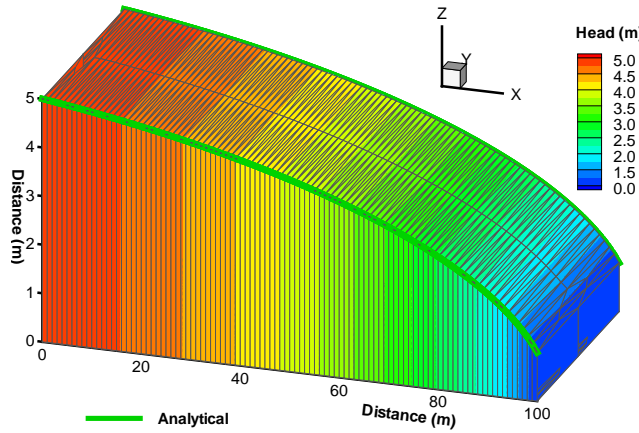


Figure 5.6.13: Benchmark example results of unconfined aquifer with prisms.

5.7 2D steady state flow in porous media with a discrete fracture

5.7.1 Definition

This example illustrates the disturbance of the uniform flow in porous media caused by the presence of a fracture. Consider a 2D infinite horizontal plane of porous media with an embedded fracture. Uniform flow with specific discharge q_0 occurs from the left side to the right of the domain. The fracture extends to infinity in the directions normal to the plane. The middle point of the fracture is placed at the center of the plane. The shape of the fracture is shown in Figure 5.7.14. The fracture has a length of L and is inclined with angle β . The fracture aperture b may vary with positions. In this example, it is assumed that the shape corresponds to that obtained from the normal displacements of the sides of a pressurized crack in an elastic medium. This gives

$$b = b_{\max} \sqrt{1 - x'^2} \quad (5.10)$$

where x' is the normalized local coordinate systems. b_{\max} is the aperture at the center $x' = 0$. Assuming the volume of the fracture is sufficiently small as compared to that of porous media, the flow in the porous media can be modeled ignoring the width of the fracture. The flow in the fracture is assumed to be laminar along the fracture surface. Hydraulic conductivity of the fracture

is constant and independent of the aperture variation. The pressure variation across the fracture is neglected.

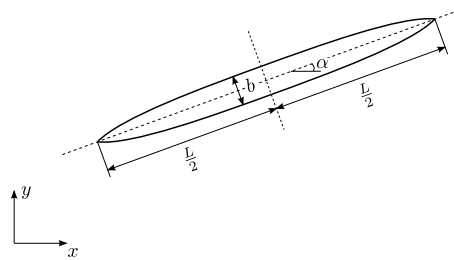


Figure 5.7.14: Fracture geometry

Table 5.5: Model parameters

Symbol	Parameter	Value	Unit
α	fracture angle	45	°
b_{\max}	maximum fracture aperture	0.05	m
L	fracture length	2.0	m
K_f	fracture hydraulic conductivity	1.0×10^{-3}	m/s
K_m	porous medium hydraulic conductivity	1.0×10^{-5}	m/s
q_0	specific discharge	1.0×10^{-4}	m/s

5.7.2 Solution

Analytical solution

Strack [99] has derived an exact solution for this problem as the potential flow. The obtained complex potential Ω is given as

$$\Omega = -A\sqrt{(Z-1)(Z+1)} + AZ - \frac{1}{2}q_0Le^{i\alpha}Z + C \quad (5.11)$$

for the dimensionless variable Z

$$Z = X + iY = \frac{z - \frac{1}{2}(z_1 + z_2)}{\frac{1}{2}(z_2 - z_1)} \quad (5.12)$$

with the endpoints of the fracture z_1 and z_2 . A is defined as

$$A = \frac{\frac{1}{2}K_f b_{\max}}{K_m L + K_f b_{\max}} q_0 L \cos \alpha \quad (5.13)$$

and C is the integration constant. In this example, the constant is simply considered as zero.

Numerical solution

Numerical solution can be obtained by solving steady state liquid flow problem in a hybrid system of a discrete fracture model and continuum model (porous media). The fracture is represented as a 1D hydraulic conduit. The domain is set up in a finite space as a square with length of 10 m as depicted in Figure 5.7.15. To compare numerical results with the analytical solution, pressure calculated by the analytical solution is utilized as prescribed pressure at the lateral boundaries, i.e. $p_{\text{in}} = 496465 \text{ Pa}$ and $p_{\text{out}} = -496465 \text{ Pa}$. It is assumed that the fracture aperture does not vary with positions and has constant value even at the endpoints, $b = b_{\max}$.

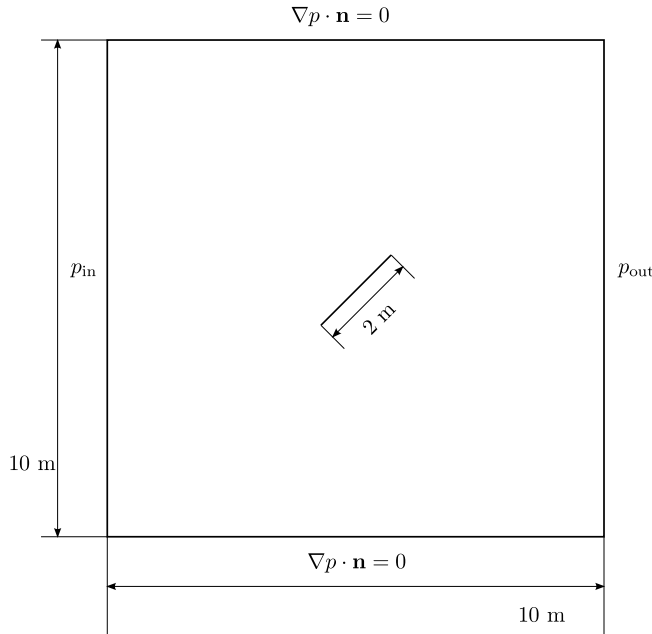


Figure 5.7.15: Computational area

5.7.3 Results

Pressure distribution obtained by the analytical solution is shown in Figure 5.7.16. Lateral uniform flow is disturbed in the vicinity of the inclined fracture where the flow is faster than in surrounding porous media. Figure 5.7.17 presents the pressure profile along a diagonal line from the bottom-left to the top-right. Although the numerical solution adopts the idealized fracture geometry, results show good agreements between the numerical and the analytical solution.

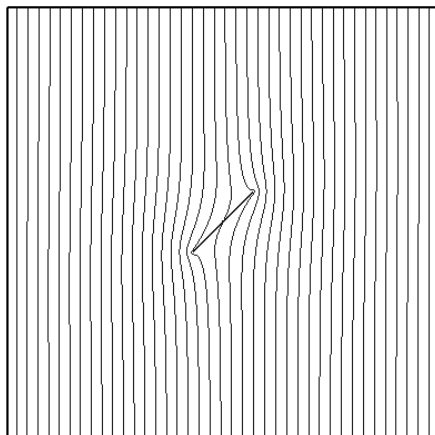


Figure 5.7.16: Pressure distribution obtained by the analytical solution

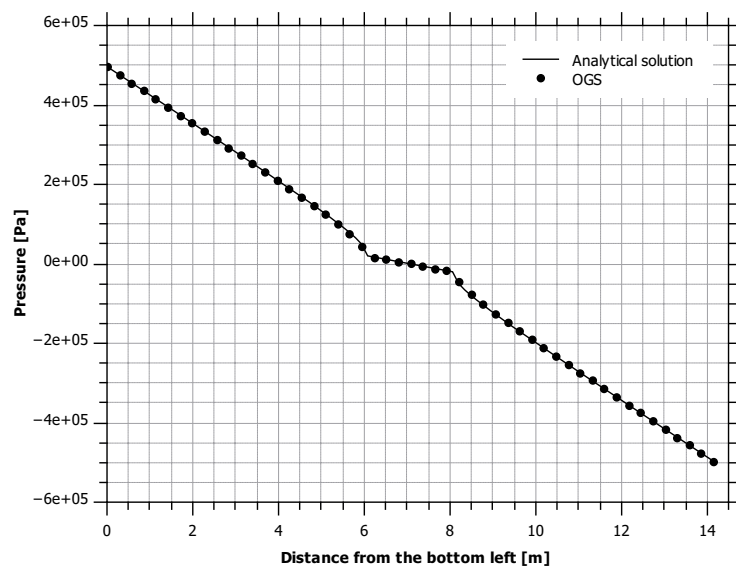


Figure 5.7.17: Pressure profile along a diagonal line from the bottom-left to the top-right

Chapter 6

Richards flow

by Thomas Kalbacher and Yanliang Du

6.1 Root water uptake in soils

Chapter 7

Overland flow

by Jens-Olaf Delfs, Martin Beinhorn and Yajie Wu

This chapter deals with surface runoff which is flow over the land surface generated by precipitation, melting of snow, or other sources. Typically, not all precipitation or snow produces runoff because storage from soil and plant roots can absorb substantial amounts of water. Infiltration excess ([100]) overland flow occurs when precipitation exceeds the rate at which water infiltrates into the soil (Test case 7.3). When the soil is saturated and depression storage filled, the precipitation, even as a light shower, immediately becomes surface runoff (Borden test case). Similarly, urbanization leads to more pronounced flow maxima during storm events, when impervious surfaces such as pavement force the runoff directly to the stream (Test case 7.2).

Horizontal flow over a flat or moderately flat surface is described by the Saint-Venant Shallow Water Equations which read

$$\begin{aligned}\phi_o \frac{\partial H}{\partial t} + \nabla H \mathbf{v} &= q \\ \frac{\partial \mathbf{v}}{\partial t} + \mathbf{v} \cdot \nabla \mathbf{v} + g \nabla h &= g(S_0 - S_f)\end{aligned}\quad (7.1)$$

where H , surface water depth, and \mathbf{v} , flow velocity, are primary variables, $g = 9.81 \text{ m/s}^2$ is the gravitational acceleration, $h = H + b$ the surface water height, b the bottom height, $S_0 = -\nabla b$ the surface slope, S_f the friction slope, q represents external sources / sinks, and $0 \leq \phi_o \leq 1$ is the surface porosity to incorporate depression storage. Equations (7.1) can be derived from the Reynolds averaged Navier Stokes Equations by integrating over water depth H and assumption hydrostatic pressure $p = \rho g(h - z)$, where ρ is the water bulk density (e.g. [101]). The result is a depth-averaged flow field $v(x, y)$, where dispersion caused by this averaging, turbulence and surface friction effects are finally incorporated in empiric resistance to flow relationships, i.e. the velocity v is a power function of the water depth H . The general form of a resistance to flow relationship for 1D flow in an irregular channel (which involves an additional averaging over the channel breadth) is given by

$$v = C S_f^j R_H^m \quad (7.2)$$

where j, m are parameters, $v(l)$ is the flow velocity in the channel course l , $R_H(l) = A/P$ the hydraulic radius of the channel, $A(l)$ its cross-section, and $P(l)$ the wetted perimeter. Remark that $R_H = H$ for 2D overland flow and $j = 1/2, m = 2/3$ result in the relationship by Manning where $n = 1/C$ is a surface roughness parameter. Neglect of the inertial terms simplifies Equations (7.1) to the diffusive wave shallow water equation, which reads

$$\phi_o \frac{\partial H}{\partial t} - \nabla \cdot \frac{C H R_H^m}{|\nabla h|^{1-j}} \nabla h = q \quad (7.3)$$

Further neglect of the hydrostatic pressure term in Equation (??) leads to the kinematic wave equation reading

$$\phi_o \frac{\partial H}{\partial t} + C(m+1) R_H^m \nabla H = q \quad (7.4)$$

Equations (7.1)-(7.4) allow to simulate small-amplitude waves (surface runoff, flood waves). The diffusive wave approximation (7.3) can capture backwater phenomena and the Saint-Venant Equations (7.1), further, dam break waves. Conditions for the applicability of the Saint-Venant approximations (kinematic and diffusive wave) are stated for instance in [102] (Test case 7.1), while shallow water equations to reproduce large-amplitude waves (e.g. ocean waves) can be found in [103].

External forcing (precipitation, infiltration, outflow, etc.) can be incorporated in the surface flow Equations (7.1)-(7.4) with source /sink terms q . A normal depth q_{norm} sink term assumes that water flows under uniform (normal) conditions at a downstream boundary while a critical depth q_{crit} sink term represents free outfall:

$$q_{\text{norm}} = -CS_o^j H^m \quad (7.5)$$

$$q_{\text{crit}} = -\sqrt{gH^3} \quad (7.6)$$

A [104] term q_{GA} provides an effective precipitation rate $q_{\text{prec}}^{\text{eff}} = q_{\text{prec}} - q_{\text{GA}}$ for overland flow on an infiltrating surface. Since water infiltrates into dry soil as a sharp wetting front, the Green and Ampt infiltration model assumes that soil saturation above and below the wetting front and the soil-water suction immediately below the wetting front remain constant. The infiltration source term $q_{\text{GA}}(t)$ and the depth of the wetting front $a'(t)$ read

$$\begin{aligned} q_{\text{GA}} &= K' \left(\frac{H - \Psi}{a'} \right) \\ a' &= \frac{\int_0^t q_{\text{GA}}(s) ds}{\Delta\Theta}. \end{aligned} \quad (7.7)$$

where Ψ the effective capillary drive, K' is related to the saturated soil hydraulic conductivity in chapter Richards flow, and $\Delta\Theta$ the initial moisture deficit.

7.1 One-dimensional surface flow

7.1.1 Definition

[105] compared surface runoff predictions with the Saint-Venant Equations (7.1), the diffusive wave approximation (7.3), and the kinematic wave approximation (7.4) at an inclined plane. In the selected test case (Table 7.1 for surface roughness) the plane length is $L = 100$ m, the slope $S_0 = 0.01$, the precipitation rate $4 \cdot 10^{-3}$ m/s which results in a kinematic wave number of $k = S_0 L / H Fr^2 = 10$ and Froude number of $Fr = v / \sqrt{gH} = 0.5$. A normal depth boundary condition (7.5) is assigned at the outlet. The simulation time is 4 min, time step length 1 s, and grid size 1 m.

Table 7.1: Material properties.

Symbol	Parameter	Value	Unit
n	Manning friction	[0.0548]	s/m ^{1/3}

7.1.2 Solution

Figure 7.2.2 compares the surface runoff at the normal depth outlet of different surface runoff simulators. The kinematic wave solution is analytically obtained. The results of the Saint-Venant and diffusive wave solvers match well while the kinematic wave equation results in a faster rise of the hydrograph.

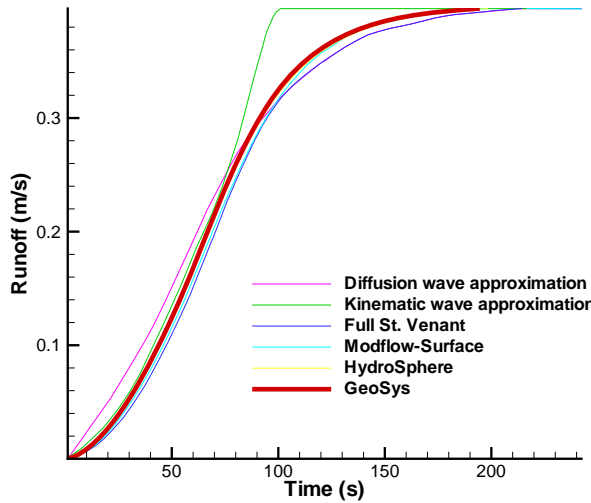


Figure 7.1.1: Outflow comparison for one-dimensional surface runoff test case.

7.2 Surface flow on a tilted V-catchment

7.2.1 Definition

In the synthetic test case by [106] precipitation with a rate of $3 \cdot 10^{-6}$ m/s is applied for 90 min on an impervious V-catchment followed by a recession period of additional 90 min. The V-catchment consists of two sloping planes

800 m wide and 1000 m long joined by 20 m wide and 1000 m long channel. At the catchment base (channel region) the surface roughness was reduced (Table 7.2) and the slope set at $S_0 = 0.02$. The hillslopes additionally have a slope of $S_0 = 0.05$ towards the channel. At the channel outlet the water leaves free-falling (critical depth sink term (7.6)) while at the remaining boundaries no-flow is imposed. A structured (rectangular) grid (100 m \times 100m) a time-step maximum length of 1 min are selected.

Table 7.2: Material properties.

Symbol	Parameter	Value	Unit
n	Manning friction (Hillslope)	[0.015]	s/m ^{1/3}
n	Manning friction (Channel)	[0.15]	s/m ^{1/3}

7.2.2 Solution

Figure 7.2.2 compares critical depth outflow of different surface runoff simulators. The simulated hydrographs reach a maximum roughly after 60 min and the entire water has almost left the catchment after the simulation time of 180 min.

7.3 Infiltration excess (Horton) overland flow

7.3.1 Definition

In the classic experiments by [107] a light oil was applied with a constant rate of $q_{\text{prec}} = 6.944 \times 10^{-5}$ m/s for 15 min on an initially drained soil flume with a length of 12.2 m, a width of 0.051 m and a uniform slope of 0.01. Measured outflow at the lower flume end is compared with 1D surface runoff simulations for a grid size of 12.2 cm and a constant time step length of 1 s. Parameters are stated in Table 7.3 for flow resistance (7.2) and a Green Ampt source term (7.7) (cmp. with chapter Surface-subsurface flow coupling). A critical depth sink term (7.6) is assigned at the flume outlet.

7.3.2 Solution

Fig. 7.3.3 compares measured surface runoff with model predictions at the flume outlet. First, precipitation completely infiltrates (stage I). After about 7 min surface runoff starts and produces a fast rising hydrograph (stage II). As soon

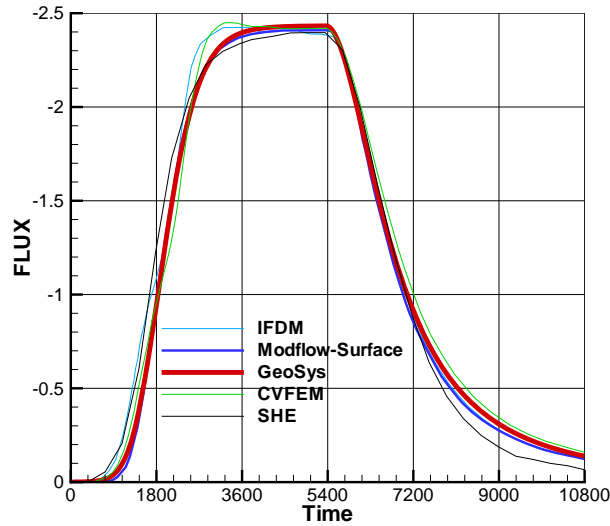


Figure 7.2.2: Runoff at channel outlet for tilted V-catchment test case.

Table 7.3: Material properties.

Symbol	Parameter	Value	Unit
n	Manning friction	[0.15]	s/m ^{1/3}
K	Conductivity	[2.3×10^{-5}]	m/s
Ψ	Effective capillary drive	[0.13]	m
$\Delta\Theta$	Initial moisture deficit	[0.3]	—

as precipitation from the entire flume surface has reached the outlet, the hydrograph turns flat. Infiltration rate continues declining as the soil becomes saturated such that surface runoff still increases in the later part of the experiment (stage III). The experimental hydrograph exhibits a considerable dip during stage III which is attributed to gas phase movement ([107]).

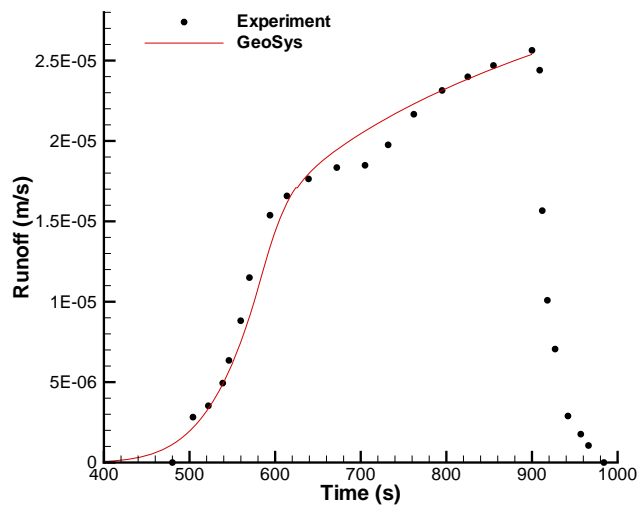


Figure 7.3.3: Comparison of measured and simulated Horton overland flow.

Chapter 8

Gas flow

by Ashok Singh and Olaf Kolditz

The subject of this chapter is the movement of gases in porous media. In contrast to groundwater hydraulics, gas flow is more complicated because of its compressibility. Significant variations in gas density and viscosity can result also from temperature fluctuations (so-called Klinkenberg effect). According to the kinetic theory of gases, its viscosity should not depend on the pressure. This is not necessarily the case for conditions typically existing in natural gas reservoirs [108]. At a fixed temperature, the viscosity of gas can vary by tens of percents as the formation pressure changes by a few Mega Pascale. Another problem concerns the evidence of turbulent flow which results in additional friction effects. The present study is verified with existed analytical solutions. Simulation of compressible flows in porous media is neccessary for different applications such as air movement in soils, gas production or CO₂ storage if carbon dioxide is injected in a gaseous state.

The theory of gas seepage was developed first by [109], [110], and [111], who worked out a number of analytical approximations to solve the nonlinear problem. To this end, following assumption is made

- Gravitational forces are neglected
- No phreatic surfaces are formed
- Idealized material properties

The state of the compressible fluid within a considered closed system may be isothermal (const. temperature), adiabatic (const. heat content), or polytropic (const. change of heat content).

The equation of gas flow in a porous medium can be derived from the mass balance of gas

$$\frac{\partial(n\rho)}{\partial t} + \nabla \cdot (\rho n \mathbf{v}) = \rho Q_\rho \quad (8.1)$$

where ρ is gas density, \mathbf{v} is velocity vector, n is porosity and Q_ρ is source/sink term.

The equation of state for an ideal gas represents its compressibility as pressure and temperature changes.

$$\rho = \frac{pM}{RT} \quad (8.2)$$

where p is gas pressure, R is the universal gas constant, M is molecular weight of gas and T is temperature in Kelvin.

Since gas density ρ is depending on pressure and temperature, hence for compressible gas flow, mass balance equation (8.1) become

$$\frac{n}{p} \frac{\partial p}{\partial t} - \frac{n}{T} \frac{\partial T}{\partial t} + \frac{1}{p} \nabla p - \frac{1}{T} \nabla T + \nabla \cdot (n \mathbf{v}) = Q_\rho \quad (8.3)$$

In addition with the momentum balance equation, which can be expressed in form of an extended Darcy's law for non-linear flow.

$$n\mathbf{v} = -\frac{\mathbf{k}}{\mu} \nabla p \quad (8.4)$$

where \mathbf{k} is permeability tensor, μ is fluid viscosity, the gas mass balance equation reads as

$$\frac{n}{p} \frac{\partial p}{\partial t} - \frac{n}{T} \frac{\partial T}{\partial t} + \frac{1}{p} \nabla p - \frac{1}{T} \nabla T - \nabla \cdot \left(\frac{\mathbf{k}}{\mu} \nabla p \right) = Q_\rho \quad (8.5)$$

which is a non-linear equation with respect to gas pressure p . For isothermal case temperature related term should be neglected and for nonisothermal case temperature value can get from heat transport equation.

We will present following two benchmarks for verification of compressible gas flow code. In first benchmark density is changing only due to pressure and temperature is constant, i.e. isothermal case whereas in second benchmark we proved phenomenon of Joule-Thomson processes during carbon sequestration and enhance gas recovery.

- Isothermal compressible gas flow (8.3.1)
- Joule-Thomson cooling processes (8.3.5)

At the end of the chapter we present an application example dealing with:

- Air flow through porous medium (section 8.4)

8.1 Material functions

For non-isothermal air flow we have to consider pressure and temperature dependencies of air viscosity $\mu(p, T)$ (section 8.1.1), specific heat capacities $c_p(p, T)$ and heat conductivities $\lambda(p, T)$ (section 8.1.2) as well ([112]).

8.1.1 Air dynamic viscosity

The Reichenberg viscosity model ([113]) is used for the non-isothermal flow of air. The pressure and temperature dependencies of air viscosity are shown in Fig. 8.1.1.

$$\mu(p, T) = \mu_0(T) \left(1 + \frac{A p_r^{\frac{3}{2}}}{B p_r + (1 + C p_r^D)^{-1}} \right) \quad (8.6)$$

with the following parameters:

$$\begin{aligned} p_r &= \frac{p}{p_{\text{crit}}} & T_r &= \frac{T}{T_{\text{crit}}} \\ A &= \frac{\alpha_1}{T_r} \exp(\alpha_2 T_r^a) & B &= A(\beta_1 T_r - \beta_2) \\ C &= \frac{\gamma_1}{T_r} \exp(\gamma_2 T_r^c) & D &= \frac{\delta_1}{T_r} \exp(\delta_2 T_r^d) \\ p_{\text{crit}} &= 33.9 \times 10^4 \text{ Pa} & T_{\text{crit}} &= 126.2 \text{ K} \\ \alpha_1 &= 1.9824 \times 10^{-3} & \alpha_2 &= 5.2683 & a &= -0.5767 \\ \beta_1 &= 1.6552 & \beta_2 &= 1.2760 \\ \gamma_1 &= 0.1319 & \gamma_2 &= 3.7035 & c &= -79.8678 \\ \delta_1 &= 2.9496 & \delta_2 &= 2.9190 & d &= -16.6169 \end{aligned} \quad (8.7)$$

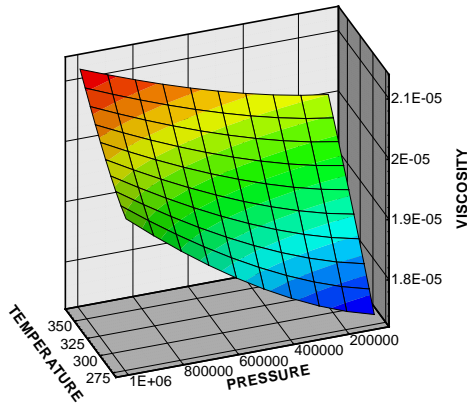


Figure 8.1.1: Air viscosity as a function of temperature (in Kelvin) and pressure (in Pa).

8.1.2 Thermal properties

Beside the flow characteristics such as air viscosity, the thermal properties, such as heat capacity and thermal conductivity of gas and solid are important for heat transport. As an example, Fig. 8.1.2 depicts the thermal properties of the gas. Fig. 8.1.2 (left) shows the temperature dependence of specific heat capacity of air at atmospheric pressure corresponding to equation (8.8) from [114] and compared with experimental data by [115]. Fig. 8.1.2 (right) illustrates the temperature dependence of thermal conductivity of air at atmospheric pressure corresponding to equation (8.9) from [114] and compared with experimental data by [115]. The pressure dependency of thermal properties can be neglected in the present pressure regimes.

$$c_p = a_0 + a_1 T + a_2 T^2 + a_3 T^3 + a_4 T^4 \quad (8.8)$$

where coefficients $a_0 = 1.0613$; $a_1 = -4.3282 \times 10^{-4}$; $a_2 = 1.0234 \times 10^{-6}$; $a_3 = -6.4747 \times 10^{-10}$; $a_4 = 1.3864 \times 10^{-13}$.

$$\lambda = b_0 + b_1 T + b_2 T^2 + b_3 T^3 + b_4 T^4 + b_5 T^5 \quad (8.9)$$

where coefficients $b_0 = 7.488 \times 10^{-3}$; $b_1 = -1.7082 \times 10^{-4}$; $b_2 = 2.3758 \times 10^{-7}$; $b_3 = -2.2012 \times 10^{-10}$; $b_4 = 9.46 \times 10^{-14}$; $b_5 = -1.579 \times 10^{-17}$.

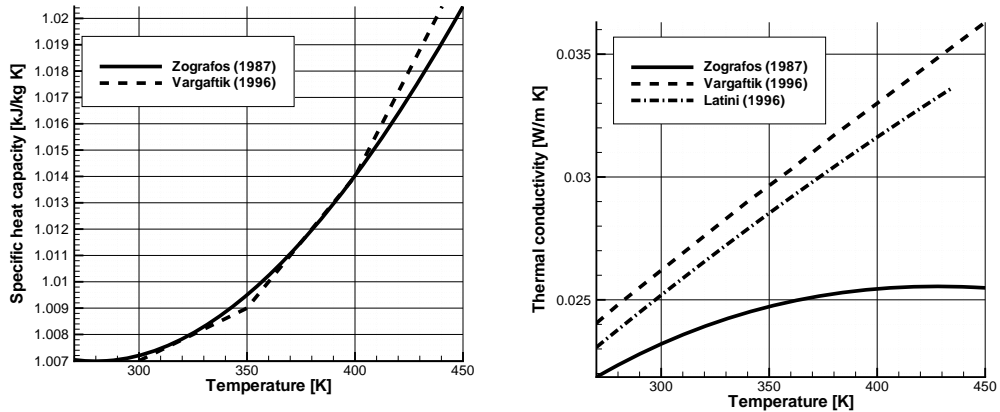


Figure 8.1.2: Thermal properties of air: specific heat capacity (left), thermal conductivity (right).

8.2 Element test

8.2.1 Definition

This example is presented for code verification of different element types, i.e. lines, triangles, quads, tetrahedra, triangle prisms and hexahedra [116]. We consider a non-linear problem, flow of a compressible fluid through the porous medium. In this case the hydraulic conductivity is pressure dependent.

The discretization with different element types is shown in Fig. 8.2.3. The initial gas pressure distribution is equal to $1.01325 \times 10^5 \text{ Pa}$; everywhere in the model domain. There are Dirichlet boundary condition set at left end, i.e. $p^g(x = 0\text{m}) = 9.5500 \times 10^4 \text{ Pa}$, and right end, i.e. $p^g(x = 100\text{m}) = 1.01325 \times 10^5 \text{ Pa}$, in order to extract gas from the domain. The material parameters of the fluid and the porous medium are given in Tab. 8.1.

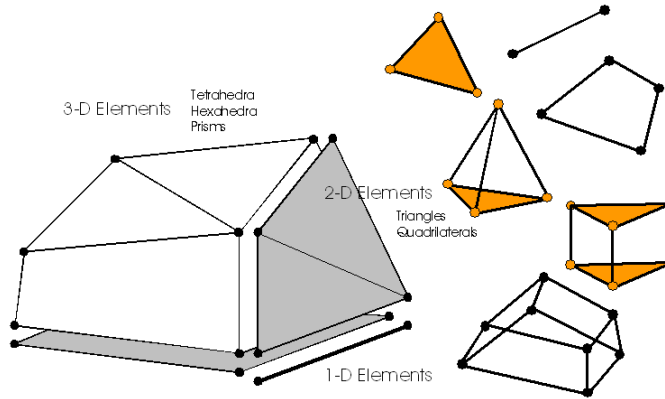


Figure 8.2.3: Different element types.

Table 8.1: Material parameters.

Symbol	Parameter	Value	Unit
L	Model length	0.05	m
A	Cross section area	1	m^2
μ	Dynamic viscosity	1.78×10^{-5}	Pas
n	Porosity	0.005	—
\mathbf{k}	Permeability	2.77×10^{-19}	m^2
Δt	Time step	3×10^2	s
Δx	Space step	0.005	m

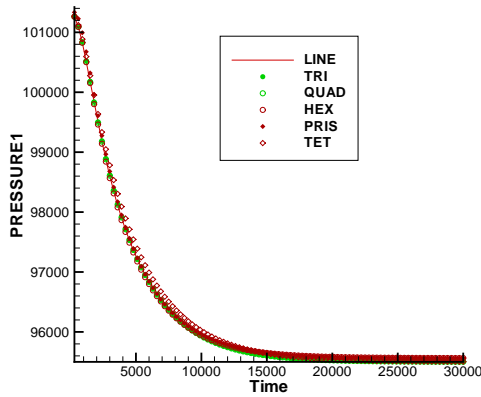


Figure 8.2.4: Evolution of gas pressure at the outlet observation point.

8.2.2 Results

Fig. 8.2.4 depicts the temporal evolution of gas pressure at the observation point at the outlet. The numerical results of all implemented element types compare very well. Small deviation occur from different numbers of Gauss integration points.

8.3 Verifications

Two test examples presented for 1-D compressible gas flow in a porous media. Analytical solution exists for both under the steady state condition. The first test case is dealing with density changing with pressure only, i.e. isothermal case (sec. 8.3.1). The second example shows Joule-Thomson processes with heat dissipation during carbon sequestration and enhance gas recovery.

8.3.1 Isothermal compressible gas flow

8.3.2 Definition

We consider a simple 1D test example where gas is injected at constant pressure into the porous medium. The material parameters are summarized in Tab. 8.2.

8.3.3 Solution

Analytical solution

For isothermal flow with Dirichlet boundary conditions, i.e. $p(x = 0, t) = p_1$ and $p(x = L, t) = p_2$, there exists an analytical solution,

$$p(x) = \sqrt{(p_2^2 - p_1^2) \frac{x}{x_2 - x_1} + p_1^2} \quad (8.10)$$

which is used for verification of the present numerical solution.

According to Darcy's law (8.4) the volumetric gas flux at reference conditions can be approximated as follows

$$Q_0 = A \frac{T_0}{T^* p_0} \frac{\mathbf{k}}{\mu} \frac{(p_2^2 - p_1^2)}{2(x_2 - x_1)} \quad (8.11)$$

Table 8.2: Model parameters.

Symbol	Parameter	Value	Unit
L	Model length	100	m
A	Cross section area	1	m^2
n	Porosity	0.35	—
\mathbf{k}	Permeability	2.7×10^{-11}	m^2
μ	Gas dynamic viscosity	1.76×10^{-5}	Pa s
p_0	Initial condition	101325	Pa
p_1, p_2	Boundary conditions	$3 \times 10^6, 1.01325 \times 10^5$	Pa
Δt	Time step	1, 10, $10^2, 10^3, 10^4$	s
Δx	Space step	1	m

Numerical solution

The numerical model consists of 100 line elements connected by 101 nodes along the x-axis. The distances of the nodes Δx is one meter. At $x = 0$ m there is a constant pressure boundary value is 3×10^6 Pa. Whereas at $x = L$ pressure boundary value is 1.01325×10^5 Pa.

8.3.4 Results

Fig. 8.3.5 shows the comparison of present numerical solution with analytical. Steady state is reached after about 1.0×10^4 s.

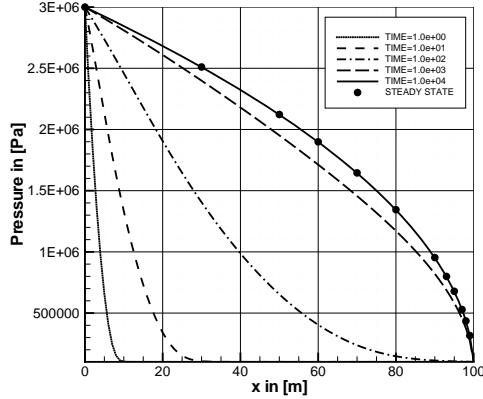


Figure 8.3.5: Comparison of analytical (\bullet) and numerical solutions.

8.3.5 Joule-Thomson cooling processes

8.3.6 Definition

Flow in permeable media is not an isothermal process because there is a temperature change resulting from fluid expansion and viscous dissipation heating. The test benchmark is formulated for the injection of compressed cryogenic CO₂ in a one-dimensional horizontal reservoir column. Material parameters are presented in Tab 8.3.

8.3.7 Solution

Analytical solution

For such case there exists an analytical solution with the boundary value at $x = 0$ is T_0 and at $x = L$ is $\nabla T = 0$.

$$T = L_+ \exp(m_+ x) + L_- \exp(m_- x) + \frac{1}{\beta_T} \quad (8.12)$$

where

$$m_{\pm} = u_x \left(\frac{\rho c_p}{\kappa_{\text{eff}}} \pm \sqrt{\left(\frac{\rho c_p}{\kappa_{\text{eff}}} \right)^2 + \frac{4\beta_T \mu}{k \kappa_{\text{eff}}}} \right)$$

and L_+ and L_- are integration constants to be determined by boundary conditions.

Table 8.3: Model parameters.

Symbol	Parameter	Value	Unit
L	Column radius	100	m
n	Porosity	0.35	—
ρ, ρ^s	Densities	$\frac{pM}{z_{sc}RT}, 2460$	kg m^{-3}
k	Permeability	2.7×10^{-11}	m^2
μ	Dynamic viscosity	1.9836×10^{-5}	Pa s
κ, κ^s	Heat conductivities	0.026374, 2.5	$\text{W m}^{-1}\text{K}^{-1}$
c_p, c_p^s	Heat capacities	$1.067 \times 10^3, 1.2 \times 10^3$	$\text{J kg}^{-1}\text{K}^{-1}$
β_T	Thermal expansivity	$-\frac{1}{\rho_0} \frac{\partial \rho}{\partial T}$	K^{-1}

Numerical solution

Finite element solution has been obtained through solving the mass and energy balance equations. Within a time step mass balance equation for pressure is solved with temperature changes in return the energy balance equation is then solved for temperature with obtained fluid velocity. This is so called staggered approach and executed until solution become steady.

The physical domain has been discretized in 100 line element which size is varying between $\Delta x = 0.4$ m to $\Delta x = 4.3498$ m. This helps to capture the sharp gradient of temperature present near the injection point. Concerning to the time step size, at beginning of the simulation $\Delta t = 1$ s with step by step increasing, it reaches to $\Delta t = 1.0 \times 10^4$ s.

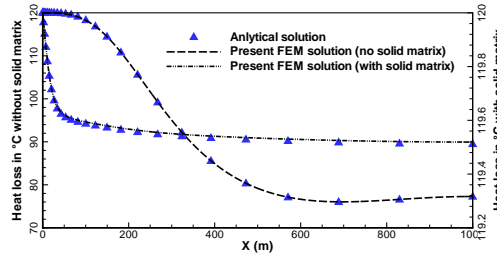


Figure 8.3.6: Comparison of present solution (FEM) with analytical solution due to equation. (8.12).

8.3.8 Results

Based on the above discussion OpenGeoSys (OGS) capable to show the Joule-Thomson process in carbon sequestration with enhanced gas recovery. In Fig.

8.3.6 we have presented comparison of temperature profile produced from OGS with those of analytical solution, i.e. equation (8.12). In the figure ‘**without solid matrix**’ mean the case where we do not account heat provided by solid matrix by setting $c_p^s = 0, \kappa^s = 0$ whereas case ‘**with solid matrix**’ mean we have accounted heat provided by solid matrix.

Figure shows that as we inject CO₂ (at temperature 393.15 K which is lower than inversion temperature ≈ 1500 K), its pressure falls with high gradient. It means as expansion starts, the average distance between molecules grows. Because of intermolecular attractive forces, expansion causes an increase in the potential energy of the gas. As no external work is extracted and process is adiabatic, the total energy of the gas remains constant because of the conservation of energy. The increase in potential energy thus implies a decrease in kinetic energy and therefore temperature falls.

8.4 Air flow example

8.4.1 Definition

We consider the same test example definition as for isothermal gas flow in sec. 8.3.1. Now we use pressure and temperature dependent material properties described in section 8.1. The model parameters are summarized in Tab. 8.4.

Table 8.4: Model parameters

Symbol	Parameter	Value	Unit
L	Model length	100	m
n	Porosity	0.35	—
ρ, ρ^s	Densities	(8.2), 2650	kg m ⁻³
k	Permeability	2.7×10^{-11}	m ²
μ	Dynamic gas viscosity	(8.6)	Pa s
p_0	Initial condition	101325	Pa
T_0	Initial condition	288	K
p_2	Boundary condition	101325	Pa
T_1	Boundary condition	343	K
Q_ρ	Injection rates	1 – 10	kg s ⁻¹
α_L, α_T	Heat dispersion length	1, 0.1	m
λ^g, λ^s	Heat conductivities	(8.9), 2.5	W m ⁻¹ K ⁻¹
c_p^g, c_p^s	Heat capacities	(8.8), 2300	J kg ⁻¹ K ⁻¹

8.4.2 Solution

The numerical model consists of 100 line elements connected by 101 nodes along the x-axis. The distances of the nodes Δx is one meter. At $x = 0\text{m}$, we injecting air with rates of 1 kg s^{-1} and 10 kg s^{-1} , which temperature is 343 K . And at $x = L$, pressure boundary value is $1.01325 \times 10^5 \text{ Pa}$ and $\nabla T = 0$.

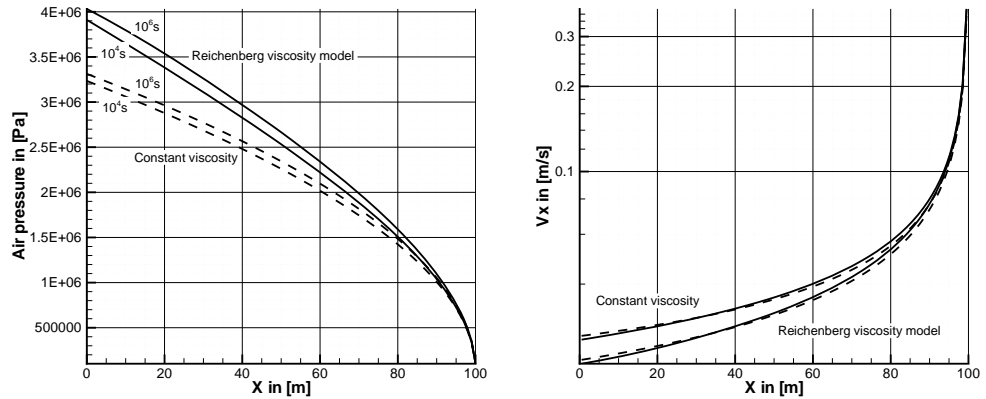


Figure 8.4.7: Hydraulic profiles evolution: Air pressure (top), Air velocity (bottom).

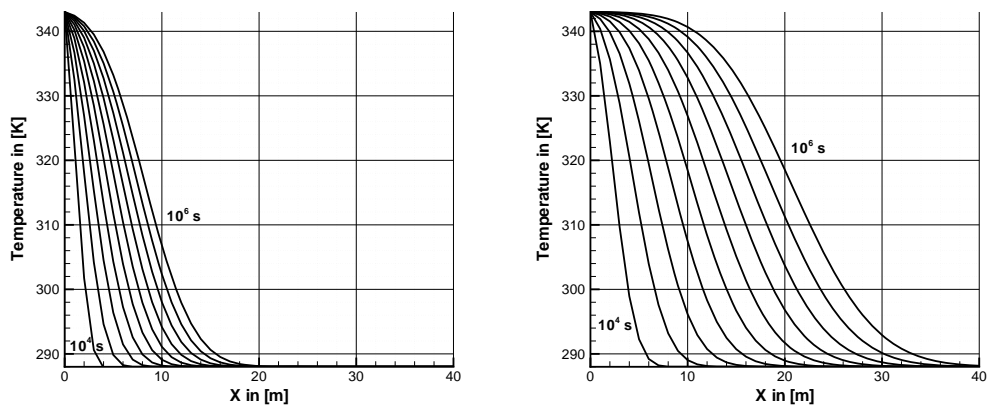


Figure 8.4.8: Air temperature profiles evolution. 1 kg s^{-1} air injection rate (top), 10 kg s^{-1} air injection rate (bottom).

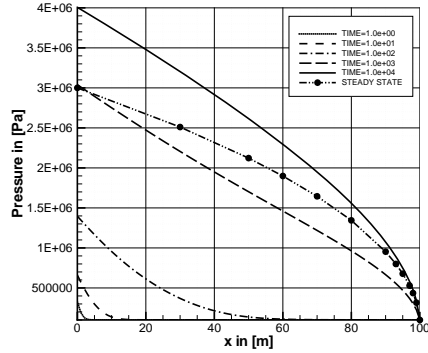


Figure 8.4.9: Temporal evolution of air pressure profiles for non-isothermal gas flow.

8.4.3 Results

Fig. 8.4.7 show the air pressure (left) and velocity distributions (right) along the soil column. Simulations were run with constant viscosities and those corresponding to the Reichenberg model (section 8.1.1) which takes pressure and temperature changes into account.

The corresponding temperature profiles for different air injection rates are depicted in Fig. 8.4.8. The different shapes of the thermal profile curves indicate the transition between diffusion (left) and advection dominated regimes (right).

Fig. 8.4.9 shows the temporal evolution of air pressure profile for non-isothermal air flow. In order to see the non-isothermal effects we plotted the analytical steady state solution for isothermal flow along with present numerical solution for non-isothermal flow. As a consequence of the viscosity increase resulting from the Reichenberg model the steady state pressure is larger for non-isothermal conditions.

Chapter 9

Deformation processes

by Uwe Grke, Norihiro Watanabe, Joshua Taron, Wenqing Wang

This chapter is dedicated to the analysis of pure deformation processes in solid continua. Within the context of porous media mechanics, the generalized local momentum balance Eq. (2.73) discussed in Sec. 2.3.2 serves as governing equation describing mechanical deformation. In fact, the specific expression of the momentum balance Eq. (2.73) defines the equilibrium conditions in porous media (here, considering swelling and thermal stresses caused by the coupling of mechanical to other physical and chemical processes). The effective stress principle has been established in order to define the stress state in the solid skeleton of porous media (cf. Sec. 2.5.1). Within this context σ_{eff} indicates the stress tensor applied to a substitute continuum representing the solid skeleton smeared over the volume of the porous medium under consideration, and being characterized by a reduced partial density compared to the material density of the solid skeleton. Material models, which are well-known from solid mechanics are transferred directly to the description of the material behavior of the solid skeleton in porous media mechanics.

Assuming small strains, the equilibrium conditions in solid mechanics are defined by the following specific formulation of the balance of linear momentum:

$$\nabla \cdot \boldsymbol{\sigma} + \rho \mathbf{g} = 0 \quad (9.1)$$

where $\boldsymbol{\sigma}$ is the Cauchy's stress tensor, ρ is the mass density, and $\rho \mathbf{g}$ is the volume force with the gravity vector \mathbf{g} . The coefficients of the displacement vector \mathbf{u} are the primary variables, which will become evident introducing an appropriate constitutive relation describing the specific stress-strain behavior of the material under consideration into the weak formulation of Eq. (9.1). For more details about the systematics of typical material classes see Sec. 2.5.2.

In general, the deformation problem can be considered as an initial-boundary value problem with Neumann type and Dirichlet type boundary conditions accordingly given by

$$\boldsymbol{\sigma} \cdot \mathbf{n} = \mathbf{t} \quad \text{or} \quad \mathbf{u} = \mathbf{u}_\Gamma, \quad \forall \mathbf{x} \in \partial\Omega \quad (9.2)$$

where \mathbf{n} defines the normal vector to the part of the surface with given traction boundary conditions \mathbf{t} , and \mathbf{u}_Γ are prescribed boundary displacement values.

Subsequently, the following benchmarks for deformation problems with increasing complexity (e.g., regarding the material behavior) are presented:

Elasticity:

- Plane strain confined compression (9.1.1)
- Plane strain confined compression – Excavation in homogeneous media (9.1.2)
- Plane strain confined compression – Excavation in heterogeneous media (9.1.3)
- Strain driven three-dimensional unconfined compression (9.1.4)
- Load driven three-dimensional unconfined compression (9.1.5)

- Nonlinear elastic axisymmetric triaxial compression (9.1.6)
- Transverse isotropic elastic tensile test (9.1.7)

Elastoplasticity:

- Compression of a plate with a hole (9.2.1)
- Twodimensional strain localization problem (9.2.2)
- Cam-Clay plasticity (9.2.3)

Viscoplastic creep:

- Creep of a thick-walled cylinder (9.3.1)
- Thermally driven creep in rock salt (9.3.2)
- Stationary creep in rock salt (9.3.3)
- Transient creep in rock salt (9.3.4)

9.1 Elasticity

For small strains of solid continua, it is mostly justified to assume isotropic elastic material behavior. Most substantial details of the theory of linear isotropic elasticity, represented by the generalized Hooke's law, are discussed in Sec. 2.5.3.

In many technical applications considering small strains, the elastic material parameters are assumed to be constant, and the stress-strain curves are nearly linear. However, the typical response of certain geological materials to monotonic loading (without load reversal) shows a nonlinear stress-strain behavior. Considering only elastic effects during load application, Hooke's law cannot be used to describe the observed material properties. Therefore, so-called pseudo-elastic constitutive models are frequently used for the analysis of nonlinear stress-strain curves, particularly in soil and rock mechanics. In a generalized manner, they are based on the assumption of an explicit stress-strain relation considering a stress- and strain-dependent material matrix:

$$\boldsymbol{\sigma} = \mathbf{C}_4(\boldsymbol{\sigma}, \boldsymbol{\varepsilon}) \cdot \boldsymbol{\varepsilon}_{\text{el}}. \quad (9.3)$$

Based on the so-called *Lubby1* model (cf. [117]), a nonlinear elastic approach with strain-dependent Young's modulus

$$E(\varepsilon_v) = \frac{E_0}{1 + a \varepsilon_v^n} \quad (9.4)$$

but constant Poisson's ratio is proposed. Here, ε_v is the equivalent strain, and E_0 , a as well as n are material parameters. The equivalent strain is defined by

$$\varepsilon_v = \sqrt{\frac{2}{3} \boldsymbol{\varepsilon}_{\text{el}} \cdot \boldsymbol{\varepsilon}_{\text{el}}}. \quad (9.5)$$

If the material properties are independent of orientations and directions of the technical or natural object under consideration, the material behavior is called *isotropic*. Otherwise, the material is known as *anisotropic* one. Anisotropy is closely connected with distinguished orientations in the material structure. Among others, fiber-reinforced and layered materials are typical anisotropic materials.

From the point of view of modeling and numerical simulation special cases of anisotropy like *orthotropy* are of particular interest. Orthotropic materials are characterized by mutually orthogonal two-fold axes of rotational symmetry. A special class of orthotropic materials represent the so called *transverse isotropic* materials. They are characterized by a plane of isotropy featuring the same material properties independent of the direction of observation within this plane, and different material properties in the direction normal to this plane. Within this context, the normal to the plane of isotropy can be considered as the direction of anisotropy. Most of layered materials, biological membranes as well as rocks (e.g. sandstone, shale) are typical materials which can be considered as transverse isotropic ones.

In case of transverse isotropy, the Hooke's law (2.105) has to be modified establishing a unit vector \mathbf{a} which defines the direction perpendicular to the plane of isotropy (normal vector, direction of anisotropy – defining, e.g., the direction of a single fiber family of a fiber-reinforced material).

$$\begin{aligned}\sigma_{ij} = & \lambda \delta_{ij} \varepsilon_{kk} + 2\mu_T \varepsilon_{ij} \\ & + 2(\mu_L - \mu_T)(a_i \varepsilon_{jl} a_l + a_l \varepsilon_{li} a_j) \\ & + \alpha(a_i a_j \varepsilon_{kk} + a_k \varepsilon_{kl} a_l \delta_{ij}) \\ & + \beta a_k \varepsilon_{kl} a_l a_i a_j\end{aligned}\quad (9.6)$$

Linear elastic transverse isotropic material is characterized by 5 independent material parameters like λ , μ_T , μ_L , α and β given in Eqn. (9.6). In some cases these parameters are called *invariants* of the transverse isotropic elastic Hooke's law. They can be defined w.l.o.g. by the following (engineering) elastic constants which can be obtained experimentally:

- E_i – Young's modulus within the plane of isotropy,
- ν_i – Poisson's ratio within the plane of isotropy,
- E_a – Young's modulus w.r.t. the direction of anisotropy,
- ν_{ia}, ν_{ai} – Poisson's ratio w.r.t. the direction of anisotropy,
- G_a – shear modulus w.r.t. the direction of anisotropy.

There exist some relations between these parameters.

$$G_i = \frac{E_i}{2(1 + \nu_i)} = \mu_i \quad (\text{shear modulus within the plane of isotropy}) \quad (9.7)$$

$$\nu_{ai} = \nu_{ia} \frac{E_a}{E_i} \quad (9.8)$$

As mentioned above, the invariants of the transverse isotropic elastic Hooke's law can be expressed by the presented elastic parameters.

$$\lambda = \frac{E_i(\nu_i + \nu_{ia}\nu_{ai})}{\tilde{D}}$$

$$\mu_T = G_i$$

$$\mu_L = G_a$$

$$\alpha = \frac{E_i(\nu_{ai}(1 + \nu_i - \nu_{ia}) - \nu_i)}{\tilde{D}}$$

$$\beta = \frac{E_a(1 - \nu_i^2) - E_i[(\nu_i + \nu_{ia}\nu_{ai}) + 2(\nu_{ai}(1 + \nu_i - \nu_{ia}) - \nu_i)]}{\tilde{D}} - 4G_a + 2G_i$$

$$\begin{aligned} \text{with } \tilde{D} &= 1 - \nu_i^2 - 2\nu_{ia}\nu_{ai} - 2\nu_{ia}\nu_i\nu_{ai} \\ &= (1 + \nu_i)(1 - \nu_i - 2\nu_{ia}\nu_{ai}) \end{aligned}$$

The coordinates of the material tensor for linear elastic transverse isotropic material are defined as follows:

$$\begin{aligned} C_{ijkl} &= \lambda \delta_{ij} \delta_{kl} + 2\mu_T \delta_{ik} \delta_{jl} \\ &\quad + 2(\mu_L - \mu_T)(a_i \delta_{jk} a_l + a_k \delta_{il} a_j) \\ &\quad + \alpha(a_i a_j \delta_{kl} + a_k a_l \delta_{ij}) \\ &\quad + \beta a_i a_j a_k a_l \end{aligned} \quad (9.9)$$

9.1.1 Plane strain confined compression

Definition

This example deals with numerical analyses of a part of the whole rock mass based on special conditions concerning symmetry, structure of the rock mass and material behavior. In order to simulate an initial state of stress in different depths, a pressure at least at one boundary has to be applied which represents the load of the overburden. In addition to this the stresses decrease with depth because of the gravity and the density of the rock mass (Fig. 9.1.1).

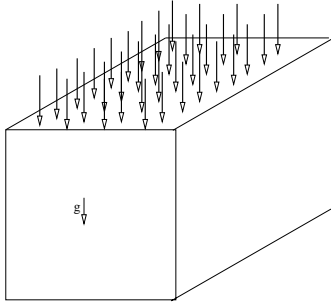


Figure 9.1.1: Conceptual model of elastic foundation

Solution

The calculation area has the size of $50\text{ m} \times 50\text{ m}$ (length and height), and the problem is simplified under plane strain conditions. The quadrilateral mesh is illustrated in Fig. 9.1.2(a), which is refined in one corner in order to be used directly to conduct subsequently an elastic excavation simulation.

Regarding boundary conditions, a uniformly distributed pressure of 23.75 MPa is prescribed for the top boundary. Such kind of boundary conditions are so called tractions in the context of mechanics, and they are treated as Neumann type boundary conditions. Boundary conditions are illustrated in more detail in Fig. 9.1.2(b).

Homogeneous material properties are assumed within the whole domain. Table 9.1 represents the corresponding material parameters.

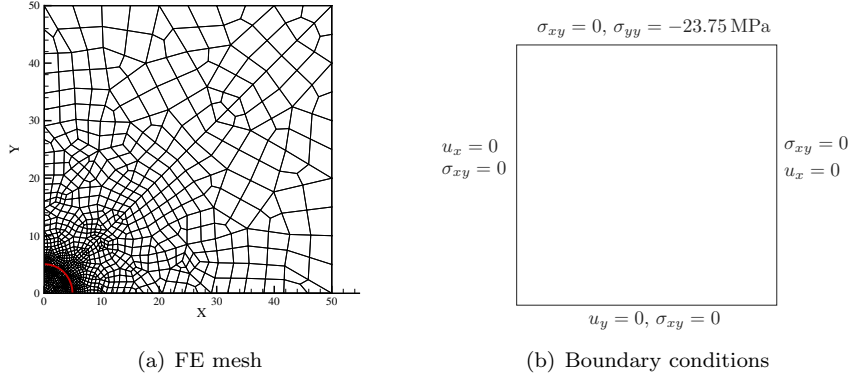


Figure 9.1.2: Finite element model. Left: Spatial discretization (1150 quadrilateral elements, 1101 nodes); Right: Boundary conditions

Table 9.1: Material parameters

Symbol	Parameter	Value	Unit
E	Young's modulus	25	GPa
ν	Poisson's ratio	0.3	—
ρ	Density	2500	$\text{kg}\cdot\text{m}^{-3}$

For this simple elastic problem, the following analytical solution exists:

$$\sigma_{yy} = -23.75 - \rho h \quad (9.10)$$

where ρ is the solid density and h is the height from top to bottom boundary.

Results

Fig. 9.1.3 (left) shows the distribution of vertical stress in the domain, which implies that the discretization error is very small. Fig. 9.1.3 (right) shows a linear variation of stress σ_{yy} along with height.

The numerical result of σ_{yy} at the bottom boundary is -24.97 MPa , which is very close to the analytic solution, $\sigma_{yy} = -25.0 \text{ MPa}$.

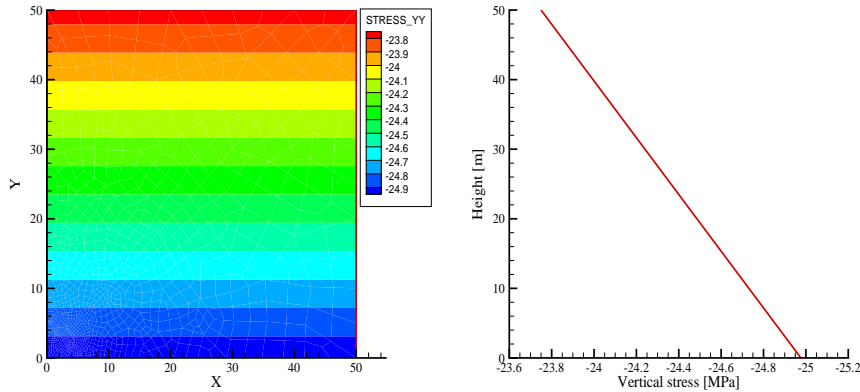


Figure 9.1.3: Result of vertical stress, σ_{yy} (MPa). Left: domain distribution.
Right: Vertical profile

9.1.2 Plane strain confined compression – Excavation in homogeneous media

Definition

This is the second step of the simulation described in the previous section, Sec. 9.1.1. A long cylindrical tunnel is driven in the rock mass, which is schematically shown in Fig. 9.1.4.

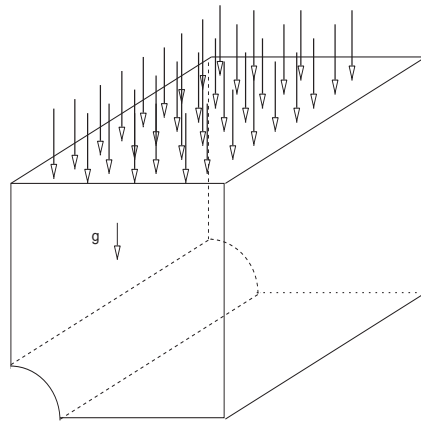


Figure 9.1.4: Excavation in rock mass

Solution

The deformation due to the excavation is simulated under the assumption of plane strain. Finite element mesh, initial conditions and material parameters are the same as specified in Sec. 9.1.1. The tunnel has a radius of 5 m. The released loading approach is applied to simulate the excavation.

Results

Fig. 9.1.6 shows the distribution of vertical displacements and coefficients of the stress tensor in the domain after excavation.

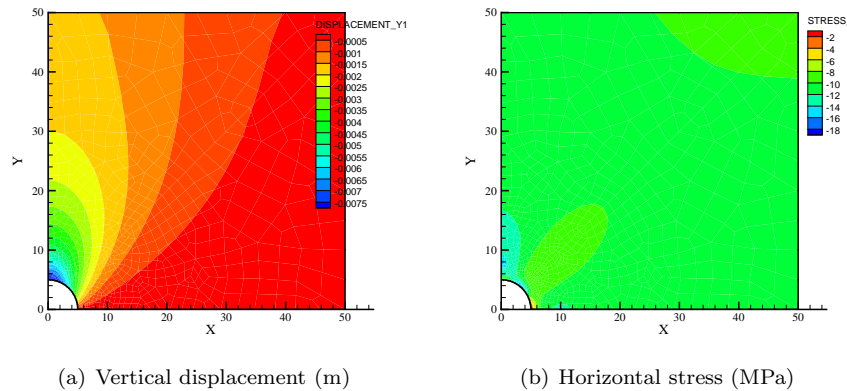


Figure 9.1.5: Vertical displacements and horizontal stress after excavation

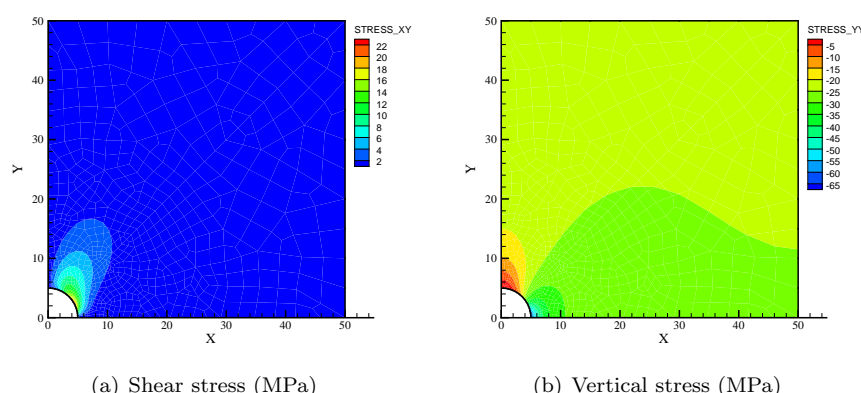


Figure 9.1.6: Shear stress and vertical stress after excavation

9.1.3 Plane strain confined compression – Excavation in heterogeneous media

Definition

Differing from the homogeneous case, the deformation of the excavation problem defined in Sec. 9.1.2 is analyzed herewith defining the initial conditions as functions of the coordinates, and assuming four different material domains (cf. Fig. 9.1.7).

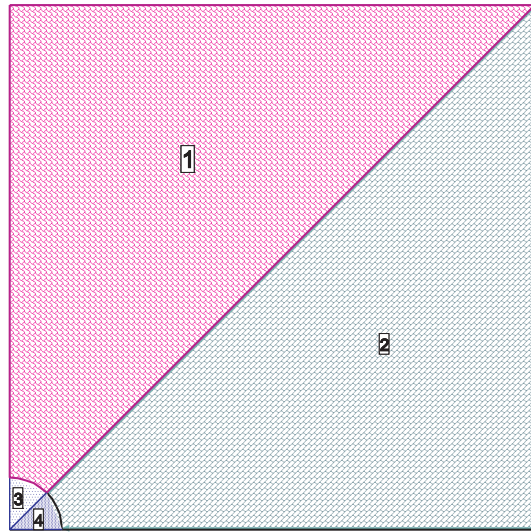


Figure 9.1.7: Excavation in heterogeneous rock mass

Solution

The initial stresses are assumed to be linearly distributed within a material domain. The expressions of these distribution are given in Table 9.2.

As depicted in Fig. 9.1.7, the domain consists of four different materials denoted by 1, 2, 3 and 4. Within this context, only the Young's modulus is assumed to differ for the material domains under consideration (cf. Table 9.3).

Table 9.2: Initial stress distribution as function of coordinates (in kPa; material domains cf. Fig. 9.1.7)

Material domain	σ_{xx}	σ_{yy}	σ_{zz}
1	$-23.75 - 0.2y$	$-23.75 - 0.2y$	cf. σ_{xx}
2	$-24.75 - 0.5y$	$-24.75 - 1.3y$	cf. σ_{xx}
3	$-26.75 - 10.0x - 12.0y$	$-26.75 - 20.0x - 16.0y$	cf. σ_{xx}
4	$-27.75 - 10.0x - 14.0y$	$-27.75 - 20.0x - 18.0y$	cf. σ_{xx}

Table 9.3: Material parameters (different Young's moduli are given in the order of the material domains)

Symbol	Parameter	Value	Unit
E	Young's modulus	25.0; 26.0; 30.0; 28.0	GPa
ν	Poisson's ratio	0.3	—
ρ	Density	2500	$\text{kg}\cdot\text{m}^{-3}$

Results

Fig. 9.1.8 shows the distribution of displacements after excavation, and Fig. 9.1.9 shows the distribution of different coefficients of the stress tensor after excavation.

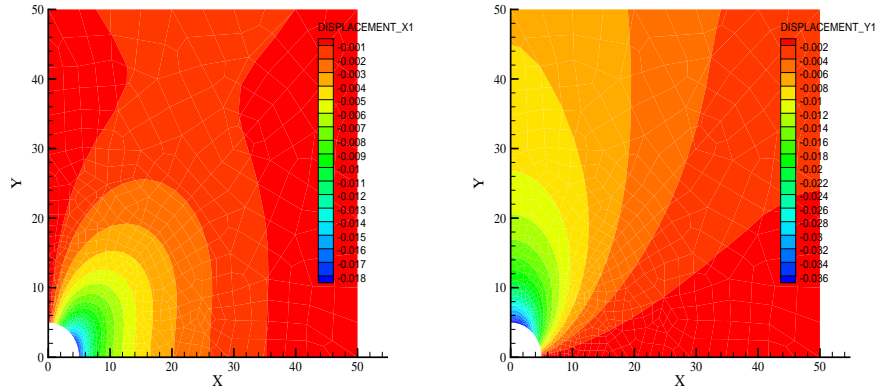


Figure 9.1.8: Distribution of displacement (m)

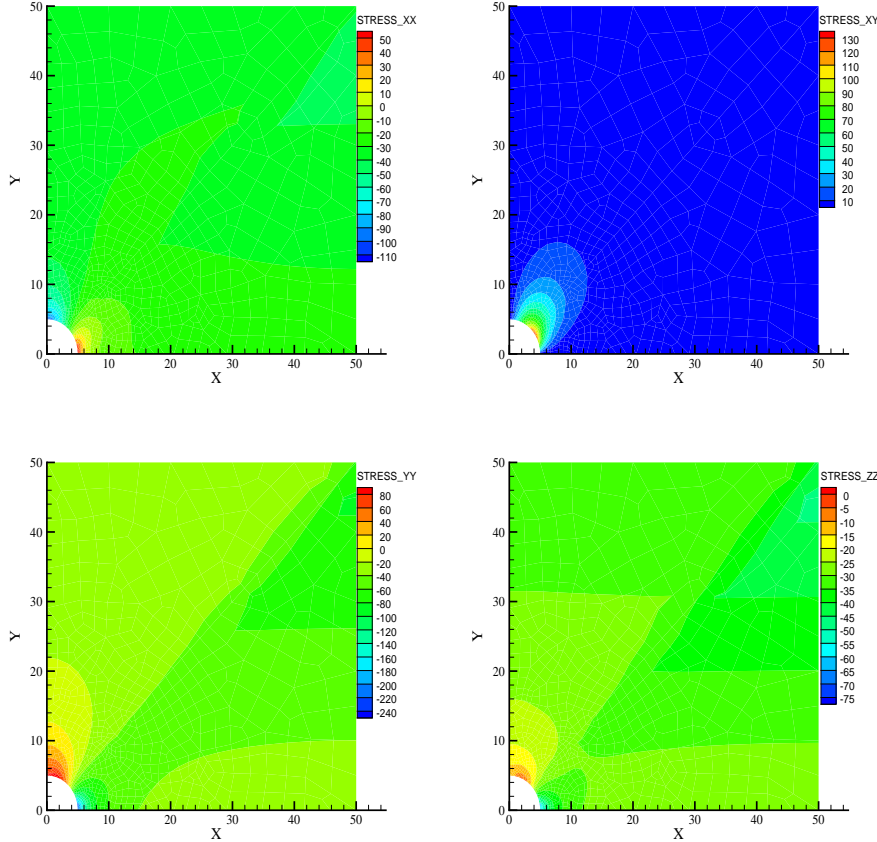


Figure 9.1.9: Distribution of stresses (kPa)

9.1.4 Strain driven threedimensional unconfined compression

Definition

A quarter of an elastic cylinder is compressed at the top applying prescribed uniform deformations as boundary condition (cf. Fig. 9.1.10). Assuming homogeneous isotropic linear elastic material behavior and constant loading, the axial stress coefficient σ_{zz} and the displacement vectors in the nodes of the finite element grid are calculated, which are caused by the given external loading.

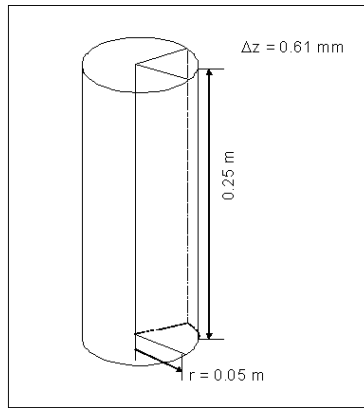


Figure 9.1.10: Calculation area: a quarter of a cylinder

Solution

The calculation area for the threedimensional simulation consists of a quarter of the cylinder under consideration (cf. Fig. 9.1.11). The model includes 4000 elements and 4947 nodes. Deformations in x -direction are suppressed in the y - z -plane and deformations in y -direction are suppressed in the x - z -plane. Furthermore, axial deformations are suppressed at the bottom of the calculation area. At the top of the model boundary conditions are prescribed assuming a constant displacement of 0.61 mm causing compression of the cylinder. The used material parameters are shown in Tab. 9.4.

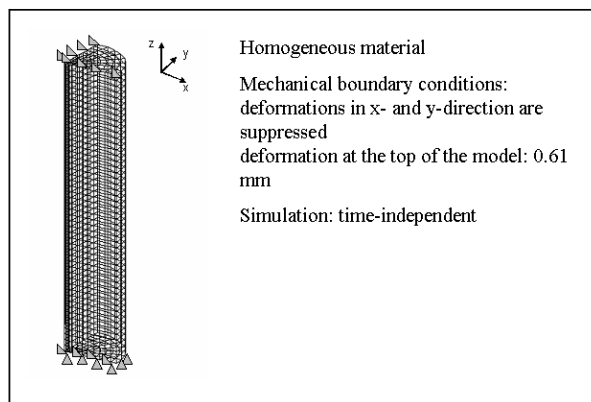


Figure 9.1.11: Finite element model: spatial discretization and boundary conditions

In order to solve the homogeneous problem analytically, some constraints have to be considered: the stresses in x - and y -direction are equal to zero, because

Table 9.4: Material parameters

Symbol	Parameter	Value	Unit
E	Young's modulus	7	GPa
ν	Poisson's ratio	0.3	—
ρ	Density	2500	$\text{kg}\cdot\text{m}^{-3}$

the body expands homogeneously in radial direction. Thus the stress-strain equations defined by Hooke's law (2.105) can be simplified as follows:

$$\varepsilon_{zz} = \frac{\Delta z}{z} = \frac{1}{E} \cdot \sigma_{zz} \quad (9.11)$$

$$\varepsilon_{xx} = \varepsilon_{yy} = \frac{1}{E} \cdot (-\nu \cdot \sigma_{zz}) \quad (9.12)$$

With the given strain in z -direction, the axial stress σ_{zz} is defined using Eqn. 9.11 as

$$\frac{\Delta z}{z} = -2.44 \times 10^{-3} \quad \text{and} \quad \sigma_{zz} = -1.71 \times 10^7 \text{ Pa}$$

In this way, the strains in x - and y -direction are known.

$$\varepsilon_{xx} = 7.32 \times 10^{-4}$$

Results

As can be seen in Fig. 9.1.12, the numerical results meet exactly the analytical solutions. In this figure, axial strain and the resulting axial stress are presented along a polyline from top to bottom of the calculation area.

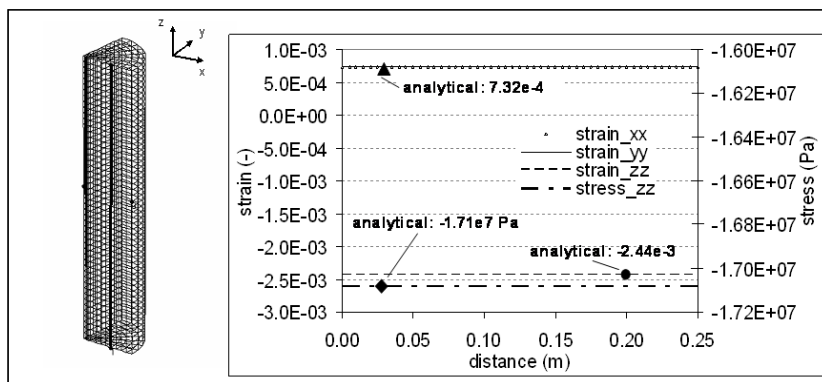


Figure 9.1.12: Resulting axial strain and axial stress

9.1.5 Load driven threedimensional unconfined compression

Definition

This example is similar to the previous one, differing in the kind of prescribed external loading: the calculation area undergoes traction boundary conditions (given surface stress) applied to the top of the model, while resulting deformation is unknown. In order to check out easily whether the simulated results correspond to the analytical solutions, the value of the prescribed axial stress coefficient σ_{zz} on the top of the calculation area is chosen to have the same value as the resulting one obtained in the previous example.

Solution

The finite element model has the same characteristics as the model in Sec. 9.1.4. At the top of the model a constant compressive surface stress in axial direction with a value of 1.71×10^7 Pa is given as source term. The simulation with OpenGeoSys requires the input of the external load in terms of surface tractions as source term in z -direction at the single nodes of the stressed boundary. The displacement boundary conditions are the same as in the previous example except of the axial displacement on the top of the model. The used material parameters are shown in Tab. 9.4.

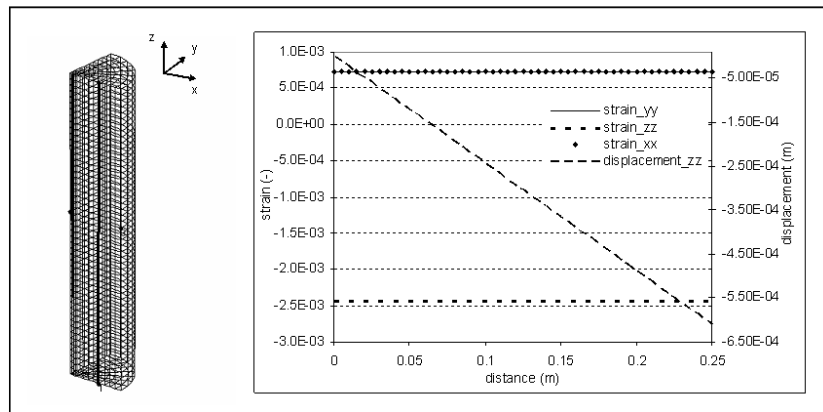


Figure 9.1.13: Strains and displacement in z -direction

Results

The analytical solution and the numerical results are identical to that of the previous example. The calculated axial displacement as a result of the constant

load on the top of the model is 6.1×10^{-4} m. The numerical results that are shown in Fig. 9.1.13 meet the analytical solutions exactly.

9.1.6 Nonlinear elastic axisymmetric triaxial compression

Definition

Triaxial short-term compression under axisymmetric conditions is carried out to verify the nonlinear elastic isotropic material model (modified Lubby1 approach). The loading in principal axes includes a radial pressure as well as an axial displacement, and is realized in two steps. It is resulting in a homogeneous stress-strain state.

Solution

For the calculation, the cross-section of a cylindrical sample with a radius of 30 mm and a height of 120 mm is studied. Details of the model (geometry, mesh, boundary conditions) according to K.-H. Lux and F. Werunsky (unpublished report, 2008) are presented in Fig. 9.1.14.

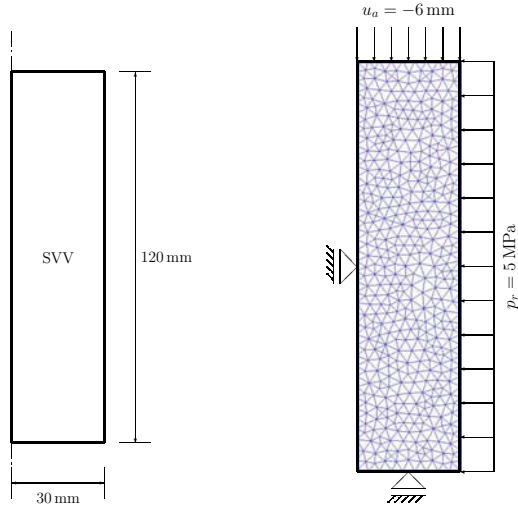


Figure 9.1.14: Triaxial compression of a cylindrical sample. Axisymmetric model. Left: Geometry. Right: Finite element grid and boundary conditions

Initial conditions do not have to be given for the problem under consideration. As the bottom edge is fixed in vertical direction, the left-hand edge is fixed in horizontal direction for symmetry reasons (axis of rotation). On the right-hand

edge initially a radial casing pressure of 5 MPa is applied within 20 seconds with a constant stress rate. While keeping constant this radial pressure, a subsequent stroke-driven axial compressive loading is applied within the following 1440 seconds with a constant strain rate. The maximum axial displacement is 6 mm which corresponds to a 5 % reduction of the sample's height (for the complex loading history cf. Fig. 9.1.15).

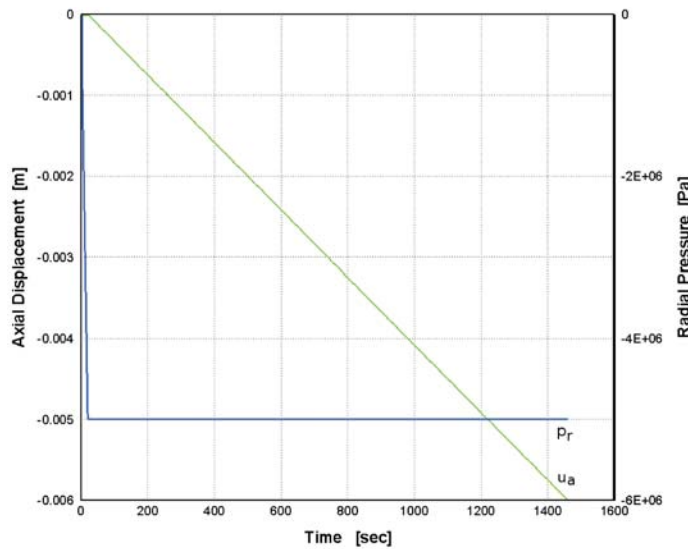


Figure 9.1.15: Triaxial compression of a cylindrical sample. Loading history for short-term experiments. Radial casing pressure (stress rate $\dot{p}_r = 0.25 \text{ MPa}\cdot\text{s}^{-1}$) with subsequent axial displacement (strain rate $\dot{\varepsilon}_a = 3.47 \times 10^{-5} \text{ s}^{-1}$)

The material parameters referring to the modified Lubby1 relation (9.4) are summarized in Tab. 9.5. Within this context, the initial Young's modulus and the Poisson's ratio are close to values known for rock salt.

Table 9.5: Material parameters

Symbol	Parameter	Value	Unit
E_0	Initial Young's modulus	21.4	GPa
ν	Poisson's ratio	0.335	—
a	Factor in (9.4)	2750	—
n	Exponent in (9.4)	1.0	—

Results

The representation of the axial stress vs. the axial strain in Fig. 9.1.16 shows on exemplarily chosen material parameters the noticeable difference between the linear (Hooke's model) and the nonlinear (modified Lubby1 model) elastic models even at small strains. Within the context of the studied case, the stress response will be overestimated by a multiple using the linear Hooke's law.

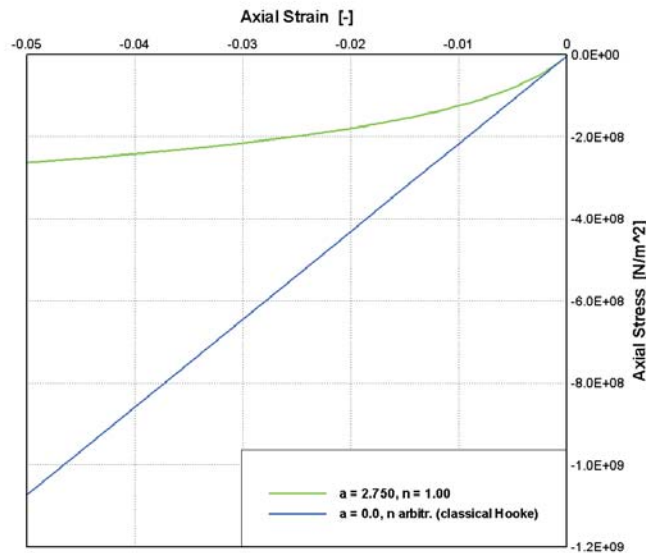


Figure 9.1.16: Triaxial compression of a cylindrical sample. Stress-strain curves regarding the axial load response. Comparison of linear elastic (Hooke) and nonlinear elastic (modified Lubby1 (9.4)) material models

9.1.7 Transverse isotropic elastic tensile test

Definition

Tension of a quadratic plate according to Schröder [118], Kohlmeier [119] and Fiolka [120] is carried out to verify the linear elastic transverse isotropic material model. Within this context, a laminated material structure perpendicular to the plane under consideration is assumed. The direction of anisotropy within this plane, which is defined by a vector α is perpendicularly oriented to the material layers.

Solution

During simulation, the direction of anisotropy is rotated counterclockwise starting with an angle φ of $\varphi = 0^\circ$ and ending with $\varphi = 180^\circ$. Consequently, as in OpenGeoSys the direction of anisotropy is assumed to be directed parallel to the local \bar{y} -axis, and the angle of rotation is defined as the rotation between the global x -axis and the local \bar{x} -axis, the input angle changes in the range of $\varphi = -90^\circ \dots 90^\circ$.

Assuming plane strain conditions for the twodimensional case, the quadratic plate has an edge length of $l = 10$ mm, and was analyzed using triangular and rectangular elements respectively. For details of this model (geometry, boundary conditions, material orientation) see Fig. 9.1.17.

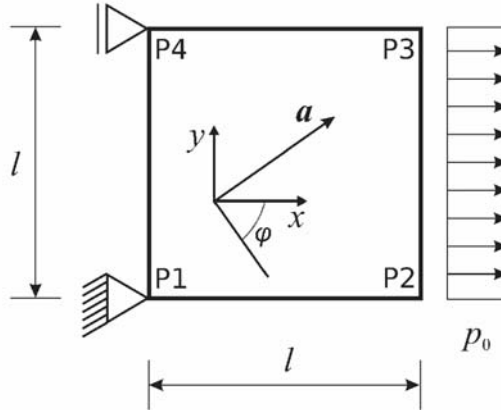


Figure 9.1.17: Tensile test. Model definition according to Kohlmeier [119]. Vector \mathbf{a} defines the direction of anisotropy.

To verify the linear elastic transverse isotropic material model in the threedimensional case, the tensile test was simulated using a rectangular sample with an edge length $l = 10$ mm and a height $h = 1$ mm. According to the twodimensional case, a vertically arranged laminated material structure is assumed. The direction of anisotropy, which is defined by a vector \mathbf{a} is perpendicularly oriented to the material layers. During simulation, the direction of anisotropy is rotated counterclockwise in the xy -plane from $\varphi = 0^\circ$ to $\varphi = 180^\circ$.

Within the context of the different opportunities offered by the input structure of OpenGeoSys to define the anisotropy direction, the coefficients of the unit normal vector which is parallel to the direction of anisotropy are given as $n_x = \cos \varphi$, $n_y = \sin \varphi$, and $n_z = 0$. Considering the case that the basis vectors of the local Cartesian coordinate system for transverse isotropic materials are provided by consecutive rotations of the plane of isotropy about the global $y(x_2)$ -axis and

the $\bar{x}(\bar{x}_1)$ -axis of the once rotated system, the angle α has a constant value of 90° , whereas the angle β changes from 0° to -180° . Using the angles known from applications in structural geology to generate the constitutive rotation matrices, the dip ϕ has the constant value of 90° , and the azimuth varies from $90^\circ \dots 0^\circ$ ($0^\circ \leq \varphi \leq 90^\circ$) and $360^\circ \dots 270^\circ$ ($90^\circ \leq \varphi \leq 180^\circ$) respectively. For details of the threedimensional model (geometry, boundary conditions, material orientation) see Fig. 9.1.18.

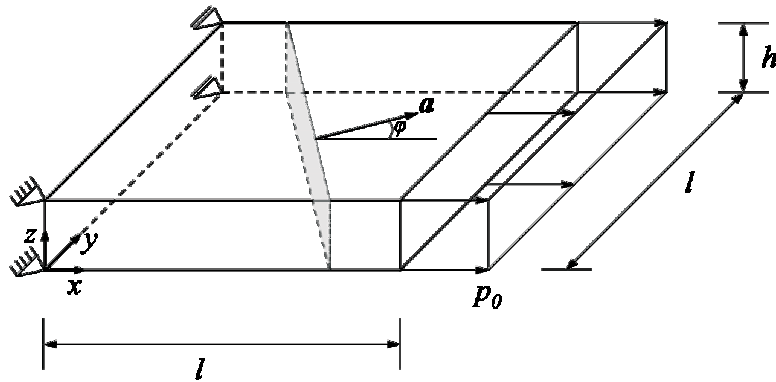


Figure 9.1.18: Tensile test. Threedimensional model definition according to Fiokla [120]. Vector a defines the direction of anisotropy.

Initial conditions do not have to be given for the problem under consideration. The left-hand edge is fixed in horizontal direction. To avoid rigid body motions, the left lower corner node is fixed in both vertical and horizontal directions. A distributed tension load of $p_0 = 0.2$ MPa is applied at the right-hand edge. In the threedimensional case, the plane strain condition was realized preventing any displacement in z -direction on the upper and lower boundary surfaces of the sample.

The material parameters are summarized in Tab. 9.6.

Table 9.6: Material parameters

Symbol	Parameter	Value	Unit
E_i	Young's modulus	561.12	MPa
E_a	Young's modulus	1311.83	MPa
ν_i	Poisson's ratio	0.6032	–
ν_{ia}	Poisson's ratio	0.1838	–
G_a	Shear modulus	375.00	MPa

Results

The numerical results obtained with *OpenGeoSys* are compared to values given in [119]. They include displacement coefficients of various corner nodes of the plate depending on the anisotropy direction, and show a good agreement (cf. Fig. 9.1.19).

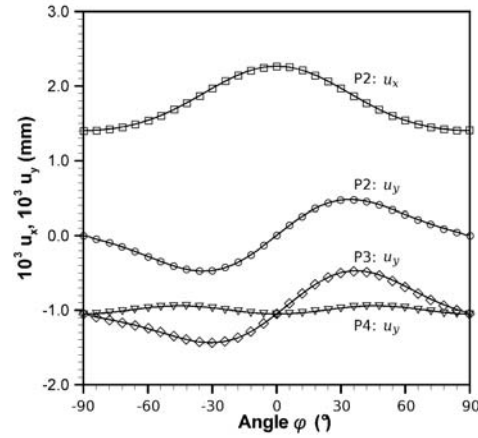


Figure 9.1.19: Tensile test. *OpenGeoSys* results (symbols) at length $l = 10$ mm and an edge load of $p_0 = 0.2$ MPa compared to the reference solution given by Schröder [118] and Kohlmeier [119] (continuous lines).

9.2 Elastoplasticity

As discussed in Sec. 2.5.4, plasticity is a property of solid materials, which is characterized by non-reversible deformations and plastic yielding of the material. The last mentioned material property can be mathematically described introducing so-called yield conditions $\Phi_{\text{pl}}(\boldsymbol{\sigma})$. Fig. 9.2.20 illustrates geometrically three typical yield conditions defined in the principal stress space. If the stress path of any material point is located inside of one of these surfaces, the point undergoes elastic deformation, if it is located on the boundary of the specific yield surface, plastic yielding is observed. The yield status of a material point is determined checking the Kuhn-Tucker conditions for loading or unloading:

$$\dot{\Phi}_{\text{pl}} \leq 0, \quad \lambda_{\text{pl}} \Phi_{\text{pl}} = 0 \quad \text{or} \quad \lambda_{\text{pl}} \geq 0 \quad (9.13)$$

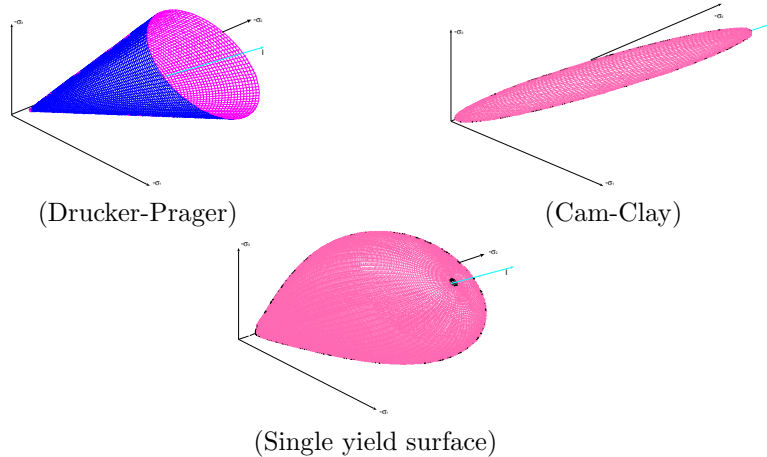


Figure 9.2.20: Yield surface

In metal plasticity, usually so-called associative plasticity models are used, which are characterized by coaxiality of the plastic strain increment and the normal vector established in the current stress point of the yield condition. Usually, the mechanical behavior of geomaterials (in particular soils, and clay-rich materials) is of more complex nature compared to metals, and depends on porosity, stress state and direction of external loading. Frequently, shear deformation (shear bands) associated with strain localization, dilation and/or a coupling of these properties can be observed. Localization problems are of unstable nature, i. e., softening may occur at a certain point of loading. As these phenomena cannot be modeled using classical plasticity approaches, usually so-called non-associated plasticity models are introduced. They are characterized by the definition of a plastic potential $\hat{\Phi}_{\text{pl}}(\boldsymbol{\sigma})$ instead of the yield condition. Within this context, the

increment of the plastic strain tensor will still be defined using Eq. (2.113), but substituting the yield condition with the plastic potential. Two typical plastic models suited to address strain localization phenomena are described below.

Drucker-Prager model

This model is a function of two stress invariants and a hardening parameter κ with the following yield condition and plastic potential:

$$\Phi_{\text{pl}}(\boldsymbol{\sigma}, \kappa) = \sqrt{\frac{2}{3}\boldsymbol{\sigma}_d \cdot \boldsymbol{\sigma}_d} + \alpha \text{tr}(\boldsymbol{\sigma}) - y(\kappa) = 0 \quad (9.14)$$

$$\hat{\Phi}_{\text{pl}}(\boldsymbol{\sigma}, \kappa) = \sqrt{\frac{2}{3}\boldsymbol{\sigma}_d \cdot \boldsymbol{\sigma}_d} + \beta \text{tr}(\boldsymbol{\sigma}) - y(\kappa) = 0 \quad (9.15)$$

where α is a coefficient related to the internal frictional angle, $y(\kappa)$ is the yield stress depending on the hardening parameter.

Cam-Clay model

Similar to the Drucker-Prager model, the Cam-Clay model is a function of both of the first and the second stress invariants. The generalized Cam-Clay model is defined as:

$$\Phi_{\text{pl}}(\boldsymbol{\sigma}, \kappa) = \frac{2}{3}\boldsymbol{\sigma}_d \cdot \boldsymbol{\sigma}_d + M^2 p_s (p_s - p_{scn}) = 0 \quad (9.16)$$

with $p_s = \text{tr}(\boldsymbol{\sigma})/3$, where M is the slope of the critical state line and p_{scn} is the isotropic preconsolidation pressure. The rate of p_s is given by

$$\frac{dp_s}{d\varepsilon_{\text{pl}}^v} = \frac{(1+e)p_s}{\lambda_c - \kappa_c} \quad (9.17)$$

where e is the void ratio, $\varepsilon_{\text{pl}}^v$ defines the volumetric plastic strain, λ_c is the virgin compression index and κ_c is the swelling/recompression index.

The model also describes the nonlinear elastic behavior of clay-like media before plastic yielding occurs, in which the bulk modulus K is dependent of stress status as

$$K = \frac{1+e}{\kappa_c} p_s = 0 \quad (9.18)$$

9.2.1 Compression of a plate with a hole

Definition

Compression and/or tension of a plate with a hole is a typical plane strain benchmark for the modeling of elastoplastic material behavior, and is defined in [121]. Here, this example is analyzed to compare the behavior of two approaches on pure plastic deformation problems.

Solution

In the present simulation, a quarter of the perforated plate is considered because of the symmetry of the problem. The model set-up is shown in Fig. 9.2.21. The radius of the hole is 10 mm. Two points (point 1 and point 2) are specified to monitor the evolution of variables. Point 1 is located at one third of the distance from point 3 to point 4.

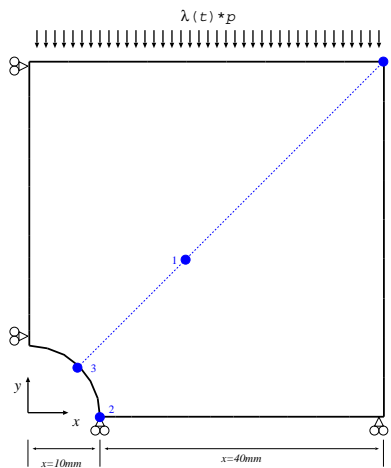


Figure 9.2.21: One quarter of the compressed steel plate with a hole

Traction boundary conditions, $p = 100 \cdot \lambda(t)$ MPa are prescribed on the top, where $\lambda(t)$ denotes a time-dependent scaling factor. The particular case of cycling loading is analyzed defining a scaling factor as shown in Fig. 9.2.22 assuming $\lambda_{\max} = 4.1$.

The finite element grid using triangular elements is shown in Fig. 9.2.23, and the material parameters obtained from [121] are presented in Table 9.7.

Results

The load is applied within 60 time steps with a constant increment for the loading factor $\Delta\lambda = \lambda_{\max}/10$. As shown in Fig. 9.2.24, plastic strain and

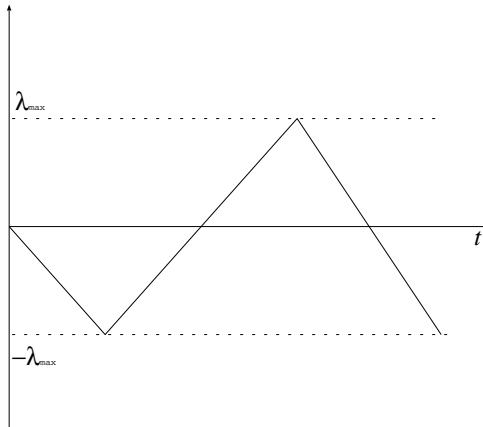


Figure 9.2.22: Time dependent scaling factor for external loading

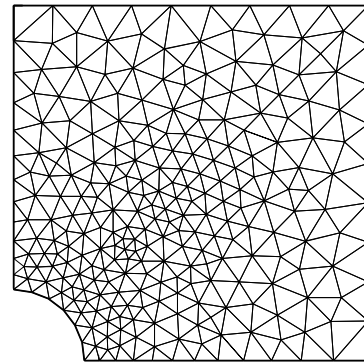


Figure 9.2.23: Finite element grid: 269 nodes and 484 elements

Table 9.7: Material parameters

Symbol	Parameter	Value	Unit
E	Young's modulus	206.9	GPa
ν	Poisson's ratio	0.29	—
σ_0	Initial yield stress	0.45	GPa

vertical strain show similar distributions, which are typical for elastoplastic material behavior according to the von Mises model. The evolution of the horizontal displacement at point 1 and at point 2 as functions of the periodic scaling factor $\lambda(t)$ are shown on Fig. 9.2.25.

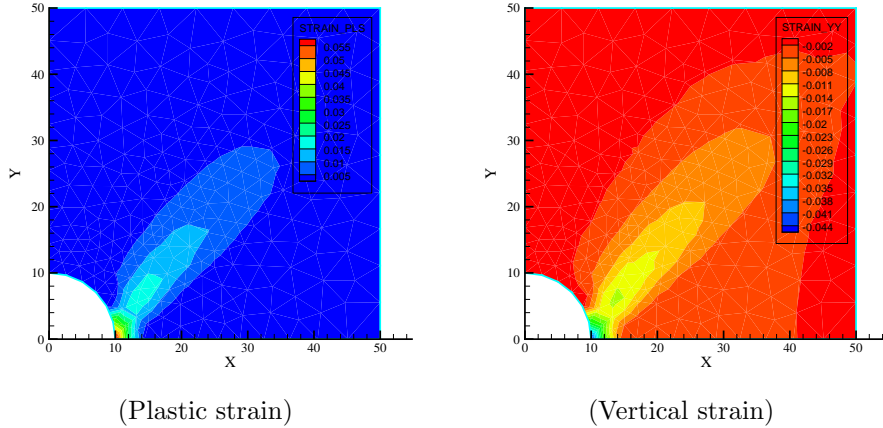


Figure 9.2.24: Distribution of plastic strain and vertical strain at $\lambda_{\max}/10$

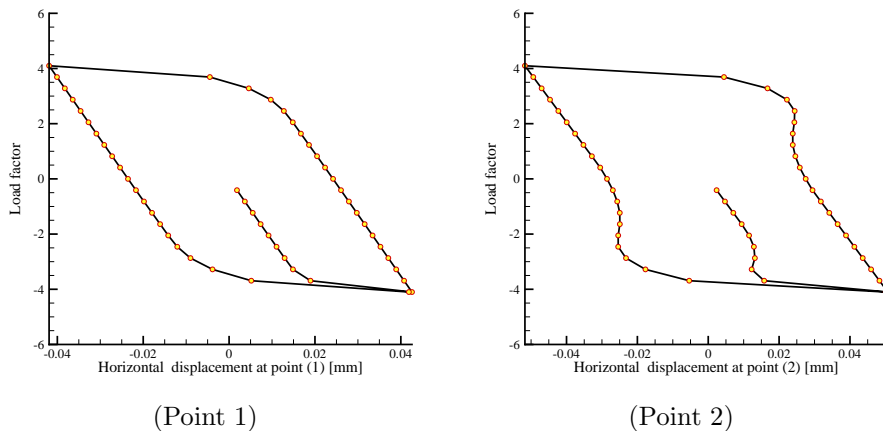


Figure 9.2.25: Evolution of horizontal displacement vs. scaling factor

9.2.2 Twodimensional strain localization problem

Definition

In this benchmark, a plane strain failure problem is analyzed with triangular and quadrilateral elements, correspondingly. An enhanced strain approximation is used to simulate the displacement discontinuity after failure appears. Neighbor relationships of an element object are essential data for designing the deforming

mesh and to determinate the evolution of the discontinuity orientation within the context of failure analysis.

From the viewpoint of the bifurcation theory, strain localization is a bifurcation phenomenon, which takes place when the velocity field moves away from the branch of continuous solutions and follows a new path of discontinuous solutions. If standard finite elements are applied to this problem, the mesh has to be refined adaptively near the localization area. Additionally, the system of equations will be an ill-posed one. The strong discontinuity approach with enhanced strain elements avoids an ill-posed system of equations, thus avoiding mesh sensitivity of the analysis [122].

Solution

The set-up of the twodimensional compression problem as proposed by [123] is shown in Fig. 9.2.26. The geometry of the specimen is simplified as rectangular with the dimensions of $1\text{ m} \times 3\text{ m}$.

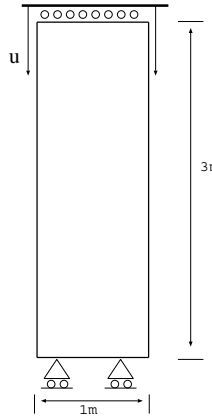


Figure 9.2.26: Plane strain twodimensional localization test

The bottom of the specimen is supported by horizontal roles, and its top surface is allowed to move only vertically with the axial displacement u_z . Both lateral surfaces are considered to be free of tractions.

The non-associative flow rule is adopted for the Drucker-Prager model with material parameters presented in Table (9.8).

Results

Fig. 9.2.27 shows the deformed model exhibiting localization. The stress response at the top surface to the prescribed displacements is discussed in Fig. 9.2.28. These results agree well with data presented in [123].

Table 9.8: Material parameters

Symbol	Parameter	Value	Unit
E	Young's modulus	20.0	MPa
ν	Poisson's ratio	0.4	—
α	Factor in (9.15)	0.233345	—
β	Factor in (9.15)	0.141421	—
σ_0	Initial yield stress	29.69	kPa
H	Hardening modulus	100	kPa
H_δ	Localized softening modulus	-1000	kPa

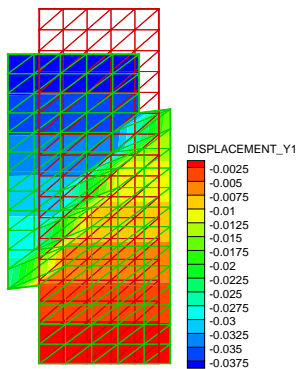


Figure 9.2.27: Deformed contour with distribution of the axial displacements

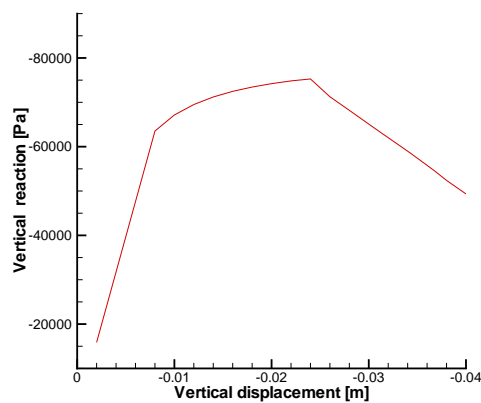


Figure 9.2.28: Axial stress at the top as function of the axial displacement

9.2.3 Cam-Clay plasticity

Definition

This axisymmetric benchmark is usually discussed to verify a critical state plastic mode, e.g., the Cam-Clay model.

Solution

For the finite element solution, a quarter of a cylindrical specimen is considered with a diameter of 5 cm and a length of 10 cm. The bottom surface is roller supported, and a vertical (axial) displacement is prescribed at the top surface until the specimen is compressed at 50 % of the initial length. Displacements of the top surface in radial direction are allowed. The lateral surface of the cylinder is free of tractions. The material parameters are summarized in Table 9.9.

Table 9.9: Material parameters

Symbol	Parameter	Value	Unit
ν	Poisson's ratio	0.30	–
M	Slope of critical state line	1.20	–
λ_c	Virgin compression index	0.20	–
κ_c	Swelling / recompression index	0.02	–
p_{scn0}	Initial preconsolidation pressure	60.00	–
e_0	Initial void ratio	1.50	–

Results

The relationship between von Mises type stress, the second stress invariant, and the axial strain is illustrated in Fig. 9.2.29. The results agree well with data presented in [124].

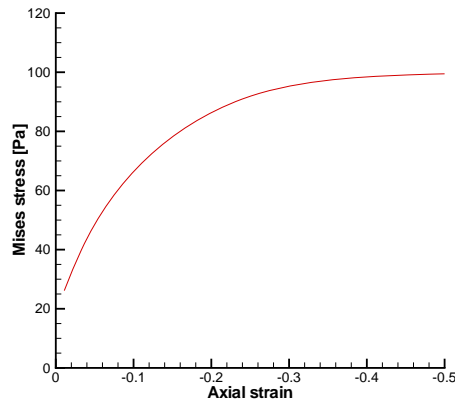


Figure 9.2.29: Axial strain vs. von Mises type stress

9.3 Viscoplastic creep

Creep is a typical effect of viscoplastic material behavior, and represents a time- and/or temperature-dependent deformation process of solid continua affected by constant load. As discussed in Sec. 2.5.6, similar to plastic potential, a creep potential Φ_c is introduced in order to describe the creep behavior.

Usually, a stationary creep model is sufficient to describe the creep phenomena in geological media such as soil and rock. The application of Norton's model Eq. (2.126) associated with an explicit Euler scheme for time discretization of the differential equation Eq. (2.124) results in the following incremental form of the calculation of the creep strain tensor:

$$\Delta \boldsymbol{\varepsilon}_c = \alpha \left(\frac{3}{2} \right)^{\frac{n+1}{2}} \left(\sqrt{\frac{3}{2} \boldsymbol{\sigma}_d \cdot \cdot \boldsymbol{\sigma}_d} \right)^{n-1} \Delta t \boldsymbol{\sigma}_d \quad (9.19)$$

with the time step size Δt .

Viscoplastic creep is mainly caused by diffusion and dislocations at the microscale, and results in hardening as well as recovery aspects. Hou and Lux propose an evolutional equation for the (viscoplastic) creep strain rate considering stationary as well as transient creep, damage impact, hardening and recovery (cf. [125, 126, 127]). Neglecting damage effects, this approach is known as Lubby2 model.

$$\dot{\boldsymbol{\varepsilon}}_c = \frac{3}{2} \left[\frac{1}{\eta_k} \left(1 - \frac{\varepsilon_{tr}}{\max \varepsilon_{tr}} \right) + \frac{1}{\eta_m} \right] \boldsymbol{\sigma}_d \quad (9.20)$$

Here ε^{tr} denotes the equivalent transient creep strain

$$\varepsilon_{tr} = \sqrt{\frac{2}{3} \boldsymbol{\varepsilon}_{tr} \cdot \cdot \boldsymbol{\varepsilon}_{tr}} \quad (9.21)$$

with $\boldsymbol{\varepsilon}_{tr} = \boldsymbol{\varepsilon}_c - \boldsymbol{\varepsilon}_{st}$ ($\boldsymbol{\varepsilon}^{st}$ – stationary creep fraction). In addition to the equivalent transient creep strain the generalized representation of the von Mises equivalent deviatoric stress s_v is defined.

$$s_v = \sqrt{\frac{3}{2} \boldsymbol{\sigma}_d \cdot \cdot \boldsymbol{\sigma}_d} \quad (9.22)$$

Furthermore, the following material functions are suggested, considering only hardening, and neglecting recovery effects:

$$\max \varepsilon^{tr} = \frac{s_v}{G_k} \quad (9.23)$$

$$G_k = \bar{G}_k^* \exp(k_1 s_v) \quad (\text{Kelvin shear modulus}) \quad (9.24)$$

$$\eta_k = \bar{\eta}_k^* \exp(k_2 s_v) \quad (\text{Kelvin viscosity modulus}) \quad (9.25)$$

$$\eta_m = \bar{\eta}_m^* \exp(m s_v) \exp(lT) \quad (\text{Maxwell viscosity modulus}) \quad (9.26)$$

As T denotes the absolute temperature, the following material parameters are necessary to model various constitutive effects:

- \bar{G}_k^* , k_1 hardening,
- $\bar{\eta}_k^*$, k_2 transient creep, and
- $\bar{\eta}_m^*$, m , l stationary creep.

9.3.1 Creep of a thick-walled cylinder

Definition

In this example, creep behavior of a thick-walled cylinder is discussed, which is subjected to a constant inner normal pressure.

Solution

The inner and the outer radius of the cylinder are 4 mm and 6.4 mm respectively, at a height of 1 mm. Quadrilateral elements are used for the spatial discretization of the axisymmetric finite element model (cf. Fig. 9.3.30). The boundary conditions are as follows: normal pressure $p = 2.515 \text{ MPa}$ at the inner surface and zero normal stress at the outer surface. Furthermore, displacements in axial direction are suppressed at the top and the bottom surfaces.

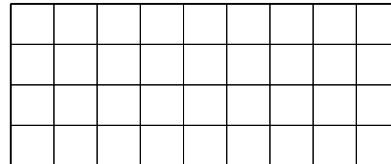


Figure 9.3.30: Finite element grid of the thick-walled cylinder

A homogeneous initial stress distribution is assumed in the domain, applying the following values for the coefficients of the stress tensor in cylindrical coordinates: $\sigma_{rr}^0 = \sigma_{\theta\theta}^0 = \sigma_{zz}^0 = -50 \text{ Pa}$. The parameters of Norton's creep model are given in Table 9.10.

Table 9.10: Material parameters of Norton's creep model

Symbol	Parameter	Value	Unit
E	Young's modulus	137.8	GPa
ν	Poisson's ratio	0.48	—
α	Norton model factor	6.415×10^{-10}	—
n	Norton Model exponent	4	—

The numerical results can be compared with Balley's analytical solution for the rate of radial displacements

$$\dot{u}_r = \alpha \frac{3^{\frac{n+1}{2}}}{2n^n} \frac{r_a^2 r_b^2 p^n}{(r_b^{2/n} - r_a^{2/n})r}$$

and for the equilibrated state of the first stress invariant

$$\sigma_v = \frac{2\sqrt{3}}{2n} \frac{p (r_b/r)^{\frac{2}{n}}}{(r_b/r_a)^{2/n} - 1}$$

Results

Figs. 9.3.31 and 9.3.32 show the distribution of the first stress invariant σ_v and of radial displacements along the cross section of the sample wall compared to the pure elastic solution. This demonstrates that σ_v decreases at about 26 % at the inner surface of the thick-walled cylinder until the asymptotic creep state is reached. In contrast, the radial displacements increase at about 200 %.

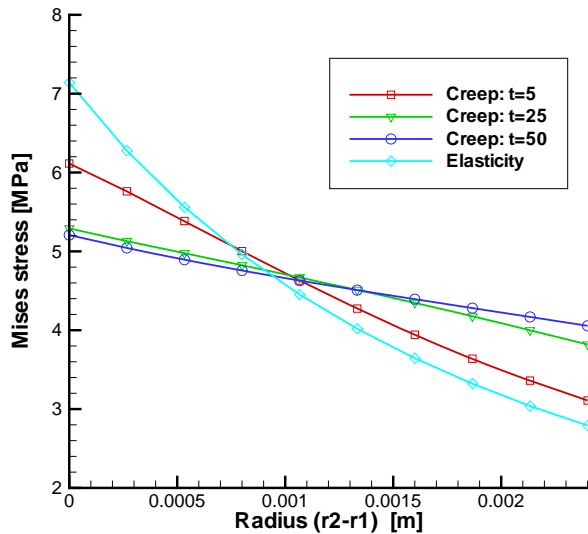


Figure 9.3.31: Profiles of the first stress invariant during creep at different times, $t = 5, 25, 50$ sec compared to the elastic solution

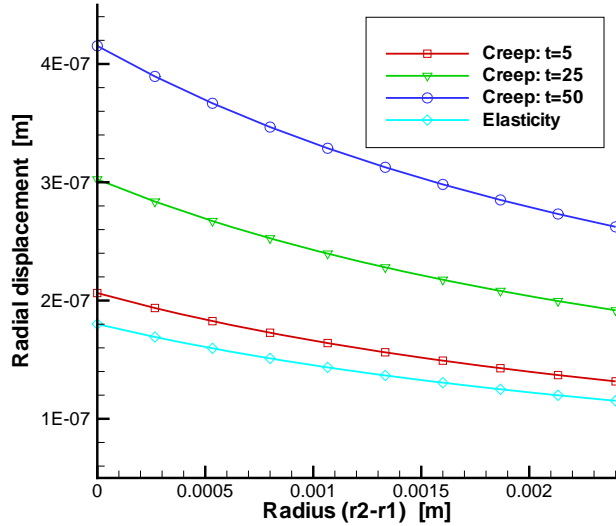


Figure 9.3.32: Profiles of radial displacements during creep at different times, $t = 5, 25, 50$ sec compared to the elastic solution

9.3.2 Thermally driven creep in rock salt

Definition

Several models exists for the evaluation of the effect of stationary creep in rock salt. One of those models is the so-called BGra-model Eq. (9.27), which is valid for an external load between 5 Mpa and 25 Mpa within a temperature range of 22-200° C ([128]).

$$\dot{\varepsilon}_c = A e^{-\frac{Q}{RT}} \left(\frac{\sigma}{\sigma^*} \right)^n \quad (9.27)$$

In a cylindrical sample of rock salt stress relaxation is caused by a temperature decrease of 30 K. The aim of the example is to calculate the resulting strain variation with time within the solid body using the stationary creep model BGra (9.27). The results of the simulation defining an axisymmetric model are compared to a threedimensional solution.

Solution

For the numerical simulation a cylindrical core sample as shown in Fig. 9.3.33 is selected.

Fig. 9.3.34 shows the axisymmetric finite element model (mesh, boundary conditions etc.) arranged in the x - z -plane. The dimensions of this model are: radius

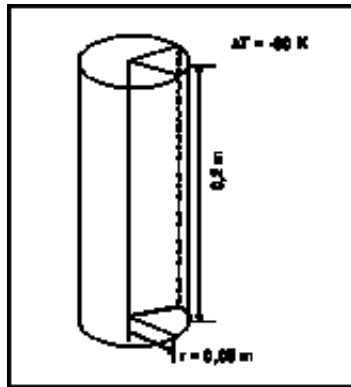


Figure 9.3.33: Core sample model

(x -direction) 0.05 m and height 0.2 m. A relatively coarse mesh consisting of 228 triangular elements and 139 nodes is used.

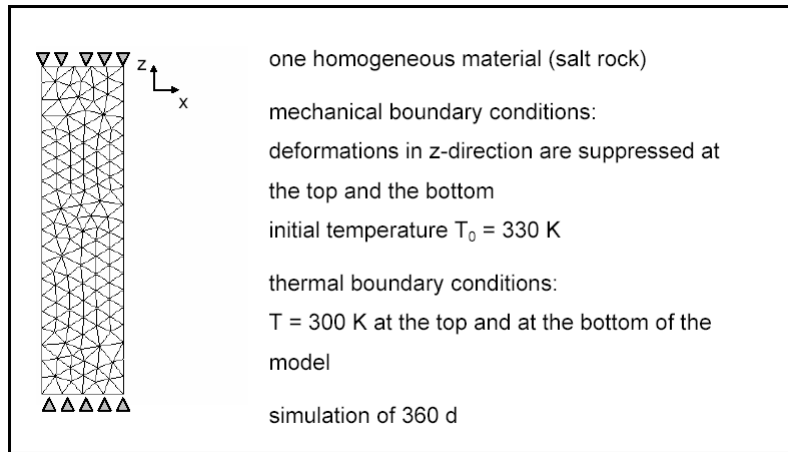


Figure 9.3.34: Details of the axisymmetric finite element model

Vertical deformation at the top and the bottom surfaces are suppressed. The initial temperature in the whole area is 330 K. At the top and the bottom of the model thermal boundary conditions are prescribed defining a temperature of 300 K. Based on these conditions, the stress relaxation during the cooling down is simulated.

The material parameters referred to the creep model Eq. (9.27) are presented in Table 9.11.

In Table 9.12, material and process parameters of the thermo-elastic part of the constitutive model are given.

Table 9.11: Material parameters of the creep model

Symbol	Parameter	Value	Unit
A	Factor of the creep model	0.18	d^{-1}
Q	Activation energy	54	$\text{kJ}\cdot\text{mol}^{-1}$
R	Gas constant	8.31447	$\text{J}\cdot\text{K}^{-1}\cdot\text{mol}^{-1}$
n	Material constant	5	—
σ^*	Reference effective stress	1	MPa

Table 9.12: Material parameters and heat process conditions of the thermo-mechanical creep model

Symbol	Parameter	Value	Unit
E	Young's modulus	25	GPa
ν	Poisson's ratio	0.27	—
α	Thermal expansion coefficient	4.0×10^{-5}	K^{-1}
c	Thermal capacity	1	$\text{J}\cdot\text{kg}^{-1}\cdot\text{K}^{-1}$
λ	Thermal conductivity	100	$\text{W}\cdot\text{m}^{-1}\cdot\text{K}^{-1}$
T_0	Initial temperature	330	K
T	Temperature after cooling down	300	K

The numerical simulation of the stress relaxation process over a time of 360 days is performed within 360 time steps of constant time step length.

In order to evaluate the numerical results of the relaxation problem, the following analytical solution of Eq. (9.27) for the problem under consideration has been proposed (Eickemeier 2007, personal communication) in respect of the stress increment for the current time step:

$$\Delta\sigma_{i+1} = \frac{(\dot{\varepsilon}_0^c - A(\sigma/\sigma^*)^n)E_q\Delta t}{1 - E_q/\sigma^*A^*\Delta t\xi n(\sigma/\sigma^*)^{n-1}} \quad (9.28)$$

with

$$A^* = Ae^{-Q/RT} \quad (9.29)$$

Here, the initial creep strain rate $\dot{\varepsilon}_0^c$ is assumed to be zero, E_q is the weighted Young's modulus of the steel plates, which are used to apply the external load and to support the sample, and the rock salt sample (in this case, only rock salt is considered), and the parameter ξ is defined as $\xi = 0.5$.

Results

For the analytical solution of Eq. (9.28) the axial stress of the previous time step is used. Time step increment is $\Delta t = 1 \text{ d}$. In the threedimensional case, the

results are shown for node 705, which is located at point ($x, y, z = 0.05, 0, 0.12$). This node is identical to node 76 of the axisymmetric model (cf. Fig. 9.3.35).

The comparison of the increment of axial stresses $\Delta\sigma_{i+1}$ analytically obtained using Eq. (9.28) shows identical results to the numerical values at node 705 of the threedimensional model and node 76 of the axisymmetric model. Both stress increments $\Delta\sigma_{i+1}$ obtained by OpenGeoSys and the scientific special purpose finite element code ANSALT (cf. [129]) are equal to 3.05×10^{-3} MPa. The results of axisymmetric as well as threedimensional numerical simulations are shown in Fig. 9.3.35, and show an excellent agreement.

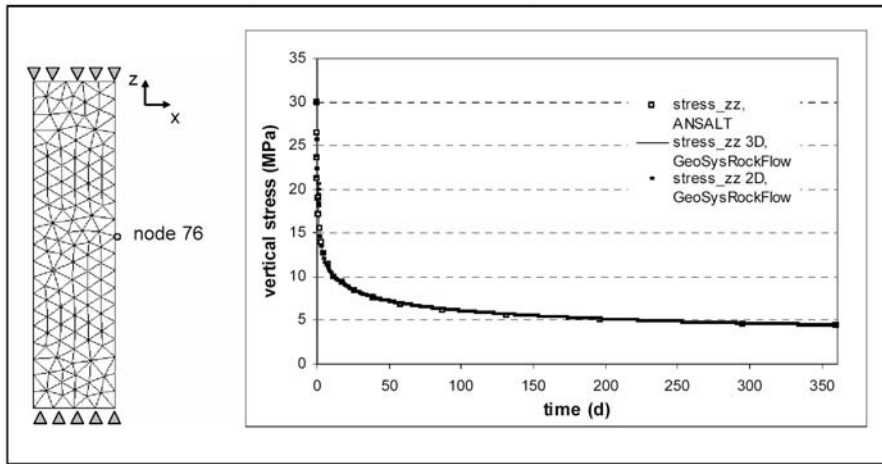


Figure 9.3.35: Comparison of numerical results (OpenGeoSys vs. ANSALT) for axial stresses

9.3.3 Stationary creep in rock salt

Definition

With respect to the benchmark discussed in the previous section Sec. 9.3.2, the creep process is now assumed to be caused by a constant external load at the bottom of the solid and a constant high temperature at the same time. The aim of this example is to calculate the resulting strain variation with time using the stationary creep model BGra (9.27).

Solution

For the simulation with OpenGeoSys almost the same finite element models (i.e., axisymmetric and threedimensional case) as for the previous benchmark in Sec. 9.3.2 are selected. The only difference is in the height of the model,

which is now 0.25 m. The initial temperature in the whole domain is 373.15 K. A constant load of 5 MPa is applied at the bottom surface of the model. The numerical simulation of the creep process over a time of 100 days is performed within 100 time steps of constant time step length.

In order to compare numerical solutions with an analytical one, Eq. (9.27) is transformed into the following expression:

$$A = \frac{\Delta \varepsilon_{\text{eff}}}{e^{-Q/RT} \sigma_{\text{eff}}} \quad (9.30)$$

with

$$\begin{aligned} \sigma_{\text{eff}} &= \frac{1}{\sqrt{2}} \sqrt{(\sigma_1 - \sigma_2)^2 + (\sigma_2 - \sigma_3)^2 + (\sigma_3 - \sigma_1)^2} \\ \Delta \varepsilon_{\text{eff}} &= \frac{\varepsilon_{\text{eff}}(t + \Delta t) - \varepsilon_{\text{eff}}(t)}{\Delta t} \\ \varepsilon_{\text{eff}} &= \frac{\sqrt{2}}{3} \sqrt{(\varepsilon_1 - \varepsilon_2)^2 + (\varepsilon_2 - \varepsilon_3)^2 + (\varepsilon_3 - \varepsilon_1)^2} \end{aligned} \quad (9.31)$$

For the considered calculation steps, the stresses of the corresponding time period are assumed to be constant. Eq. (9.30) is solved for node 25 (see Fig. 9.3.36) of the axisymmetric finite element model.

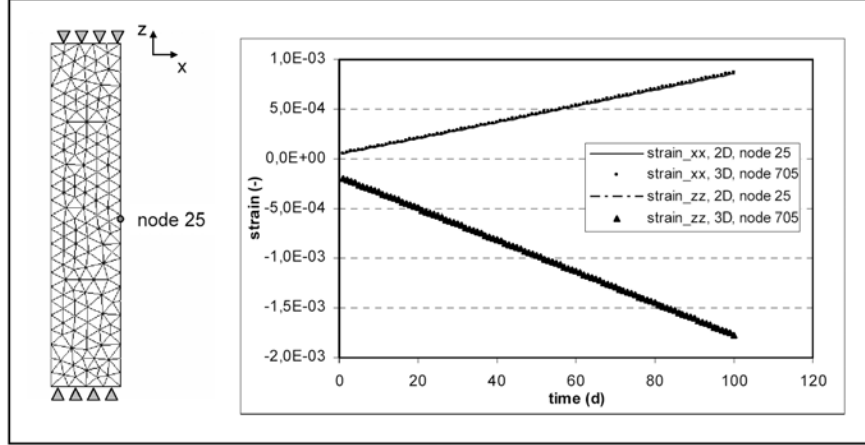


Figure 9.3.36: Comparison of numerical strain results (x - and z -directions) for the axisymmetric and the threedimensional models

Results

The effective stress value σ_{eff} at node 25 for the given time period is 5.03 MPa, which was calculated using Eq. (9.32). The strain at the end of the first

time step is $\varepsilon_{\text{eff}}(t_1) = 1.72 \times 10^{-3}$, and at the end of the second time step: $\varepsilon_{\text{eff}}(t_2) = 1.73 \times 10^{-3}$, which, again, is calculated using Eq. (9.32). Considering Eq. (9.30) the analytically obtained value of the parameter A is equal to 0.19, which corresponds approximately to the input value of A of 0.18 defined in the previous example. The results of the comparison between the axisymmetric model and the threedimensional model are shown in Figs. 9.3.36 and 9.3.37. These results are identical.

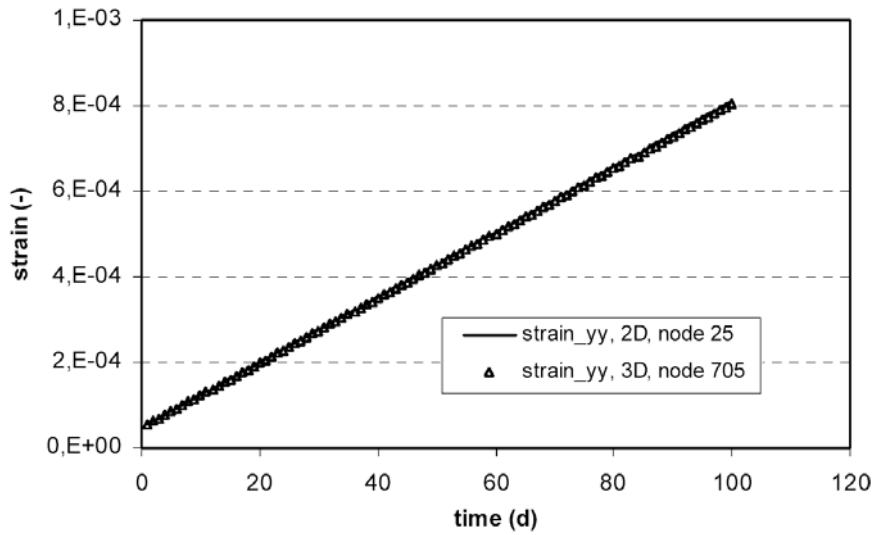


Figure 9.3.37: Comparison of numerical strain results (y -direction) for the axisymmetric and the threedimensional models

9.3.4 Transient creep in rock salt

Definition

Triaxial long-term compression under axisymmetric conditions is carried out to verify the Lubby2 creep model Eq. (9.20), and to study transient as well as stationary creep behavior assuming isothermal conditions and neglecting damage processes.

Solution

As described in Sec. 9.1.6, for the calculation, the cross-section of a cylindrical sample with a radius of 30 mm and a height of 120 mm is studied. The loading in principal axes includes a radial pressure as well as an axial pressure, and is realized in two steps. It is resulting in a homogeneous stress-strain state. Details of the model (geometry, mesh, boundary conditions) according to K.-H. Lux and F. Werunsky (unpublished report, 2008) are presented in Fig. 9.3.38.

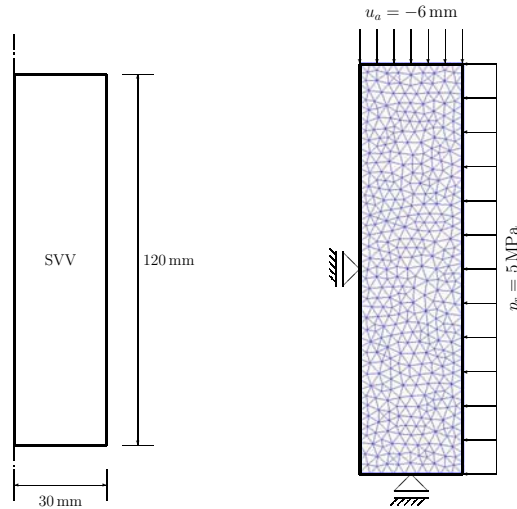


Figure 9.3.38: Triaxial compression of a cylindrical sample. Axisymmetric model. Left: Geometry. Right: Finite element grid and boundary conditions.

Initial conditions do not have to be given for the problem under consideration. As the bottom edge is fixed in vertical direction, the left-hand edge is fixed in horizontal direction for symmetry reasons (axis of rotation). On the right-hand edge initially a radial casing pressure of 5 MPa is applied within 60 seconds with a constant stress rate. While keeping constant this radial pressure, a subsequent

stress-driven axial compressive loading is applied within the following 1440 seconds with a constant stress rate. The maximum axial pressure is 18 MPa. In the following, both the radial and the axial pressures are kept constant for 20 days (for the loading history cf. Fig. 9.3.39).

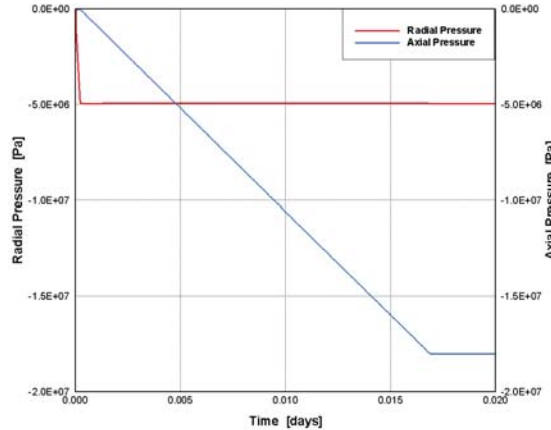


Figure 9.3.39: Triaxial compression of a cylindrical sample. Loading history for long-term creep experiments. Radial casing pressure (stress rate $\dot{p}_r = 0.083 \text{ MPa}\cdot\text{s}^{-1}$) with subsequent axial pressure (stress rate $\dot{p}_a = 0.0125 \text{ MPa}\cdot\text{s}^{-1}$). Each pressure loading with subsequent constant values over 20 days.

The modified Lubby1 model was considered to generate the fourth-order elastic material matrix for the creep model under consideration. Within this context, the material parameters referring to the modified Lubby1 relation (9.4) are given in Tab. 9.13. The material parameters for the creep fraction (Lubby2 (9.20)) are given in Tab. 9.14. Within this context, the initial Young's modulus, the Poisson's ratio and all the creep parameters are close to values known for rock salt according to K.-H. Lux, M. Rutenberg and F. Werunsky (unpublished report, 2008).

Table 9.13: Material parameters for the elastic fraction of the material model (cf. Sec. 9.1.6)

Symbol	Parameter	Value	Unit
E_0	Initial Young's modulus	21.4	GPa
ν	Poisson's ratio	0.335	—
a	Factor in (9.4)	27500	—
n	Exponent in (9.4)	1.0	—

Table 9.14: Material parameters for the creep fraction of the material model

Symbol	Parameter	Value	Unit
$\bar{\eta}_m^*$	Maxwell viscosity in (9.26)	1.09×10^7	MPa·d
m	Factor in (9.26)	-0.219	MPa $^{-1}$
l	Factor in (9.26)	0.0	K $^{-1}$
$\bar{\eta}_k^*$	Kelvin viscosity in (9.25)	1.45×10^5	MPa·d
k_1	Factor in (9.24)	-0.146	MPa $^{-1}$
k_2	Factor in (9.25)	-0.121	MPa $^{-1}$
\bar{G}_k^*	Kelvin shear modulus in (9.24)	7.0×10^4	MPa

Results

The representation of the axial stress vs. the axial strain in Fig. 9.3.40 shows the complex creep behavior of the sample under consideration.

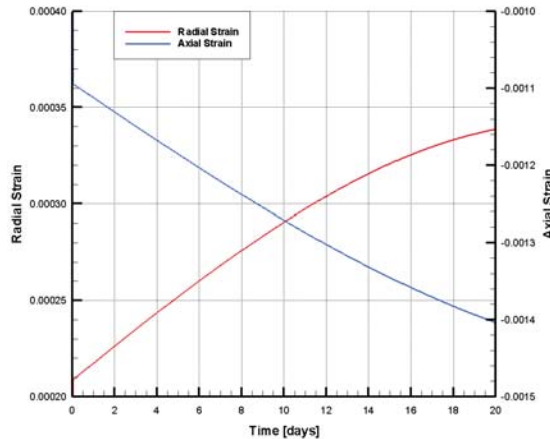


Figure 9.3.40: Triaxial compression of a cylindrical sample. Numerical simulation of the transient and stationary creep behavior using the Lubby2 model (9.20).

Chapter 10

Mass transport

by Sebastian Bauer, Christof Beyer, Chris McDermott, Georg Kosakowski, Stefanie Krug, Chan-Hee Park, Geraldine Pichot, Haibing Shao, Yuanyuan Sun, Joshua Taron

The mass transport in a homogeneous, saturated aquifer can be influenced by convection, diffusion, decay and biodegradation, sorption and chemical reactions. For a steady state 1-dimensional flow through a homogeneous isotropic medium with constant material parameters the following differential equation (10.1) is applied.

$$\frac{\partial C}{\partial t} + \frac{\rho_b}{R} \cdot \frac{\partial S}{\partial t} + \frac{q}{R} \cdot \frac{\partial C}{\partial x} = D_{xx} \cdot \frac{\partial^2 C}{\partial x^2} - \lambda \cdot C \quad (10.1)$$

with

- C – dissolved concentration ($\text{kg}\cdot\text{m}^{-3}$),
- S – sorbed concentration ($\text{kg}\cdot\text{kg}^{-1}$),
- t – time (s),
- ρ_b – bulk density ($\text{kg}\cdot\text{m}^{-3}$),
- R – retardation factor (-),
- q – flow rate ($\text{m}\cdot\text{s}^{-1}$),
- x – distance (m),
- D_{xx} – dispersion coefficient in x-direction ($\text{m}^2\cdot\text{s}^{-1}$),
- λ – decay rate (s^{-1}).

This equation is used to calculate the concentration distribution under consideration of decay and sorption with the linear Henry-isotherm. The retardation coefficient R for the Henry isotherm is related to the Henry sorption coefficient K_D in the following way.

$$R = 1 + \frac{\rho_b}{\Phi} K_D = 1 + \frac{1 - \Theta}{\Phi} \rho_s K_D \quad (10.2)$$

with

$$\begin{aligned}\Phi &= \text{porosity } (-), \\ \rho_s &= \text{density } (\text{kg} \cdot \text{m}^{-3}),\end{aligned}$$

with the initial and boundary conditions

$$C(x, t = 0) = C_I \quad \forall x$$

with C_I - concentration at time I .

$$C(x = 0, t) = C_0 \quad \forall t, \quad \frac{\partial C}{\partial x}(x \rightarrow \infty, t) = C_I \quad \forall t > 0$$

with C_0 - initial concentration.

The following analytical solution is significant:

$$\begin{aligned}C = C_1 &+ (C_0 - C_1) \cdot \frac{1}{2} \left[\exp \left(\frac{v \cdot x(1 - \gamma)}{2 \cdot D_{xx}} \right) \cdot \operatorname{erfc} \left(\frac{x - v \cdot \gamma \cdot t/R}{2 \cdot \sqrt{D_{xx} \cdot t/R}} \right) \right. \\ &\left. + \exp \left(\frac{v \cdot x(1 + \gamma)}{2 \cdot D_{xx}} \right) \cdot \operatorname{erfc} \left(\frac{x + v \cdot \gamma \cdot t/R}{2 \cdot \sqrt{D_{xx} \cdot t/R}} \right) \right] \quad (10.3)\end{aligned}$$

with v - velocity

$$\gamma = \sqrt{1 + 4 \cdot \lambda \cdot R \cdot D_{xx}/v^2}. \quad (10.4)$$

Equation (10.3) is the basis for the verification of the numerical simulation results for the 1-dimensional mass transport. All described equations and all analytical solutions of equation (10.3) are taken from [130].

10.1 Diffusion

Diffusion is a process that equates concentration differences of gaseous or dissolved matter or energy. The particles move from higher to lower concentrations by Brownian movement in dependence on the temperature. In an aquifer, diffusive transport appears when convective transport is not that relevant (small velocities).

The extent of diffusion is also dependent on the diffusing substance and the medium. In addition, diffusion in soils is influenced by other factors, e.g. tortuosity. The finer a soil the stronger are the interacting forces between the soil matrix and the diffusing molecules. The diffusion coefficient which has to be given in OGS is the so-called apparent diffusion coefficient.

$$D_a = \frac{D_e}{\Phi} \quad (10.5)$$

with D_e - effective diffusion coefficient.

10.1.1 Axisymmetric model

Definition

This diffusion model is built to reproduce a field study in clay. This in situ test consists of a borehole where a solution is circulated that contains tracer substances like HTO. These tracers diffuse into the adjacent clay. The aim of the investigation is to simulate the HTO distribution after 300 d, the final test time, and to compare the simulation results of OGS to those that are calculated by HYDRUS 1 D (Simunek et al. [?]) and PHAST (Parkhurst et al. [?]).

To build a proper model of the tracer test, a one-dimensional axisymmetric model with 3.8 cm of borehole radius and 21.2 cm horizontal distance in the clay soil is created. As initial condition a constant pressure of 0 was specified in the whole model and the concentration relation c/c_0 of 1 within the distance of the borehole radius and of 0 within the clay domain. The pressure boundary condition corresponds to the initial condition. The calculation model includes 310 elements and 311 nodes. Table 10.1 shows the used parameters for the clay and the apparent diffusion constant D_a of HTO. The calculation is performed for the test duration of 300 days with fitted time step lengths from 0.001 d to 1 d (Bahr, 2007 [?]). The porosity in the modelled borehole is assumed to be 1 in order to evoke the simulation of a tracer reservoir that supplies the tracer solution into the clay.

Symbol	Parameter	Value	Unit
ρ	Density	2.5	$t \cdot m^{-3}$
Φ	Porosity	0.15	–
K	Permeability	$1.0 \cdot 10^{-11}$	m^2
D_a	Diffusion coefficient	$3.6 \cdot 10^{-10}$	$m^2 \cdot s^{-1}$

Table 10.1: Model parameters

The aim of the presented calculation example is the evaluation of the numerical simulation results by comparing them with numerical results of two other simulation programmes. The comparison is made by the use of Hydrus 1 D, which is a one-dimensional transport model especially for the solute transport in soils. The second programme, PHAST, is linked to the chemical software PHREEQC. The simulation with both programmes was made under consideration of the same boundary conditions and parameters (Bahr, 2007 [?]).

Results

In Figure 10.1.1 you can find the concentration distributions over the width of 0.25 m after a simulation time of 300 days that were calculated by means of

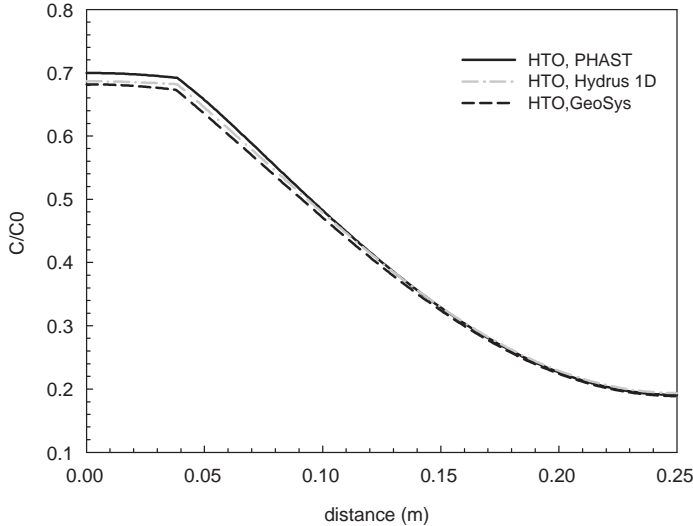


Figure 10.1.1: Concentration distributions after 300 d

OGS, PHAST and Hydrus 1D (Bahr, 2007 [?]). The numerical results accord well to each other. Thus, the comparison shows that the diffusion process can be well reproduced by the use of an axisymmetric numerical model.

10.1.2 Anisotropy

Definition

The aim of this example is to simulate the transport of a tracer by molecular diffusion in an anisotropic porous medium. The side length of the square numerical model is 1 m. At the left corner at the bottom of the model a constant concentration is diffusing into the calculation area. Diffusion is the only process for tracer transport, there are no pressure differences in the whole area. Because of the anisotropy of the soil material the tracer has to diffuse much faster in x-direction than in vertical direction. This has to be evaluated by comparing the concentration distributions in both directions.

As initial condition the pressure and tracer concentration were set to 0 in the whole area. At the left corner at the bottom of the model a concentration relation c/c_0 of 1 is specified along two polylines of the length of 0.3 m. The boundary conditions correspond to the initial conditions. The calculation model includes 736 triangular elements and 409 nodes. Table 10.2 shows the used parameters for the simulation. As the porous medium is assumed to be anisotropic,

which influences diffusion, the value for tortuosity is set equal to 1 in x-direction and 0.1 in y-direction.

Symbol	Parameter	Value	Unit
Φ	Porosity	0.4	–
K	Permeability	$1.0 \cdot 10^{-15}$	m^2
ρ	Density water	1000	kg/m^{-3}
η	Viscosity water	0.001	$\text{Pa} \cdot \text{s}$
α_T	Dispersion length	10.0	m
D_a	Diffusion coefficient	$6.0 \cdot 10^{-10}$	m^2/s

Table 10.2: Model parameters

The calculation is made for 30 time steps with a length of $1 \cdot 10^7$ seconds. The calculation model is sketched in Figure 10.1.2.

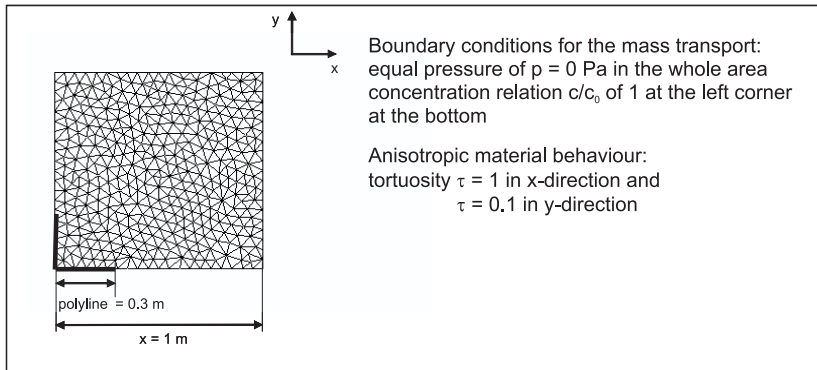


Figure 10.1.2: Benchmark definition

As the process of diffusion is dependent on the actual concentration in the porous medium and on the point in time, an analytical solution for the present calculation model is not possible. Therefore, the results of the numerical simulation are solely evaluated in a qualitative way by comparing the concentration distributions in horizontal and vertical direction.

Results

In Figure 10.1.3 you can find the concentration distributions over the model side length of 1 m in x- and y-direction, respectively, after a simulation time of $1 \cdot 10^8$ seconds. Assuming a small tortuosity of 0.1, the component is not yet transported over the whole transport length of 1 m in vertical direction, while in horizontal direction the concentration relation equals approximately 0.3 at

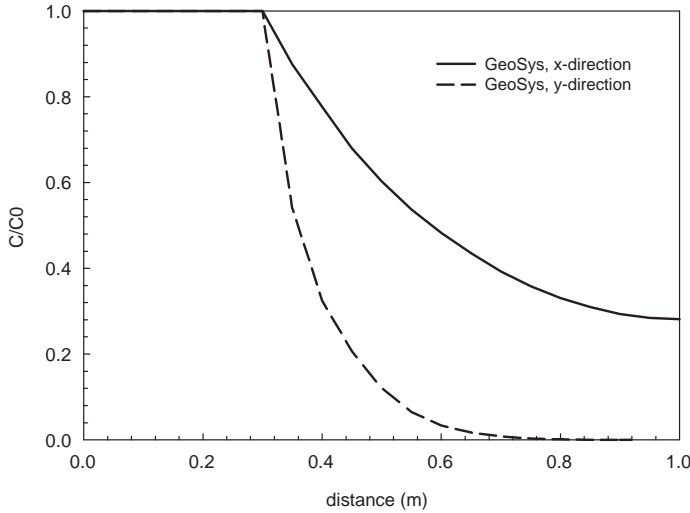
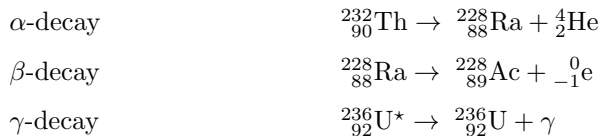


Figure 10.1.3: Concentration distributions in x- and y-direction

the opposite border of the model. The shown trend in the change of diffusion velocity by assuming different tortuosities in x- and y-direction in order to specify anisotropic material behaviour for molecular diffusion has a comprehensible characteristic.

10.2 Decay

Radioactive decay is the change in the composition of a core by emitting particles and/or electro-magnetic radiation. Different kinds of radioactive decay are i.e. decay as a result of emission of negatrons or positrons and decay under emission of γ -rays.



The above given examples show that the radioactive decay is an irreversible process. The following differential equation describes the decay as first order reaction (without chain development):

$$\frac{\partial C}{\partial t} = -\lambda \cdot C \quad (10.6)$$

with λ - decay rate (s^{-1}).

The integration of this equation causes an exponential decay term in the following form.

$$C(t) = C_0 \cdot e^{-\lambda \cdot t} \quad (10.7)$$

with C_0 - initial concentration ($kg \cdot m^{-3}$).

The decay values are commonly expressed as the so-called half life ($t_{1/2}$). This is the point of time when half of the substance is degraded. The relation between the half-life T and the decay rate results from:

$$e^{-\lambda \cdot t} = \frac{1}{2} \Rightarrow \lambda = \frac{\ln(2)}{T} \cong \frac{0.693}{T} \quad (10.8)$$

10.2.1 Definition

The aim of this example is to simulate the mass transport with the influence of decay, but without any sorption. At the left side of the considered aquifer there is a volume source of $0.1 \text{ m}^3/\text{d}$, at the right side there is a constant water pressure of 20 kPa. The tracer substance in the source volume is distributed by a stationary flow in the homogeneous aquifer. The mass distribution after 100 days has to be calculated. Figure 10.2.4 shows a sketch of the calculation area.

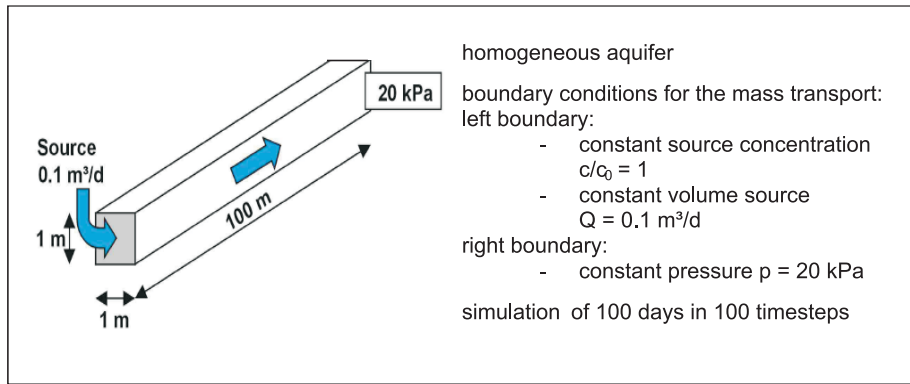


Figure 10.2.4: Calculation area: homogeneous aquifer

The following simplifications are assumed: (1) no sorption, exclusively decay of components (2) homogeneous aquifer, saturated, stationary flow. For the 1-dimensional calculation the calculation area is simplified as a line of a length of 100 m with 100 elements and 101 nodes. As boundary conditions the relative concentration amounts 1 and the source volume of the fluid phase with $0.1 \text{ m}^3/\text{d}$ is given at the left border of the calculation area and a constant pressure of 20 kPa at the right boundary. The used parameters of the soil are listed in Table 10.3. The calculation is divided into 100 time steps with a constant time step

Symbol	Parameter	Value	Unit
Φ	Porosity	0.2	–
K	Permeability	$1.0 \cdot 10^{-12}$	m^2
ρ	Density water	1000	kg/m^3
η	Viscosity water	0.001	$Pa \cdot s$
α_L	Dispersion length	5.0	m
λ	Decay in solved phase	$2.0 \cdot 10^{-7}$	s^{-2}

Table 10.3: Model parameters

length of 1 day. That means, the flow and transport processes in the aquifer within 100 days are simulated.

The concentration distribution at a special point in time and over a given distance is calculated by equation (10.3). Hereby the retardation coefficient is set equal to 1. The analytical solutions are depicted in Figure 10.2.5 as single symbols.

10.2.2 Results

In Figure 10.2.5 you can find the concentration distribution over the whole length of the 1 D model at the final simulation time of 100 days. Obviously, the numerical results meet well the analytical solutions.

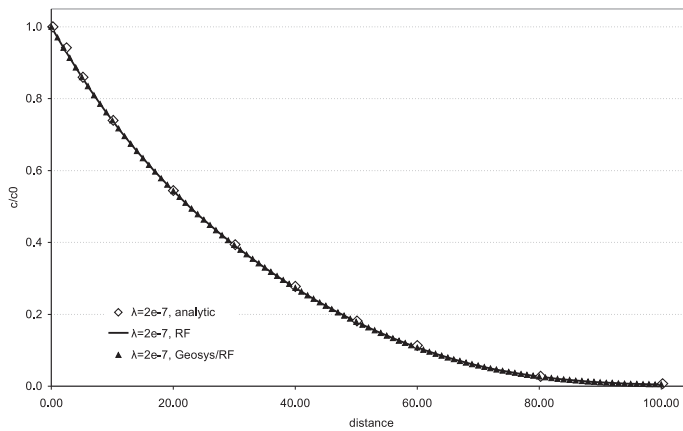


Figure 10.2.5: Concentration distribution after 100 d (decay)

10.3 Sorption

Exchange processes, like sorption, between the solid and the liquid phase in the multiphase system of an aquifer can be caused by physical (Van-der-Waals-forces) or chemical bonds. Sorption processes can be reversible (adsorption-desorption) if the chemical environment is changing. When the transport in a multiphase system is simulated, the mass exchange between the liquid and the solid phase has to be included. The equations that describe the sorption processes are called sorption isotherms. Sorption isotherms describe the relation between the substance that is adsorbed on the solid matrix and the one which is dissolved in the fluid phase. Those equations are only valid under isothermal conditions. The isotherms that are listed below, base on the assumption that the adsorbed substance and the dissolved one are in the state of equilibrium.

$$\text{Henry :} \quad S = K_D \cdot C \quad (10.9)$$

$$\text{Freundlich :} \quad S = K_1 \cdot C^{K_2} \quad (10.10)$$

$$\text{Langmuir :} \quad S = \frac{K_1 \cdot C}{1 + K_2 \cdot C} \quad (10.11)$$

with

K_D , K_1 , K_2 - distribution coefficients,

S - concentration of the adsorbed species (kg/kg),

C - concentration of the dissolved species (kg/m³).

The distribution coefficients are dependent on the substance and the specific soil properties like the pH. The linear Henry-isotherm is often used when there are low concentrations. Non-linear sorption processes are reproduced by the Freundlich or the Langmuir isotherm. Then the retardation is dependent on the solute concentration. In addition, the use of the Langmuir isotherm assumes a constant amount of sorption space at the solid surface. A maximum concentration for the adsorbed substance on the solid matrix is exclusively considered by the Langmuir isotherm [130]. This maximum concentration c_{\max} is included in the distribution coefficient K_1 ($K_1 = c_{\max} \cdot K_2$). The distribution coefficient K_2 of the Langmuir isotherm stands for the affinity between solid and sorbed solute. The distribution coefficients do not have comparable values: each sorption isotherm has to be considered separately with its specific constants.

10.3.1 Linear sorption (Henry isotherm)

The aim of this example is to simulate the solute transport in an aquifer by convection with the influence of retardation as a result of sorption. The solute

transport is influenced by linear sorption processes. That means, the Henry-isotherm is relevant to calculate the solute concentration. The calculation area and boundary conditions are the same as described for the precedent example.

The following simplifications are assumed: (1) exclusively linear sorption (Henry-isotherm), no decay of components (2) homogeneous aquifer, saturated, stationary flow (Fig. 10.2.4). The soil parameters are the same as listed in Table 10.3, but decay is not considered during these simulation runs. For the different simulation runs the Henry-sorption coefficients are varied as listed in Table 10.4 in order to evaluate the influence of sorption on the mass transport. The retardation coefficients R are calculated by solving equation (10.2).

K_D value [m^3/kg]	Retardation coefficient [-]
0	1
$6.8 \cdot 10^{-6}$	1.05
$6.8 \cdot 10^{-5}$	1.54
$6.8 \cdot 10^{-4}$	6.44

Table 10.4: Variation of K_D -values and retardation coefficients as input variables

Results

The concentration distribution at a special point in time and over a given distance is calculated by equation (10.3). Hereby the decay term γ is set equal to 1. The analytical solutions are depicted in Figure 10.3.6 as single symbols. In Figure 10.3.6 you can find the concentration distribution over the whole length of the 1 D model at the final simulation time of 100 days. Obviously, the numerical results meet well the analytical solutions.

10.3.2 Non-linear sorption (Freundlich isotherm)

Definition

The non-linear Freundlich isotherm is often used to describe real sorption processes. Therefore, in this example, the transport process by including the Freundlich isotherm is calculated in the same way as in the precedent example (same model and boundary conditions). As there exists no opportunity to calculate analytically the solute transport with non-linear sorption, the results of the simulation have to be compared with solutions of the transport equation with linear sorption in order to evaluate the simulation results.

The following simplifications are assumed: (1) non-linear sorption (Freundlich isotherm), no decay of components (2) homogeneous aquifer, saturated, sta-

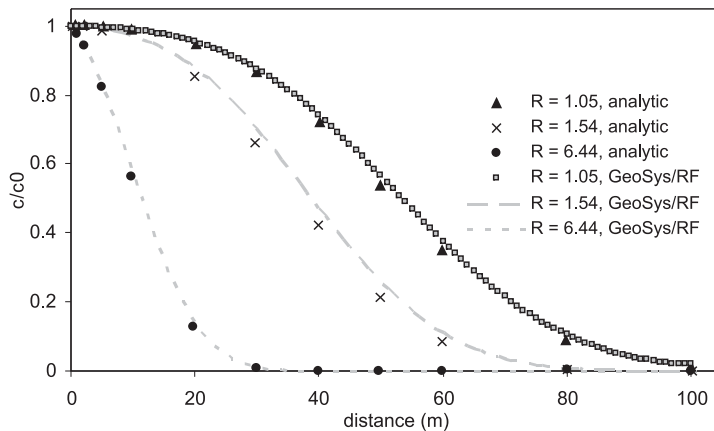


Figure 10.3.6: Concentration distribution after 100 d (Henry sorption)

tionary flow (Fig. 10.2.4). The soil parameters are the same as listed in Table 10.3(except decay). For the different simulation runs the Freundlich-sorption coefficients (K_1) are varied in the same way as the K_D -values that are listed in Table 10.1. The exponent K_2 was constant with a value of 1.

The dependence of sorbed molecules on the amount of molecules in dilution is given by equation (10.11). The concentration distribution at a special point in time and over a given distance cannot be calculated analytically by equation (10.3) when a non-linear sorption process is assumed. A possibility to test the correctness of the simulation results for transport with Freundlich sorption is to choose values of distribution coefficients in order to create a concentration distribution which is approximately linear and must therefore almost be equal to the results of transport by use of the Henry isotherm.

Results

As the values for the Freundlich coefficients were chosen in that way, that the concentration distribution between sorbed and solute concentrations is almost linear, the results of the simulation runs have to be equal to the results that are obtained by using the linear Henry isotherm. In Figure 10.3.7 the concentration distribution of the solute over the model length of 100 m is shown. As the concentrations of the transport simulation by using the Freundlich isotherm match those of the simulation runs with linear sorption, these results for non-linear sorption are reasonable. Additionally to this test, the values for the constant K_2 were changed to 0.8 in order to prove a difference between linear and non-linear sorption. The results of the comparison are shown in Figure 10.3.8. These numerical results show the effect of the application of a non-linear sorption isotherm: the higher the influence of sorption (large value of sorption

coefficient K_D resp. K_1) the higher the difference of solute concentration values between non-linear and linear sorption. However, the results for both isotherms were not evaluated quantitatively.

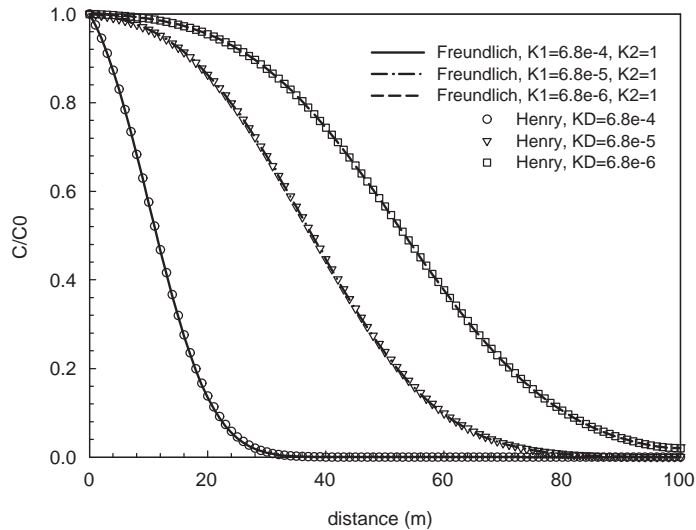


Figure 10.3.7: Concentration distribution after 100 d (Freundlich compared to Henry sorption)

10.3.3 Non-linear sorption (Langmuir isotherm)

Problem definition

The non-linear Langmuir isotherm is used to describe sorption processes that are restricted by a maximum concentration of sorbed molecules. In this example, the transport process by including the Langmuir isotherm is calculated in the same way as in the precedent examples for mass transport. As there exists no opportunity to calculate analytically the solute transport with non-linear sorption, the results of the simulation have to be compared with solutions of the transport equation with linear sorption in order to evaluate the simulation results.

The following simplifications are assumed: (1) non-linear sorption (Langmuir isotherm), no decay of components (2) homogeneous aquifer, saturated, stationary flow (Fig. 10.2.4). The soil parameters are the same as listed in Table 10.3(except decay). In order to create a Langmuir equation which has almost the same linear characteristic as the Henry equation, the Langmuir sorption

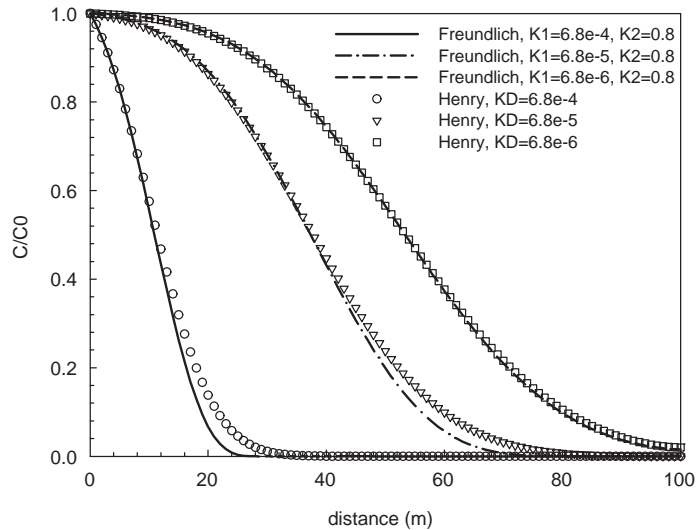


Figure 10.3.8: Different concentration distributions after 100 d (Freundlich compared to Henry sorption)

coefficients, K_1 , were varied in the same way as the Henry coefficients (K_D values in Table 10.4) for the different simulation runs. The K_2 coefficients stand for the affinity between solid and sorbed solute. Thus, the K_2 value can not be set equal to 0, because this would cause a transport without any sorption. When K_2 equals 1, there is no effect on the binding affinity. Therefore, the coefficient K_2 was set constant with a value of 1 in order to approximate the linear characteristic of the Henry equation (10.10).

The dependence of sorbed molecules on the amount of molecules in dilution is given by equation (10.11). The concentration distribution at a special point in time and over a given distance cannot be calculated analytically by equation (10.3) when a non-linear sorption process is assumed. Therefore, the simulation results are compared with the results for the mass transport by using the linear Henry isotherm. The non-linear Langmuir isotherm was forced to be almost linear in the way as described above. Now the results of the transport by using the Langmuir isotherm can be compared with the results that were obtained by the transport simulation with the linear Henry isotherm.

Results

In Figure 10.3.9 the concentration distributions over the whole model length by using the linear Henry isotherm and the non-linear Langmuir isotherm are depicted. Obviously, the results for each specified distribution constant are

almost equal. This result is correct, because it was provoked by the choice of the sorption coefficients.

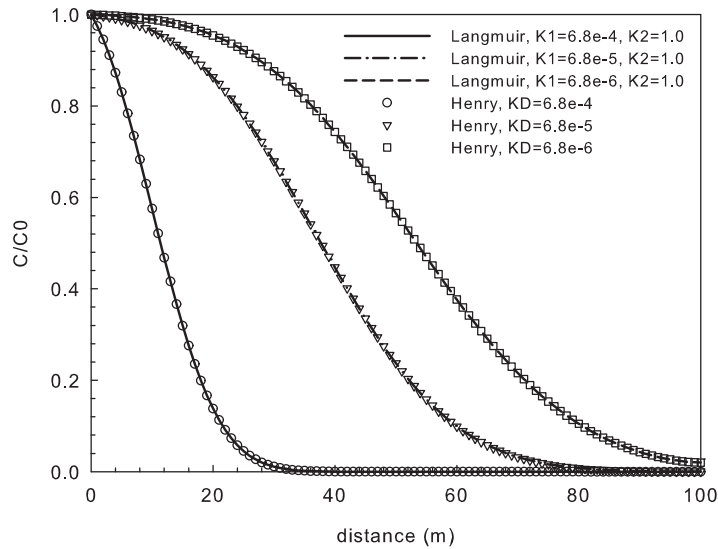


Figure 10.3.9: Concentration distribution after 100 d (Langmuir compared to Henry sorption)

In order to show that the results by the use of the Langmuir isotherm are actually different to those by using the Henry isotherm, the K_2 values were changed to a value of 0.8, so that the Langmuir isotherm got a real non-linear gradient. As the results show (Fig. 10.3.10), the differences between the concentration distributions are evident.

10.4 Sorption and decay

10.4.1 Single component

Definition

The aim of this example is to simulate the solute transport in an aquifer by convection with the influence of retardation as a result of sorption. Additionally, the transported mass will be degraded. The calculation area and boundary conditions are the same as described in chapter ??.

The following simplifications are assumed: (1) linear sorption, decay of components (2) homogeneous aquifer, saturated, stationary flow (Fig. 10.2.4). The soil

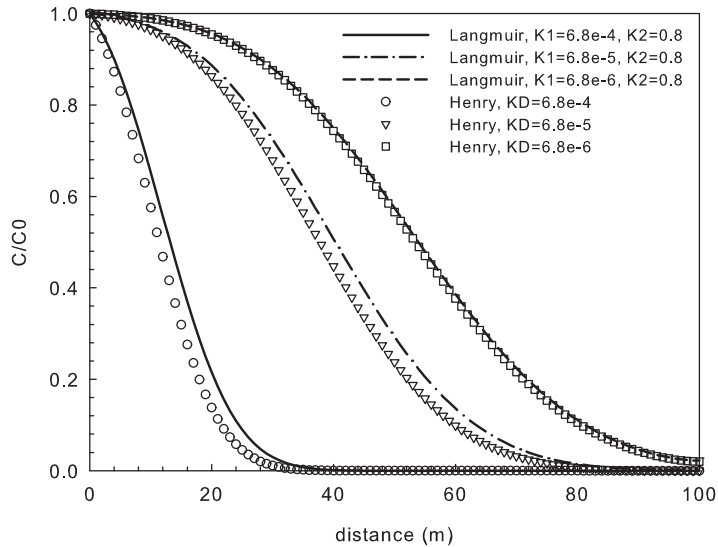


Figure 10.3.10: Different concentration distributions after 100 d (Langmuir compared to Henry sorption)

parameters are the same as listed in Table 10.3. The decay rate λ is $2 \cdot 10^{-7} \text{ s}^{-1}$. For the different simulation runs the Henry sorption coefficients are varied as listed in Table 10.4 to evaluate again the influence of sorption on mass transport. The concentration distribution at a special point in time and over a given distance is calculated by equation (10.3). The analytical solutions are depicted in Figure 10.4.11 as single symbols.

Results

The influence of radioactive decay on the transport process can be recognised at the typical declining exponential curves in Figure 10.4.11. According to the different sorption coefficients the transport is retarded. Obviously, the numerical results (lines) meet well the analytical solutions. Therefore, it can be summarised that the transport under the combined consideration of both decay and sorption can be reproduced by the numerical simulation.

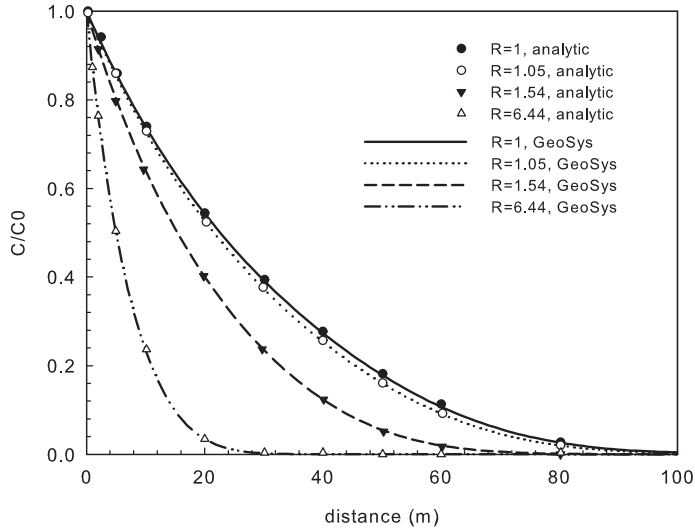


Figure 10.4.11: Concentration distributions after 100 d (sorption and decay)

10.4.2 Multi components

Definition

The aim of this example is to simulate the transport of several components with different sorption behaviour and decay. The calculation area and boundary conditions are the same as described for the precedent example. The mass distribution after 100 days has to be calculated.

The following simplifications are assumed (Fig. 10.2.4):

- Component 1: no sorption, no decay
- Component 2: decay
- Component 3: linear sorption
- Component 4: linear sorption, decay
- Aquifer: homogeneous, saturated, stationary flow

The soil parameters are the same as listed in Table 10.3. The decay rate λ for components 2 and 4 is $2 \cdot 10^{-7} \text{ s}^{-1}$, the Henry sorption coefficient K_D for component 3 is $6.4 \cdot 10^{-4} \text{ kg/m}^{-3}$ ($R = 6.44$). The concentration distribution at a special point in time and over a given distance is calculated by equation (2.44). The analytical solutions are depicted in Figure 10.4.12 as single symbols.

Results

In Figure 10.4.12 you can find the concentration distribution of the 4 different components over the whole length of the 1D-model at the final simulation time of 100 days. As the comparison of each single component with the analytical results of the "one-component-transport" shows, the numerical results for the multi component transport are reasonable.

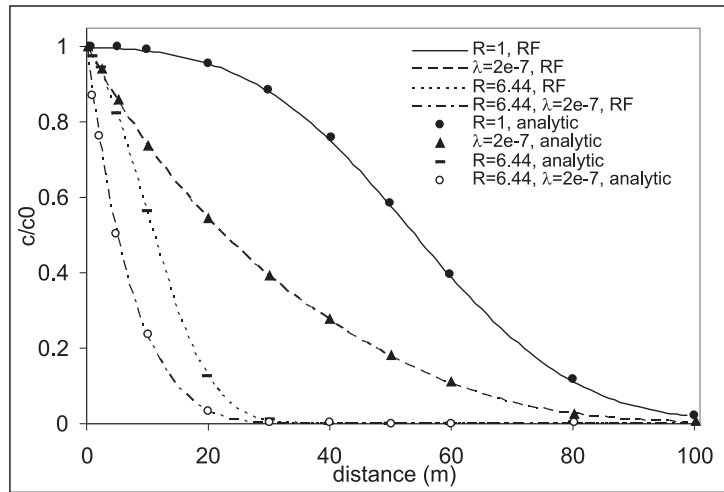


Figure 10.4.12: Concentration distributions of the four components after 100 d

10.5 Matrix diffusion

10.5.1 Definition

This benchmark is introduced to verify the matrix diffusion function. It simulates advective-dispersive transport of a solute in an one-dimensional fracture with constant aperture, with and without the effect of matrix-diffusion. The geometry and the material parameters are chosen to fit the parameters extracted from experiments conducted during the Colloid Radionuclide Retardation Experiment at Nagra's Grimsel test site [131]. The result from GS/RF is compared with that from PICNIC, and they fit well.

The geometry and material parameters in PICNIC and OGS are summarized in Table 10.5 and the conceptual model is shown in Figure 10.5.13. PICNIC solves the one-dimensional problem, whereas in OGS a two-dimensional discretization was chosen. A rectangular domain of 5.2m × 0.5m was discretized with 1155 nodes and 2080 triangular elements. One of the shorter domain edges was

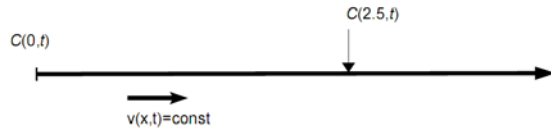


Figure 10.5.13: Conceptual setup of the 1D problem

chosen as inflow boundary and fluid was injected at the boundary-nodes in such a way, that the resulting fluid velocity matches exactly the value from Table 10.5. The concentration is fixed at the inflow boundary. In 2.5m distance the breakthrough curve is recorded. The outflow boundary is assumed to be far away and should not influence the observed breakthrough curve.Picnic V2.2 and OGS (Rev. 1535).

As defining exactly the same transport boundary conditions in OGS and PICNIC is not possible, the following procedure was used to get the inflow boundary condition as similar as possible:

1. The system was calculated for injecting a pulse of solute with a constant flux for a time length of 50s with PICNIC. The concentration vs. time was recorded for the inflow-leg.
2. The concentrations vs. time extracted from PICNIC's inflow-leg were applied (fixed) to the inflow boundary of the OGS system.

These procedures work, as long as advective fluxes are much higher than the dispersive-diffusive fluxes over the boundary. The outflow boundary condition is set to infinity, i.e. a semi-infinite problem is calculated. In OGS the domain is set to 5m, double the distance between inflow boundary and observation point. This prevents the outflow boundary condition to influence the tracer breakthrough at the observation point.

10.5.2 Results

For the investigated two cases, advection and dispersion(ADE) only and ADE plus matrix diffusion(MD), the PICNIC and OGS solutions are in general very similar (see Figure 10.5.14).

Symbol	Parameter	Value	Unit
L	Distance between boundary and observation points	2.5	m
α_T	Transverse dispersion (OGS only)	—	m
ρ	Bulk matrix density	2670	kg/m ³
$2b$	Fracture aperture	0.55×10^{-3}	m
v	Fluid velocity	7.05×10^{-4}	m/s
α_L	Longitudinal dispersion (OGS only)	0.1	m
Pe	Peclet number (PICNIC only)	25	—
ε_p	Matrix porosity	0.3	—
D_p	Diffusion constant in rock matrix	7.4×10^{-11}	m ² /s

Table 10.5: Geometry and material properties for the simulations

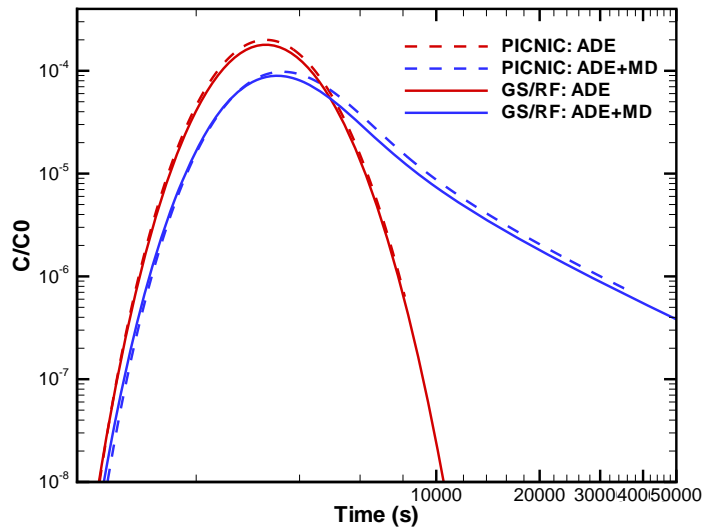


Figure 10.5.14: Breakthrough of the ADE and the ADE+MD solutions calculated with PICNIC and OGS

10.6 Particle tracking

The classical advection-dispersion equation of a conservative solute in porous media can be written as [132]

$$\frac{\partial C}{\partial t} = -\nabla \cdot (\mathbf{v} C) + \nabla \cdot (\mathbf{D} \nabla C) \quad (10.12)$$

where C is the concentration (ML^{-3}), \mathbf{v} is the pore velocity vector (ML^{-1}), and \mathbf{D} is the hydrodynamic dispersion tensor (L^2T^{-1}), t is time (T^2) and ∇ is the differential operator.

The random walk particle tracking (RWPT) method is issued from stochastic physics. The stochastic differential equation is [133]

$$\mathbf{x}(t_i) = \mathbf{x}(t_{i-1}) + \mathbf{v}(\mathbf{x}(t_{i-1}))\Delta t + Z\sqrt{2\mathbf{D}(\mathbf{x}(t_{i-1}))\Delta t} \quad (10.13)$$

where \mathbf{x} is the coordinates of the particle location, Δt is the time step, and Z is a random number whose mean is zero and variance is unit.

It has been shown that this equation is equivalent to an equation that is slightly different from the advection-dispersion equation (10.12). To be equivalent to equation (10.12), the modified velocity [134] and dispersion tensor [132] are expressed as

$$\mathbf{v}_i^* = \mathbf{v}_i + \sum_{j=1}^3 \frac{\partial \mathbf{D}_{ij}}{\partial x_j} \quad (10.14)$$

$$\mathbf{D}_{ij} = \alpha_T |\mathbf{v}| \delta_{ij} + (\alpha_L - \alpha_T) \frac{\mathbf{v}_i \mathbf{v}_j}{|\mathbf{v}|} + \mathbf{D}_{ii}^d \quad (10.15)$$

where δ_{ij} is the Kronecker symbol, α_L is the longitudinal dispersivity, α_T is the transverse dispersivity, D_{ij}^d is the tensor of molecular diffusion coefficient, and \mathbf{v}_i is the component of the mean pore velocity in the i th direction.

The equivalent stochastic differential equation to (10.12) in three dimensional problems can be written as [135, 136, 137]

$$\begin{aligned} x_{t+\Delta t} &= x_t + \left(\mathbf{v}_x(x_t, y_t, z_t, t) + \frac{\partial D_{xx}}{\partial x} + \frac{\partial D_{xy}}{\partial y} + \frac{\partial D_{xz}}{\partial z} \right) \Delta t \\ &\quad + \sqrt{2D_{xx}\Delta t} Z_1 + \sqrt{2D_{xy}\Delta t} Z_2 + \sqrt{2D_{xz}\Delta t} Z_3 \\ y_{t+\Delta t} &= y_t + \left(\mathbf{v}_y(x_t, y_t, z_t, t) + \frac{\partial D_{yx}}{\partial x} + \frac{\partial D_{yy}}{\partial y} + \frac{\partial D_{yz}}{\partial z} \right) \Delta t \\ &\quad + \sqrt{2D_{yx}\Delta t} Z_1 + \sqrt{2D_{yy}\Delta t} Z_2 + \sqrt{2D_{yz}\Delta t} Z_3 \\ z_{t+\Delta t} &= z_t + \left(\mathbf{v}_z(x_t, y_t, z_t, t) + \frac{\partial D_{zx}}{\partial x} + \frac{\partial D_{zy}}{\partial y} + \frac{\partial D_{zz}}{\partial z} \right) \Delta t \\ &\quad + \sqrt{2D_{zx}\Delta t} Z_1 + \sqrt{2D_{zy}\Delta t} Z_2 + \sqrt{2D_{zz}\Delta t} Z_3 \end{aligned} \quad (10.16)$$

where Z_i is a random number whose mean is zero and variance is unit.

Together with equation (10.15), the spatial derivatives of the dispersion coefficients can be expressed as a function of the derivatives of velocity. Note that to obtain the derivatives of velocity, velocity has to be continuous mathematically.

For this end, we interpolate velocity at any location in an element from the known velocity at the element nodes.

Since the proposed RWPT method makes use of the FEM for velocity estimation, the derivative of velocity within each element is computed as in Fig. 10.6.15 and written as

$$\begin{aligned}\frac{\partial \mathbf{v}_x}{\partial x} &= \frac{\mathbf{v}(x_R) - \mathbf{v}(x_L)}{l_x}; \quad \frac{\partial \mathbf{v}_y}{\partial y} = \frac{\mathbf{v}(y_U) - \mathbf{v}(y_D)}{l_y}; \quad \frac{\partial \mathbf{v}_z}{\partial z} = \frac{\mathbf{v}(z_N) - \mathbf{v}(z_S)}{l_z} \\ \frac{\partial \mathbf{v}_x}{\partial y} &= \frac{\partial \mathbf{v}_x}{\partial z} = \frac{\partial \mathbf{v}_y}{\partial z} = \frac{\partial \mathbf{v}_y}{\partial x} = \frac{\partial \mathbf{v}_z}{\partial x} = \frac{\partial \mathbf{v}_z}{\partial y} \simeq 0\end{aligned}\quad (10.17)$$

where x_L and x_R are the intersectional points of the element edges with an extension of a line parallel to the global x axis at which velocities are $\mathbf{v}(x_L)$ and $\mathbf{v}(x_R)$, y_D and y_U are the intersectional points of the element edge from down to up with extension of the line parallel to the global y axis at which velocities are $\mathbf{v}(y_D)$ and $\mathbf{v}(y_U)$, z_S and z_N are the intersectional points of the element edge from south to north with extension of the line parallel to the global z axis at which velocities are $\mathbf{v}(z_S)$ and $\mathbf{v}(z_N)$, and l_x , l_y , and l_z are the length of each intersectional line respectively.

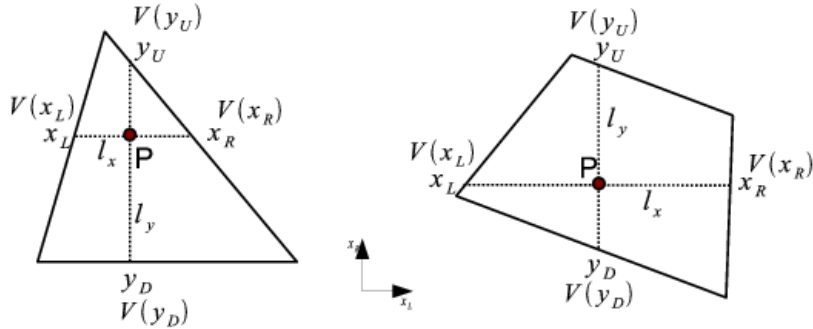


Figure 10.6.15: Spatial derivatives of velocity for a particle in triangular and quadrilateral elements (V is velocity)

Thus, the derivatives of the dispersion coefficients are as follows [138]

$$\begin{aligned}
\frac{\partial D_{xx}}{\partial x} &= \mathbf{v}_x \frac{\partial \mathbf{v}_x}{\partial x} \left[\alpha_L \left(\frac{2}{\mathbf{v}} - \frac{\mathbf{v}_x^2}{\mathbf{v}^3} \right) - \alpha_T \frac{\mathbf{v}_y^2 + \mathbf{v}_z^2}{\mathbf{v}^3} \right] \\
\frac{\partial D_{xy}}{\partial y} &= (\alpha_L - \alpha_T) \left[\frac{\partial \mathbf{v}_y}{\partial y} \frac{\mathbf{v}_x}{\mathbf{v}} - \frac{\mathbf{v}_x \mathbf{v}_y^2}{\mathbf{v}^3} \frac{\partial \mathbf{v}_y}{\partial y} \right] \\
\frac{\partial D_{xz}}{\partial z} &= (\alpha_L - \alpha_T) \left[\frac{\partial \mathbf{v}_z}{\partial z} \frac{\mathbf{v}_x}{\mathbf{v}} - \frac{\mathbf{v}_x \mathbf{v}_z^2}{\mathbf{v}^3} \frac{\partial \mathbf{v}_z}{\partial z} \right] \\
\frac{\partial D_{yy}}{\partial y} &= \mathbf{v}_y \frac{\partial \mathbf{v}_y}{\partial y} \left[\alpha_L \left(\frac{2}{\mathbf{v}} - \frac{\mathbf{v}_y^2}{\mathbf{v}^3} \right) - \alpha_T \frac{\mathbf{v}_x^2 + \mathbf{v}_z^2}{\mathbf{v}^3} \right] \\
\frac{\partial D_{yx}}{\partial x} &= (\alpha_L - \alpha_T) \left[\frac{\partial \mathbf{v}_x}{\partial x} \frac{\mathbf{v}_y}{\mathbf{v}} - \frac{\mathbf{v}_y \mathbf{v}_x^2}{\mathbf{v}^3} \frac{\partial \mathbf{v}_x}{\partial x} \right] \\
\frac{\partial D_{yz}}{\partial z} &= (\alpha_L - \alpha_T) \left[\frac{\partial \mathbf{v}_z}{\partial z} \frac{\mathbf{v}_y}{\mathbf{v}} - \frac{\mathbf{v}_y \mathbf{v}_z^2}{\mathbf{v}^3} \frac{\partial \mathbf{v}_z}{\partial z} \right] \\
\frac{\partial D_{zz}}{\partial z} &= \mathbf{v}_z \frac{\partial \mathbf{v}_z}{\partial z} \left[\alpha_L \left(\frac{2}{\mathbf{v}} - \frac{\mathbf{v}_z^2}{\mathbf{v}^3} \right) - \alpha_T \frac{\mathbf{v}_x^2 + \mathbf{v}_y^2}{\mathbf{v}^3} \right] \\
\frac{\partial D_{zx}}{\partial x} &= (\alpha_L - \alpha_T) \left[\frac{\partial \mathbf{v}_x}{\partial x} \frac{\mathbf{v}_z}{\mathbf{v}} - \frac{\mathbf{v}_z \mathbf{v}_x^2}{\mathbf{v}^3} \frac{\partial \mathbf{v}_x}{\partial x} \right] \\
\frac{\partial D_{zy}}{\partial y} &= (\alpha_L - \alpha_T) \left[\frac{\partial \mathbf{v}_y}{\partial y} \frac{\mathbf{v}_z}{\mathbf{v}} - \frac{\mathbf{v}_z \mathbf{v}_y^2}{\mathbf{v}^3} \frac{\partial \mathbf{v}_y}{\partial y} \right]
\end{aligned} \tag{10.18}$$

Because velocity is not derivable at the interface of two adjacent element in a nonuniform flow, computing dispersion coefficient derivatives by using a finite element approach would yield erroneous values [138]. To prevent the errors, a particle is coded to have information of an element index and the velocity estimation is continuous even at the elemental boundaries in this method. Thus, the derivatives of dispersion coefficients will be computed accordingly. This is an improved approach from the work by [138].

10.6.1 Particle tracking in porous medium: 1D case study

Definition

A one-dimensional homogenous aquifer is chosen to simulate a soil column experiment conducted by Harter et al. [139]. In the experiment, a constant flow rate was established, 2.5 pore volumes NaCl - tap water solution and 2.5 pore volumes *Cryptosporidium parvum* solution (1×10^5 oocysts per mL) were injected respectively, the outflow was continuously collected. Fig. 10.6.16 shows the schematic description of the experiment.

NaCl - tap water solution is used as tracer, which experiences only advection and dispersion. The *Cryptosporidium parvum* can be classified as biological colloid. Colloids moving in porous media experience advection, dispersion, sorption-desorption, and filtration.

Analytical solution

For the one-dimensional transport including sorption-desorption and filtration through a homogeneous medium the following differential equation is applied

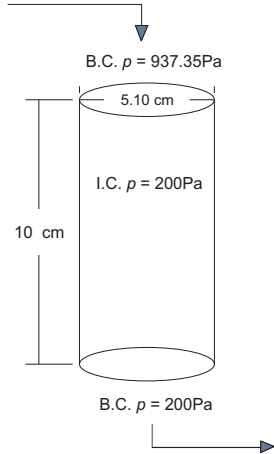


Figure 10.6.16: Soil column experiment

$$\frac{\partial C}{\partial t} + \frac{\rho_b}{n} \frac{\partial C_S}{\partial t} = v \alpha_L \frac{\partial^2 C}{\partial x^2} - v \left(\frac{\partial C}{\partial x} + \lambda C \right) \quad (10.19)$$

where C is dissolved concentration ($\text{kg}\cdot\text{m}^{-3}$), C_S is sorbed concentration ($\text{kg}\cdot\text{kg}^{-1}$), t is time (s), ρ_b is bulk density ($\text{kg}\cdot\text{m}^{-3}$), n is porosity (-), v is velocity ($\text{m}\cdot\text{s}^{-1}$), α_L is longitudinal dispersivity (m), x is distance (m), λ is filtration coefficient (m^{-1}).

The instantaneous, linear sorption model assumes that

$$C_S = K_d C \quad (10.20)$$

where K_d is the partitioning coefficient ($\text{m}^3 \cdot \text{kg}^{-1}$). The retardation coefficient R is

$$R = 1 + \frac{\rho_b}{\theta} K_d \quad (10.21)$$

The dispersion coefficient in x -direction D_{xx} ($\text{m}^2 \cdot \text{s}^{-1}$) is

$$D_{xx} = v \alpha_L \quad (10.22)$$

The analytical solution for a pulse input (inject time from 0 to τ) is:

$$C = \frac{1}{2} C_0 \left[\exp \left(\frac{vx(1-\gamma)}{2D_{xx}} \right) \operatorname{erfc} \left(\frac{x-v\gamma t/R}{2\sqrt{D_{xx}t/R}} \right) + \exp \left(\frac{vx(1+\gamma)}{2D_{xx}} \right) \operatorname{erfc} \left(\frac{x+v\gamma t/R}{2\sqrt{D_{xx}t/R}} \right) \right] \quad (10.23)$$

for $t \in (0, \tau)$,

$$\begin{aligned} C = & \frac{1}{2}C_0 \left[\exp\left(\frac{vx(1-\gamma)}{2D_{xx}}\right) \operatorname{erfc}\left(\frac{x-v\gamma t/R}{2\sqrt{D_{xx}t/R}}\right) \right. \\ & + \exp\left(\frac{vx(1+\gamma)}{2D_{xx}}\right) \operatorname{erfc}\left(\frac{x+v\gamma t/R}{2\sqrt{D_{xx}t/R}}\right) \\ & - \exp\left(\frac{vx(1-\gamma)}{2D_{xx}}\right) \operatorname{erfc}\left(\frac{x-v\gamma(t-\tau)/R}{2\sqrt{D_{xx}(t-\tau)/R}}\right) \\ & \left. - \exp\left(\frac{vx(1+\gamma)}{2D_{xx}}\right) \operatorname{erfc}\left(\frac{x+v\gamma(t-\tau)/R}{2\sqrt{D_{xx}(t-\tau)/R}}\right) \right] \quad (10.24) \end{aligned}$$

for $t \in (\tau, \infty)$, where

$$\gamma = \sqrt{1 + 4v\lambda RD_{xx}/v^2} \quad (10.25)$$

Numerical solution

The calculation area is simplified to a line with the length of 0.1m. For the numerical model 100 elements and 101 nodes are included. Head gradient is set by giving two constant pressures at both left and right boundaries to establish a uniform velocity field with the value of 7.1 md^{-1} .

The number of pore volume (x -axis) is calculated by

$$P_V = \frac{vt}{L} \quad (10.26)$$

where v is the seepage velocity, L is the length of the soil column. Considering the Courant number, the time step size is set by assigning P_V to 0.01. In the simulation, 100 particles per time steps are loaded near the left boundary for 250 time steps.

The filtration process is described by using the filtration coefficient. The sorption-desorption process is described by the two-rate model from Johnson et al. [140]. In the two-rate model, desorption is governed by two different rate coefficients

$$N/N_0 = Ae^{-k_1 t} + (1-A)e^{-k_2 t} \quad (10.27)$$

where N is the number of particles remaining on the medium at time t , N_0 is the initial number of particles on the medium at the time of initial sorption, A is a weighting factor, k_1 and k_2 are the fast and slow sorption rate coefficient, respectively. Relative parameters are listed in Tab. 10.6.

Table 10.6: Model parameters for the column experiment

Symbol	Parameter	Value	Unit
k	Permeability	1.114476^{-11}	m^2
α_L	Longitudinal dispersivity	0.005	m
n	Porosity(tracer)	0.5	—
n	Porosity(colloid)	0.42	—
A	Weighting factor	0.9	—
k_1	Fast sorption rate coefficient	0.1	—
k_2	Slow sorption rate coefficient	0.001	—
λ	Filtration coefficient	5.2	m^{-1}

Results

The tracer experiences only advection and dispersion, which means in Equation (10.19), $C_S = 0$, $\lambda = 0$. The results of RWPT simulation for the distribution of concentration over time are compared to those of measured value from the experiment by Harter, the analytical solution, and the OGS simulation with mass transport method. The comparison results are shown in Fig. 10.6.17.

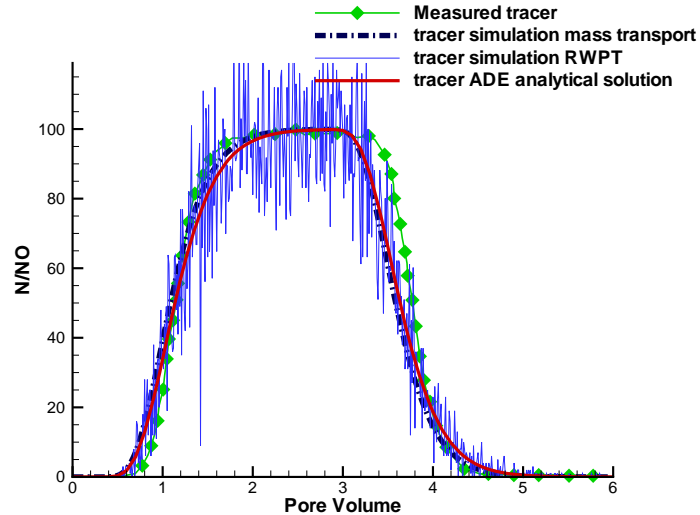


Figure 10.6.17: Tracer transport with advection and dispersion

In the colloid transport simulation, the number of particles leaving the right boundary is counted each time step. The number is then converted to concentration in order to obtain the corresponding breakthrough curve over time. The

comparison with the measured value from the experiment by Harter are shown in Fig. 10.6.18.

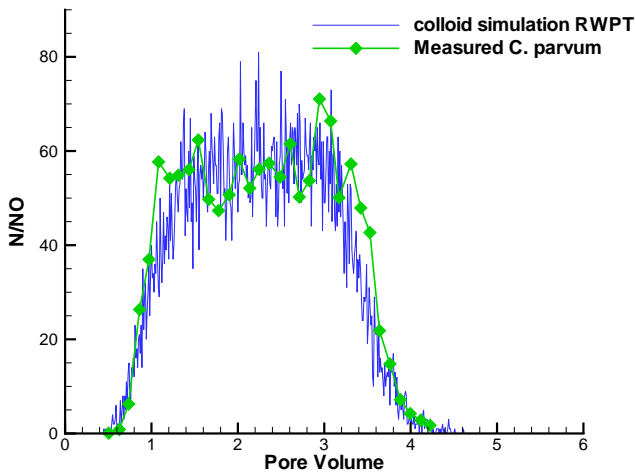


Figure 10.6.18: Colloid transport with sorption-desorption and decay

10.6.2 Particle tracking in porous medium: 2D case study

Definition

A two-dimensional homogeneous aquifer is chosen to verify advective dispersive transport. The dimension of the model domain is 100 m by 60 m where the uniform velocity field is held constant in the x direction (Fig. 10.6.19).

Analytical solution

The stated problem can be solved with an analytical solution provided by [94].

$$C(x, y, t) = \frac{C_0 A}{4\pi t \sqrt{D_{xx} + D_{yy}}} \exp \left[-\frac{(x - x_0)^2}{4D_{xx}t} - \frac{(y - y_0)^2}{4D_{yy}t} \right] \quad (10.28)$$

where C_0 is the initial concentration.

Numerical solution

The domain is discretized with quadrilateral elements of 0.5 m by 0.5 m. The same grid density is also used for converting particle distributions to element

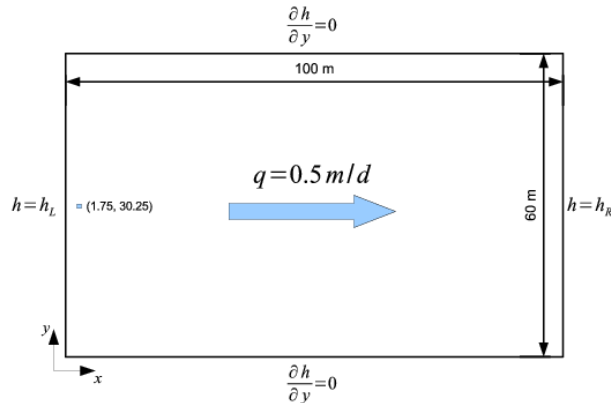


Figure 10.6.19: Particle tracking in 2D homogeneous aquifer

concentrations. The head gradient of one in the x direction is set by assigning two constant boundary conditions along both left and right sides, thus obtains the uniform velocity field with the value of 0.5 md^{-1} .

The initial source load is applied to an area with dimensions of 0.1 m by 0.1 m to have an initial concentration of $C_0 = 1 \text{ kgm}^{-3}$. The material properties for this model setup are given in Tab. 10.7.

Table 10.7: Material properties

Symbol	Parameter	Value	Unit
k	Permeability	1.114^{-11}	m^2
α_L	Longitudinal dispersivity	0.1	m
α_T	Transverse dispersivity	0.1	m

Results

The comparison with the analytical solution is provided in Fig. 10.6.20. The number of particles used for this simulation is 50000. This is significantly less than the number of particles reported by [141], who reported that up to 2.5 million particles were necessary to achieve smoothness of the solution due to oscillations around the contours. As the oscillations observed here for the method proposed are smaller than reported by [141], the proposed method allows to dramatically reduce the number of particles required for a smooth solution by about two orders of magnitude.

In addition, various numbers of particles used to solve the same problem produces particle clouds are shown in Fig. 10.6.21.

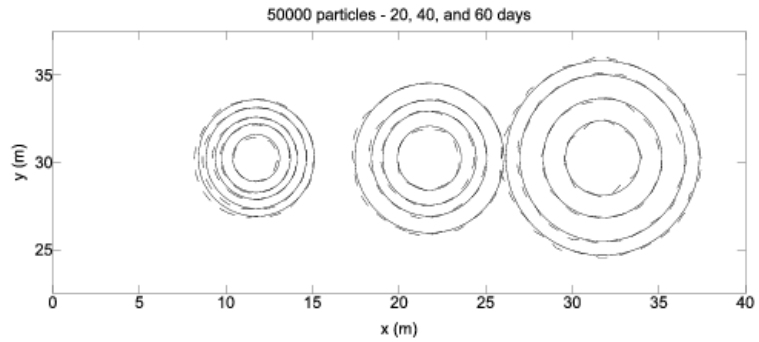


Figure 10.6.20: Transport results of the RWPT method compared with the analytical solution for 50000 particles at 20, 40, and 60 days: The solid line is the analytical solution, the dotted line is the RWPT result. Contour lines are shown for $C = 2.6e^{-4}, 1.6e^{-4}, 1.0e^{-4}, \text{ and } 4e^{-5}$.

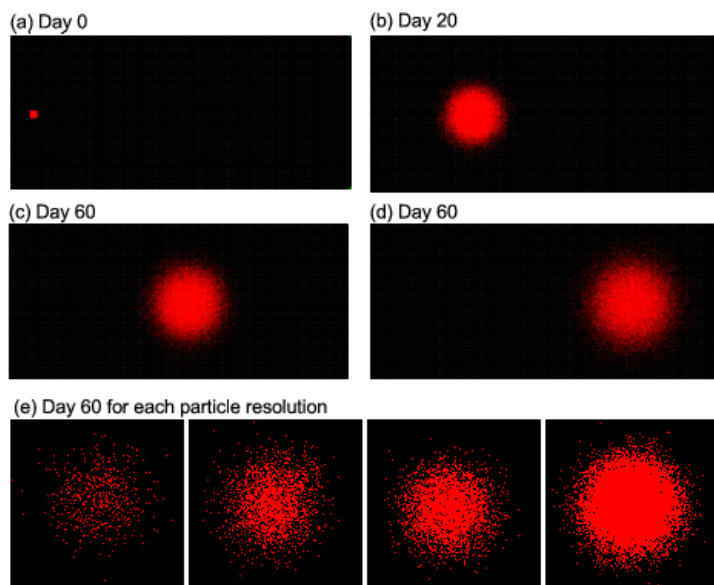


Figure 10.6.21: (a-d)Particle clouds of 50000 particles at 0, 20, 40, and 60 days,
(e) Particle clouds of 1000, 5000, 10000, and 50000 particles at
60 days

10.6.3 Particle tracking in porous medium: 3D case study

Definition

A three-dimensional homogeneous aquifer is chosen to verify advective dispersive transport. The side length of the cube model domain is 100 m. The velocity field is held constant in the diagonal direction from bottom left to top right (Fig. 10.6.22).

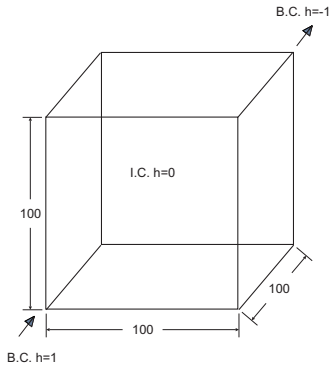


Figure 10.6.22: Particle tracking in 3D homogeneous aquifer

Analytical solution

The stated problem can be solved with an analytical solution provided by [94].

$$C(x, y, z, t) = \frac{C_0 V}{8 (\pi t)^{3/2} \sqrt{D_{xx} D_{yy} D_{zz}}} \exp \left[-\frac{(x - x_0)^2}{4 D_{xx} t} - \frac{(y - y_0)^2}{4 D_{yy} t} - \frac{(z - z_0)^2}{4 D_{zz} t} \right] \quad (10.29)$$

where C_0 is the initial concentration.

Numerical solution

The domain is discretized with tetrahedral elements. The same grid density is used for converting particle distributions to element concentrations. The head gradient is set by assigning two constant boundary conditions on the diagonal joint points.

The initial source load is applied to an area close to the bottom left of the domain to have an initial concentration of $C_0 = 1 \text{ kgm}^{-3}$. The material properties for this model setup are given in Tab. 10.8.

Table 10.8: Material properties

Symbol	Parameter	Value	Unit
k	Permeability	6.0804^{-10}	m^2
α_L	Longitudinal dispersivity	0.005	m
α_T	Transverse dispersivity	0.005	m
n	Porosity	0.2	—

Results

The advection-dispersion of the particles pulse across the cube is shown in Fig. 10.6.23.

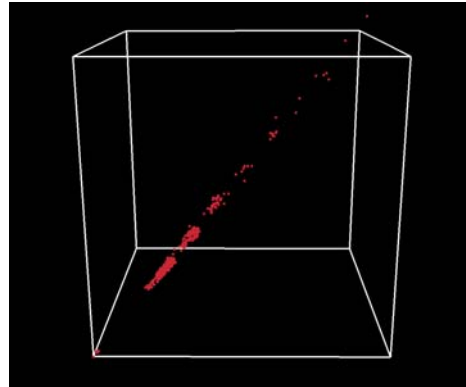


Figure 10.6.23: Particle clouds in the cube

The result of RWPT simulation for the distribution of concentration over time is compared to the analytical solution. The comparison result is shown in Fig. 10.6.24.

10.7 RWPT in fractures

by Joshua Taron and Geraldine Pichot

Fractures may be defined through direct measurement or geo-statistical reproduction. In the benchmarks of this report, both methods will be utilized. Where fractures are directly measured, the methodology utilizes a laser profiler. Profiles (elevation measurements) are taken of each fracture surface, and these are manipulated numerically. Point-wise fracture aperture is the difference between the top and bottom surfaces at corresponding locations. Statistically reproduced

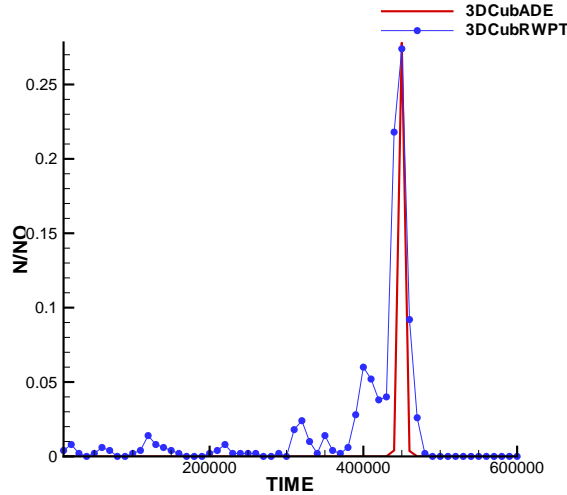


Figure 10.6.24: Breakthrough curves for particle tracking with advection and dispersion

fractures, reproduce roughness of the aperture (not each surface) to achieve a desired mean and standard deviation. The result is used directly as fracture aperture in numerical simulations.

For a fracture represented by two parallel (planar) plates, permeability is a function of the fracture aperture by the cubic law,

$$k = \frac{b^2}{12}.$$

For a uniformly fracture rock mass, the cubic law takes form as $b^3/12s$, where s is fracture spacing.

The aperture, b , however, represents only the mechanical state of the fracture. In reality, observed flow rates are dependent on the hydraulic state of the fracture. In other words, fracture roughness matters. We therefore distinguish two different apertures: the so-called "void" aperture, b_v , and the "hydraulic" aperture, b_h . The void aperture is the mean geometrically measured distance between the two fracture surfaces, including only those points that are not in contact (as the name implies, including only voids). The hydraulic aperture is a correction from this value ($b_h \leq b_v$), with one possibility known as the geometric correction [[142]],

$$b_h^3 = \exp \langle \ln (k) \rangle = \exp (3 \langle \ln (b_v) \rangle),$$

where the angled brackets indicate that the mean is taken over the logarithm of the pointwise void aperture. Therefore, as an approximation to reality, the (effective) true permeability of a rough fracture is given by,

$$k = \frac{b_h^2}{12}.$$

In what follows, we use this permeability to approximate behavior of the fracture and to generate an analytical solution for (qualitative) comparison to simulations within rough fractures, where permeability occurs point-wise (and mechanically) as $k_i = b_i^2/12$. Therefore, this is an *effective permeability*, and shall be used as an attempt to approximate (or provide reference to) true flow behavior in a rough fracture from a single bulk property.

10.7.1 Uncertainty in flow, Preferential flow

To examine changes to flow characteristics, we utilize two alternate forms of mass transport: the classical advection-dispersion equation (ADE) and random walk particle tracking (Fig. 10.7.25). The RWPT simulator within OGS is modified to allow a continuous source of particles (numerically approximate to a Neumann concentration boundary) for comparison with results from ADE simulations. For comparison, dispersion is not allowed within the RWPT simulation: particles are only advected with the flow. Therefore, particles represent the 50% concentration breakthrough if particles are imagined as concentrations. The plot for each stress state is shown at a different absolute time, but each corresponds to the same dimensionless time, $t_D = v \cdot t/L$, where t is current time and L is total flow length, with v calculated from the mean b_h . Therefore, if b_h is a good approximation of behavior, the concentration advance in each plot should be approximately of the same extent. Note that this is true, but also that the increasing tendency for preferential flow with stress lends to increasingly less uniform concentration advance: with increasing stress, a given point in the geometry will record strongly different behavior than its neighbors.

10.8 ?Compositional gas flow

by Ashok Singh

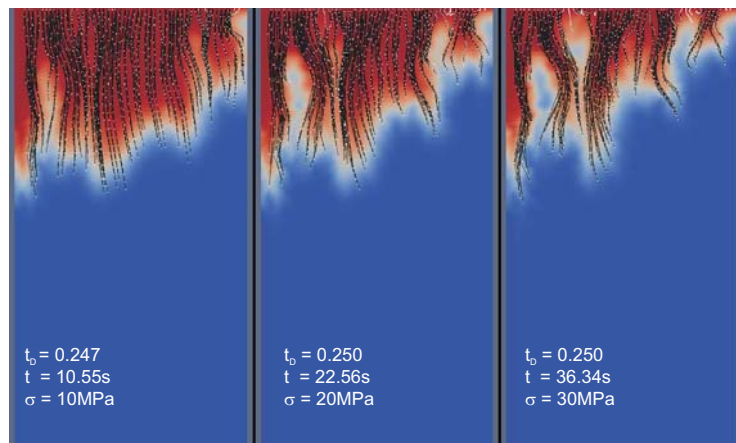


Figure 10.7.25: RWPT vs. ADE at different stress states. Two separate simulations are conducted and overlay one another. Particle pathlines (black) and particles (white) are illustrated, and overlay contours (red = higher concentration) generated from the ADE simulation.

Chapter 11

Coupled processes

The below Tab. 11.1 shows some of the important coupling phenomena during THMC processes in porous media. Among the modeling challenges in this field are following topics

- T:** Temperature depending material properties and reaction rates,
- H:** Multi-phase flow with phase changes coupled to reactive transport,
- M:** Cracking due to gas pressure, thermal stresses, de-saturation,
- C:** Gas production, pore space clogging due to precipitation.

Table 11.1: Thermal coupled phenomena

T dependent parameters	TH Vapor flux Convection	TM Thermal stress Cracking	TC Partial pressure (T) Reaction rates
HT Advection	H	HM Consolidation Swelling stress	HC Advection Partial pressure (p)
MT	MH Consolidation Cracking	M	MC Pressure solution
CT Reaction heat	CH Convection	CM Chemical damage	C

Part III

Examples for Coupled Processes

Chapter 12

Surface/subsurface flow

by Jens-Olaf Delfs and Ed Sudicky (tbc)

Chapter 13

Density dependent flow

by Marc Walther, Jens-Olaf Delfs, Chan-Hee Park, Jude Musuuza, Florin Radu, Sabine Attinger

13.1 Theory

13.1.1 Governing Equations

The governing equations used for variable density flow consist of three fundamental conservation equations: (i) continuity equation of flow, (ii) momentum equation, and (iii) contaminant transport equation. In addition, these three equations are linked to the equations of the bulk fluid density and the hydrodynamic dispersion equations.

Equation of the Bulk Fluid Density

The linearized equation of the bulk fluid density under an isothermal state was formulated in terms of hydraulic head as,

$$\rho = \rho_0 (1 + \lambda_h (h - h_0) + \lambda_c C) \quad (13.1)$$

where h is the hydraulic head, λ is the reference hydraulic head, ρ is the density of fluid, ρ_0 is the reference density of the fluid, λ_h represents the coefficient of compressibility of the fluid associated with the change of the hydraulic head at constant mass fraction of the solute, λ_C is the coefficient of expansivity resulting from the change of the mass concentration of the solute at constant hydraulic head, and C is the relative concentration.

The relationship between density and concentration can also be approximated using other representations such as an exponential function as given by Kolditz et al. [1998]. The equations describing the relationship between density and other relevant parameters are formulated based on experiments and are approximate relationships.

Another equation for describing the relationship between density and concentration (or mass fraction) is provided by Herbert et al. [1988] and used by Oldenburg and Pruess [1995]. This equation was derived from the assumption that when two liquids are well mixed, the masses or the volumes of respective components are additive. In this study, among these equations which describe the relationship between density and concentration, the linear equation obtained from the experiments is chosen to describe the relation between the bulk fluid density and concentration.

Continuity equation of flow

The macroscopic mass balance equation of the fluid averaged over a representative elementary volume (REV) in a porous medium is

$$\frac{\partial (S\phi\rho)}{\partial t} + \nabla \cdot (\phi\rho\vec{v}) = \rho Q_\rho \quad (13.2)$$

where S is the saturation ratio, ϕ is the porosity, t is the time, \vec{v} is the fluid velocity vector, and ρQ_ρ is the source term of the fluid mass in an aquifer. Based on Equation 13.2, the flow equation for a variably saturated porous medium can be written in terms of hydraulic head and mass concentration,

$$\phi \frac{\partial S}{\partial t} + SS_0^h \frac{\partial h}{\partial t} + S\phi\lambda_C \frac{\partial C}{\partial t} + \nabla \cdot \vec{q} + \lambda_c \vec{q} \cdot \nabla C = Q_\rho \quad (13.3)$$

where S_0^h is the specific storativity of a porous medium with respect to hydraulic head change and \vec{q} is the Darcy velocity vector. The head-based flow equation, Equation 13.3, has the advantage over pressure-based flow equations because numerically large static pressures may dominate the dynamic pressure differences that cause motion. The resulting pressure-based numerical scheme may therefore operate at less than optimum numerical efficiency. A more efficient way is to write the flow equation in terms of a quantity that can be directly related to the driving forces. Such a quantity is the equivalent freshwater hydraulic head, defined as $h = \frac{p}{\rho_0 g} + z$ [Frind, 1982].

Momentum equation of flow (the Darcy Equation) and dispersive flux

The momentum balance equation for variable-density fluid flow in a porous medium in terms of hydraulic head can be given as

$$\vec{q} = \phi \vec{v} = -\frac{\hat{k} \rho_0 \vec{g}}{\mu} \left(\nabla h + \left(\frac{\rho - \rho_0}{\rho_0} \right) \vec{e} \right) \quad (13.4)$$

where \hat{k} is the tensor of permeability of a porous medium and \vec{e} is the unit vector in the gravitational direction. The dispersion tensor can be written as Bear [1979]

$$\hat{D} = \gamma D_m \hat{\delta} + \alpha_T |v| \hat{\delta} + (\alpha_L - \alpha_T) \frac{\vec{v}_i \vec{v}_j}{|v|} \quad (13.5)$$

where γ is the tortuosity, D_m is the coefficient of molecular diffusion, $\hat{\delta}$ is the Kronecker-delta (unit tensor), α_T is the transverse dispersivity, v is the characteristic value of macroscopic velocity, α_L is the longitudinal dispersivity, and i and j are the velocities in and directions respectively.

Solute transport equation

The solute transport with a source is governed by the following advection-dispersion equation

$$\frac{\partial(\phi C)}{\partial t} + \nabla \cdot (\phi \vec{v} C) - \nabla \cdot (\phi \hat{D} \cdot \nabla C) = Q_C \quad (13.6)$$

where Q_C is the source term of the solute in terms of mass concentration. Ignoring the expansivity resulting from the change of mass concentration λ_C , Equation 13.6 can be written as follows

$$\phi \frac{\partial C}{\partial t} + (1 - \phi) \lambda_h C \frac{\partial h}{\partial t} + \phi \vec{v} \cdot \nabla C - \nabla \cdot (\phi \hat{D} \cdot \nabla C) + C Q_\rho = Q_C \quad (13.7)$$

Kolditz et al. [1998] defined approximation level of density variations in the mass equations when Equation 13.2 and 13.6 are expanded.

13.2 The Elder Problem

13.2.1 Definition

The Elder problem is a benchmark to verify density-dependent flow such as free convection, seawater intrusion, and possibly enhanced gas recovery with CO₂.

Model description. The Elder Problem is a good example of free convection phenomena, where the fluid flow is driven purely by the density differences of the fluids. Figure 13.2.1 illustrates the boundary conditions of the Elder problem. Table 13.1 presents the specific parameters for the Elder problem used in this application.

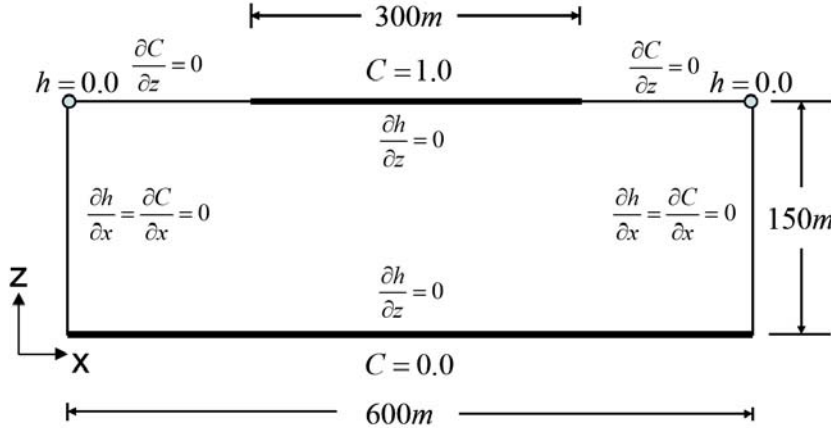


Figure 13.2.1: Boundary conditions of the Elder problem

Symbol	Quantity	Value	Unit
D_m	Molecular diffusion coefficient	3.565e-6	$m^2 s^{-1}$
k	Permeability	4.845e-13	m^2
μ	Dynamic viscosity	10e-6	$kg m^{-1} s^{-1}$
g	Gravitational coefficient	9.81	ms^{-2}
α_L, α_T	Longitudinal and transverse dispersivity	0, 0	m
ϕ	porosity	0.1	—
ρ_0, ρ_s	Density of water and saltwater	(1,1.2)e3	$kg m^{-3}$

Table 13.1: Parameters for the Elder problem

13.2.2 Results

The mesh was created with hexahedral elements for further expansion to 3D applications. The grid density level is defined as the l th level that consists of 2^{2l+1} identical square elements. Based on the definition of the grid density, the number of the hexahedral elements is 8192. The isochlor is defined as a ratio of a density difference to the maximum density difference. Figure 13.2.2 shows the numerical results obtained from OPENGEOSYS as the solution of the Elder problem.

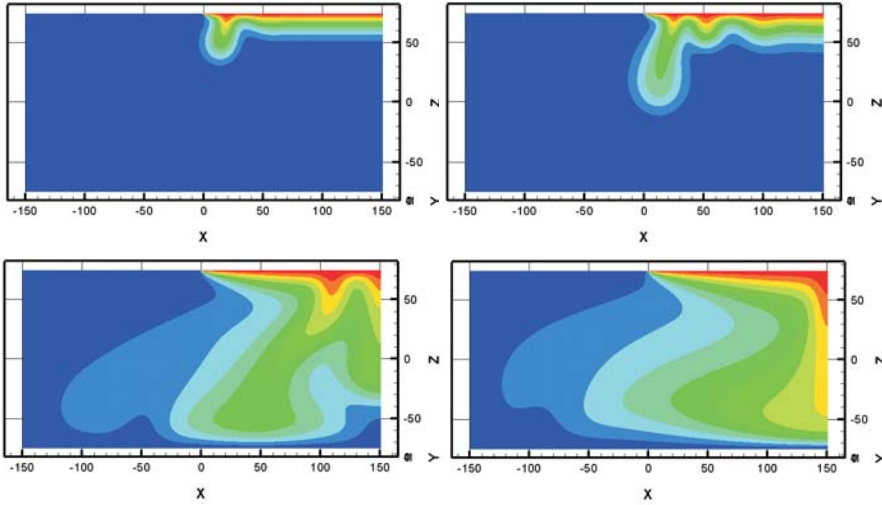


Figure 13.2.2: Isochlors of the Elder problem for 1, 2, 10, and 20 year at regular grid of level 6

13.3 The Goswami Problem

13.3.1 Definition

This example shows density dependent groundwater flow under unconfined conditions. The benchmark is based on experimental and modelling data aquired by GOSWAMI ET AL, 2007 [143], who show a HENRY-like (see [144]) saltwater intrusion experiment using a laboratory-scale tank.

GOSWAMI showed three steady-state (SS-1, SS-2, SS-3), differing in the hydraulic gradient, and two transient (TS-1, TS-2) experiments, one advancing front condition (from the final states of experiments SS-1 to SS-2) and one receding front condition (SS-2 to SS-3) experiment, and concurrent simulations with SEAWAT.

The model set-up will be as close as possible to the one used by GOSWAMI exemplarily showing the simulations of SS-1 and TS-1 with OPENGEOSYS.

Method. Modifying the Richards-Flow equation [145] with a linear approach as described by SUGIO ET AL, 1987 [146] the hydraulic flow equation is solved for the unconfined flow. Additionally, the MASS_TRANSPORT and RICHARDS_FLOW processes are coupled via a density correlation as a function of concentration.

Boundary and initial conditions. Boundary conditions are shown in figure 13.3.3: bottom and top horizontal boundaries are *no-flow*, vertical right and left

hand side boundaries are described via linear pressure gradients (including the appropriate densities of fresh water $\rho_f = 1000 \text{ kg} \cdot \text{m}^{-3}$ or salt water $\rho_s = 1026 \text{ kg} \cdot \text{m}^{-3}$), vertical right and left hand side boundary ISOCHLOR concentrations C_i are fresh water (i.e. $C_i = 0$) and salt water (i.e. $C_i = 1$), respectively.

For the SS-1 simulation, initial conditions are fresh water for the whole domain, i.e. a linear pressure gradient with $p_{(z=0.25m)} = 0 \text{ Pa}$ and $C_i = 0$.

For the TS-1 simulation, initial conditions are the hydraulic and mass transport steady state of SS-1.

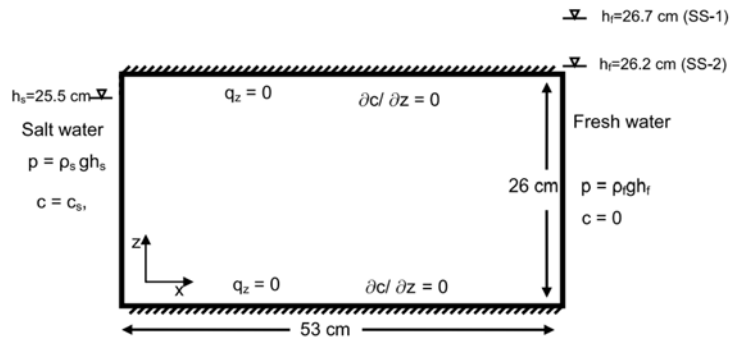


Figure 13.3.3: Model domain and boundary conditions after GOSWAMI ET AL, 2007 [143]

Material properties. The homogeneous, isotropic domain material equals a medium coarse sand. The corresponding parameters are listed in table 13.2.

Table 13.2: Parameters of simulation

Parameter	Setting
Porosity [-]	0.385
Permeability [m^2]	$1.239 \cdot 10^{-9}$
Reduced permeability [m^2]	0.0001
Permeability reduction pressure [Pa]	-100

Model domain, grid discretization. The dimensions of the laboratory tank were $0.53 \times 0.26 \times 0.027 \text{ m}^3$; following these measures, a 2D model domain was

set up. The grid discretization was uniform with rectangular quad-elements sized $\Delta x = \Delta z = 5 \cdot 10^{-4} m$.

Time stepping, Dispersivity, Diffusivity. Time step was chosen to be $\Delta t = 10 s$ up to a simulation time of $t_{final} = 4800 s = 80 min$ (time until steady state of simulation); to the end of the simulation, time step size was increased up to $\Delta t = 160 s$.

Longitudinal dispersivity α_L was determined by GOSWAMI's laboratory experiments to $\alpha_L = 10^{-3} m$, transversal dispersivity α_T was assumed to be $\alpha_T = 0.1 \cdot \alpha_L = 10^{-4} m$.

Diffusion effects were neglected due to the highly advective flow regime.

Stability. Based on these model configurations, PECLET criterium is met within acceptable ranges with

$$Pe = \frac{\Delta t \cdot v}{\Delta x} = \frac{10 s \cdot 2 \cdot 10^{-4} ms^{-1}}{5 \cdot 10^{-3} m} = 0.4 < 1. \quad (13.8)$$

However, COURANT criterium is exceeded by its reglementations with

$$Co = \frac{\Delta x}{\alpha} = \frac{5 \cdot 10^{-3} m}{10^{-4} m} = 50 \not< 2, \quad (13.9)$$

which causes some oscillations around the left side ISOCHLOR boundary condition.

13.3.2 Results

Steady state. Figure 13.3.5 shows the OPENGEOSYS simulation result of the steady-state scenario SS-1 and the typical circulation patterns of a saltwater intrusion, figure 13.3.4 shows the comparison of the experimental measurements with the modeling software outputs of SS-1 for SEAWAT and OPENGEOSYS; the scenario simulations fit very well to the experimental observations. The slight deviations of both simulations may be due to the misfit of the COURANT criterium, to inhomogeneities within the sand material, or to the measurement technique used to obtain the 0.5-ISOCHLOR isolines, which was a simple visual observation of the dyed salt water. GOSWAMI describes it as follows: “*The color variations [...] indicate that the dispersion zone is relatively narrow and is estimated to be about 1cm wide. Therefore the wedge delineation line [...] (which is assumed to be the 0.5 isochlor) has an error in the range of $\pm 0.5 cm$ [...]*”. As the dispersion zone was estimated to be about 1cm wide an in such a way identified 0.5-ISOCHLOR isoline could very well also be a 0.1 or 0.9-ISOCHLOR isoline.

Note: Recently, an interesting work was done by this group concerning this issue, i.e. image analysis used for concentration measurements: see [147].

Table 13.3: Simulation results: right boundary influx [$cm^3 \cdot s^{-1}$]

Origin of value	SS-1
Experiment	1.42
SEAWAT	1.46
OPENGEOSYS	1.41

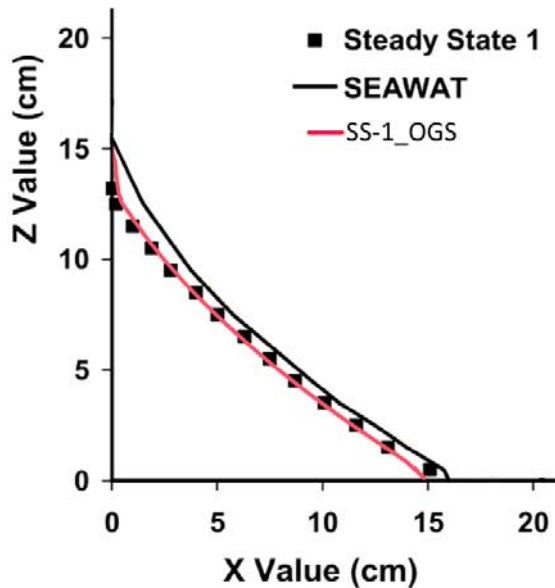


Figure 13.3.4: Comparison of the 0.5-ISOCHLOR concentration isolines of GOSWAMI's experimental data with his SEAWAT and the OPENGEOSYS steady-state simulation

In addition, tab. 13.3 shows an overview of the right boundary's inflow from GOSWAMI's measured experimental data, the SEAWAT results and the equivalent values simulated with OPENGEOSYS. Again, both simulation outputs resemble the measured experimental data within acceptable error limits.

Transient state. Figure 13.3.6 depicts the comparison of the transient simulation of the experiment with both numerical models. While SEAWAT seems to fit the measurements quite well, OPENGEOSYS shows slight differences; both results however, resemble the experimental data in an adequate way.

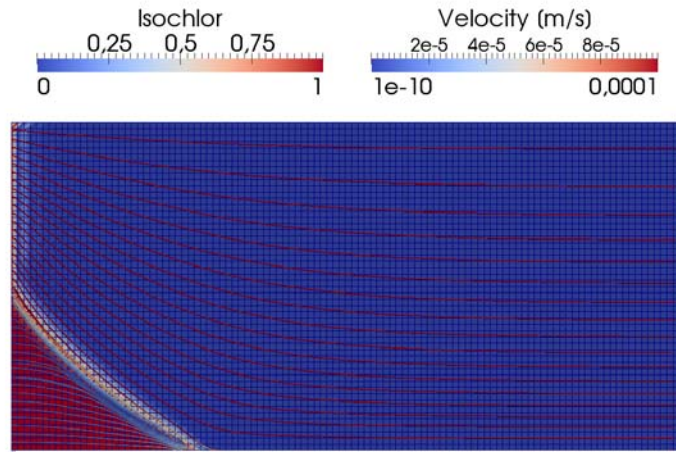


Figure 13.3.5: ISOCHLOR-concentration, flow field and grid resolution of the OPENGEOSYS steady-state simulation SS-1

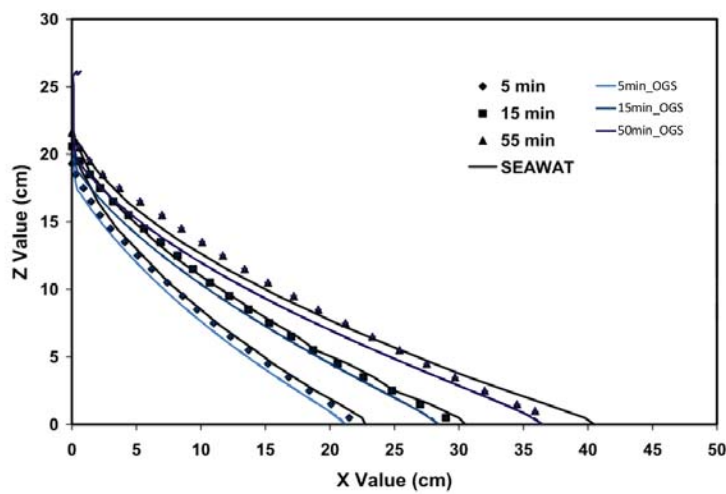


Figure 13.3.6: Comparison of the 0.5-ISOCHLOR concentration isolines of GOSWAMI's experimental data with his SEAWAT and the OPENGEOSYS transient simulation TS-1

13.4 The Schincariol Problem

13.4.1 Definition

The studies investigated the fingering patterns that result when for example saline water intrudes into a confined coastal aquifer. The configuration used in [148] was used where a solute was allowed to flow into the study domain shown in Fig. 13.4.7 with pressure heads maintained over the vertical boundaries to sustain a mean horizontal flow.

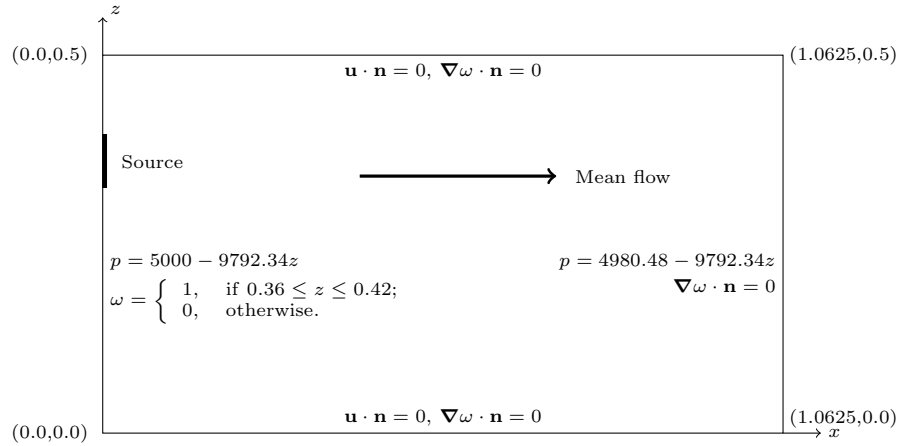


Figure 13.4.7: Model set-up

Domain setup. Using the simulation parameters in Table 13.4, the grid and time steps were refined until a solution free of numerical artifacts was obtained.

13.4.2 Results

Their results at the approximate Péclet and Courant numbers were nearly exactly reproduced in [149] as shown in Fig. 13.4.8. The Péclet and Courant numbers reported in the figure were obtained with mesh sizes of 0.3 with 4 refinements and a time step of 1hr; 0.3 with 5 refinements and a time step of 45min; and 0.2 with 5 refinements and a time step of 57min. The reproducibility of the results makes the problem defined by [148] a suitable reference from which further investigations can be founded.

Due to the rotation of the velocity field caused by density variations in the boundary layer, some salt accumulates and is trapped in the tip of the plume. Therefore, the ever-present lobe at the tip does not count as a finger and Fig. 13.4.8(c) is considered to be free from instabilities. That numerically

Table 13.4: Simulation parameters

Parameter	Notation	Value	Unit
Porosity	ϕ	0.38	–
Molecular diffusion coefficient of NaCl	D_m	1.61×10^{-9}	$m^2 \cdot s^{-1}$
Longitudinal dispersivity	α_{\parallel}	1.0×10^{-3}	m
Transverse dispersivity	α_{\perp}	2.0×10^{-4}	m
Mean flow velocity	v_0	2.75×10^{-6}	$m \cdot s^{-1}$
Domain Length in flow direction	L	1.0625	m
Viscosity of pure water at $20^\circ C$	μ_0	1.002×10^{-3}	$Pa \cdot s$
Maximal viscosity of solution (2000mg/l NaCl at $20^\circ C$)	μ_{max}	1.006×10^{-3}	$Pa \cdot s$
Density of pure water at $20^\circ C$	ρ_0	998.2	$kg \cdot m^{-3}$
Maximal density of solution (2000mg/l NaCl at $20^\circ C$)	ρ_{max}	999.7	$kg \cdot m^{-3}$
Tortuosity	ς	0.35	–
Gravity vector	\mathbf{g}	-9.81	$m \cdot s^{-2}$
Mean permeability	k_0	5.7×10^{-11}	m^2

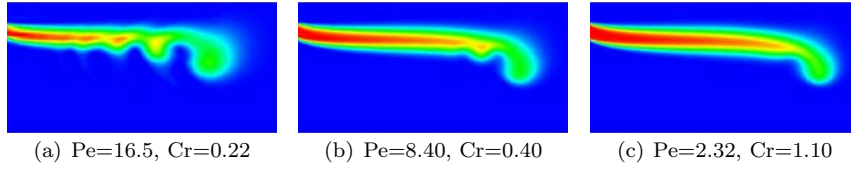


Figure 13.4.8: A reproduction of Schincariol results with full equations

stable configuration was further used by [148] to study the effect of periodically varying the width of the inflow region and by [150] to study the effect of medium heterogeneity on fingering patterns. It was also used in [149] to investigate the effects of physical variables like density, viscosity and flow velocity on the evolution of fingers.

Sample results from numerical studies in [149] without the Oberbeck-Boussinesq approximation are shown in Fig. 13.4.9.

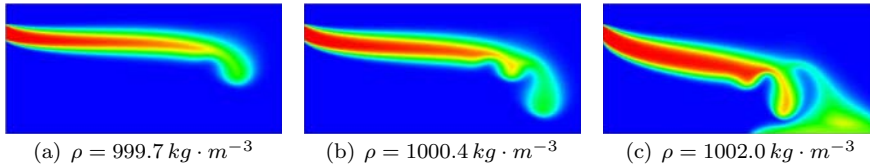


Figure 13.4.9: Fingering patterns at various densities

Chapter 14

Multiphase flow processes

by Chan-Hee Park, Joshua Taron, Ashok Singh, Wenqing Wang, Chris McDermott

In this chapter, we consider two-phase flow processes and examine two alternate combinations of primary variables in the solution of the governing equations: (1) pressure-pressure and (2) pressure-saturation. These combinations are explained in the following sections.

14.1 Isothermal Two-Phase Flow

This section ignores temperature effects and the partially saturated sample is treated as an immiscible two-phase system within the voids of the solid skeleton. In the pressure-pressure formulation the primary variables are (1) gas pressure p^g and (2) capillary pressure p^c . In the pressure-saturation formulation the primary variables are non-wetting phase saturation S^{nw} and wetting-phase pressure p^w . In the benchmarks shown here, both fluids are assumed incompressible.

Mass balance equation

Consider two-phase flow in porous media, e.g liquid (denoted by l) and gas (denoted by g). For each phase in two-phase fluid flow, mass conservation is given by the following equation,

$$\frac{\partial}{\partial t} (nS^g \rho_k^g + nS^l \rho_k^l) + \nabla \cdot (\mathbf{J}_k^g + \mathbf{J}_k^l) = Q_k, \quad (14.1)$$

where S is saturation, ρ stands for phase density, n is the porosity, \mathbf{J} is total flux. The subscript k in equation (14.1) denotes the component, e.g air ($k = a$)

or water ($k = w$), within each phase, $\gamma = (g, l)$. For any phase $\gamma = (g, l)$, an advection vector $\mathbf{J}_{A_k}^\gamma$ and a diffusion vector $\mathbf{J}_{D_k}^\gamma$ comprise the total flux, i.e,

$$\mathbf{J}_k^\gamma = \mathbf{J}_{A_k}^\gamma + \mathbf{J}_{D_k}^\gamma. \quad (14.2)$$

According to Darcy's law, the advective part of the total flux may be written as

$$\mathbf{J}_{A_k}^\gamma = -\rho_k^\gamma \frac{\mathbf{k} k_{rel}^\gamma}{\mu^\gamma} (\nabla p^\gamma - \rho^\gamma \mathbf{g}), \quad (14.3)$$

where \mathbf{k} is the intrinsic permeability, k_{rel}^γ is the relative permeability of the phase, and μ^γ is the viscosity.

The diffusive part of the total flux is given by Fick's law

$$\mathbf{J}_{D_k}^\gamma = -n S^\gamma \rho^\gamma \mathbb{D}_k^\gamma \nabla \left(\frac{\rho_k^\gamma}{\rho^\gamma} \right), \quad (14.4)$$

where \mathbb{D} is the diffusion coefficient tensor. Since $\rho^\gamma = \rho_a^\gamma + \rho_w^\gamma$, we have

$$\mathbf{J}_{D_w}^\gamma + \mathbf{J}_{D_a}^\gamma = \mathbf{0} \quad (14.5)$$

under the assumption $\mathbb{D}_a^\gamma = \mathbb{D}_w^\gamma$.

Consider a water-air mixture. We expand the mass balance equation (14.1) with the flux defined in equations (14.2) based upon the above equations (14.2, 14.3, 14.4). For the water component, the diffusive part of the total flux takes the form

$$\mathbf{J}_{D_w}^l = -n S^l \rho^l \mathbb{D}_w^l \nabla \left(\frac{\rho_w^l}{\rho^l} \right), \quad \mathbf{J}_{D_w}^g = -n S^g \rho^g \mathbb{D}_w^g \nabla \left(\frac{\rho_w^g}{\rho^g} \right). \quad (14.6)$$

Obviously, $\mathbb{D}_w^l = \mathbf{0}$. Therefore, the mass balance equation for water component can be written as follows

$$\begin{aligned} & \frac{\partial}{\partial t} (n S^g \rho_w^g + n S^l \rho_w^l) - \nabla \cdot \left[\rho_w^l \frac{\mathbf{k} k_{rel}^l}{\mu^l} (\nabla p^l - \rho^l \mathbf{g}) \right] \\ & - \nabla \cdot \left[\rho_w^g \frac{\mathbf{k} k_{rel}^g}{\mu^g} (\nabla p^g - \rho^g \mathbf{g}) \right] - \nabla \cdot \left[n S^g \rho^g \mathbb{D}_w^g \nabla \left(\frac{\rho_w^g}{\rho^g} \right) \right] = Q_w. \end{aligned} \quad (14.7)$$

Since the capillary pressure p^c is chosen as one of the two unknowns of equation (14.1) and $S^g = 1 - S^l$, equation (14.7) becomes

$$\begin{aligned} n(\rho_w^l - \rho_w^g) \frac{\partial S^l}{\partial t} + (1 - S^l)n \frac{\partial \rho_w^g}{\partial t} - \nabla \cdot \left[\rho_w^l \frac{\mathbf{k}k_{rel}^l}{\mu^l} (\nabla(p^g - p^c) - \rho^l \mathbf{g}) \right] \\ - \nabla \cdot \left[\rho_w^g \frac{\mathbf{k}k_{rel}^g}{\mu^g} (\nabla p^g - \rho^g \mathbf{g}) \right] - \nabla \cdot \left[nS^g \rho^g \mathbb{D}_w^g \nabla \left(\frac{\rho_w^g}{\rho^g} \right) \right] = Q_w. \end{aligned} \quad (14.8)$$

Similar to the previous procedure, the diffusion part of the total flux of air component can be written as

$$\mathbf{J}_{D_a}^l = -nS^l \rho^l \mathbb{D}_a^l \nabla \left(\frac{\rho_a^l}{\rho^l} \right), \quad \mathbf{J}_{D_a}^g = -nS^g \rho^g \mathbb{D}_a^g \nabla \left(\frac{\rho_a^g}{\rho^g} \right). \quad (14.9)$$

The density shift from air component to liquid ρ_a^l is very small and can be omitted. Therefore, we can assume $\mathbf{J}_{D_a}^l \approx 0$. As a consequence, the mass balance equation for air component is derived:

$$\begin{aligned} \frac{\partial}{\partial t} (nS^g \rho_a^g) - \\ \nabla \cdot \left[\rho_a^g \frac{\mathbf{k}k_{rel}^g}{\mu^g} (\nabla p^g - \rho^g \mathbf{g}) \right] - \nabla \cdot \left[nS^g \rho^g \mathbb{D}_a^g \nabla \left(\frac{\rho_a^g}{\rho^g} \right) \right] = Q_a. \end{aligned} \quad (14.10)$$

Expanding the temporary derivative term of equation (14.10) yields

$$\begin{aligned} -n\rho_a^g \frac{\partial S^l}{\partial t} + (1 - S^l)n \frac{\partial \rho_a^g}{\partial t} - \\ \nabla \cdot \left[\rho_a^g \frac{\mathbf{k}k_{rel}^g}{\mu^g} (\nabla p^g - \rho^g \mathbf{g}) \right] - \nabla \cdot \left[nS^g \rho^g \mathbb{D}_a^g \nabla \left(\frac{\rho_a^g}{\rho^g} \right) \right] = Q_a. \end{aligned} \quad (14.11)$$

The mass balance equations (14.8) and (14.11) are exactly the same as described in [151].

Pressure-pressure (pp) scheme

Based on the description of isothermal two-phase flow above, (14.8) and (14.11) can be modified in order to obtain governing equation for the isothermal two-phase flow in a porous medium. In this formulation primary variables are gas pressure p^g , and capillary pressure p^c .

The basic equations of the isothermal two-phase flow system are:

$$n\rho_w \frac{\partial S_w}{\partial p_c} \dot{p}_c + \nabla \cdot \left[\rho_w \frac{\mathbf{k} k_{relw}}{\mu_w} (-\nabla p^g + \nabla p^c + \rho_w \mathbf{g}) \right] = Q_w \quad (14.12)$$

$$\begin{aligned} -n\rho_a \frac{\partial S_w}{\partial p_c} \dot{p}_c + n(1 - S_w) \left(\frac{\partial \rho_a}{\partial p^g} \dot{p}^g + \frac{\partial \rho_a}{\partial p_c} \dot{p}_c \right) + \\ \nabla \cdot \left[\rho_a \frac{\mathbf{k} k_{rela}}{\mu_a} (-\nabla p^g + \rho_a \mathbf{g}) \right] = Q_a \end{aligned} \quad (14.13)$$

Pressure-saturation (pS) scheme

Based on the description of the isothermal two-phase flow above, (14.8) and (14.11) can be modified in order to obtain governing equation for the isothermal two-phase system. Primary variables of this formulation are wetting phase pressure p_w , and non-wetting phase saturation S_{nw} . The equations are simply algebraic manipulations of those in the previous section.

14.1.1 Liakopoulos experiment

Definition

This benchmark is based on an experiment by Liakopoulos [152] and is proposed by Lewis and Schrefler [14](pp 167–174). The Liakopoulos test case is already described and used for unsaturated consolidation in Chapter 6. There you can find the complete problem definition.

The benchmark is simulated with different element types using the pressure-pressure scheme. The grids used in such simulations are illustrated in Fig. 14.1.1.

Results

The temporal evolution of vertical profiles of primary variables (capillary and gas pressure) are given in Fig. 14.1.2. Fig. 14.1.3 shows the vertical profiles for water saturation as a secondary variable. The results agree well with the findings by Lewis and Schrefler [14].

The results of the element test are depicted in Fig. 14.1.4 for capillary pressure. A comparison if the results between the two-phase flow model and the Richards model can be found in Chapter 6.

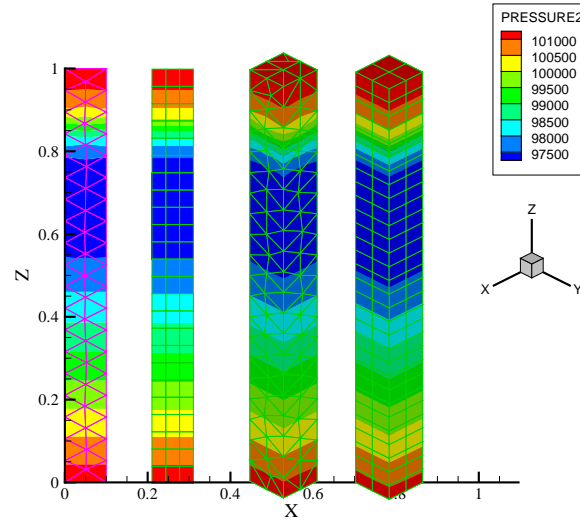


Figure 14.1.1: Grids with different element types for the Liakopoulos benchmark.

Property	Symbol	Value	Unit
Porosity	n	—	2.975×10^{-1}
Permeability	κ	m^2	4.5000×10^{-13}
Liquid dynamic viscosity	μ_w	$Pa.s$	1.0000×10^{-3}
Gas dynamic viscosity	μ_a	$Pa.s$	1.8×10^{-5}
Liquid density	ρ_w	$kg.m^{-3}$	1.0000×10^3
Gas density	ρ_a	$kg.m^{-3}$	Ideal Gas Law's
Capillary pressure	p^c	Pa	Experimental Curve
Relative permeability	κ_{relw}	—	Experimental Curve
Relative permeability	κ_{rela}	—	Brook-Corey functions

Table 14.1: Material parameters for the Liakopoulos problem.

14.1.2 Buckley-Leverett problem

Buckley and Leverett [153] developed a semi-analytical solution for the displacement of two immiscible fluids in porous media. Assuming constant fluid density and porosity, and no source/sink terms, the fluid mass balance equation can be simplified to obtain

$$n \frac{\partial S^\gamma}{\partial t} = -\nabla \cdot \mathbf{q}^\gamma. \quad (14.14)$$

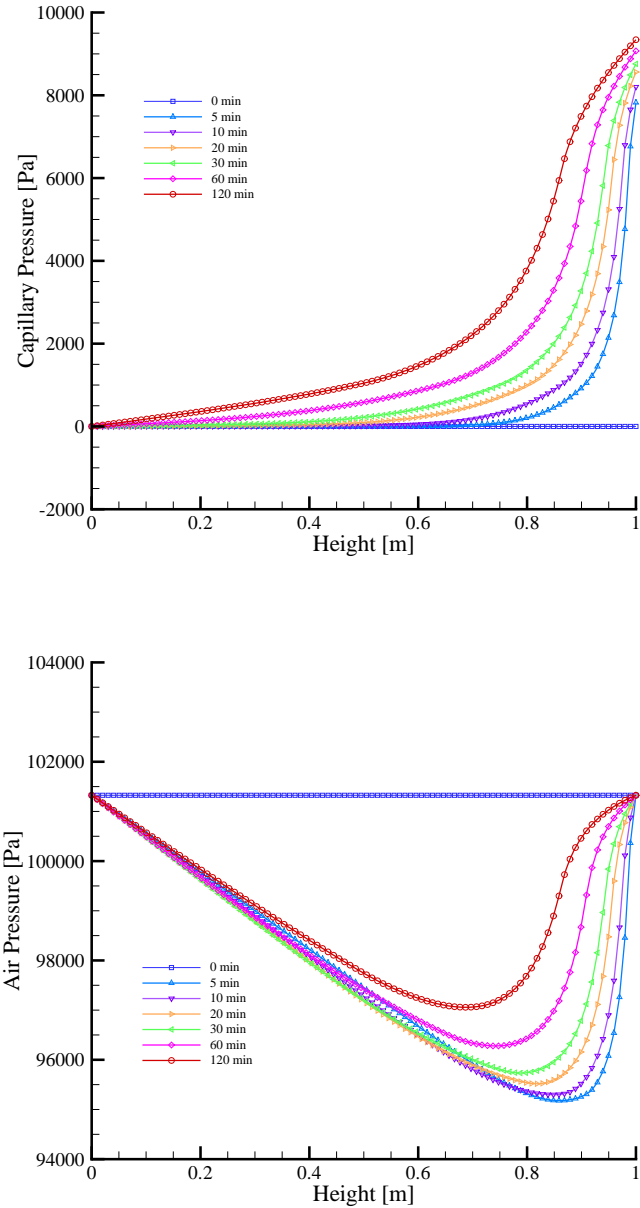


Figure 14.1.2: Vertical profiles of capillary (top) and gas pressures (bottom).

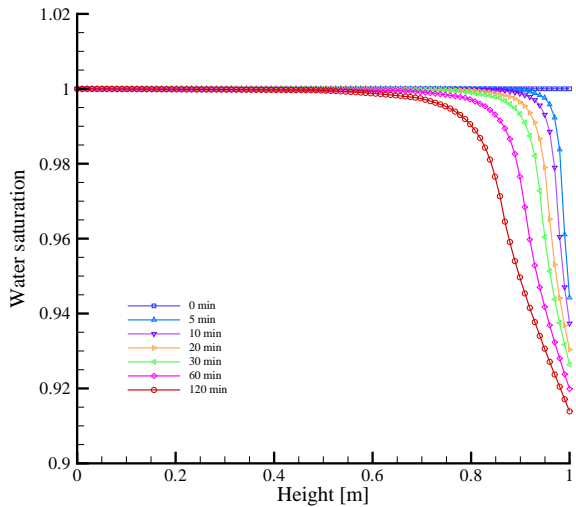


Figure 14.1.3: Profile of water saturation.

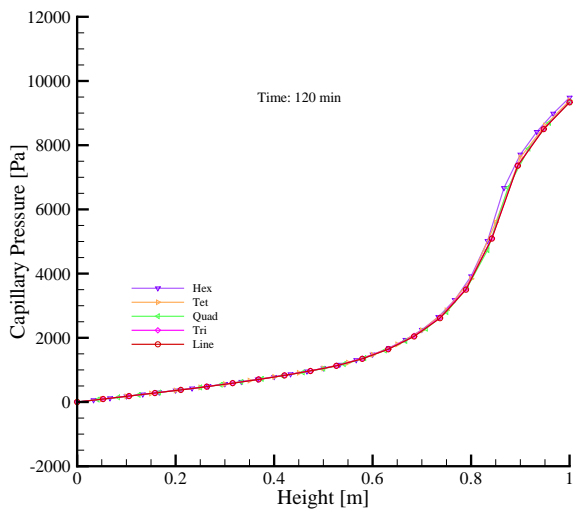


Figure 14.1.4: Results of element test.

Buckley and Leverett derived the following expression

$$\frac{\partial S^l}{\partial f^l} = \frac{q_{tot}}{n} \frac{\Delta t}{\Delta x} \quad (14.15)$$

with the fractional flow function $f^\gamma = q^\gamma / q_{tot}$

$$f^1 = \left(1 + \frac{\mu_1}{k_1} \frac{k_2}{\mu_2} \right)^{-1} \quad (14.16)$$

where 1 and 2 are the fluid phase numbers. The position of the shock front separating the two fluid phases can be calculated from the following expression

$$\Delta x = -\frac{q_{tot}}{n} \frac{\partial f^l}{\partial S^l}. \quad (14.17)$$

Buckley and Leverett suggested that the capillary pressure is a function of the saturation only. Note that the original Buckley-Leverett solution considered phases of water and oil. Moreover, they assumed that the condition that the derivative of the capillary pressure with respect to saturation is zero ($dp_{cwo}/dS_{wo} = 0$) is a sufficient approximation that both gradients of water and oil are equal to each other

$$\frac{\partial p_w}{\partial x} = \frac{\partial p_o}{\partial x} + \frac{\partial p_{cwo}}{\partial x} = \frac{\partial p_o}{\partial x} + \frac{dp_{cwo}}{dS^w} \frac{\partial S^w}{\partial x} = \frac{\partial p_o}{\partial x}. \quad (14.18)$$

Definition

The Buckley Leverett problem is frequently used to test numerical models for the functional relation between relative permeability and saturation. In comparison to the analytical solution, the problem is simplified to describe one fluid displacing the other residing fluid in aquifers or reservoirs. In the derivation of the analytical solution, the effect caused by capillary forces between two fluids is not considered.

A non-wetting phase displaces a wetting phase from left to right. The initial total velocity of the two-phase system is 1.0 m/s . The ratio of the dynamic viscosities is one, residual saturations are zero and the Brooks-Corey function ($\lambda = 2$) is used for the relative permeabilities. A space-time discretization of delta x = 0.025 m and delta t = 0.005 . The total simulation time is 0.4 s .

Results: pS-Global

The mass conservation equation is converted to a volumetric one by dividing through by fluid density,

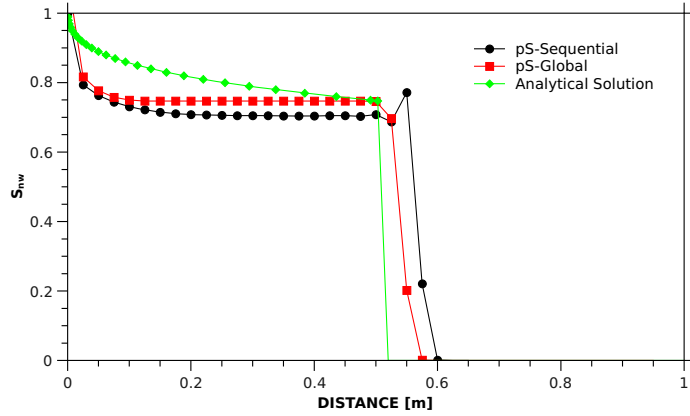


Figure 14.1.5: Comparison of coupling schemes and analytical solution for the BL problem.

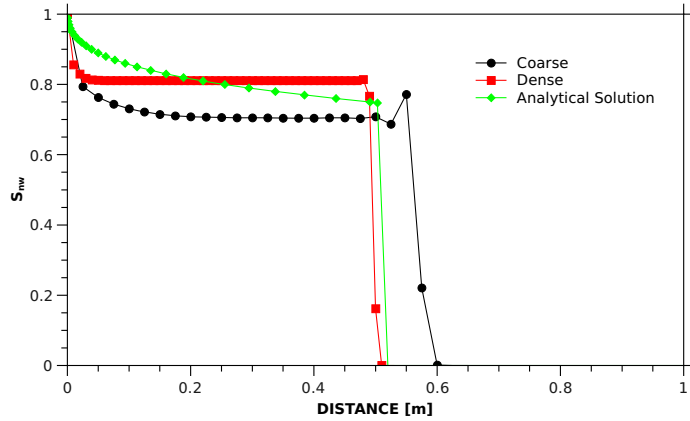


Figure 14.1.6: Comparison of grid discretizations for the BL problem with sequential coupling.

$$n \frac{\partial S_w}{\partial t} - \nabla \cdot \left(\frac{\mathbf{k} k_{relw}}{\mu_w} (\nabla p_w - \rho_w \mathbf{g}) \right) = q_w \quad (14.19)$$

$$n \frac{\partial S_{nw}}{\partial t} - \nabla \cdot \left(\frac{\mathbf{k} k_{relnw}}{\mu_{nw}} (\nabla p_{nw} - \rho_{nw} \mathbf{g}) \right) = q_{nw}. \quad (14.20)$$

In the pressure-saturation scheme, OpenGeoSys solves these two equations in a global-implicit scheme or as a total pressure based sequential coupling. As shown in Fig. 14.1.5, the global-implicit scheme produces more accurate result compared to that obtained by the sequential-coupling scheme. The result has little oscillation and is closer to the analytical solution, particularly in the location of the sharp front of the intruding fluid.

One important note is that the global scheme is sensitive to matrix solvers. The LIS solver (BiCG with Jacobi preconditioned) works well on Windows. However, this iterative solver for this benchmark takes much more time than the PARDISO (a parallel direct solver) that works only on Unix with OpenGeoSys.

Results: pS-Sequential

Adding (14.19) and (14.20) and using the relation $S_{nw} + S_w = 1$ and $p^c(S_w) = p_{nw} - p_w$, we get the equation for wetting phase pressure, p_w and non-wetting phase saturation, S_{nw} .

$$-n \frac{\partial S_{nw}}{\partial t} - \nabla \cdot \left(\frac{\mathbf{k} k_{relw}}{\mu_w} (\nabla p_w - \rho_w \mathbf{g}) \right) = q_w \quad (14.21)$$

$$\begin{aligned} \nabla \cdot \left(\frac{\mathbf{k} k_{relw}}{\mu_w} (\nabla p_w - \rho_w \mathbf{g}) \right) + \nabla \cdot \left(\frac{\mathbf{k} k_{relnw}}{\mu_{nw}} (\nabla p_w + p_c - \rho_{nw} \mathbf{g}) \right) + \\ q_w + q_{nw} = 0 \end{aligned} \quad (14.22)$$

In (14.21), non-wetting phase saturation, S_{nw} can be easily solved explicitly with the known pressure obtained from (14.22). The analytical solution for the frontal location of the infiltrating fluid is compared with alternate discretizations in Fig. 14.1.6. The diffusion term for saturation omitted in the BL equation makes the analytical solution purely advective, with a sharp advancing front. Handling this purely advective transport in numerical models introduces some numerical dispersion, and tighter discretizations will capture the low diffusive front with greater accuracy.

Results: CO_2 Injection

Based on the Buckley and Leverett solution, we assume saturated CO_2 displacing H_2O with constant fluid properties. Fig. 14.1.7 shows the saturation profile, S_w , along 1 m column calculated with line element with space-time discretization of $\delta x = 0.025$ m and $\delta t = 0.005$ s. The total simulation time is 0.4 s; using the global implicit pressure-saturation model. Based on linear relation between saturation and relative permeability, the saturation profile, S_w is shown in Fig. 14.1.8.

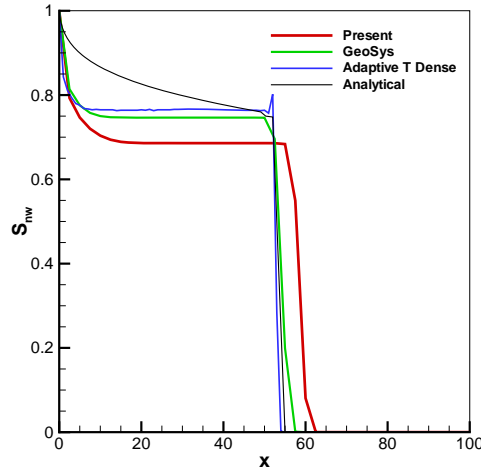


Figure 14.1.7: Saturation profile obtained with present analysis along with others.

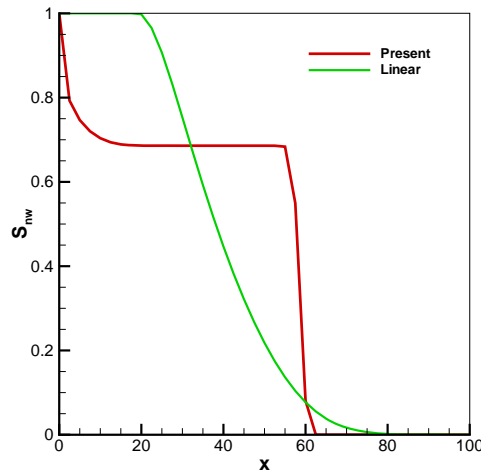


Figure 14.1.8: Saturation profile obtained with Brooks-Corey relative permeability function and a linear permeability-saturation function.

Property	Symbol	Value	Unit
Column length	L	m	1.0
Porosity	n	—	2.0×10^{-1}
Permeability	κ	m^2	1.0×10^{-10}
Water dynamic viscosity	μ_w	$Pa.s$	1.0×10^{-3}
Gas dynamic viscosity	μ_{nw}	$Pa.s$	7.0343×10^{-4}
Water density	ρ_w	$kg.m^{-3}$	1.0×10^3
Gas density	ρ_{nw}	$kg.m^{-3}$	7.73×10^2
Capillary pressure	$p^c(S)$	Pa	0
Relative permeability	$\kappa_{rel}(S)$	—	Brook-Corey functions

Table 14.2: Material parameters for the BL problem.

14.1.3 McWhorter problem

It is assumed that the flow of both wetting and non-wetting phases can be adequately described by Darcy's law if the phases are immiscible and incompressible

$$n \frac{\partial S^\gamma}{\partial t} + \nabla \cdot \mathbf{q}^\gamma = 0, \gamma = w, nw \quad (14.23)$$

$$\mathbf{q}^\gamma = -\mathbf{K} \lambda^\gamma \nabla p^\gamma \quad (14.24)$$

where λ_w and λ_{nw} are mobility of the wetting and non-wetting fluid. Both phase are linked by the state equation $S_w + S_{nw} = 1$ and $p_c = p_g - p_w$. Here total flux, $\mathbf{q}_t = \mathbf{q}_w + \mathbf{q}_{nw}$ and p_c is a function of S_w .

A formulation that is often used for two phase flow problems is the so-called fractional flow model. The attractiveness of this formulation is that the model becomes more accessible to analysis. Subtracting equation (14.1.24) for both phases we have

$$\mathbf{q}_w = f \mathbf{q}_t - D \frac{\partial S_w}{\partial x} \quad (14.25)$$

where

$$f = \frac{1}{1 + \frac{\lambda_{nw}}{\lambda_w}}, \quad D = -\lambda_{nw} f \frac{\partial p_c}{\partial S_w}. \quad (14.26)$$

The first term on the right of equation (14.25) dictates the rate at which flux is injected on the boundary and the second term represent the additional force due to the gradient of capillary pressure. Inserting equation (14.25) into equation (14.28) for the wetting phase and assuming that total flux, \mathbf{q}_t is space invariant

$$\frac{\partial}{\partial x} \left(D \frac{\partial S_w}{\partial x} \right) - \mathbf{q}_t \frac{\partial f}{\partial S_w} \frac{\partial S_w}{\partial x} = n \frac{\partial S_w}{\partial t}. \quad (14.27)$$

In the last benchmark (Buckley and Leveret) it is assumed that the force due to the gradient of capillary pressure is very small relative to total flux, \mathbf{q}_t , and hence the second order term is suppressed in the equation.

Including capillarity, model verification can occur against the analytical solution of McWhorter and Sunada (1990). They developed an exact quasi-analytical solution of equation (14.27) for unidirectional displacement of a non-wetting phase by a wetting phase using the concept of a fractional flow function.

The fractional flow function is defined as the ratio of wetting phase flux, \mathbf{q}_w to the total flux, \mathbf{q}_t . It has been shown that this ratio is function of S_w only, when \mathbf{q}_t is inversely related to square root of the time.

Definition

The test benchmark problem for capillary effects is formulated as if the instantaneous displacement occurs in a one-dimensional horizontal reservoir initially occupied by oil. Solution has been obtained by solving the governing equations (14.13) by the pressure-pressure scheme described above. Different from the Buckley-Leverett problem, here flow is governed by capillary forces when water saturation at the left end of the horizontal column is kept to be one, while the right end is kept to be zero flux. Therefore, no source term exists, and flow is by capillary force alone.

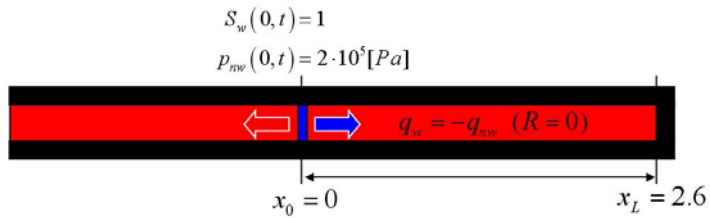


Figure 14.1.9: Schematic of the benchmark formulated to test McWhorter and Sunada's analytical solution.

Results

Based on the above discussion OpenGeoSys produces an agreeable solution. Fig. 14.1.10 shows the water saturation profile, S_w with a fine grid along with 2.6m long horizontal column for different time steps. Line elements have been used with the time and space discretization $\delta t = 0.5s$ and $\delta x = 0.05m$ respectively.

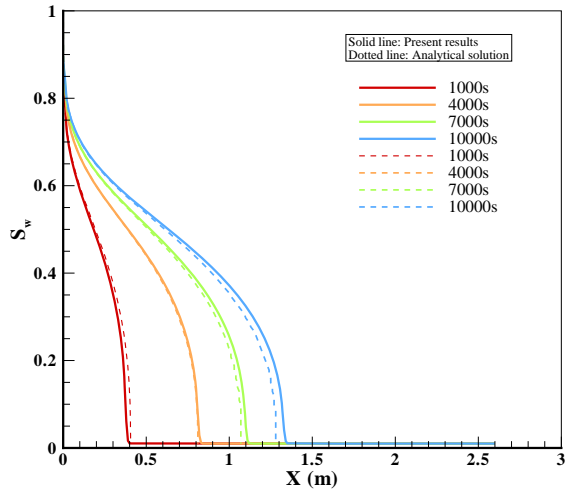


Figure 14.1.10: Water saturation, S_w profile of the present result along with analytical solution based on one by McWhorter.

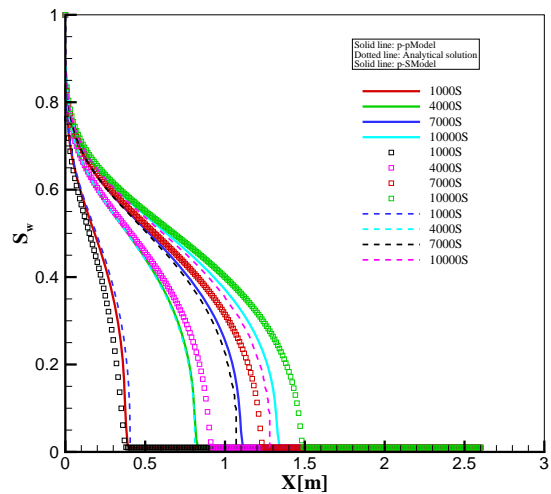


Figure 14.1.11: Water saturation, S_w profile in sequential iterative coupling scheme.

Next, we solve exactly same problem using the total pressure based pressure-saturation model in a sequential iterative coupling scheme. Unlike the pressure-pressure model, one downside for the total-pressure-based saturation model is that it is less accurate for problems dominated by capillarity (see Fig. 14.1.11). Since the pressure-pressure model directly solves for capillary pressure as a primary variable, the model has an advantage for the capillary related problems. On the other hand, the total-pressure-based saturation model is limited to the problems when dP_c/dS_w is close to zero. The condition for dP_c/dS_w close to zero is caused physically in the case of fractures, shear zones, and transitions between heterogeneities.

Property	Symbol	Value	Unit
Column length	L	m	2.6
wetting dynamic viscosity	μ_w	$Pa.s$	1.0×10^{-3}
non-wetting dynamic viscosity	μ_{nw}	$Pa.s$	1.0×10^{-3}
wetting phase density	ρ_w	$kg.m^{-3}$	1.0×10^3
Non-wetting phase density	ρ_{nw}	$kg.m^{-3}$	1.0×10^3
Permeability	\mathbf{K}	m^2	1.0×10^{-10}
Porosity	n	--	3.0×10^{-1}
Residual saturation of water	S_{rw}	--	0
Residual saturation of oil	S_{nrw}	--	0
Entry pressure	p_d	Pa	5.0×10^3
Soil distribution index	λ	--	2.0
Capillary pressure	$p^c(S_{eff})$	Pa	Brooks-Corey model
Relative permeability	$\kappa_{rel}(S_{eff})$	--	Brooks-Corey model

Table 14.3: Material parameters for the McWhorter problem.

14.1.4 Kueper problem

Both primary variable schemes are now further tested with a benchmark chosen to examine two-phase flow in heterogeneous media. Kueper and Frind (1991) developed a model to simulate their experiment for DNAPL penetration (Kueper et al., 1989). The simultaneous movement of a dense non-wetting phase (DNAPL) through an initially wetting phase (water) saturated heterogeneous porous media may be represented mathematically as a case of two-phase flow. A distinctive feature of the solution is that the primary variables solved for, wetting phase pressure and wetting phase saturation, are both existent throughout the solution domain regardless of whether the non-wetting phase is present.

The continuity equation of each phase (γ) can be defined by

$$\frac{\partial(n\rho^\gamma S^\gamma)}{\partial t} + \nabla \cdot (\rho^\gamma \mathbf{q}^\gamma) = \mathbf{Q}^\gamma, \gamma = w, nw \quad (14.28)$$

where n is porosity, S^γ is saturation, ρ^γ is density, \mathbf{Q}^γ is a source or sink term, and \mathbf{q}^γ is the Darcy velocity for phase γ defined by

$$\mathbf{q}^\gamma = -\mathbf{K} \frac{\kappa_r^\gamma}{\mu^\gamma} (\nabla p^\gamma - \rho^\gamma \mathbf{g}), \gamma = w, nw \quad (14.29)$$

where κ_r^γ is relative permeability, μ^γ is viscosity, p^γ is pressure for phase γ , \mathbf{K} is intrinsic permeability tensor and \mathbf{g} is the gravitational vector.

Inherently for saturation, the sum of all saturation in pore space is

$$\sum S^\gamma = 1. \quad (14.30)$$

Assuming relative preference (i.e., wettability) of the fluid to media exists and it is not negligible, the capillary pressures relation for a two-phase system is defined over representative elementary volume (REV) by

$$p_c = p_{nw} - p_w \quad (14.31)$$

where p_c is capillary pressure, p_{nw} is pressure for the non-wetting phase fluid and p_w is the wetting phase fluid.

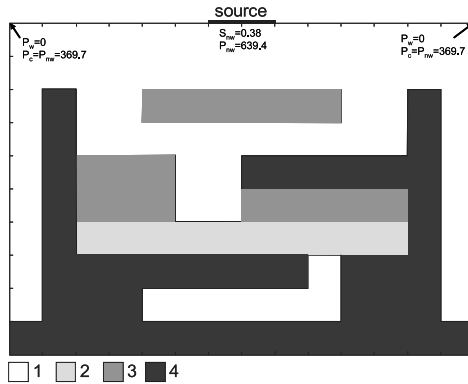


Figure 14.1.12: Configuration of heterogeneous media in parallel-plate cell.

Definition

A $60\text{cm} \times 80\text{cm} \times 0.6\text{cm}$ parallel-plate glass-lined cell was packed with four types of sands and initially fully saturated with water. The configuration of the assembled sand lenses and the two sets of the boundary conditions for the $p_w - S_{nw}$ and $p_c - p_{nw}$ schemes are illustrated in Fig. 14.1.12. Concerning to the constitutive relation between relative permeability and saturation and capillary pressure and saturation, they have used the Brooks-Corey model.

Properties of sands for the Brooks-Corey model are measured experimentally and summarized in the following tables. The numerical solutions obtained from the $p_w - S_{nw}$ scheme and the $p_c - p_{nw}$ scheme for the benchmark Kueper and Frind (1991) are compared against each other in Fig. 14.1.13.

Fluid properties	Unit	Wetting fluid	Non-wetting fluid
Density	$kg \cdot m^{-3}$	1.0×10^3	1.0×10^3
Viscosity	$Pa \cdot s$	1.0×10^{-3}	1.0×10^{-3}
Residual saturation	-	0.0	0.0
Maximum saturation	-	1.0	1.0

Table 14.4: Fluid and medium properties.

Medium properties	Unit	Medium
Δx	m	0.01
Δt	s	100
Porosity	-	0.3
Intrinsic permeability	m^2	1×10^{-10}
Brook-Corey's index	-	2
Entry pressure	Pa	5×10^3

Table 14.5: Space and time discretization.

Property	P_d (Pa)	λ (-)	S_{wr} (-)	$k(m^2)$	n (-)
1	369.73	3.86	0.078	5.04×10^{-10}	0.40
2	434.45	3.51	0.069	2.05×10^{-10}	0.39
3	1323.95	2.49	0.098	5.26×10^{-11}	0.39
4	3246.15	3.30	0.189	8.19×10^{-12}	0.41

Table 14.6: Hydraulic properties of sands for the Brooks-Corey model.

Results

Both schemes produce DNAPL plume propagation physically until the plume reaches the less permeable media under the top medium in the model domain. The striking difference occurs at the interface between these two media. While the pwSnw scheme simulates the plume to infiltrate into the less previous medium, the $p_c - p_{nw}$ scheme forces the plume to bypass the less previous medium. A similar experiment and simulation comparison against experimental observation are also conducted by Helming and Huber (1998). They have reported unphysical fluid behavior captured by the $p_w - S_{nw}$ scheme, a

phenomenon that can be avoided with fully upwind technique (Helming and Huber, 1998).

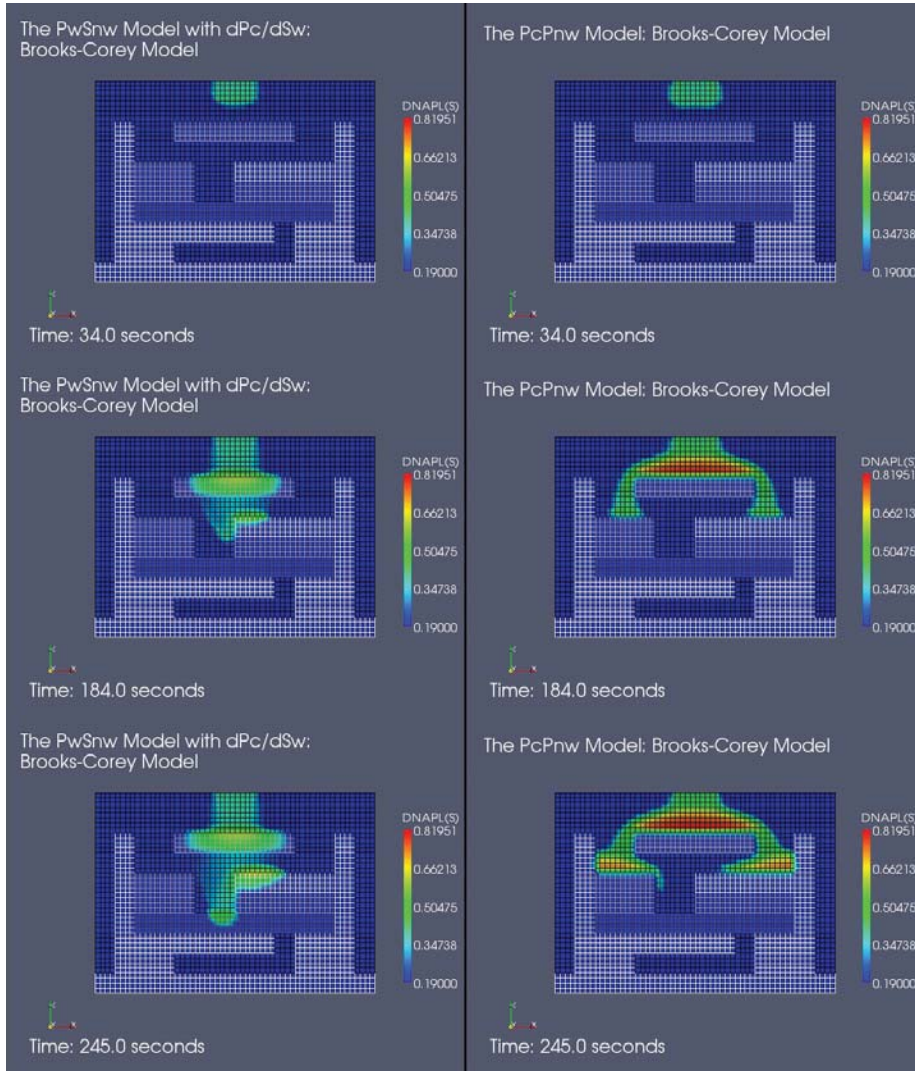


Figure 14.1.13: Comparison of the results obtained from the $p_w - S_{nw}$ and $p_c - p_{nw}$ schemes. The second column shows good agreement with observed distribution of DNAPL of the experiment (Kueper and Frind 1991).

14.2 Non-Isothermal Two-Phase Flow

The multiphase formulation is now extended to examine temperature effects in porous systems.

14.2.1 Heat Pipe problem

When an unsaturated porous medium is subjected to a constant heat flux and the temperature is sufficiently high, water is heated and vaporizes. Vapor flows under its pressure gradient towards the cooler end where it condenses. Vaporization and condensation produce a liquid saturation gradient, creating a capillary pressure gradient inside the porous medium. Condensate flows towards the hot end under the influence of a capillary pressure gradient. This is a heat pipe in an unsaturated porous medium

Udell and Fitch derived the pressure gradient of each phase in two-phase flow with heat transfer. The generalized form of the Darcy's law is used to calculate velocity fields

$$\frac{dp^g}{dx} = \frac{\eta q \nu^g}{\mathbf{k} k_{rg} H_{vap}} \quad (14.32)$$

$$\frac{dp^l}{dx} = -\frac{\eta q \nu^l}{\mathbf{k} k_{rl} H_{vap}} \quad (14.33)$$

where η is the ratio of heat transport caused by convection to the total heat-flux q (see Helming [1997]), p is phase pressure; $\nu^\gamma = \frac{\mu_\gamma}{\rho_\gamma}$; x is space coordinate in the x-direction; \mathbf{k} is intrinsic permeability; $k_{r\gamma}$ is relative permeability and H_{vap} is latent heat of water. γ is the phase superscript and g, l stand for gas and liquid phase, respectively. Gas pressure is the sum of two partial pressure, i.e. $p^g = p_a^g + p_w^g$.

The density of the gas phase is the sum of air and vapor density. Air density is according to ideal gas equation,

$$\rho_{ga} = \frac{M_a p_a}{RT}. \quad (14.34)$$

Energy transport is described by Zhou et al. [1990] as

$$q = -\kappa_{app} \frac{\partial dT}{dx} + \dot{m}_{vap} H_{vap} \quad (14.35)$$

where, T is temperature, κ_{app} is apparent thermal conductivity. Since capillary pressure is the difference of phase pressure, hence from Eq. 1, the capillary pressure gradient is

$$\frac{dp^c}{dx} = \frac{\eta q}{k H_{\text{vap}}} \left[\frac{\nu^g}{k_{\text{rg}}} + \frac{\nu^l}{k_{\text{rl}}} \right]. \quad (14.36)$$

Brooks-Corey presented a water saturation-capillary pressure relation in the following form

$$S = \left(\frac{Pd}{p^c} \right)^\lambda \quad (14.37)$$

By comparing this with Leverett's [1941] non-dimensional form we get $Pd = \sigma_0 \left(\frac{n}{K} \right)^{0.5}$ and n is medium porosity. σ_0 is interfacial tension at reference temperature T_0 . Here, S is scaled as following

$$S = \frac{S_w - S_{\text{lr}}}{1 - S_{\text{lr}} - S_{\text{gr}}}. \quad (14.38)$$

The constants $S_{\text{lr}}, S_{\text{gr}}$ are residual saturations. And for interfacial tension we have used following correlation given by Olivella and Gens[2000]

$$\sigma(T) = 0.3258C^{1.256} - 0.148C^{2.256}; \quad T \leq 633.15\text{K}, \quad (14.39)$$

where, $C = 1.0 - \frac{T}{647.3 \text{ K}}$. The Brooks-Corey relative permeability relations are

$$k_{\text{rg}} = (1 - S)^2 \left(1 - S^{\frac{2+\lambda}{\lambda}} \right); \quad k_{\text{rl}} = S^{\frac{2+3\lambda}{\lambda}}. \quad (14.40)$$

Using Eqs. (14.36-14.37), we can write following forms of saturation gradient

$$\frac{dS}{dx} = \frac{S^{1.5}}{P_d} \frac{2\eta q}{k H_{\text{vap}}} \left[\frac{\nu^g}{k_{\text{rg}}} + \frac{\nu^l}{k_{\text{rl}}} \right]. \quad (14.41)$$

Now Eq. (14.41) is integrated over two-phase zone. Where two-phase zone can be defined by imposing the limits of integration (see Udell [1985]): $S = S_0$ at $x = 0$ and $S = S_1$ at $x = L$. The saturation vapor density ρ_{sat} , depends on temperature, and is estimated by following relation

$$\rho_{\text{sat}} = 1.0 \times 10^{-3} \exp \left(a - \frac{b}{T} \right), \quad (14.42)$$

where the constants $a = 19.81$ and $b = 4975.9$. In the porous medium, we must account for a decrease in vapor density due to capillarity. The amount of decrease in vapor density is describe by the Kelvin equation as follows

$$\rho_{\text{gw}} = \rho_{\text{sat}} \exp \left(-\frac{M_w p^c}{\rho^l R T} \right) \quad (14.43)$$

where M_w is water molecular weight; ρ^l is liquid density and R is universal gas constant. From Eqs. (14.42-14.43), we get temperature as function of vapor density and capillary pressure as

$$T = \frac{A}{B} \quad (14.44)$$

where

$$A = b + \frac{M_w p^c}{\rho^l R}; B = a - 3 - \log(\rho_{gw})$$

ρ_{gw} is temperature dependent, which introduces difficulty for the temperature calculation. Hence we need to know temperature gradient, which is possible from Eq. (14.44) along with the vapor pressure gradient

$$\frac{dp_{gw}}{dx} = \frac{\eta q \nu_w^g}{k k_{rg} H_{vap}}. \quad (14.45)$$

The form of the temperature gradient is

$$\frac{dT}{dx} = \frac{\frac{BM_w}{\rho^l R} \frac{dp^c}{dx} + \frac{A}{\rho_{gw}} \frac{dp_{gw}}{dx}}{B^2 + \frac{A}{T}}. \quad (14.46)$$

Apparent thermal conductivity can be obtained from heat flux divided by temperature gradient (see Udell [1985]). The coupled differential Eqs. (14.32), (14.36), (14.41) and (14.46) are integrated using an Euler method with the following boundary conditions at $x = 0$

$$S = S_0; \quad p^g = p_0^g; \quad p^c = p_0^c; \quad T = T_0. \quad (14.47)$$

Material parameters are presented in Table 14.7.

Definition

The test benchmark problem for heat pipe effects is formulated in one-dimension. A horizontal column of length 2.6 m is filled with fluid subjected to a constant heat flux at the right end where left end temperature maintained below to the saturation temperature.

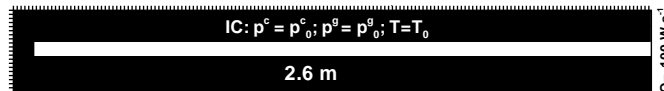


Figure 14.2.14: Schematic of the benchmark.

Results

In order to establish non-isothermal two-phase flow in the OpenGeoSys, we have verified numerical solutions with analytical results. Profile of water saturation S_w , gas phase pressure p^g , liquid phase pressure p^l and temperature T are presented in Figs. 14.2.15, and 14.2.16. Numerical solutions are agreeable. Line elements have been used with variable time steps and a non uniform space discretization. We use a combined monolithic/ staggered coupling scheme i.e. monolithic for the two-phase flow and staggered for the heat transport.

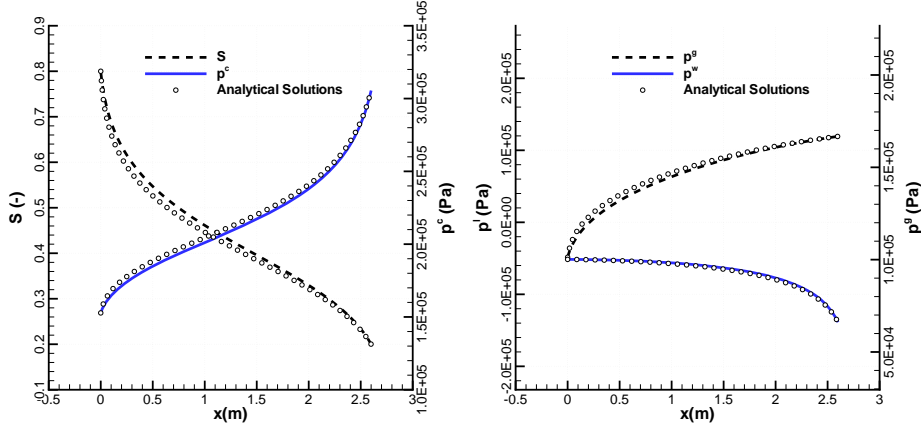


Figure 14.2.15: Comparison of water saturation and pressure profiles from present solution with analytical solution.

Table 14.7: Material parameters for the heat pipe problem.

Meaning	Symbol	Value	Unit
Column length	L	m	2.6
Liquid dynamic viscosity	μ^l	Pa.s	1.0×10^{-3}
Gas dynamic viscosity	μ^g	Pa.s	1.0×10^{-5}
Liquid density	ρ^l	kg.m ⁻³	1.0×10^3
Permeability	k	m ²	1.0×10^{-13}
Porosity	n	--	0.3
Residual saturation of water	S_{rl}	--	0.2
Residual saturation of oil	S_{rg}	--	0
Soil distribution index	λ	--	2.0
Capillary pressure	$p^c(S)$	Pa	Brooks-Corey model
Relative permeability	$\kappa_{r\gamma}(S)$	--	Brooks-Corey model

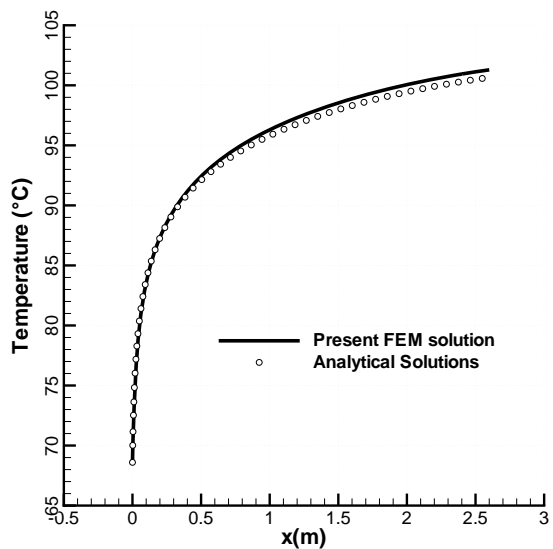


Figure 14.2.16: Comparison of temperature profile from present solution with analytical solution.

Chapter 15

Consolidation (H^nM) processes

by Joshua Taron, Norihiro Watanabe, Wenqing Wang

The purpose of the benchmarks in this chapter is to test the validity of coupled hydro-mechanical (HM) and two-phase hydro-mechanical (H^2M) processes. Mechanical compression generates a fluid pressure response, while pressure storage and dissipation modify the mechanical condition via the effective stress. The tests we use are convenient and fundamental validations of the deformation and flow modules, most importantly guaranteeing that the coupling is correct between them.

We examine real systems, where fluids, solids, and solid grains are compressible. In the single phase case, comparisons are made between two finite element coupling schemes: 1) Monolithic: solid and fluid equations solved in a single matrix and 2) Staggered: solid and fluid equations solved iteratively. Two-phase flow consolidation is also examined and then an adapted form of extended finite elements (XFEM) is used to observe the fluid-mechanical interaction in a discrete fracture-matrix system.

15.1 Single phase consolidation

Let us begin by introducing a few governing equations.

Fluid mass and momentum balance

Linear momentum balance for the fluid follows Darcy:

$$v_{ri} = \phi(v_i - v_{si}) = -\frac{k_{ij}}{\mu} \left(\frac{\partial p}{\partial x_j} + \rho g_j \right), \quad (15.1)$$

for the intrinsic permeability, k_{ij} , dynamic viscosity, μ , and density, ρ . The subscript r considers that fluid velocity is relative to motion of the deformable solid (v_{si}), so that v_i is absolute fluid velocity, and v_{ri} is relative. Conservation of fluid mass requires,

$$\frac{\partial}{\partial t} (\phi\rho) + \frac{\partial}{\partial x_i} (\phi\rho v_i) = 0. \quad (15.2)$$

Fluid properties are functions of temperature and pressure. The fluid density time derivative appearing in the mass balance equation may be expanded to

$$\frac{d\rho}{dt} = \rho \left(\frac{1}{K_f^p} \frac{dp}{dt} - \frac{1}{K_f^T} \frac{dT}{dt} \right), \quad (15.3)$$

with fluid compressibility given by $1/K_f^p = (1/\rho)(\partial\rho/\partial p)|_T$ and for the fluid thermal expansion coefficient $1/K_f^T = -(1/\rho)(\partial\rho/\partial T)|_p$. In these definitions we utilize moduli (K = inverse compressibility). Also, because thermal effects are not considered in these examples, the temperature dependence may be neglected. Utilizing the Lagrangian total derivative of a component relative to the moving solid, $d_s/dt = \partial/\partial t + v_{si}\partial/\partial x_i$, and a moving fluid, $d_f/dt = \partial/\partial t + v_{fi}\partial/\partial x_i$, substituting for absolute fluid velocity and dividing through by density gives,

$$\phi \left(\frac{1}{K_f^p} \frac{dp}{dt} + \frac{d_s\phi}{dt} + \frac{\partial v_{si}}{\partial x_i} \right) = -\frac{\partial}{\partial x_i} (v_{ri}). \quad (15.4)$$

To obtain the porosity time derivative, we expand the solid mass balance to obtain

$$\frac{d_s\phi}{dt} = \frac{(1-\phi)}{\rho_s} \frac{\partial \rho_s}{\partial t} + (1-\phi) \frac{\partial v_{si}}{\partial x_i}. \quad (15.5)$$

Substituting this gives,

$$\frac{\phi}{K_f^p} \frac{dp}{dt} + \left[\frac{\partial v_{si}}{\partial x_i} + \frac{(1-\rho_s)}{\rho_s} \frac{\partial \rho_s}{\partial t} \right] = -\frac{\partial}{\partial x_i} (v_{ri}). \quad (15.6)$$

Utilizing Biot's formulation to represent the solid density time derivative and assuming small strain yields the full fluid mass balance ([154] and [155]),

$$\left(\frac{\phi}{K_f^p} + \underbrace{\frac{(\alpha - \phi)}{K_g}}_A \right) \frac{dp}{dt} + \underbrace{\alpha \frac{\partial v_{si}}{\partial x_i}}_B = -\frac{\partial}{\partial x_i} (v_{ri}), \quad (15.7)$$

where K_g is the solid grain bulk modulus, and α is the Biot-Willis coefficient ($\alpha = 1 - K/K_g$ in an ideal, fully interconnected porous media). The bracketed terms A and B represent important couplings from the mechanical system to that of the fluid. All are vital in the HM procedure and without them the equation simplifies to a standard fluid flow equation with fluid compressibility storage in the pressure time derivative.

Solid momentum balance

We begin with the concept of effective stress,

$$\sigma'_{ij} = \sigma_{ij} + \alpha p \delta_{ij}, \quad (15.8)$$

for the effective stress, σ' , and the total stress, σ ; negative in compression. Balance of linear momentum is defined by,

$$\frac{\partial \sigma_{ij}}{\partial x_j} + F_i = 0, \quad (15.9)$$

for the body force, $F = \rho_m g$ and where $\rho_m = \phi \rho_f + (1 - \phi) \rho_s$ is density of the mixture. From the definition of strain, $\varepsilon_{ij} = (\partial u_i / \partial x_j + \partial u_j / \partial x_i) / 2$, and an arbitrary stress-strain relationship of the form $\sigma = \mathbf{D}\varepsilon(\mathbf{u})$, we write the displacement formulation of mechanical equilibrium (neglecting thermal effects) for isotropic linear elasticity,

$$\frac{\partial}{\partial x_j} \left[G \frac{\partial u_i}{\partial x_j} + (\lambda + G) \frac{\partial u_j}{\partial x_i} - \alpha p \delta_{ij} \right] + F_i = 0, \quad (15.10)$$

where G and λ are the Lamè constants. Changes to the fluid system are therefore visited in mechanical equilibrium via the effective stress.

Numerical solution scheme

The numerical solution of Eqs. 15.7 and 15.10 can be obtained with any convenient method. In these benchmarks, we use a standard Galerkin finite element spatial discretization with time discretization following a generalized first order finite difference scheme, as implemented in OpenGeoSys. Note that Eq. 15.10

is an equilibrium equation, and has no time dependency other than that imposed by coupling terms to fluid behavior. The result is a set of coupled linear equations in pressure, p , and solid displacement, u . The two equations may be solved sequentially and iteratively, or monolithically as a single system. We present results using both solution schemes in the following benchmarks.

15.1.1 Terzaghi consolidation: Monolithic and staggered approaches

In the HM problem, mechanical compression generates a fluid pressure response, while pressure storage and dissipation affect the mechanical condition via the effective stress. Terzaghi has provided the framework to test such a problem. A cartoon of the problem to be examined is shown in Fig. 15.1.1. This test is a necessary, but not fully sufficient condition for correct implementation of a hydromechanical simulator. It guarantees correct implementation of the coupling relationships between the 1)fluid and 2)mechanical system.

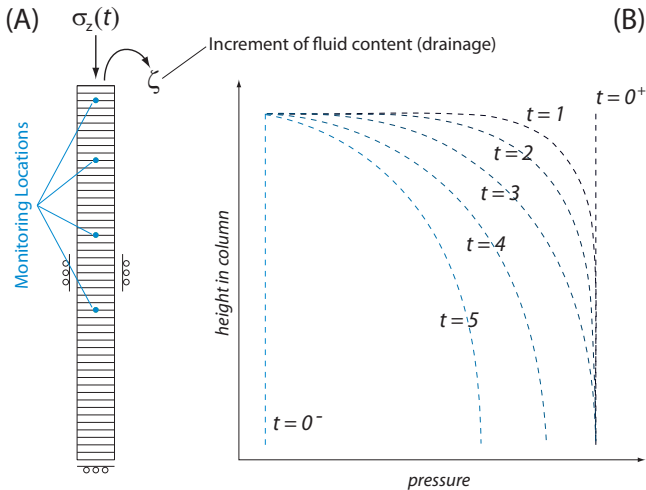


Figure 15.1.1: Terzaghi problem. A.) 2-D column ($p = 0$ initially) stress applied to top of column which is a free draining boundary. Other boundaries are no-flow and roller displacement. Stress may be applied as a single step-load, or as a function of time. Pressure and displacement are monitored in time at specific locations. B.) Anticipated (conceptual) pressure profiles within the column with the progression of time for a step-load of applied stress (in full column, not at monitoring locations).

Definition

For a single fluid phase, the analytical solution for pressure dissipation is available. The analytical solution to this problem has been utilized a number of times for this very purpose. Beginning from the 1-D fluid diffusion equation of hydrogeology (simply a fluid mass balance equation),

$$\frac{\partial p}{\partial t} - c \frac{\partial^2 p}{\partial z^2} = 0, \quad (15.11)$$

where c is 1-D fluid diffusivity. The pore pressure response to a vertical load, σ_z , applied linearly over time ($\sigma_z^{t=0^-} = 0$) to the top of the column at a rate, $\dot{\sigma}_z = d\sigma_z/dt$, is, ([156], Eq. 6.50),

$$\frac{p(z,t)}{p_0} = \left\{ 1 - \left(\frac{L-z}{L} \right)^2 - \frac{32}{\pi^3} \left[\sum_{m=0}^{\infty} \frac{(-1)^m}{(2m+1)^3} \exp[-\psi^2 ct] \cos[\psi(L-z)] \right] \right\}, \quad (15.12)$$

where the total pressure generation is

$$p_0 = \frac{L^2}{2c} (B_v \dot{\sigma}_z), \quad (15.13)$$

for the factor, $\psi = (2m+1)\pi/(2L)$, the total column length, L , and the location in the column (downward from the applied stress), z . The 1-D Skempton coefficient,

$$B_v = -\frac{\delta \bar{p}}{\delta \sigma_{zz}} \Big|_{\varepsilon_{xx}=\varepsilon_{yy}=\zeta=0} = \frac{\alpha}{K_v S_v}, \quad (15.14)$$

is given purely by micromechanical, poroelastic considerations from the uniaxial drained bulk modulus, K_v , and the 1-D specific storage, S_v (Table 15.1). The 1-D diffusivity is also a derivative of the 1-D storage:

$$c = \frac{k}{\mu S_v}, \quad (15.15)$$

and also the permeability, k , and viscosity, μ . See Table 15.1, [157], and [156] for additional details regarding poroelastic relationships. If utilizing an applied step load at time $t = 0^+$ we can generate another analytical solution for pressure, and also displacement. For this validation, we utilize only the linear loading rate. Because displacement is the primary variable in our FEM formulation, the displacement must be accurate in order to generate the correct pressure response: we find no need to reproduce the results of a step load analysis here.

Parameter	Description	Equation
B	Skempton coefficient	$\alpha/[\alpha - \phi(1 - \alpha) + \phi K/K_f]$
K^u	Undrained bulk modulus	$K/(1 - \alpha B)$
G	Shear modulus	$3K(1 - 2\nu)/(2 + 2\nu)$
ν^u	Undrained Poisson's ratio	$(3K^u - 2G)/(6K^u + 2G)$
B_v	Uniaxial Skempton coefficient	$B(1 + \nu_u)/(3 - 3\nu_u)$
K_v	Uniaxial bulk modulus	$3K(1 - \nu)/(1 + \nu)$
K_v^u	Uniaxial undrained bulk modulus	$3K^u(1 - \nu^u)/(1 + \nu^u)$
S_v	Uniaxial storage	$\alpha/(K_v B_v)$

Table 15.1: Fundamental poroelastic relationships. Many potential combinations are available, these representing only one possibility.

We choose a rather long (50m) column of rock with material properties similar to those of Berea sandstone (Table 15.2). The column is discretized uniformly into 50 FEM grid cells. Geometry is shown in Fig. 15.1.1, which shows a single column surrounding by displacement roller boundaries allowed to compress from the top where a loading rate, $\dot{\sigma}_z$, is applied at time $t = 0^+$. Fluid pressure is initially null. Compression of the column leads to a rapid pressure increase and a subsequent drainage of pressure over time from the top of the column. The load is applied quickly enough to allow pressure to build with time. The topmost boundary is free drainage for fluid flow, all others being no-flow.

Property	Symbol	Unit	Value
<i>Berea sandstone</i>			
Drained bulk modulus	K	GPa	8.0
Poisson ratio	ν	—	0.20
Porosity	ϕ	—	0.19
Permeability	k	m^2	1.9×10^{-13}
Biot-Willis coefficient	α	—	0.8
<i>Westerly granite</i>			
Drained bulk modulus	K	GPa	25.0
Poisson ratio	ν	—	0.25
Porosity	ϕ	—	0.02
Permeability	k	m^2	5.0×10^{-15}
Biot-Willis coefficient	α	—	0.6

Table 15.2: Solid properties.

Property	Symbol	Unit	Value
Bulk modulus	K_f	GPa	2.27
Density	ρ	kg/m ³	997.05
Viscosity	μ	Pa × s	8.9008 × 10 ⁻⁴

Table 15.3: Fluid properties.

Results

Simulations are conducted using both a staggered (fluid and solid equations solved iteratively) and monolithic (fluid and solid equations solved in a single matrix) with OpenGeoSys. Results are shown in Fig. 15.1.2 for two alternate material property scenarios: Berea sandstone and Westerly granite. The solution is accurate in all cases. We note a small inaccuracy in the slower loading rate for sandstone that illustrates the impact of tolerance in the time step control. Here, we add one extra data set (small dots) with tighter time control, which shows that tighter accuracy can be achieved with this adjustment.

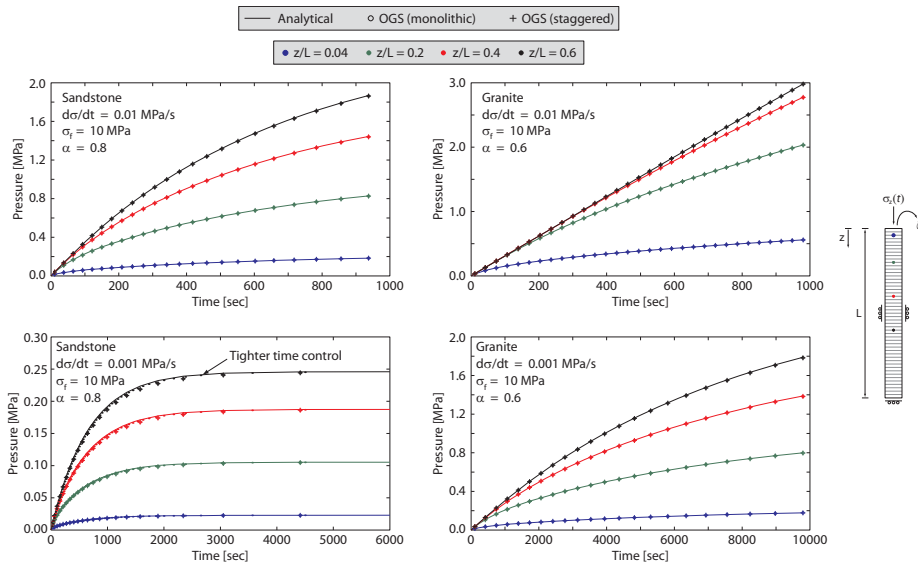


Figure 15.1.2: Results of HM coupling.

While the monolithic solution is unconditionally stable for an implicit time-stepping scheme, the staggered solution suffers limitations. When the fluid becomes highly incompressible relative to the solid, the solution will diverge. We provide the general criterion that stability is achieved with $B_v < 0.5$. This

criterion is generally independent of loading rate. The implications of this are important, such that for Westerly granite if incompressible grains are used the solution is unstable at $25^\circ C$ for the properties of Table 15.2. Stability can be enforced by increasing the value of porosity that is used, or decreasing α , or with any adjustment that brings B_v above 0.5. The staggered solution is stable for all realistic cases (everything compressible) we have tried. For very sharply applied loads such as a step load applied at $t = 0^+$, however, the staggered solution will become unstable even with this criterion. It is important for a given problem and set of solid/fluid properties to examine stability with the above benchmark before extending to the full system.

Time steps are adaptively controlled with a tolerance based on the rate of pressure change over a time step. Such a scheme is capable of ensuring accuracy in HM or H^2M problems. Note the importance of the tolerance in Fig. 15.1.2.

15.1.2 Distributed footing: Poroelastic cube (3D)

We consider a vertical cross-section through homogeneous soil. Due to symmetry we can limit the investigation to half of the domain. The model domain is then extending 8 meters in length and 5 meters in height. The problem is solved in 2D and 3D space, respectively.

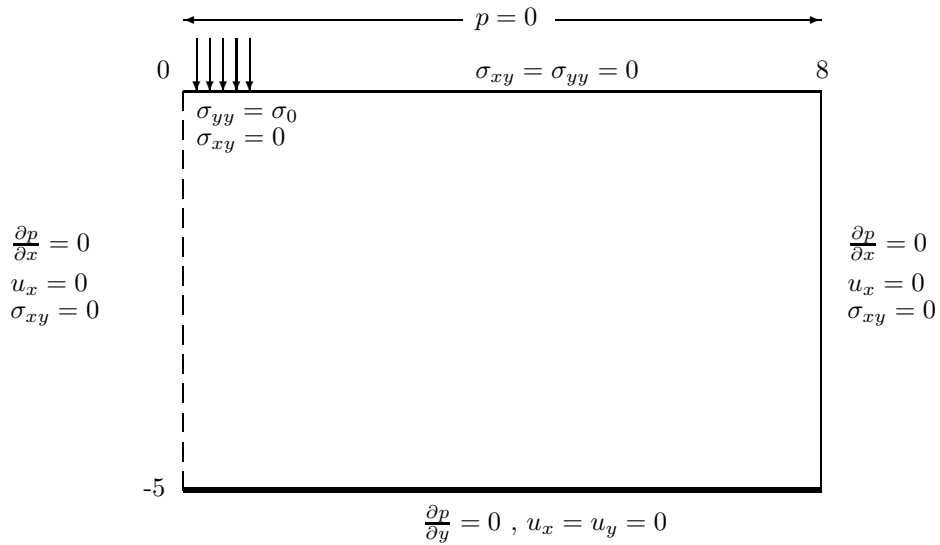


Figure 15.1.3: Conceptualization of the footing problem. Properties are Young's modulus, $E = 3 \times 10^4 \text{ N/m}^2$, Poisson's ratio, $\nu = 0.2$, permeability, $k = 10^{-10} \text{ m}^2$, and fluid viscosity, $\mu = 10^{-3} \text{ Pa s}$.

Definition

A strip loading is imposed ($\sigma_{yy} = \sigma_0$ in $x \in [0, 1]$), with zero stresses ($\sigma_{yy} = \sigma_{xy} = 0$ in $x \in (1, 8]$) and zero pressure at the top; no horizontal flux, no horizontal displacements and zero shear stresses at left and right boundaries with no vertical flux and no displacement at the bottom (Fig. 15.1.3).

Results

The 3D geometry expands the 2D domain by extruding the 2D shape by 1m in the off-plane direction (15.1.4). Results at the critical step, i.e., the first step, are shown in Fig. 15.1.6, 15.1.7 and 15.1.5. The results produced using the 2D model with triangular elements and the 3D model with tetrahedral elements match each other well, thus providing confidence in higher dimensions.

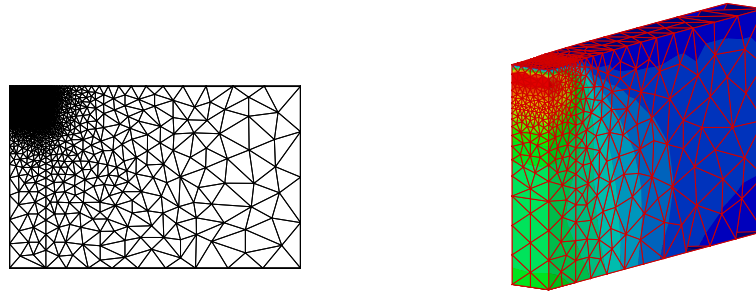


Figure 15.1.4: Mesh geometry.

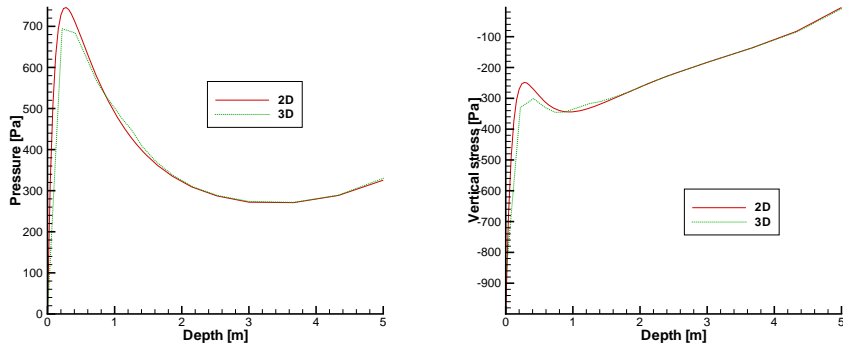


Figure 15.1.5: Comparison along symmetric axis.

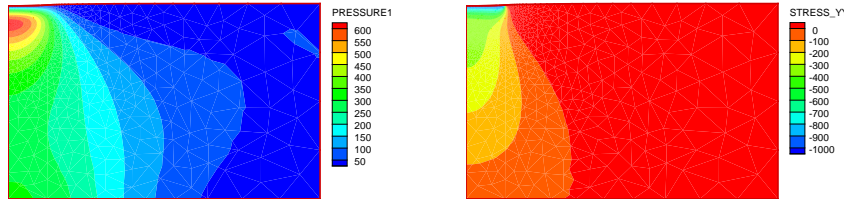


Figure 15.1.6: 2D contours.

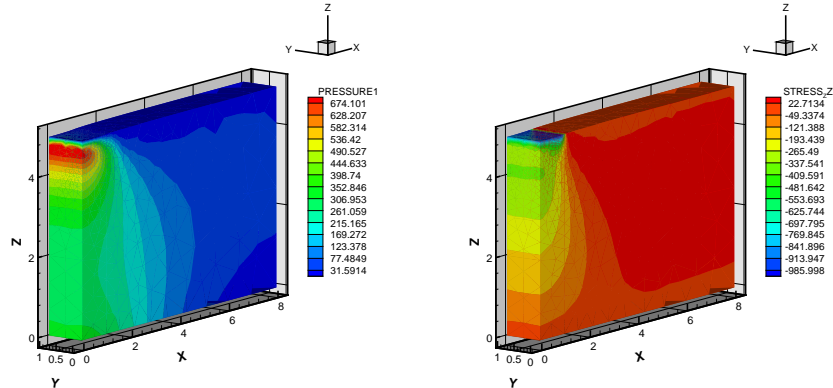


Figure 15.1.7: 3D contours.

15.1.3 Distributed footing: Poroelastic cube (3D) with dynamic consolidation

Considering the same problem design as the previous section, the mechanical calculation is now extended to allow for time-dependent deformation. In other words, solid displacements are no longer solved to equilibrium, so that solid velocity may be non-zero following solution of the mechanical system.

Definition

All stresses and pressure are zero at the beginning of deformation. Strip loading ($\sigma_{yy} = \sigma_0$ in $x \in [0, 1]$), zero stresses ($\sigma_{yy} = \sigma_{xy} = 0$ in $x \in (1, 8]$) and zero pressure at the top; no horizontal flux, no horizontal displacements and zero shear stresses at left and right hand sides; no vertical flux and no displacements at bottom (Figure 15.1.3).

Material parameters are given in Table 15.4.

Property	Value	Unit
Young's modulus	3×10^4	N/m ²
Poisson's ratio	0.2, 0.4	—
Permeability	10^{-10}	m ²
Fluid viscosity	10^{-3}	Pa s

Table 15.4: Material properties of dynamic consolidation problem.

Results

Time duration is ten time steps. The following figures, Fig. 15.1.8–15.1.11 show the distribution of state variables within the domain after 10 time steps. Such distribution is similar to the static case illustrated in Fig. 15.1.6.

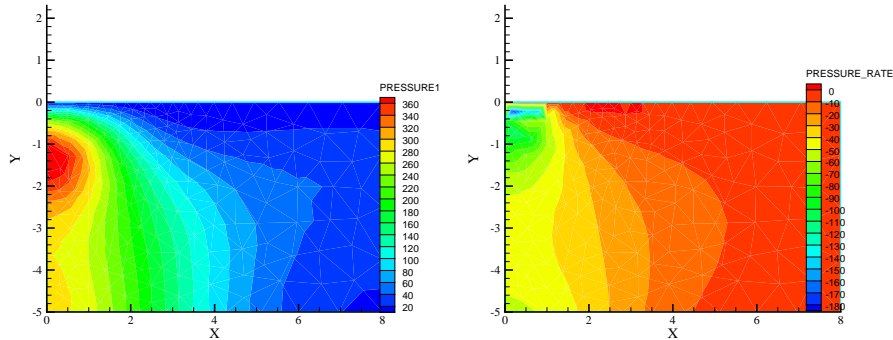


Figure 15.1.8: Fluid pressures p and rate of fluid pressure \dot{p}

15.2 Unsaturated (Richards) consolidation

Fluid mass and momentum balance

The general fluid mass balance equation for a multi-phase fluid system is simply an extension of Eq. 15.1,

$$\frac{\partial}{\partial t} (\phi S_\alpha \rho) + \frac{\partial}{\partial x_i} (\phi S_\alpha \rho v_i) = Q \quad (15.16)$$

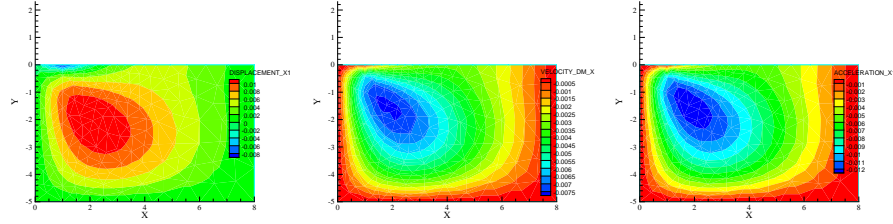


Figure 15.1.9: Displacement, its rate and acceleration: horizontal component

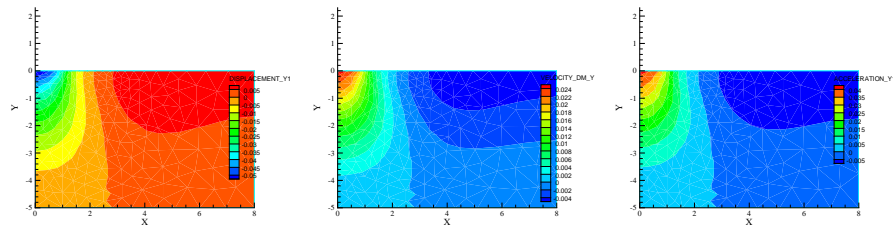


Figure 15.1.10: Displacement, its rate and acceleration: vertical component

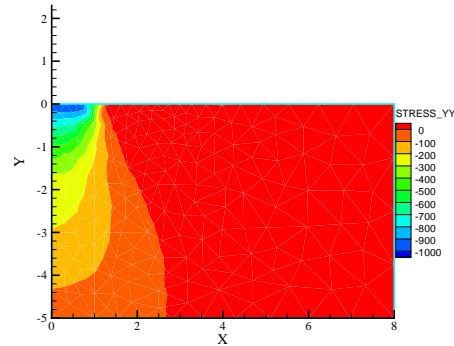


Figure 15.1.11: Vertical stress.

where S_α is saturation of fluid α and Q is the source term. We are interested in a Richards type model for the evolution of fluid pressure under the assumption that the gas phase is immobile, i.e. $v_{gi} = 0$. Assuming incompressible grains, $\alpha = 0$, and expanding terms as in the single phase case, we obtain the following Richards equation for an unsaturated deformable porous medium,

$$\left(S_w \frac{\phi}{K_w} \frac{dp_w}{dt} - \phi \rho_w \frac{dS_{nw}}{dp_c} \right) \frac{dp_w}{dt} + \nabla \cdot \left\{ \frac{\mathbf{k} k_w^r}{\mu_w} (-\nabla p_w + \rho_w \mathbf{g}) \right\} + S_w \rho_w \nabla \cdot \frac{d\mathbf{u}}{dt} = Q. \quad (15.17)$$

A constitutive equation, the water content function obtained by experiments, characterizes the relationship between p_c and S_w , and therefore the derivative dS_w/dp_c .

Solid momentum balance

The deformation process is described in the same manner as for the single phase case, but now fluid pressure acting on the grains is also dependent on the liquid saturation,

$$\nabla \cdot (\sigma - S_w p_w \mathbf{I}) + \rho \mathbf{g} = \mathbf{0} \quad (15.18)$$

FEM solution scheme

The standard Galerkin finite element approach is applied for the numerical solution of the PDEs (15.17) and (15.18) resulting into the following system of algebraic equations, here solved as a monolithic system,

$$\begin{bmatrix} \mathbf{C}_{pp} & \mathbf{C}_{pu} \\ \mathbf{0} & \mathbf{0} \end{bmatrix} \frac{d}{dt} \begin{Bmatrix} \mathbf{p}_w \\ \mathbf{u} \end{Bmatrix} + \begin{bmatrix} \mathbf{K}_{pp} & \mathbf{0} \\ \mathbf{K}_{up} & \mathbf{K}_{uu} \end{bmatrix} \begin{Bmatrix} \mathbf{p}_w \\ \mathbf{u} \end{Bmatrix} = \begin{Bmatrix} \mathbf{r}_p \\ \mathbf{r}_u \end{Bmatrix} \quad (15.19)$$

15.2.1 Terzaghi consolidation: Unsaturated

Definition

This example follows the general form of the Terzaghi consolidation used previously. Boundary conditions and model design follows roughly the experiment of Liakopoulos [152]. The physical experiment of Liakopoulos was conducted in a column packed with so-called Del Monte sand. Moisture content and tension at several points along the column were measured with tensiometers.

In the simulation, the column has a size of $0.1m \times 1m$ and is discretized into 20 quadrilateral elements (Fig. 15.2.12). Initial pressure is zero everywhere in the domain. Boundary conditions for both fluid and displacement fields are

$$\partial p / \partial \mathbf{n} = 0, \sigma_{yy} = 0, \sigma_{xy} = 0$$

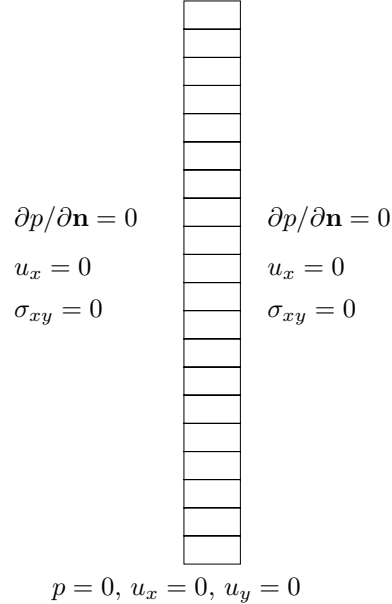


Figure 15.2.12: Boundary conditions.

depicted in Fig. 15.2.12. Such initial and boundary conditions imply that the sample is fully saturated at the beginning, the water is allowed to flow out from the bottom boundary.

Property	Value	Unit
Young's modulus, E	MPa	1.3
Poisson's ratio, ν	—	0.4
Solid grain density, ρ_s	kgm^{-3}	2000
Liquid density, ρ_w	kgm^{-3}	kgm^{-3}
Porosity, ϕ	—	0.2975
Permeability, k	m^2	4.5×10^{-13}
Water viscosity, μ_w	Pas	10^{-3}

Table 15.5: Material parameters.

The capillary pressure, $p_c(S)$, function we use is,

$$p_c = \left(\frac{1 - S}{1.9722} \times 10^{11} \right)^{\frac{1}{2.4279}}, \quad (15.20)$$

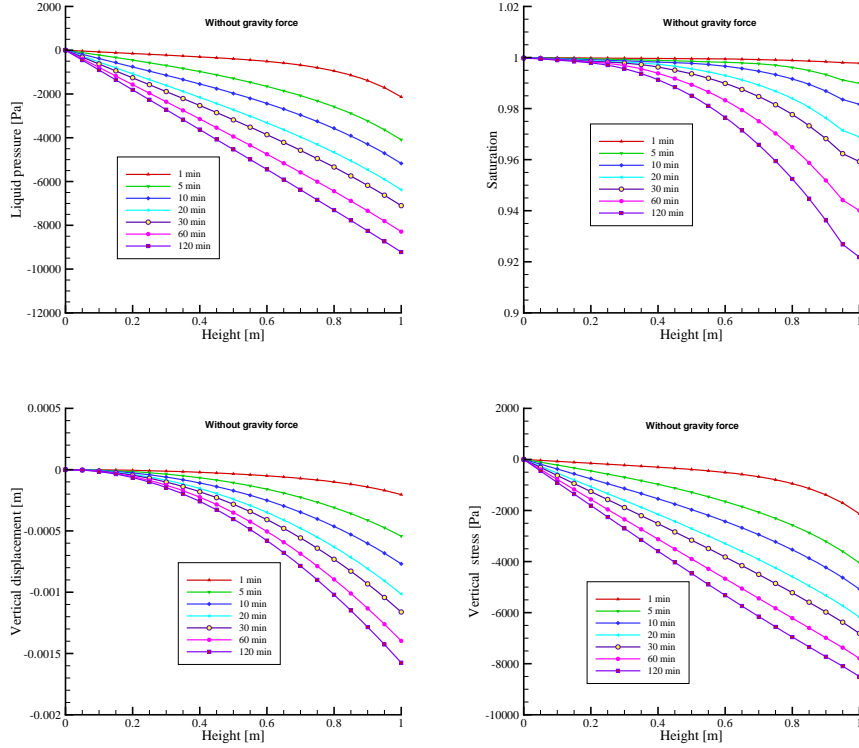


Figure 15.2.13: Simulated results without gravity force.

along with the relative permeability, $k_r(S)$, relationship,

$$k_r = 1 - 2.207(1 - S)^{1.0121} \quad (15.21)$$

fit the measured data for saturations larger than 0.84. The physical parameter are given in Table 15.5.

Results

We conduct two kinds of simulation: one including the gravity force as a load for the mechanical displacement field, and the other ignoring gravity. For the case of non-gravity, Fig. 15.2.13 shows history profile of water pressure p , water saturation S , vertical solid displacement u_y and vertical stress σ_{yy} .

The vertical profile of results obtained by taking into account the gravity force are shown in Fig. 15.2.14. If compares the saturation result with that obtained

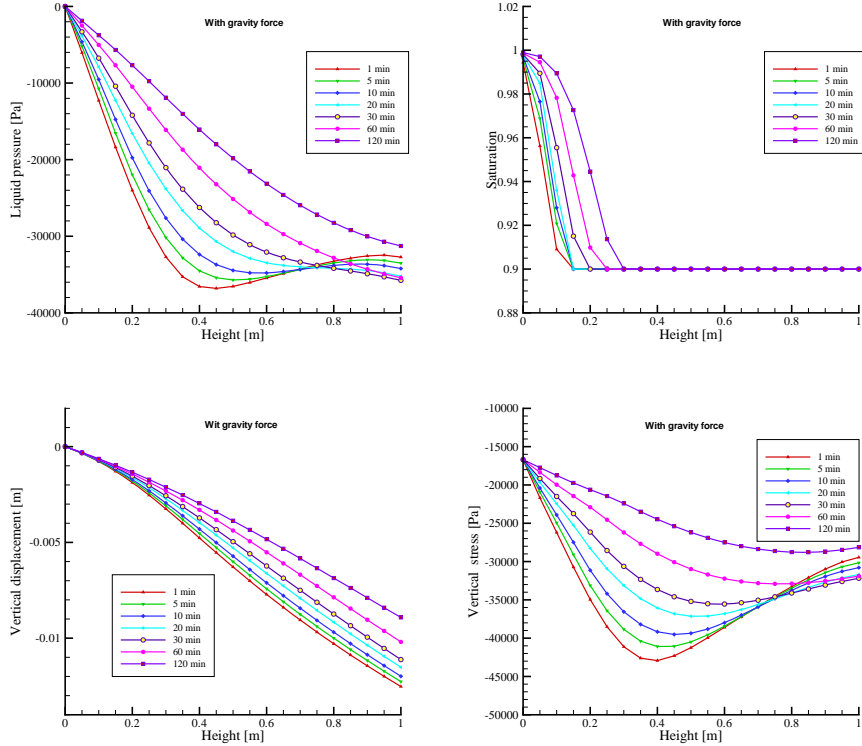


Figure 15.2.14: Simulated results with gravity force.

by ignoring the gravity force, one can easily see that the desaturation procedure is enhanced by the presence of solid gravity acting on the solid displacement field. This highlights the impact of displacement on water pressure and coupling effects between the two equation systems.

15.2.2 DECOVALEX unsaturated test case

DECOVALEX is an international code comparison project for the verification of thermo-hydro-mechanical (THM) and thermo-hydro-chemical (THC) numerical simulators [158].

Definition

The original DECOVALEX-THM benchmark definition is a 2-D problem [158]. For the comparison of different HM swelling models, we consider a simplified

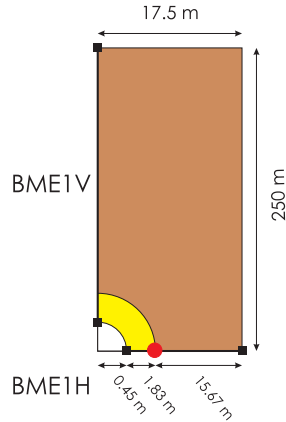


Figure 15.2.15: 2D DECOVALEX HM definition and simplification for the benchmark exercise BME1H.

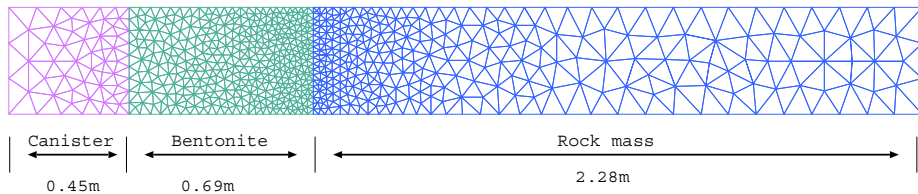


Figure 15.2.16: Mesh of the simplified BME1H model including canister, bentonite, and rock mass sections.

case representing a horizontal cross-section through the 2-D domain. Examined here is the isothermal HM consolidation problem with unsaturated flow.

The simplified model takes a rectangle shape. The mesh of the domain together with material types are shown in Fig. 15.2.16. Fig. 15.2.17 illustrates the definition of initial and boundary conditions for the horizontal cross-section. Observation points are set at $x = 0.45\text{ m}$, $x = 1.10\text{ m}$ to record temporal breakthrough curves. Material parameters for the rock mass and bentonite are given in Table 15.6.

The dependency of capillary pressure and relative permeability on liquid saturation for both rock and bentonite are depicted in Fig. 15.2.18.

Results

Fig. 15.2.19 displays a contour plot of saturation and vertical swelling stress in the domain. Swelling stress in the bentonite is clearly induced by change of

Parameter	Unit	Value
<i>Rock mass properties</i>		
Density	kg/m^3	2700
Young's modulus	GPa	35
Poisson ratio	-	0.3
Porosity	-	0.01
Saturated permeability	m^2	1.0×10^{-17}
<i>Bentonite properties</i>		
Density	kg/m^3	1600
Young's modulus	MPa	317
Poisson ratio	-	0.35
Saturated permeability	m^2	2.0×10^{-21}

Table 15.6: Solid properties of different materials.

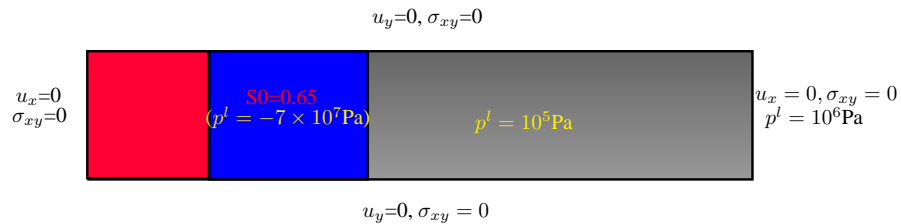


Figure 15.2.17: Simplified horizontal cross-section model.

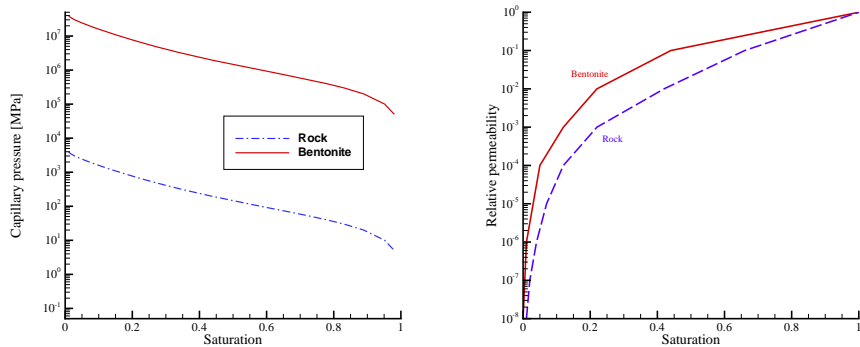


Figure 15.2.18: Capillary pressure and relative permeability functions.

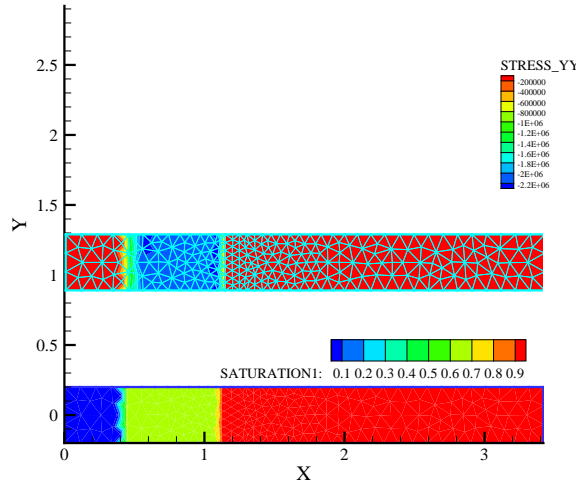


Figure 15.2.19: Distribution of saturation and vertical swelling stress

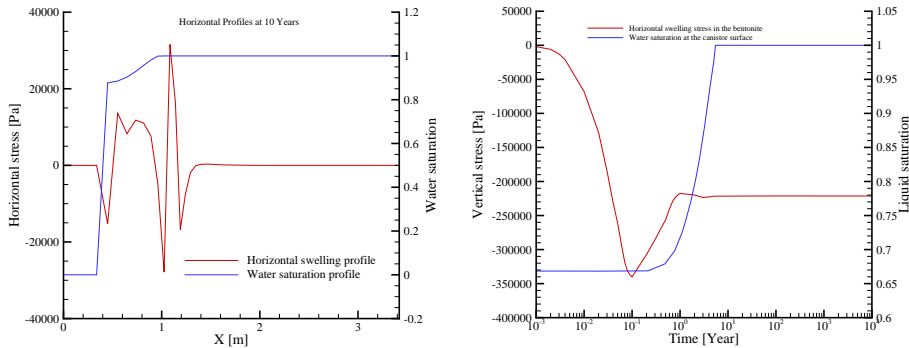


Figure 15.2.20: Horizontal profile (top) and temporal evolution at observation point (bottom) of water saturation and swelling stress

water saturation. Fig. 15.2.20 shows the simulated horizontal profiles (top) and temporal evolutions at the observation point (bottom) of water saturation and swelling stress based on the linear swelling model proposed by Rutqvist (2005) [159], which defines the increment of swelling stress to be proportional to liquid saturation increment,

$$\Delta\sigma^{sw} = \beta\Delta S_w, \quad (15.22)$$

where β is a swelling coefficient that could be called the maximum swelling stress. As the saturation change approaches unity, swelling stress approaches β .

Fig. 15.2.20 shows the simulated horizontal profiles and temporal evolutions at the observation point of water saturation and swelling stress based on the linear swelling model proposed by Rutqvist (2005) [159].

15.3 Two-phase consolidation

For the two-phase system the governing equations presented in the previous sections must be expanded slightly.

Fluid mass and momentum balance

Following the same mass balance procedure as for the single phase case, and gathering two mass balance equations, one for a wetting fluid (i.e. liquid) and one for a non-wetting (i.e. gas) fluid, we write,

$$\begin{aligned} & S_w \left(\frac{\phi}{K_w} + \frac{\alpha - \phi}{K_s} \right) \frac{dp_w}{dt} - \phi \frac{dS_{nw}}{dt} + \dots \\ & \nabla \cdot \left\{ \frac{\mathbf{k}k_w^r}{\mu_w} (-\nabla p_w + \rho_w \mathbf{g}) \right\} + \alpha S_w \nabla \cdot \frac{\partial \mathbf{u}}{\partial t} = 0 \end{aligned} \quad (15.23)$$

for mass balance of the wetting fluid, subscript w , and,

$$\begin{aligned} & S_{nw} \left(\frac{\phi}{K_{nw}} + \frac{\alpha - \phi}{K_s} \right) \frac{dp_w}{dt} + \phi \left(1 - \frac{S_{nw}}{K_{nw}} \frac{\partial p_c}{\partial S_w} \right) \frac{dS_{nw}}{dt} + \dots \\ & \nabla \cdot \left\{ \frac{\mathbf{k}k_{nw}^r}{\mu_{nw}} \left(-\nabla p_w - \frac{\partial p_c}{\partial S_w} \nabla S_{nw} + \rho_{nw} \mathbf{g} \right) \right\} + \alpha S_{nw} \nabla \cdot \frac{\partial \mathbf{u}}{\partial t} = 0 \end{aligned} \quad (15.24)$$

for mass balance of the non-wetting fluid, subscript nw . In these equations, k_α^r is relative permeability of phase α , ρ_α is density of phase α , and we have chosen wetting pressure, p_w , and non-wetting saturation, S_{nw} , as primary variables in the solution scheme. Other primary variables, such as capillary pressure, p_c , and non-wetting pressure, p_{nw} , could also have been chosen with algebraic manipulation, but our benchmark example requires constant, $p_c = 0$, capillary pressure for comparison with an analytical solution. This is not possible, of course, if p_c is a primary variable. Any viable permeability saturation function may be chosen for the example, we use the Brooks-Corey function.

For the numerical solution, storage due to two different fluids with two different compressibilities and densities is handled implicitly with solution of the above equations. For the analytical solution, we must define an effective compressibility as a function of fluid saturation and properties of each fluid. For immiscible fluids without penetrating bubbles, two compressible materials behave as resistors in series with respect to bulk modulus, thus the effective modulus is

$$\frac{1}{K_f} = \frac{S_w}{K_w} + \frac{S_{nw}}{K_{nw}}. \quad (15.25)$$

Solid momentum balance

As with the single phase case, balance of linear momentum is defined by,

$$\frac{\partial \sigma_{ij}}{\partial x_j} + F_i = 0, \quad (15.26)$$

but now the body force is a function of two fluids, $F = \rho_m g$ for the mixture density $\rho_m = \phi(S_w \rho_w + S_{nw} \rho_{nw}) + (1 - \phi) \rho_s$, and insertion of the elastic constitutive law yields for solid displacement,

$$\frac{\partial}{\partial x_j} \left[G \frac{\partial u_i}{\partial x_j} + (\lambda + G) \frac{\partial u_j}{\partial x_i} - \alpha \bar{p} \delta_{ij} \right] + F_i = 0, \quad (15.27)$$

where *mean* fluid pressure is defined as $\bar{p} = S_w p_w + S_{nw} p_{nw}$.

FEM solution scheme

For the two-phase simulations, the two fluid balance equations are solved in a single global equation, with an iterative coupling to the solid balance equation.

15.3.1 Terzaghi consolidation: Two-phase

Definition

For this comparison, we may utilize the same analytical solution as was done for the single phase case in the previous section, although the solution must represent the mean fluid pressure $\bar{p} = S_w p_w + S_{nw} p_{nw}$, for the final relationship,

$$\frac{\bar{p}(z, t)}{\bar{p}_0} = \left\{ 1.0 - \left(\frac{L-z}{L} \right)^2 - \frac{32}{\pi^3} \left[\sum_{m=0}^{\infty} \frac{(-1)^m}{(2m+1)^3} \exp[-\psi^2 ct] \cos[\psi(L-z)] \right] \right\}, \quad (15.28)$$

Property	Symbol	Unit	Value
<i>Wetting fluid properties</i>			
Bulk modulus	K_w	GPa	2.933
Density	ρ_w	kg/m ³	997.05
Viscosity	μ_w	Pas	8.9008×10^{-4}
Saturation	S_w	—	0.8
<i>Non-wetting fluid properties</i>			
Bulk modulus	K_{nw}	GPa	1.187
Density	ρ_{nw}	kg/m ³	997.05
Viscosity	μ_{nw}	Pas	8.9008×10^{-4}
Saturation	S_{nw}	—	0.2

Table 15.7: Two-phase fluid properties.

with pressure generation defined in the same manner,

$$\bar{p}_0 = \frac{L^2}{2c} (B_v \dot{\sigma}_z), \quad (15.29)$$

but where the uniaxial Skempton coefficient, B_v , must be defined (see Table 15.1) based upon the effective fluid modulus. Fluid properties are then defined for two separate fluids (Table 15.7)

Results

Initially the column is at zero pressure and is saturated uniformly with both fluids ($S_w = 0.8$) and we apply $p_c = 0$ and $k_w^r = k_{nw}^r = 0.5$. Note that we utilize a different compressibility for each fluid in order to exercise both fluid balance equations, with the analytical solution obtained using the *effective* fluid modulus, and with the *effective* modulus having an identical value to the single fluid modulus, 2.27GPa, used above in the single phase case.

Results are shown in Figs. 15.3.21 and 15.3.22 for sandstone and granite (see Table 15.2) for incompressible and compressible grains. With reference to the staggered stability criterion discussed in the HM problem above, because we are examining incompressible grains here the solution becomes unstable for granite. Therefore, an alternate value of porosity (0.06) is utilized (in the granite simulations) to ensure stability, which results in $B_v < 0.5$. Such an adjustment is not required when compressible (real) grains are used, but is utilized none-the-less for comparison with the incompressible grain solution. All results are ideally accurate.

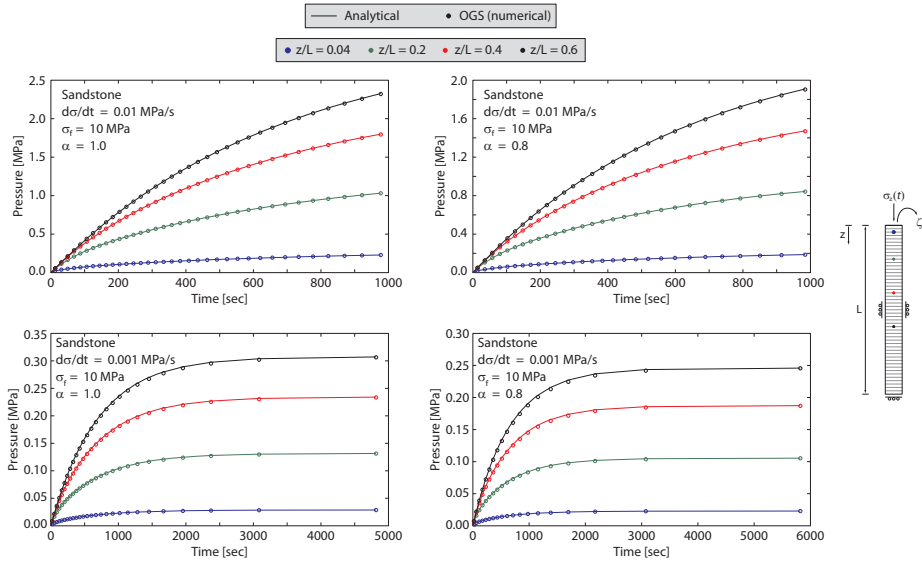


Figure 15.3.21: Sandstone solutions.

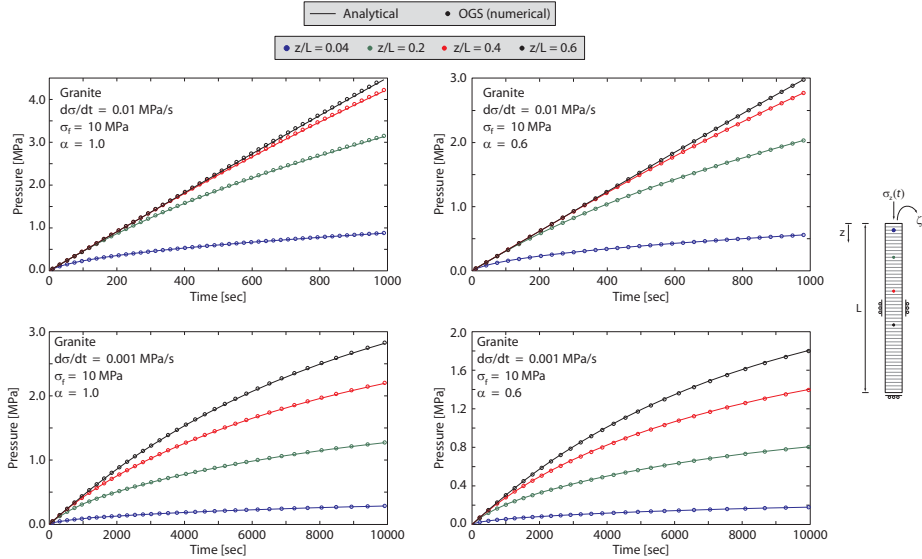


Figure 15.3.22: Granite solutions. Here, a porosity of 0.06 is used to ensure stability for the incompressible grain simulations (an adjustment that is not needed for compressible grains, but is used there also to maintain consistency).

Time steps are adaptively controlled with a tolerance based on the rate of pressure change over a time step. Such a scheme is capable of ensuring accuracy in HM or H2M problems. Note the importance of the tolerance in Fig. 15.1.2.

15.3.2 Invariant stress: Flow and storage in a compressible medium

It is also possible, and sometimes useful, to test two-phase storage and pressure dissipation in a deformable media at invariant stress. This test guarantees accurate implementation of fluid storage within the mass matrix (time derivative term) of the fluid mass balance PDE.

Definition

We utilize the same problem as above, but now no stress is applied and no mechanical equilibrium performed. The analytical solution may be derived from the Carslaw and Jaeger [160] solution for heat dissipation within a solid slab,

$$\bar{p}(z, t) = \frac{4\bar{p}_0}{\pi} \sum_{m=0}^{\infty} \left\{ \frac{1}{2m+1} \sin \left[z \left(\frac{(2m+1)\pi}{2L} \right) \right] \exp \left[-ct \left(\frac{(2m+1)\pi}{2L} \right)^2 \right] \right\}, \quad (15.30)$$

where \bar{p}_0 is initial mean pressure within the column.

Results

Results are shown in Fig. 15.3.23. We note that with an appropriate mixing rule for storage in the two phase formulation, the result is ideal. Very small

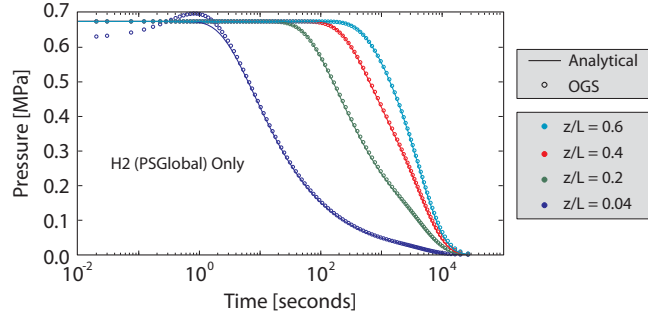


Figure 15.3.23: Two-phase flow with mechanical storage.

values of time and z can produce inaccuracies; however, this will always be the case, barring a very small mesh discretization.

15.3.3 Cam-Clay consolidation with swelling

As before, equations 15.23 and 15.24 define the fluid system. In this example, however, we choose a numerical solution in OpenGeoSys that accommodates pressure variables in the solution vector. Both equations are therefore algebraically manipulated so that the primary variables to solve for are now the capillary pressure, p_c , and the non-wetting pressure, p_{nw} ,

$$\phi \rho_w \frac{\partial S_w}{\partial p_c} \frac{dp_c}{dt} + \rho_w S_w \nabla \cdot \frac{d\mathbf{u}}{dt} + \nabla \cdot \left[\rho_w \frac{\mathbf{k} k_w^r}{\mu_w} (-\nabla p_{nw} + \nabla p_c + \rho_w \mathbf{g}) \right] = Q_w \quad (15.31)$$

$$\begin{aligned} -\phi \rho_{nw} \frac{\partial S_w}{\partial p_c} \frac{dp_c}{dt} + \phi (1 - S_w) \left(\frac{\partial \rho_{nw}}{\partial p_{nw}} \frac{dp_{nw}}{dt} + \frac{\partial \rho_{nw}}{\partial p_c} \frac{dp_c}{dt} \right) + \\ (\rho_w S_w + \rho_{nw} (1 - S_w)) \nabla \cdot \frac{d\mathbf{u}}{dt} + \nabla \cdot \left[\rho_{nw} \frac{\mathbf{k} k_{nw}^r}{\mu_{nw}} (-\nabla p_{nw} + \rho_{nw} \mathbf{g}) \right] = Q_{nw} \end{aligned} \quad (15.32)$$

where in this case we assume that solid grains are incompressible.

As in Section 14.2, swelling stress is based on the linear swelling model proposed by Rutqvist (2005) [159], which defines the increment of swelling stress to be proportional to liquid saturation increment,

$$\Delta \sigma^{sw} = \beta \Delta S_w, \quad (15.33)$$

where β is a swelling coefficient that could be called the maximum swelling stress. As the saturation change approaches unity, swelling stress approaches β .

Definition

Fig. 15.3.24 shows the axi-symmetric model domain for the confined swelling test as well as the initial and boundary conditions for the two-phase flow consolidation problem with hydraulic and fluid properties are given in Table 15.8. The parameters of the elasto-plastic swelling model are given in Table 15.9 for Cam-Clay plasticity.

Results

Fig. 15.3.25 shows the temporal evolution of water saturation on the bottom of the sample between OpenGeoSys and Code-Bright.

$$\frac{\partial p^c}{\partial y} = 0, p^g = 0.1 \text{ MPa}, u_y = 0, \sigma_{xy} = 0$$

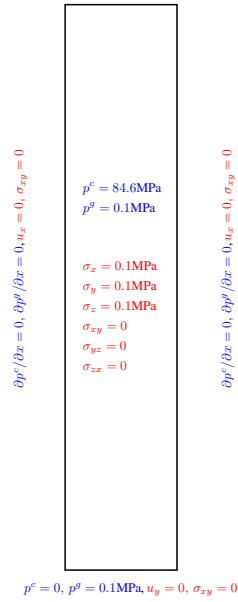


Figure 15.3.24: Model set-up with initial and boundary conditions.

Meaning	Value	Unit
Liquid density, ρ_w	1000	kg/m^3
Liquid viscosity, μ_w	10^{-3}	$Pa s$
Gas density, ρ_{nw}	Clapeyron equation	kg/m^3
Gas viscosity, μ_{nw}	1.8×10^{-5}	$Pa s$
Intrinsic permeability, k	0.6×10^{-20}	m^2
Porosity, ϕ	0.4	m^3/m^3
Media properties for liquid:		
Relative permeability	Power law $k_w^r = S_e^3$	
Residual saturation	0	—
Maximum saturation	1	—
Water retention	van Genuchten	
Exponential index, m	0.42	—
Air entry pressure, p_0	62	MPa
Relative permeability of gas, k_{nw}^r	$5.103 \times 10^{-12} [e(1 - S^t)]^{4.3}$	e , void ratio

Table 15.8: Hydraulic properties

Parameter	Value	Unit
Slope of the critical state line, M	1.5	—
Virgin compression index, λ_p	1.5	—
Swelling/recompression index, κ	0.1	—
Initial preconsolidation pressure, p_c	8.0	MPa
Initial void ratio, e	0.7	—
Poisson ratio	0.4	—
Initial ($s = 0$) elastic slope for $1 + e - p$, κ_{i0}	0.01	—
Initial ($\sigma = 0$) elastic slope for $1 + e - s$, κ_{s0}	0.25	—
Minimum bulk modulus, K_{min}	10	MPa
First parameter for κ_s , α_{ss}	-0.03	MPa $^{-1}$
Second parameter for κ_s , α_{sp}	-0.1609	—
Parameter for κ_i , α_i	-0.003	MPa $^{-1}$
Reference mean stress, p_{ref}	0.1	MPa

Table 15.9: Plasticity parameters for the Cam-Clay model

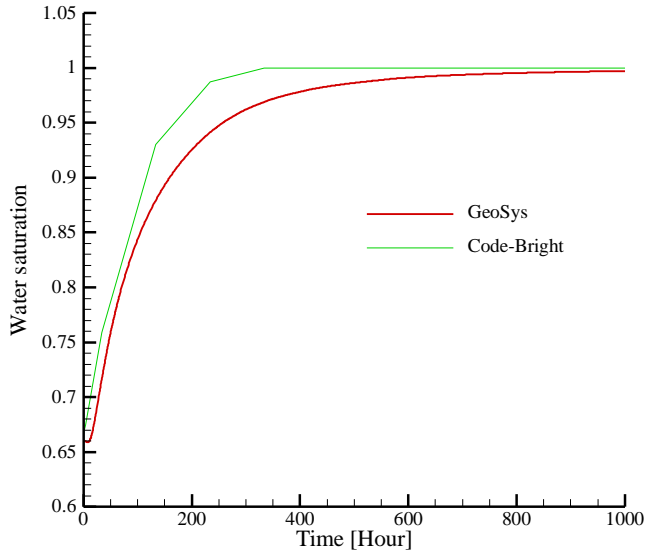


Figure 15.3.25: Water saturation evolution at the sample bottom.

15.4 Flow and mechanics in discrete fracture-matrix rock systems

15.4.1 Hydro-mechanical response of a single fracture within a rock matrix (2D)

Definition

This example is a fluid injection problem into a single discrete fracture surrounded by an impermeable rock matrix in two-dimensional space and validates

the proposed lower-dimensional interface elements with local enrichments for the nonlinear, coupled HM problem. The test case is designed to mimic the semi-analytical similarity solution available in [161], which has been used to verify numerical codes such as ROCMAS II [162], GEOCRACK [163], and FEHM [164]. Test parameters are referred to those of [164]. The solution is available based on the following assumptions:

1. The fluid compressibility is small compared to the compliance of the fracture aperture under normal effective stress. (This is valid for liquid saturated fractures.)
2. Fluid flow in a fracture is laminar flow between parallel surfaces.
3. Fracture deformation is not hysteretic.
4. The gradient in aperture along the fracture is small. There is no shear deformation of the fracture or the fracture does not dilate when sheared.
5. Displacements parallel to the fracture are negligible everywhere within the rock mass.

Figure 15.5.28 shows a sketch of the calculation model. The major fracture lies horizontally in the middle of an impermeable rock block. The fracture is subjected to a uniform in-situ stress $\sigma_{yy} = 50$ MPa normal to the fracture. Initially, fracture aperture is uniformly $b_0 = 1.0 \cdot 10^{-2}$ mm and fluid pressure is $p_0 = 11.0$ MPa along the fracture. At time $t = 0^+$, fluid is injected at the left-most edge of the fracture (in the form of constant boundary pressure, $p = 11.9$ MPa) and a sudden increase of pressure in the fracture results. The injection pressure induces elastic fracture opening and a subsequent increase of fracture permeability and storage capacity.

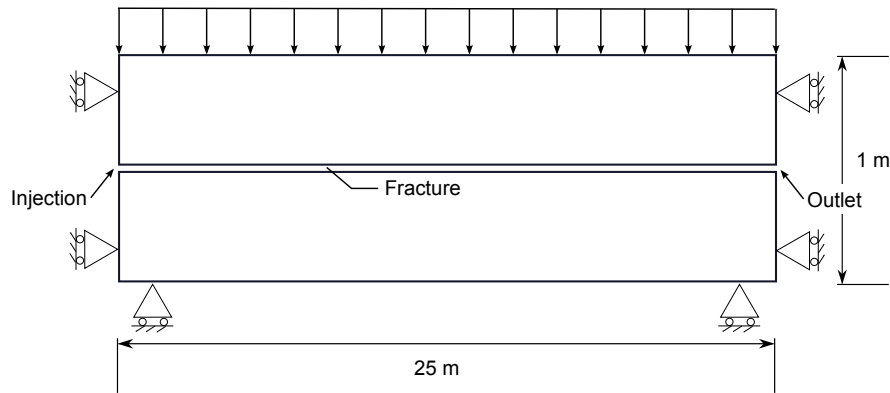


Figure 15.4.26: Fluid injection into a discrete fracture-rock matrix system.

Table 15.10: Model parameters

Symbol	Parameter	Value	Unit
<i>Fluid</i>			
ρ^l	Density	1000.0	$kg \cdot m^{-3}$
μ	Viscosity	0.001	$Pa \cdot s$
<i>Porous medium</i>			
ρ^s	Density	2716.0	$kg \cdot m^{-3}$
S_s	Specific storage	$1.0 \cdot 10^{-10}$	Pa^{-1}
k	Permeability	$1.0 \cdot 10^{-21}$	$m^2 \cdot s^{-1}$
ϕ	Porosity	0.1	%
E	Young's modulus	60	GPa
ν	Poisson ratio	0.0	—
α	Biot constant	1.0	—
<i>Fracture</i>			
b_0	Initial aperture	$1.0 \cdot 10^{-5}$	m
S_s	Specific storage	0.0	Pa^{-1}
k_n	Joint normal stiffness	100	$GPa \cdot m^{-1}$
k_s	Joint shear stiffness	100	$GPa \cdot m^{-1}$
α	Biot constant	1.0	—

Semi-analytical solution

Wijesinghe [161] derived the ordinal differential equation with the dimensionless aperture w . The semi-analytical solution can be obtained by solving the equation as an initial value problem using the fourth order Runge-Kutta method. For details, please refer to the original work [161].

Numerical solution

Boundary fluid pressure is fixed at $t = 0^+$ to 11.9 MPa at the left and 11 MPa at the right. Line elements with local enrichment were used to represent the discrete fracture and quadrilateral elements for surrounding rock matrix. Very fine vertical discretization is required near the fracture, i.e. $\Delta y=0.001$ m. The time step is selected as 10 s and a Newton-Raphson iteration is utilized to solve the nonlinear equation.

Results

Simulation results are presented in Figure 15.5.29 for pressure and fracture aperture profile along the fracture. When fluid is injected, the fracture aperture

is instantaneously opened to nearly $1.9 \cdot 10^{-2}$ mm at the injection point ($x = 0$ m). With time, this fracture opening behavior gradually propagates toward the right-most, low-pressure edge of the fracture. Linear constitutive laws dictate a linear variation in fracture aperture relative to fluid pressure. Figure 15.5.29 shows good agreement between the numerical method and the semi-analytical solution.

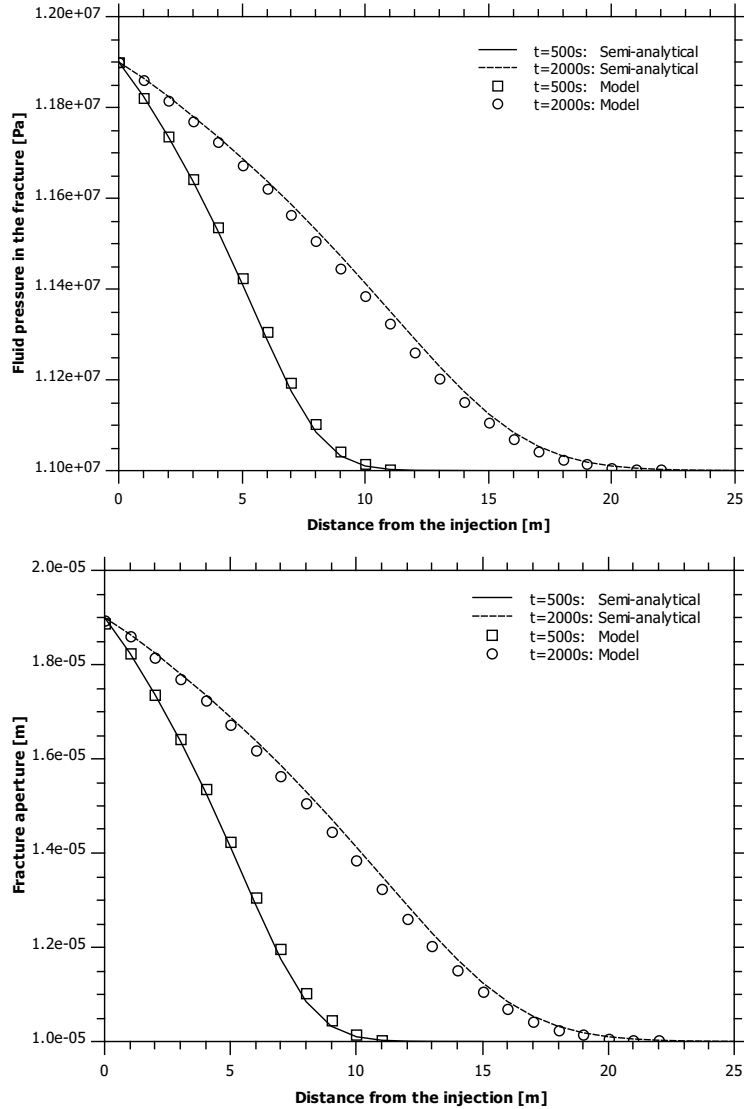


Figure 15.4.27: Profile along the fracture: pressure (left) and aperture (right).

15.5 Flow and mechanics in discrete fracture-matrix rock system (2 D)

15.5.1 Definition

This example is a fluid injection problem into a single discrete fracture surrounded by an impermeable rock matrix in two-dimensional space and validates the proposed lower-dimensional interface elements with local enrichments for the nonlinear, coupled HM problem. The test case is designed to mimic the semi-analytical similarity solution available in [161], which has been used to verify numerical codes such as ROCMAS II [162], GEOCRACK [163], and FEHM [164]. Test parameters are referred to those of [164]. The solution is available based on the following assumptions:

1. The fluid compressibility is small compared to the compliance of the fracture aperture under normal effective stress. (This is valid for liquid saturated fractures.)
2. Fluid flow in a fracture is laminar flow between parallel surfaces.
3. Fracture deformation is not hysteretic.
4. The gradient in aperture along the fracture is small. There is no shear deformation of the fracture or the fracture does not dilate when sheared.
5. Displacements parallel to the fracture are negligible everywhere within the rock mass.

Figure 15.5.28 shows a sketch of the calculation model. The major fracture lies horizontally in the middle of an impermeable rock block. The fracture is subjected to a uniform in-situ stress $\sigma_{yy} = 50$ MPa normal to the fracture. Initially, fracture aperture is uniformly $b_0 = 1.0 \cdot 10^{-2}$ mm and fluid pressure is $p_0 = 11.0$ MPa along the fracture. At time $t = 0^+$, fluid is injected at the left-most edge of the fracture (in the form of constant boundary pressure, $p = 11.9$ MPa) and a sudden increase of pressure in the fracture results. The injection pressure induces elastic fracture opening and a subsequent increase of fracture permeability and storage capacity.

15.5.2 Solution

Semi-analytical solution

Wijesinghe [161] derived the ordinary differential equation with the dimensionless aperture w . The semi-analytical solution can be obtained by solving the equation as an initial value problem using the fourth order Runge-Kutta method. For details, please refer to the original work [161].

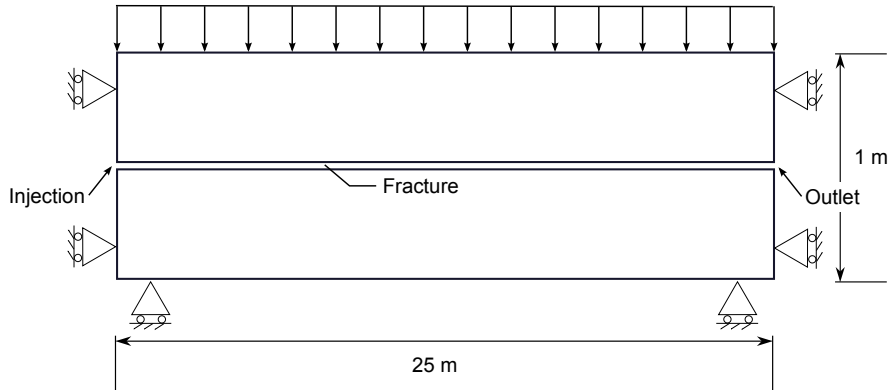


Figure 15.5.28: Fluid injection into a discrete fracture-rock matrix system

Numerical solution

Boundary fluid pressure is fixed at $t = 0^+$ to 11.9 MPa at the left and 11 MPa at the right. Line elements with local enrichment were used to represent the discrete fracture and quadrilateral elements for surrounding rock matrix. Very fine vertical discretization is required near the fracture, i.e. $\Delta y=0.001$ m. The time step is selected as 10 s and a Newton-Raphson iteration is utilized to solve the nonlinear equation.

15.5.3 Results

Simulation results are presented in Figure 15.5.29 for pressure and fracture aperture profile along the fracture. When fluid is injected, the fracture aperture is instantaneously opened to nearly $1.9 \cdot 10^{-2}$ mm at the injection point ($x = 0$ m). With time, this fracture opening behavior gradually propagates toward the right-most, low-pressure edge of the fracture. Linear constitutive laws dictate a linear variation in fracture aperture relative to fluid pressure. Figure 15.5.29 shows good agreement between the numerical method and the semi-analytical solution.

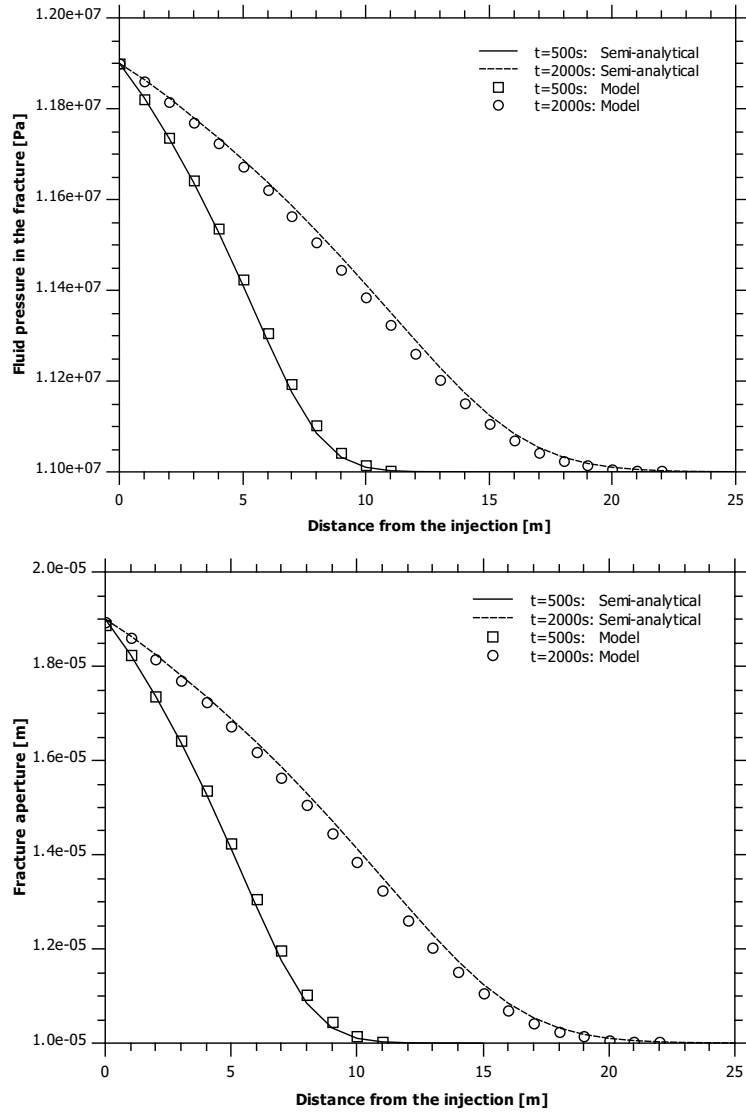


Figure 15.5.29: Profile along the fracture: pressure (left) and aperture (right)

Table 15.11: Model parameters

Symbol	Parameter	Value	Unit
<i>Fluid</i>			
ρ^l	Density	1000.0	$kg \cdot m^{-3}$
μ	Viscosity	0.001	$Pa \cdot s$
<i>Porous medium</i>			
ρ^s	Density	2716.0	$kg \cdot m^{-3}$
S_s	Specific storage	$1.0 \cdot 10^{-10}$	Pa^{-1}
k	Permeability	$1.0 \cdot 10^{-21}$	$m^2 \cdot s^{-1}$
ϕ	Porosity	0.1	%
E	Young's modulus	60	GPa
ν	Poisson ratio	0.0	—
α	Biot constant	1.0	—
<i>Fracture</i>			
b_0	Initial aperture	$1.0 \cdot 10^{-5}$	m
S_s	Specific storage	0.0	Pa^{-1}
k_n	Joint normal stiffness	100	$GPa \cdot m^{-1}$
k_s	Joint shear stiffness	100	$GPa \cdot m^{-1}$
α	Biot constant	1.0	—

15.6 Two-phase flow consolidation

Chapter 16

Thermomechanics

by Wenjie Xu, Wenging Wang, Norihiro Watanabe and Jürgen Hesser

In this chapter, we consider coupled thermo-mechanical (TM) processes in a porous medium. For heat transport problem in any medium, the governing equation is given by

$$\rho C_p T' = -\nabla \mathbf{q}_T + Q_T(\mathbf{x}, t), \quad \mathbf{x} \in \mathbb{R}^3 \quad (16.1)$$

where ρ is medium density, $C_p(T)$ is the specific heat capacity, Q_T is heat source and \mathbf{q}_T is the heat flux, which takes the forms

$$\mathbf{q}_T = -K_e \nabla T \quad (16.2)$$

for solid and

$$\mathbf{q}_T = -K_e \nabla T + n \sum_{\gamma}^{phase} (\rho^\gamma C_p^\gamma) T \mathbf{v}, \quad \gamma = \text{liquid, gaseous} \quad (16.3)$$

for porous media considering of advective and diffusive fluxes with K_e the heat conductivity. For porous media, the specific heat capacity consists of portions of solid, liquid and gaseous phase as

$$\rho C_p = \sum_{\gamma}^{phase} (\rho^\gamma C_p^\gamma) \quad (16.4)$$

where γ specifies solid, liquid or gaseous phase. The boundary conditions are given by

$$\mathbf{q}_T \cdot \mathbf{n} = q_T^r, \quad \text{or} \quad T = T_r, \quad \forall \mathbf{x} \in \partial\Omega \quad (16.5)$$

and the initial condition reads

$$T(\mathbf{x}, t) = T_0(\mathbf{x}), \quad \forall \mathbf{x} \in \Omega \quad (16.6)$$

with \mathbf{n} , the normal direction at $\mathbf{x} \in \partial\Omega$

For mechanical process, we consider the total strain rate $\Delta\epsilon$ can be admissible decomposed into components such as reversible (elastic), temperature deduced as

$$\Delta\epsilon = \mathbb{C}(\Delta\epsilon^e - \alpha \mathbf{I}\Delta T) \quad (16.7)$$

where \mathbb{C} is the constitutive tensor, α is the linear thermal expansion coefficient, \mathbf{I} is the identity tensor, and ΔT is temperature change. With the generalized Hook's law, the total stress with the thermal effect can be expressed as

$$\Delta\sigma = \mathbb{C}(\Delta\epsilon - \alpha \mathbf{I}\Delta T) \quad (16.8)$$

with σ is the stress tensor. The volume of a solid is increasing or decreasing with temperature changes. Homogeneous bodies expand evenly in each direction by increasing temperatures. In this case no variation of the stresses occurs. If the deformation of the solid is prevented, the stresses are increasing or decreasing with temperature changes. This phenomenon can be easily calculated by analytical solutions of the Hooke's linear elastic model. The equations of the mechanical behaviour base on the Hooke's law for linear elastic materials:

$$\varepsilon_x = \frac{1}{E} \cdot (\sigma_x - \nu \cdot (\sigma_y + \sigma_z)) + \alpha \cdot \Delta T \quad (16.9)$$

$$\varepsilon_y = \frac{1}{E} \cdot (\sigma_y - \nu \cdot (\sigma_x + \sigma_z)) + \alpha \cdot \Delta T \quad (16.10)$$

$$\varepsilon_z = \frac{1}{E} \cdot (\sigma_z - \nu \cdot (\sigma_x + \sigma_y)) + \alpha \cdot \Delta T \quad (16.11)$$

where ε_i are strains, σ_i are stresses, E is Young's modulus, and ν is Poisson's ratio.

16.1 Thermoelastic stress analysis in homogeneous material (3 D)

16.1.1 Definition

The top and the bottom of a solid body that consists of one homogeneous material are heated. The aim of the calculation is to find out the isotropic state of stress that is reached after the whole solid is heated. Figure 16.1.1 shows a sketch of the calculation area assuming a homogeneous solid, a constant temperature in the whole body at the beginning and a heating of the top and the bottom of the body about 10 K. Linear elastic material behaviour, isotropic thermal expansion and no gravity effect are assumed. The xy -plane is the horizontal plane. The height of the body is in z -direction. The dimensions of this 3 D-model are 10 m in all directions. As deformations in x - and y -direction

are suppressed, the increasing temperature evokes stresses within the solid. The used parameters of the solid represent the material behaviour of concrete (Table 16.1).

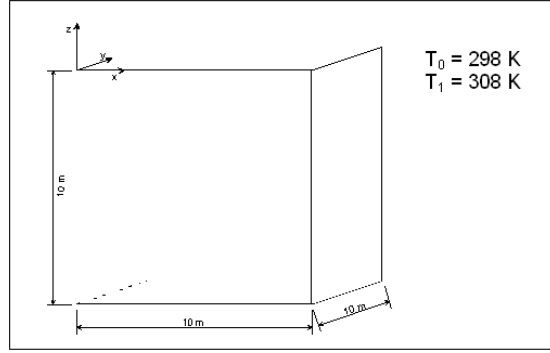


Figure 16.1.1: Calculation area with one material

Table 16.1: Model parameters

Symbol	Parameter	Value	Unit
T_0	Initial temperature (before heating)	298	K
T_1	Temperature after heating	308	K
ρ	Density of the solid	2200	$\text{kg} \cdot \text{m}^{-3}$
E	Young's modulus of the solid	25	GPa
ν	Poisson ratio	0.27	—
α	Linear thermal expansion	$6.0 \cdot 10^{-6}$	K^{-1}
c	Specific heat capacity	1.0	$\text{J} \cdot \text{kg}^{-1} \cdot \text{K}^{-1}$
λ	Thermal conductivity	1.0	$\text{W} \cdot \text{m}^{-1} \cdot \text{K}^{-1}$

16.1.2 Solution

Analytical solution

The analytical solution can be derived from the time independent equation (16.9) to (16.11) with the assumptions of no deformation and an isotropic thermal expansion:

$$\varepsilon_i \equiv 0$$

$$\sigma_x = \sigma_y = \sigma_z = -\frac{\alpha \cdot \Delta T \cdot E}{1 - 2 \cdot \nu} \quad (16.12)$$

Equation (16.12) provides the stresses after heating the solid and shows an isotropic state of stress.

Numerical solution

The dimensions of this 3 D-model are 10 m in all directions. Deformations perpendicular to the outer surfaces are suppressed. The initial temperature in the whole area is 298 K. At the top and at the bottom of the model thermal boundary conditions are set with a temperature of 308 K. Thereby the heating of the solid about 10 K is simulated. 1000 hexahedral elements and 1331 nodes are used. The calculation is divided in 384 time steps with a constant time step length of 900 seconds. That means the heating of the solid within 4 days is simulated. The calculation model is sketched in Figure 16.1.2.

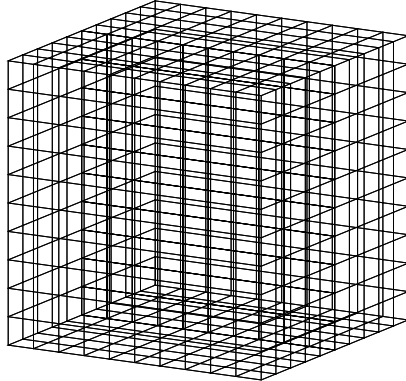


Figure 16.1.2: Mesh for TM coupling homogeneous material 3D model

16.1.3 Results

With the analytical solution in equation (16.12) and the used parameters the stress values in the solid amount. This isotropic state of stress is reached after the whole solid is heated. The temporal development of the stresses in the centre of the model (at node 665) calculated is presented in Figure 16.1.3. The results of the 3 D simulation show an exact agreement with the analytical solutions.

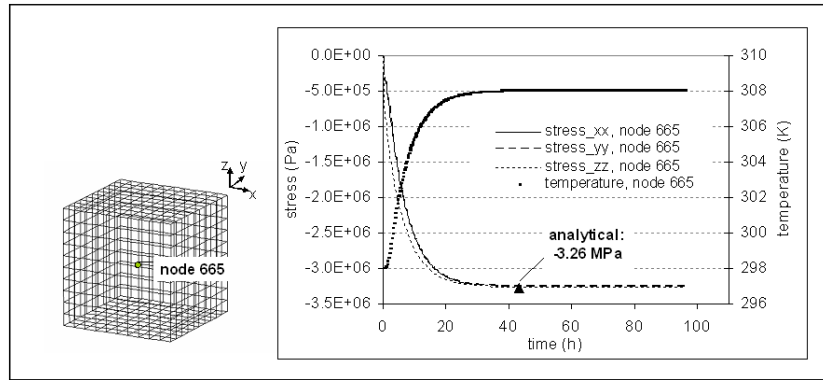


Figure 16.1.3: Temporal stress development in the centre of the calculation model (node 665)

16.2 Thermoelastic stress analysis in composite materials (3 D)

16.2.1 Definition

If there are two materials with different thermal expansions, the volume changes of the materials will be uncommon. The material with the higher thermal expansion expands more than the material with the low thermal expansion. If deformations at the outer boundaries are prevented, different states of stress will occur in these two materials. But the stresses perpendicular to the parting plane must be equal. The values of the stresses as a result of temperature changes can also easily be calculated by the Hooke's linear elastic model. The aim of this simulation is to specify the stresses at several areas in the solid. Figure 16.2.4 shows a sketch of the calculation area. The model parameters are given in Table 16.2.

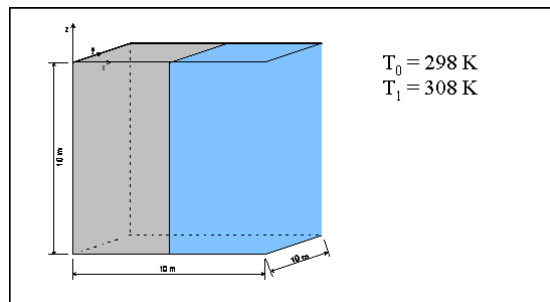


Figure 16.2.4: Calculation area with two different materials

Table 16.2: Model parameters

Symbol	Parameter	Value	Unit
T_0	Initial temperature (before heating)	298	K
T_1	Temperature after heating	308	K
ρ	Density of the solid	2200	$kg \cdot m^{-3}$
E	Young's modulus of the solid	25	GPa
ν	Poisson ratio	0.27	—
α_1	Linear thermal expansion of material 1	$6.0 \cdot 10^{-6}$	K^{-1}
α_2	Linear thermal expansion of material 2	$1.2 \cdot 10^{-5}$	K^{-1}
c	Specific heat capacity	1.0	$J \cdot kg^{-1} \cdot K^{-1}$
λ	Thermal conductivity	1.0	$W \cdot m^{-1} \cdot K^{-1}$

16.2.2 Solution

Analytical solution

The equations of the mechanical behaviour base on the Hooke's law for linear elastic materials (see equations (16.9) to (16.11)). The analytical solution can be derived from these time independent equations with the assumptions of suppressed deformations in y - and z -direction and an isotropic thermal expansion:

$$\varepsilon_x = \varepsilon_z \equiv 0$$

Additionally the stresses in x-direction (perpendicular to the parting plane between the two materials) must be equal:

$$\sigma_{x1} = \sigma_{x2}$$

where indices denote different materials. Further the expansion of the one material leads to a compression of the other material with the same value in x-direction:

$$\varepsilon_{x1} = -\varepsilon_{x2}$$

With these limiting conditions the analytical solutions are:

$$\varepsilon_{x1} = \frac{\Delta T}{2} \cdot (\alpha_1 - \alpha_2) \cdot \left(\frac{1+\nu}{1-\nu} \right) \quad (16.13)$$

$$\varepsilon_{x2} = -\varepsilon_{x1} = -\frac{\Delta T}{2} \cdot (\alpha_1 - \alpha_2) \cdot \left(\frac{1+\nu}{1-\nu} \right) \quad (16.14)$$

$$\sigma_{x1} = \sigma_{x2} = E \cdot \frac{\varepsilon_{x2} \cdot (1-\nu) - \alpha_2 \cdot \Delta T \cdot (1+\nu)}{1-\nu-2\nu^2} \quad (16.15)$$

$$\sigma_{y1} = \sigma_{z1} = \frac{\nu \cdot \sigma_{x1} - \alpha_1 \cdot \Delta T \cdot E}{1-\nu} \quad (16.16)$$

$$\sigma_{y2} = \sigma_{z2} = \frac{\nu \cdot \sigma_{x2} - \alpha_2 \cdot \Delta T \cdot E}{1-\nu} \quad (16.17)$$

Equations (16.13) to (16.17) provide the strains and stresses after heating the body of two materials. The state of stress is anisotropic.

Numerical solution

The calculation was done with a 3 D model. The xy -plane is the horizontal plane. The height of the body is in z -direction. The dimensions of this 3 D model are 10 m in all directions. The model includes 1000 hexahedral elements and 1331 nodes. Deformations perpendicular to the outer surfaces are suppressed. The initial temperature in the whole area is 298 K. At the top and at the bottom of the model thermal boundary conditions are set with a temperature of 308 K. Thereby the heating of the body about 10 K is simulated. The used parameters of the solids represent the material behaviour of concrete. The calculation is divided in 1000 time steps with a constant time step length of 0.5 seconds. A sketch of the calculation model is shown in Figure 16.2.5.

16.2.3 Results

With the analytical solution in equations (16.13) to (16.17) and the used parameters the values of the strains in x -direction at the parting plane amount

$$\varepsilon_{x1} = -5.219178 \cdot 10^{-5}$$

$$\varepsilon_{x2} = 5.219178 \cdot 10^{-5}$$

The values of the stresses are

$$\sigma_{x1} = \sigma_{x2} = -4891304.34 \text{ Pa} = -4.8913 \text{ MPa}$$

$$\sigma_{y1} = \sigma_{z1} = -3863907.08 \text{ Pa} = -3.8639 \text{ MPa}$$

$$\sigma_{y2} = \sigma_{z2} = -5918701.60 \text{ Pa} = -5.9187 \text{ MPa}$$

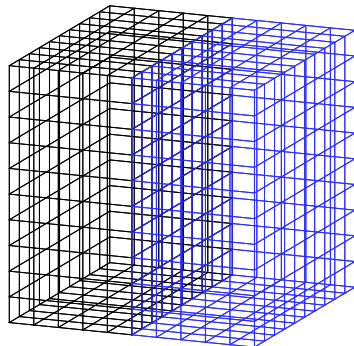


Figure 16.2.5: Mesh for TM coupling 3D model with 2 materials

This anisotropic state of stress is reached after the whole body is heated. The temporal stress developments in several nodes calculated with both RockFlow and OGS are presented in Figure 16.2.6 and Figure 16.2.7. The results of the 3D simulation show an exact agreement with the analytical solutions.

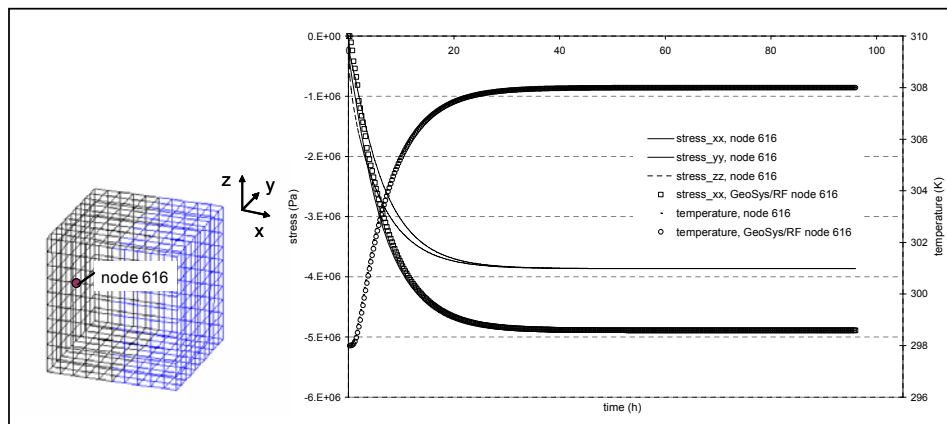


Figure 16.2.6: Temporal stress development in node 616

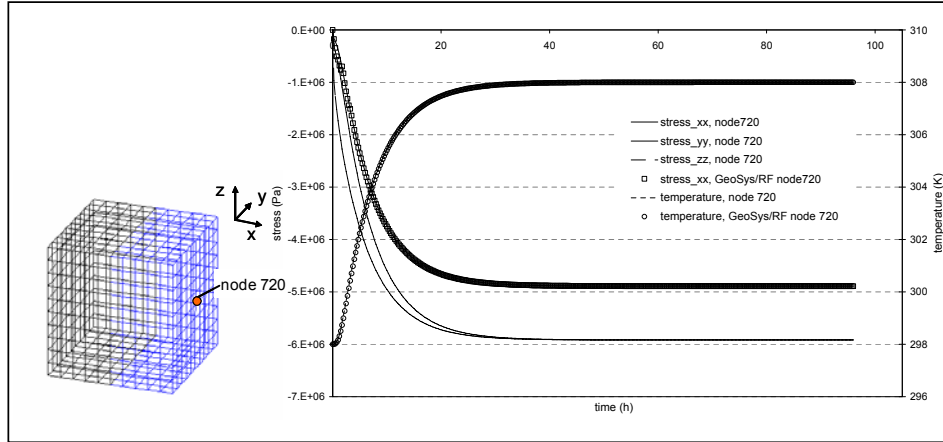


Figure 16.2.7: Temporal stress development in node 720

16.3 Thermoelastic deformation in a hollow cylinder

16.3.1 Definition

A hollow cylinder which consists of a solid of a constant temperature is exposed to a higher temperature at the surface of its hole. As a result of the increased temperature the cylinder is expanding. The aim of this calculation is to get out the radial displacement as well as the temperature distribution that are caused by the thermal expansion process by the use of an axisymmetric model. Figure 16.3.8 shows a sketch of the calculation area assuming a homogeneous solid, a constant temperature in the whole body at the beginning and a heating of the cylinder at the inner surface. Linear elastic material behaviour and isotropic thermal expansion are assumed. Deformations in y -direction at the bottom and the top and in x -direction at the right border are suppressed. The used parameters of the solid are listed in Table 16.3.

16.3.2 Solution

Analytical solution

For the hollow cylinder with the inner radius R_1 and the outer radius R_2 the following analytical solution for radial displacement u_r , stress σ_r and temperature

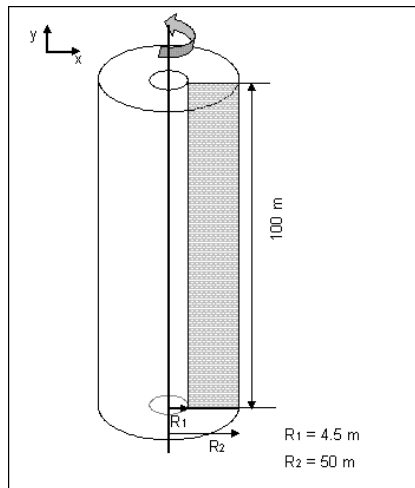


Figure 16.3.8: Calculation area (grey area)

Table 16.3: Model parameters

Symbol	Parameter	Value	Unit
T_0	Initial temperature (before heating)	25	$^{\circ}\text{C}$
q	Heat source	30	W/m^2
ρ	Density of the solid	2000	$\text{kg} \cdot \text{m}^{-3}$
E	Young's modulus of the solid	2.5	GPa
ν	Poisson ratio	0.25	—
α	Thermal expansion	$4.2 \cdot 10^{-5}$	K^{-1}
λ	Thermal conductivity	5.5	$\text{W} \cdot \text{m}^{-1} \cdot \text{K}^{-1}$

in dependency on the radius was used.

$$u_r = \frac{q R_1 \beta}{2 \psi \kappa} \cdot r \cdot \left(\ln r - \frac{1}{2} \right) + \frac{A_0}{2} r + \frac{A_1}{r} \quad (16.18)$$

$$\begin{aligned} \sigma_r &= \psi \left[-\frac{q R_1 \beta}{2 \psi \kappa} \cdot r \cdot \left(\ln r + \frac{1}{2} \right) + \frac{A_0}{2} - \frac{A_1}{r^2} \right] \\ &\quad + \lambda \left[-\frac{q R_1 \beta}{2 \psi \kappa} \cdot r \cdot \left(\ln r - \frac{1}{2} \right) + \frac{A_0}{2} + \frac{A_1}{r^2} \right] \\ &\quad - \beta \left[\frac{R_1 q}{\kappa} \ln \left(\frac{R_2}{r} \right) + T_0 \right] \end{aligned} \quad (16.19)$$

$$T(r) = \frac{R_1 q}{\kappa} \ln \left(\frac{R_2}{r} \right) + T_0 \quad (16.20)$$

where

$$\psi = \lambda + 2G \quad \text{and} \quad \beta = \alpha(3\lambda + 2G)$$

with

- λ – Lamé elastic constant
- G – shear modulus
- α – thermal expansion coefficient
- κ – thermal conductivity
- A_0, A_1 – integration constants

At the outer surface of the hollow cylinder (where $r = R_2$) there is no deformation, that means the displacement u_{R2} is zero. Therefore equation (16.18) is set equal to zero for this boundary and adapted to A_0 .

$$A_0 = -\frac{2 A_1}{R_2^2} - 2 \cdot B \cdot \left(\ln R_2 - \frac{1}{2} \right) \quad (16.21)$$

where

$$B = \frac{q R_1 \beta}{2 \psi \kappa}$$

At the inner surface of the hollow cylinder (where $r = R_1$) no stress is effected by the expansion because this boundary is phreatic. Therefore equation (16.19) is set equal to zero and A_1 is calculated by using equation (16.22).

$$A_1 = \frac{\beta \left(\frac{R_1 q}{\kappa} \ln \left(\frac{R_2}{r} \right) + T_0 \right) + \lambda B \left(\ln R_1 - \frac{1}{2} \right) + \psi B \left(\ln R_1 + \frac{1}{2} \right) - \left(\frac{\lambda + \psi}{2} \right) 2B \left(\ln R_2 - \frac{1}{2} \right)}{\frac{\lambda - \psi}{R_1^2} - \frac{\lambda + \psi}{2} \cdot \frac{2}{R_1^2}} \quad (16.22)$$

After having solved this equation, A_1 is used to calculate A_0 .

Numerical solution

The axisymmetric model is in the xy -plane. The inner radius $R1$ of the cylindrical model is 4.5 m and the outer radius $R2$ 50 m. The cylinder is 100 m high. The initial temperature in the whole area is 25°C. As boundary condition deformations in y -direction at the bottom and the top are suppressed, as well as deformations in x -direction at the right border. At the right boundary of the model a thermal boundary condition is set with a constant value of 25°C. At the left boundary a source term for heat flux of $q = 30 \text{ W/m}^2$ is defined. Thereby the continuous heating of the solid is simulated. The simulation of only one time step is done. The numerical model consists of 766 triangular elements and 426 nodes as sketched in Figure 16.3.9.

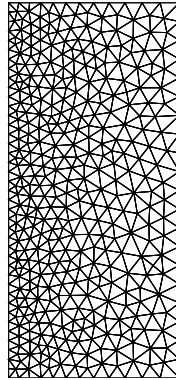


Figure 16.3.9: Mesh for TM coupling hollow cylinder model (2D axisymmetric)

16.3.3 Results

The results of the analytical equations for stresses, displacements and temperatures are compared to those of the numerical simulation by OGS. With the equations (16.22) and (16.21) and the used parameters, the integration constants in the analytical solution are obtained as:

$$A_0 = 5.96 \cdot 10^{-3}$$

$$A_1 = -1.19 \cdot 10^{-1}$$

Figure 16.3.10 shows the temperature distribution over the radius of the hollow cylinder. In Figure 16.3.11 displacements in radial direction that are caused by the thermal expansion are depicted. In addition you can find the induced stresses

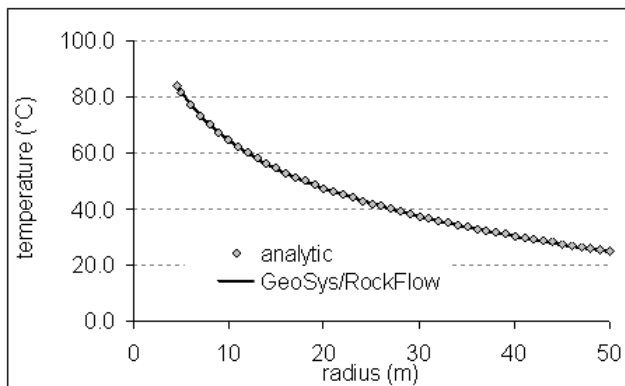


Figure 16.3.10: Temperature distribution over the radius

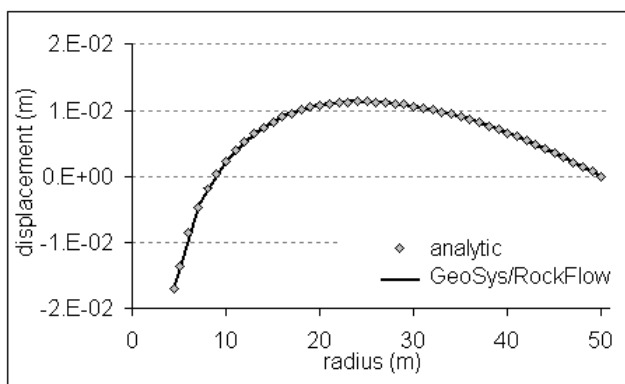


Figure 16.3.11: Displacements in radial direction

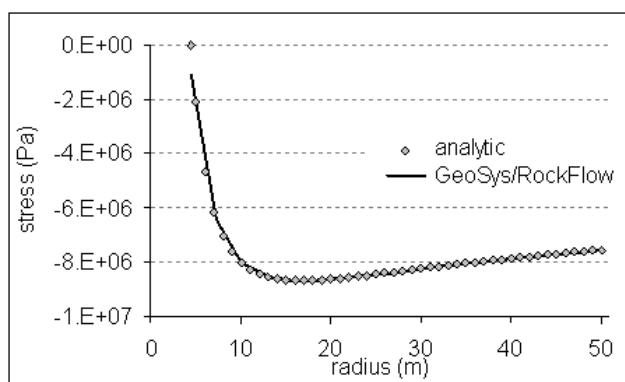


Figure 16.3.12: Stresses in radial direction

in Figure 16.3.12. Obviously, with the axisymmetric model a OGS simulation generates comprehensible results that meet well the analytic solution.

Chapter 17

Reactive Transport

by Haibing Shao, Sebastian Bauer, Florian Centler, Marco de Lucia, Shuang Jin, Mingliang Xie, Georg Kosakowski

17.1 1D reactive transport: calcite dissolution and precipitation

17.1.1 Definition

In this example, a one-dimensional column that initially contains calcite mineral is continuously flushed by water that contains magnesium chlorine (Fig. 17.1.1). With the movement of water front, calcite starts to dissolve and dolomite is formed temporarily.

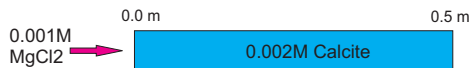


Figure 17.1.1: Model domain

Media Properties

The media properties of this model is listed in Table 17.1.

Table 17.1: Material properties

Parameter	Value	Unit
Column length	0.5	m
Effective porosity	0.32	—
Bulk density	1.8×10^3	$kg \cdot m^{-3}$
Longitudinal dispersivity	0.0067	m
Pore velocity	9.375×10^{-6}	$m \cdot sec^{-1}$
Flow rate	3×10^{-6}	$m^3 \cdot sec^{-1}$

For OpenGeoSys-GEMIPM2K calculation, all the possible chemical species need to be explicitly set up for initial and boundary conditions. In this example, all concentration values are given in the unit of $mol \cdot kg^{-1}$ water. Detailed values can be get from the *.ic and *.bc files in the corresponding benchmark folder.

17.1.2 Solution

This model can be simulated by OpenGeoSys-PHREEQC, OpenGeoSys-ChemApp, and OpenGeoSys-GEMIPM2K. In these benchmarks, we use the Nagra/PSI database [165], which provides same thermodynamic data for all three calculations. Fig. 17.1.2 shows the three simulation results. Solid lines are for

OpenGeoSys-PHREEQC, symbols "+" are for OpenGeoSys-GEMIPM2K, and triangles are for OpenGeoSys-ChemApp.

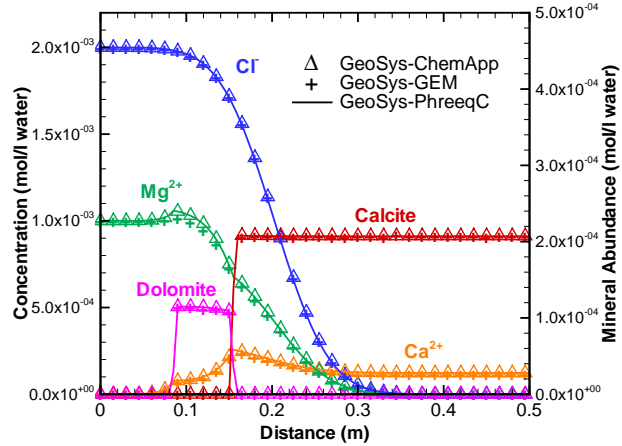


Figure 17.1.2: Benchmark results from OpenGeoSys-ChemApp, OpenGeoSys-PHREEQC, and OpenGeoSys-GEMIPM2K

17.2 1D reactive transport simulation of cation exchange process

17.2.1 Definition

This test example is taken from the PHREEQC User's Guide [166]. The simulation is made in order to reproduce the transport of solutes by saturated flow with the influence of cation exchange. The aim of the example is to check the correctness of the coupling between OpenGeoSys and PHREEQC by comparing the results of the simulations of both programs. With the calculation model the chemical composition of the effluent from a column containing a cation exchanger and a sodium-potassium-nitrate-solution is simulated. This column is flushed with 3 pore volumes of calcium chloride solution.

The 8.2 cm long column contains a sodium-potassium-nitrate solution that is in equilibrium with a cation exchanger. For the one-dimensional calculation the calculation area is simplified as a line. The calculation model includes 82 elements and 83 nodes. As initial condition the water head in the whole domain is given with 2 m. The initial state of the solution is given in table 17.2.

Table 17.2: Used parameters

Parameter	Value	Unit
Ca	0	$mol \cdot kgw^{-1}$
Cl	0	$mol \cdot kgw^{-1}$
K	2.0×10^{-4}	$mol \cdot kgw^{-1}$
Na	1.0×10^{-3}	$mol \cdot kgw^{-1}$
N(5)	1.2×10^{-3}	$mol \cdot kgw^{-1}$
pH	7	—
pe	12.5	—
Na-X	5.493×10^{-4}	$mol \cdot kgw^{-1}$
K-X	5.507×10^{-4}	$mol \cdot kgw^{-1}$
Ca-X ₂	0	$mol \cdot kgw^{-1}$

with

- pe - redox potential
- X - ion exchanger
- kgw - kilogram of water.

At the right border of the model the constant head is given with 2 m. At the left border a constant flux of $1.388 \times 10^{-6} m^3 \cdot s^{-1}$ is defined as source term. The concentration of this infiltrating CaCl_2 -solution as well as the pH and pe are given in table 17.3.

The soil material is specified by the parameters in table 17.4. The dispersion of the transported solutes in this soil is set equal to $2 \cdot 10^{-3} m$. The calculation

Table 17.3: State of the infiltration solution

Parameter	Value	Unit
Ca	6.0×10^{-4}	$mol \cdot kgw^{-1}$
Cl	1.2×10^{-3}	$mol \cdot kgw^{-1}$
pH	7	—
pe	12.5	—

is divided in 480 time steps with a constant time step length of 180 seconds. That means, the flow and transport processes in the aquifer within 1 day are simulated.

Table 17.4: Soil parameters

Parameter	Value	Unit
density ρ	2000	$kg \cdot m^{-3}$
porosity Φ	0.5	—
permeability K	1.157×10^{-5}	m^2

As this test example has the aim to validate the coupling of OpenGeoSys and PHREEQC, merely the comparison between the simulation results of both programs has to be accomplished.

17.2.2 Solution

The numerical results are shown in figure 17.2.3. The time-dependent concentrations are the values of the compared OpenGeoSys and PHREEQC models at the end node and end cell, respectively. Within the calculation time of one day the pore volume of the column model is exchanged three times. As chloride is a conservative tracer it arrives already after the exchange of about one pore volume in the effluent. As long as the exchanger contains sodium this component is eluted. Sodium is initially present in the column and exchanges with the incoming calcium. Potassium is released after sodium. When all of the potassium has been released, the concentration of calcium increases to a steady-state value. As depicted in figure 17.2.3, between the OpenGeoSys and the PHREEQC simulation results there are no differences.

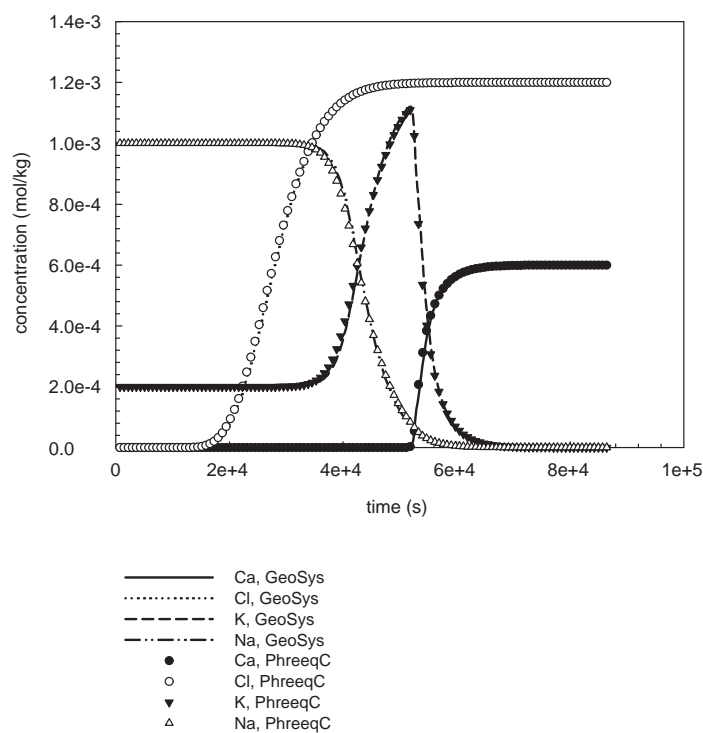


Figure 17.2.3: Effluent concentrations with time of the OpenGeoSys and PHREEQC simulations

17.3 1D reactive transport: multispecies transport with serial and parallel reactions

Reaction networks can be classified as serial and/or parallel reaction networks. Serial reaction is a reactant produces a single product and this product becomes the reactant for the next stage producing another single product. Examples of serial reactions can be denitrification, radioactive decay and dechlorination of some chlorinated solvents. In parallel reactions, the parent reactant undergoes two or more independent reactions to produce multiple products. In many biogeochemical systems, the reaction networks are the combination of serial and parallel reactions.

17.3.1 Definition

In scenario 1, sequential reductive dechlorination of chlorinated hydrocarbons from trichlorobenzene (TCB) to diclorobenzene (DCB) to monochlorobenzene (MCB) is simulated:



In scenario 2, a serial-parallel reaction network as shown in Fig. 17.3.4 is used to perform the verification. It can be decomposed into three serial reactions: $A \rightarrow B \rightarrow C_1$, $A \rightarrow B \rightarrow C_2$, $A \rightarrow B \rightarrow C_3$. For all the reactions in this scenario, first-order irreversible reactions are assumed.

An analytical solution by [167] has been used to verify the numerical results from OpenGeoSys-BRNS simulation for these two scenarios.

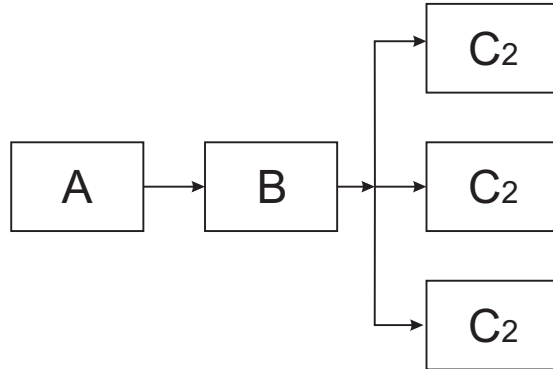


Figure 17.3.4: An example of serial-parallel reaction network.

In scenario 1, a sand column of 100 meters length is flushed constantly by water containing TCB. The microbial groups in the column then start to convert TCB to DCB and further to product MCB. In OGS-BRNS model, a line of 100 meters with spatial discretization of 2 meters is defined. Water flows from left to right

with velocity of 20 m/d. The dispersivity is 5 meters. The first order reaction rates of TCB, DCB and MCB are 0.0013, 0.00024, 0.00019 1/d respectively. The yield factor from TCB to DCB is 0.81 and from DCB to MCB is 0.765. The total simulation time is 1.5 days and temporal discretization of 0.01 day is employed. The initial and boundary conditions are

For $x \geq 0$,

$$c_{TCB}(x, 0) = c_{DCB}(x, 0) = c_{MCB}(x, 0) = 0 \quad (17.2)$$

For $t > 0$,

$$c_{TCB}(0, t) = 10.0 c_{DCB}(0, t) = c_{MCB}(0, t) = 0 c_{TCB}(\infty, t) = c_{DCB}(\infty, t) = c_{MCB}(\infty, t) = 0 \quad (17.3)$$

Scenario 2 has similar numerical settings but with different parameter values. The column length is 40 meters with spatial discretization of 1 meter. Water flow velocity is 0.4 m/d. The dispersivity is 10 meters. The total simulation time is 40 days with temporal discretization of 0.04 day. The first order reaction rates and yield factors of the five species are listed in Table 17.5.

For $x \geq 0$,

$$c_A(x, 0) = c_B(x, 0) = c_{C_1}(x, 0) = c_{C_2}(x, 0) = c_{C_3}(x, 0) \quad (17.4)$$

For $t > 0$,

$$c_A(0, t) = 1.0, \quad (17.5)$$

$$c_B(0, t) = c_{C_1}(0, t) = c_{C_2}(0, t) = c_{C_3}(0, t) = 0 \quad (17.6)$$

$$c_A(\infty, t) = c_B(\infty, t) = c_{C_1}(\infty, t) = c_{C_2}(\infty, t) = c_{C_3}(\infty, t) = 0 \quad (17.7)$$

Parameter	Value	Unit

Table 17.5: Values of first order reaction rates and yield factors for scenario 2.

17.3.2 Solution

The comparison was conducted for the concentration of all the species for scenario 1 and 2. Fig. 17.3.5 shows a very good agreement between analytical and numerical results for scenario 1. For scenario 2, as we can see from Fig. 17.3.6 and 17.3.7, the results obtained from OGS-BRNS also fit well with analytical solution.

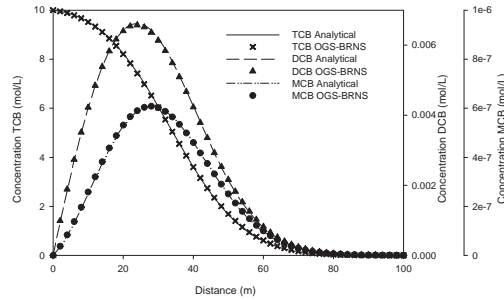


Figure 17.3.5: Comparison between concentration profiles of TCB, DCB and MCB calculated by analytical solution and OpenGeoSys-BRNS in scenario 1.

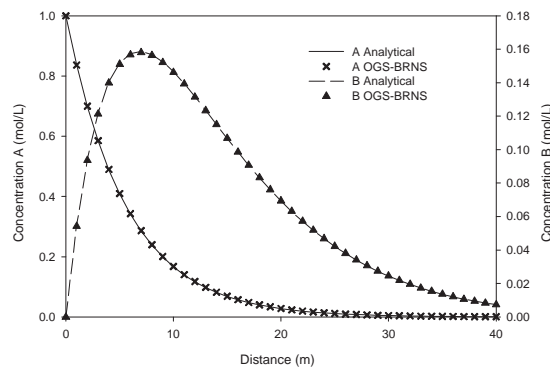


Figure 17.3.6: Comparison between concentration profiles of species A and B calculated by analytical solution and OpenGeoSys-BRNS in scenario 2.

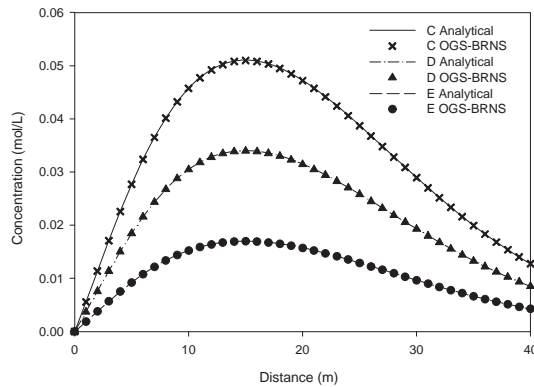


Figure 17.3.7: Comparison between concentration profiles of species C, D and E calculated by analytical solution and OpenGeoSys-BRNS in scenario 2.

17.4 1D reactive transport: Xylene degradation with multiple monod kinetics, exchange kinetics and biomass growth

17.4.1 Definition

This benchmark describes the reactive transport of xylene in a homogeneous aquifer. The main purpose is to document the ongoing reactions, which are xylene degradation under aerobic, sulfate reducing and iron reducing conditions, considering growth of the respective biomasses. Also included is the rate limited exchange of iron goethite into bioavailable iron. The aquifer is represented by a one-dimensional model of 50 m length in the x-direction and 1 m in the y- and z directions, respectively. The model is discretized by 100 line elements of constant 0.5 m length in x direction. With an isotropic hydraulic conductivity K of $2.13 \times 10^{-3} \text{ m s}^{-1}$, a porosity of 0.24 and a hydraulic gradient I of 1.3×10^{-4} , the steady state transport velocity v_a is 0.1 m d^{-1} . Longitudinal dispersivity α_L is set to 0.25 m, the diffusion coefficient D_a is set to $1.0 \times 10^{-9} \text{ m}^2 \text{ s}^{-1}$. The physical aquifer parameters are summarized in Tab. 17.6. The transport simulation is run for a period of 1000 d with a time step length of 5 d.

The model aquifer has a length of 50 m in the x-direction, 1 m in the y-direction and 1 m in the z direction. The whole domain is discretized into 100 line elements with a constant x and y dimension of 1 m. The aquifer is assumed to have a homogeneous and isotropic hydraulic conductivity. Using a gradient of 1.23×10^{-4} and a porosity of 0.24 produces a steady state transport velocity of 0.10 m d^{-1} . Xylene degradation is simulated according to the typical redox sequence.

Table 17.6: Parameters used for benchmark HC\1d_xylene_degradation

Parameter	Value	Unit
porosity $\Phi = n$	0.24	–
matrix volume fraction VOL_{MAT}	0.75	–
biomass volume fraction VOL_{BIO}	0.01	–
hydraulic conductivity K	2.13×10^{-3}	$m \cdot s^{-1}$
storage coefficient S	0.0	s^{-1}
solid density ρ_s	2000	$kg \cdot m^{-3}$
density of water ρ_w	1000	$kg \cdot m^{-3}$
viscosity water η	0.001	$Pa \cdot s$
longitudinal dispersivity α_l	0.25	m
component diffusion coefficient D	1.0×10^{-9}	$m^2 \cdot s^{-1}$

Model results are compared an older version of OpenGeoSys.

17.4.2 Solution

Results of the simulation are shown in Fig. 17.4.8 for xylene, the electron acceptors oxygen and sulfate, as well as for the biomass of the aerobic microorganisms, the sulfate reducers and the iron reducers simulation time steps of 100 days. For simulation time $t < 500$ d, one can see the advancing xylene front, a reduction of xylene concentrations is only visible for later times, when xylene concentrations reduce to about 90% of the inflow concentration. Also shown is the increasing consumption of oxygen with time, accompanied by the growth of the aerobic reducers at the inflow (left) end of the model area. After approximately 800 d, oxygen concentrations in the inflowing groundwater are reduced to almost zero within the first 20 m of the aquifer. Sulfate reducers initially decay from their initial amount, as growth is inhibited throughout the column by the still high concentrations of oxygen. Once oxygen is used up, however, sulfate reducers start to grow downstream of the oxygen reducers and sulfate concentrations in the groundwater reduce accordingly. The iron reducers decay from their initial values and start to grow only for late times $t > 80$ d and $x > 30$ m, as xylene degradation from iron reduction is inhibited by both, oxygen as well as sulfate, which is still present in concentrations larger than the inhibition concentration for iron reducers. Accordingly, the spatial distribution of bioavailable iron is still almost uniform throughout the aquifer.

Xylene degradation following multiplicative Monod kinetics with biomass growth

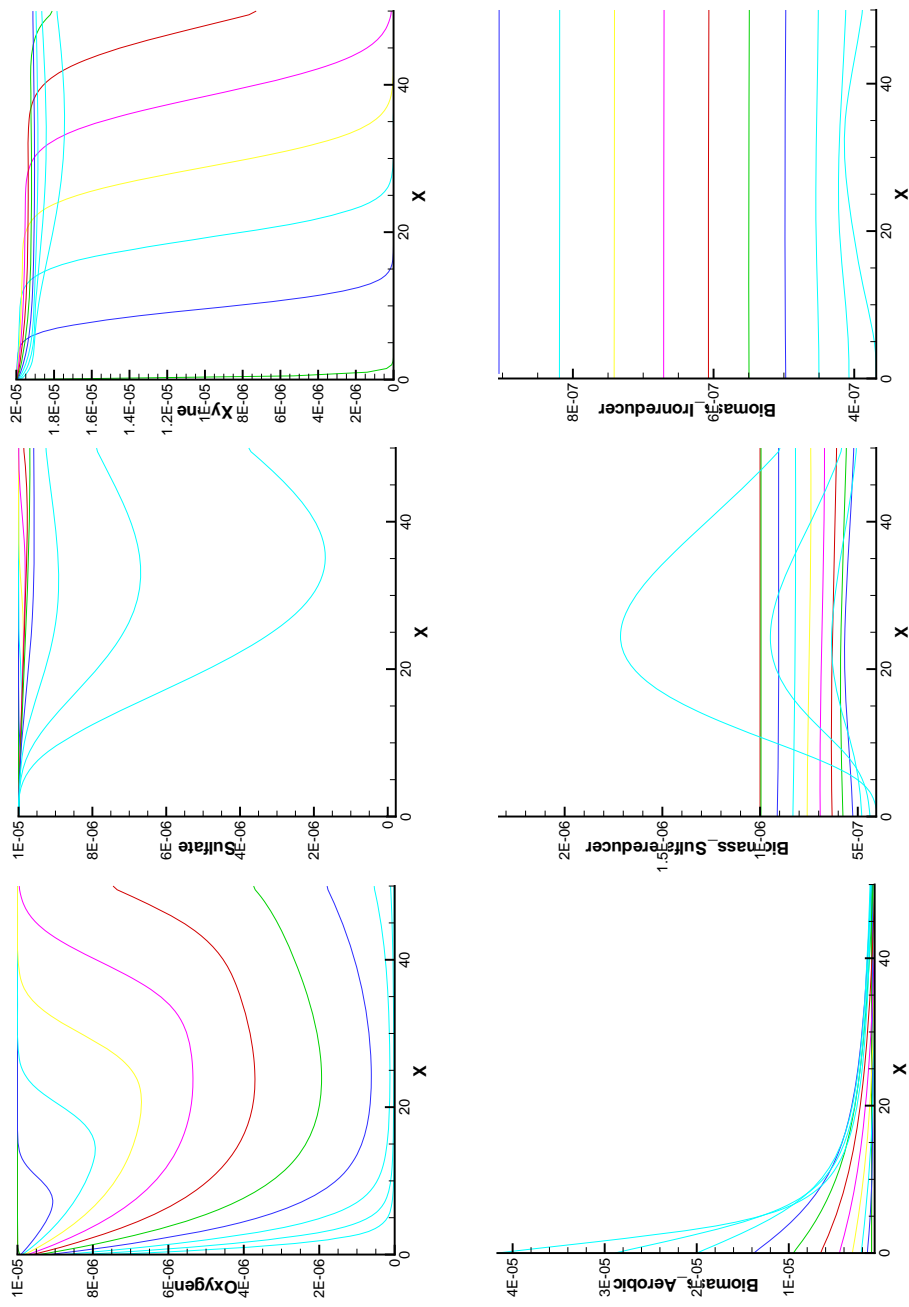


Figure 17.4.8: Profiles of oxygen, sulfate and xylene (top row, from left) and aerobic reducers, sulfate reducers and iron reducers at different times during the 1000 d simulation period.

17.5 1D reactive transport: Competition of TCE and cis-DCE-degradation for the zero valent iron surface

17.5.1 Definition

This example simulation demonstrates the use of OpenGeoSys for simulation of multi-species kinetic reactions. The reaction system was set up by D. Schäfer and published in [168]. Further, it was used for model verification of the newly implemented and developed kinetic reaction module in OpenGeoSys. The example considers flow in a one-dimensional column of 1 m length, resembling the thickness of a reactive iron barrier perpendicular to the flow direction. It involves 19 species and 16 different geochemical reactions, both first-order degradation reactions of adsorbed substances and kinetic sorption reactions of the Langmuir-type, considering competition for the available sorption sites.

The model set up consists of a 1d column with saturated ground water flow with a Darcy velocity of $5.0 \times 10^{-4} \text{ m d}^{-1}$ from left to right. Geochemical species are added to the inflowing water, and their sorption and degradation behavior is modeled. For a complete description of input parameters see the paper by Schäfer et al. (2003). Every degradation reaction follows a Langmuir-Hinshelwood-Hougen-Watson kinetics with a limited number of sites for the adsorption and desorption of chlorinated hydrocarbons on the reactive iron surface. Since all the reactive substances involved have to adsorb onto the reactive iron surface in order to be degraded, a competition for the surface sites occurs. This competition has been investigated in column studies and the observed concentration profiles were simulated with the numerical model TBC [168].

Model results are compared an older version of OpenGeoSys, which was compared to the original TBC simulations.

17.5.2 Solution

Results of the simulation are shown in Fig. 17.5.9, where profiles of the dissolved species are shown. TCE and cis-DCE are added to the inflowing water. They compete for the sorption sites, and when sorbed degrade according to a first order degradation reaction. The retardation of the reactive species compared to the conservative tracer `mobile` is clearly visible. Also, just downstream of the concentration decrease of TCE or cis-DCE, the degradation products ethane and C4-containing molecules increase. These species are again mobile and are transported with the water, so an instationary behavior is observed in Fig. 17.5.9.

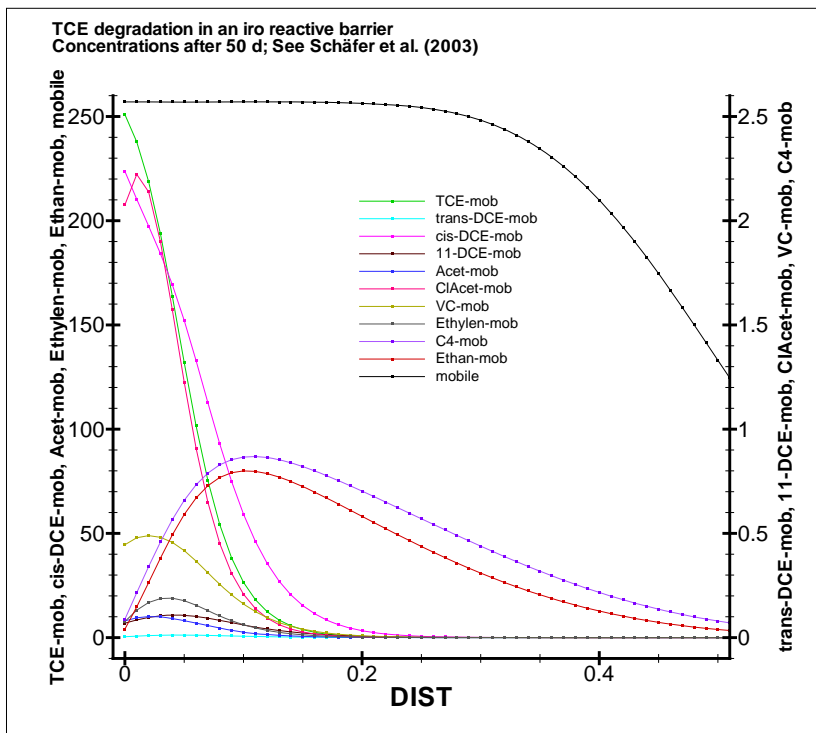


Figure 17.5.9: Concentration profiles of TCE, trans-DCE, cis-DCE, 1,1-DCE, Acetylene, chloroacetylene, C4, VC, ethene and ethane as well as the conservative tracer mobile after 50 d simulation time.

17.6 1D reactive transport: Sequential CHC degradation with isotope fractionation

17.6.1 Reaction model

When a substrate C is present in the form of light and heavy isotopes C^l and C^h and one of the isotopes is preferentially consumed by a microbial population X , a kinetic isotope fractionation effect can be observed, i.e. one of the isotopes will become enriched in the remaining fraction of electron donors relative to its isotope partner. At the same time, the preferentially consumed isotope will become enriched in the reaction product relative to the more recalcitrant isotope. The degree of isotope fractionation can be expressed by means of the fractionation factor α [-], which is a reaction specific constant and relates the isotopic ratio of the degradation reaction's product to the isotope ratio of the substrate. Often, the isotopic enrichment factor ε [-] is used to quantify the isotope effect of a reaction, which can be related to α for a one step process by

$$\varepsilon = (\alpha - 1) \cdot 1000 \quad (17.8)$$

According to Van Breukelen et al. [169], the degradation rate of the light carbon isotope substrate $d^{12}C_S/dt$ is given by the overall degradation rate dC_S/dt of substrate C_S corrected for the proportion of $^{12}C_S$ to total C_S

$$-\frac{d^{12}C_S}{dt} = \frac{d^{12}C_P}{dt} = -\frac{dC_S}{dt} \frac{^{12}C_S}{^{12}C_S + ^{13}C_S} \quad (17.9)$$

The degradation rate of the heavy isotope substrate $d^{13}C_S/dt$ then is given by

$$-\frac{d^{13}C_S}{dt} = \frac{d^{13}C_P}{dt} = -\frac{dC_S}{dt} \frac{^{13}C_S}{^{12}C_S + ^{13}C_S} (\varepsilon \cdot 10^{-3} + 1) \quad (17.10)$$

dC_S/dt can be any rate expression, such as first order, Michaelis-Menten or Monod-kinetics. Based on this concept and using the general formulation of multiple Monod kinetics of first order growth of a microbial species X from consumption of the light isotope substrate $^{12}C_S$ can be expressed by

$$\left[\frac{\partial X}{\partial t} \right]_{^{12}C_S} = \mu_{max} X \left[\prod_{j=1}^{n_M-1} \left(\frac{C_j}{K_j^M + C_j} \right) \prod_{j=1}^{n_I} \left(\frac{K_j^I}{K_j^I + C_j} \right) \right] \frac{C_S^{tot}}{C_S^{tot} + K_{C_S}^M} \frac{^{12}C_S}{C_S^{tot}} \quad (17.11)$$

where $C_S^{tot} = ^{12}C_S + ^{13}C_S$ and μ_{max} [T^{-1}] is the maximum growth rate of X with respect to substrate C . Growth of X from consumption of the heavy isotope substrate $^{13}C_S$ can be expressed accordingly by

$$\left[\frac{\partial X}{\partial t} \right]_{^{13}C_S} = \mu_{max}^* X \left[\prod_{j=1}^{n_M-1} \left(\frac{C_j}{K_j^M + C_j} \right) \prod_{j=1}^{n_I} \left(\frac{K_j^I}{K_j^I + C_j} \right) \right] \frac{C_S^{tot}}{C_S^{tot} + K_{C_S}^M} \frac{^{13}C_S}{C_S^{tot}} \quad (17.12)$$

where $\mu_{max}^* = \mu_{max}(\varepsilon/1000 - 1)$. The resulting degradation rates of $^{12}C_S$ and $^{13}C_S$ accordingly are given by

$$\frac{\partial^{12}C_S}{\partial t} = -\mu_{max} X \frac{St_{C_S}}{Y_{C_S}} \left[\prod_{j=1}^{n_M-1} \left(\frac{C_j}{K_j^M + C_j} \right) \prod_{j=1}^{n_I} \left(\frac{K_j^I}{K_j^I + C_j} \right) \right] \frac{C_S^{tot}}{C_S^{tot} + K_{C_S}^M} \frac{^{12}C_S}{C_S^{tot}} \quad (17.13)$$

$$\frac{\partial^{13}C_S}{\partial t} = -\mu_{max}^* X \frac{St_{C_S}}{Y_{C_S}} \left[\prod_{j=1}^{n_M-1} \left(\frac{C_j}{K_j^M + C_j} \right) \prod_{j=1}^{n_I} \left(\frac{K_j^I}{K_j^I + C_j} \right) \right] \frac{C_S^{tot}}{C_S^{tot} + K_{C_S}^M} \frac{^{13}C_S}{C_S^{tot}} \quad (17.14)$$

where St_{C_S} [-] and Y_{C_S} [-] are the stoichiometric and yield coefficients for substrate C_S . Degradation kinetics for the conceptually more simple Michaelis-Menten, first or zeroth order kinetics may be derived on basis of eqs. 17.11 - 17.14 assuming a constant microorganism mass and choosing appropriate values of μ_{max} , μ_{max}^* , $K_{C_S}^M$, St_{C_S} and Y_{C_S} .

For the simulation of biodegradation with isotope fractionation of a substrate species C_S by multiplicative Monod (or one of the more simplified) kinetics, heavy and light isotopes of the fractionating substrate, e.g. $^{12}C_S$ and $^{13}C_S$, must be defined as two individual species with corresponding transport processes. Also, two individual degradation reactions must be defined, requiring identical parameter values for μ_{max} , Y_{C_S} , and all K_i^M , K_i^I , and St_i . The isotopic enrichment factor ε then is used to calculate the modified maximum growth rate μ_{max}^* for the more recalcitrant isotope.

17.6.2 Definition

In this benchmark, which is based on a model of [169], sequential degradation of chlorinated hydrocarbons (CHC) from PCE to the end product ethylene (Eth), which is not further degraded, is simulated:



A contaminant source located at the upstream model boundary emits a constant concentration of PCE. All degradation reactions follow simple first order kinetics and involve an isotope fractionation effect. The one-dimensional transport model has a length of 876 m and is discretized by 120 finite line elements of 7.3

m length, respectively. Basic flow and transport model parameters are summarized in Tab. 17.7, reaction parameters for the individual species in Tab. 17.8.

Table 17.7: Parameters used for benchmark

Parameter	Value	Unit
porosity $\Phi = n$	0.25	–
matrix volume fraction VOL_MAT	0.74	–
biomass volume fraction VOL_BIO	0.01	–
hydraulic conductivity K	1.1574×10^{-4}	$m \cdot s^{-1}$
flow velocity q	1.1574×10^{-6}	$m \cdot s^{-1}$
longitudinal dispersivity α_l	1.0	m
component diffusion coefficient D	3.0×10^{-9}	$m \cdot s^{-1}$

Table 17.8: Reaction parameters used for benchmark HC\1d_isofrac

CHC species	enrichment factor ε [-]	first order rate constant $\lambda [s^{-1}]$
PCE	-5.2	6.366×10^{-8}
TCE	-8.5	3.125×10^{-8}
DCE	-17.8	2.199×10^{-8}
VC	-23.2	1.273×10^{-8}
Eth	0.0	–

Each of the mobile hydrocarbon species is defined twice, once for the light isotopologue and once for the respective heavy isotopologue. Also, an immobile microorganism species X is defined, which has an initial unit concentration of 1.0 throughout the model domain. The microorganisms degrade each of the chlorinated species (i.e. PCE, TCE, DCE and VC). Thus, a total of eight monod-type growth reactions for X , one for each isotopologue species, must be defined. Growth of X , however, is inhibited by setting the growth parameter in the *.krc file to zero in each of the reactions and microorganism decay is not included in the simulation, i.e. X is constant in time and space. Each reaction contains only a single Monod term for the respective isotopologue species. To achieve degradation kinetics of first order in each case, the half saturation concentrations $K_i^M \gg C_i$ and are hence set to a value of 1.0×10^{10} . As the effective first order rate constant is given by $\lambda_i = \mu_{max,i}/K_i^M$, parameters $\mu_{max,i}$ are set to proportionally high values in the *.krc file, i.e. ten orders of magnitude larger than indicated in Tab. 17.8. Also, the yield coefficients Y_i for the individual reactions must be set to 1.0.

Initial concentrations of all species except the microorganisms are 0.0 mol L⁻¹ throughout the model domain. For ¹²PCE and ¹³PCE the upgradient boundary conditions are constant concentrations of 9.892×10^{-4} and 1.078×10^{-4} mol L⁻¹, respectively. The hydraulic gradient of 0.01 is induced by fixed head boundary conditions of 10.0 and 9.781 m at the up- and downgradient model boundaries. The reactive transport simulation is run for a period of 20 a with 200 time steps

of 3153600 s, respectively, and using an explicit-implicit time stepping scheme ($\theta = 0.5$).

Model results are compared against the one-dimensional Domenico analytical solution including first order degradation kinetics as well as by comparison of an equivalent one dimensional simulation with PHREEQC, which was presented by Van Breukelen et al. [169].

17.6.3 Solution

Results at the end of the simulation are presented in Figs. 17.6.10 and 17.6.11. In Fig. 17.6.10, numerical simulation results for the PCE isotopologues in form of normalized concentrations C/C_0 are compared against results of the one-dimensional Domenico analytical solution including first order degradation, in which the first order degradation rate for the heavy PCE isotopologue $\lambda_{^{13}PCE} = \lambda_{^{12}PCE}(\varepsilon/1000 - 1)$. Note that for the comparison with the analytical solution kinetic reactions are suppressed on the first node of the FE mesh (i.e. on the upstream model boundary in order to correctly represent the concentration boundary condition of the analytical solution. Concentrations of the PCE isotopologues match the analytical solution over a concentration range of more than 10 orders of magnitude. Also the resulting $\delta^{13}C$ [permil] isotope signatures, which were computed by

$$\delta^{13}C = \left(\frac{R_{C_i}}{R_{Ref}} - 1 \right) 1000 \quad (17.15)$$

where R_{C_i} [-] is the isotope ratio $^{13}C_i/^{12}C_i$ of species C_i in the simulation, while R_{Ref} [-] is the isotope ratio of the international standard, i.e. in this case the Vienna Pee Dee Belemnite (V-PDB; $R_{Ref} = 0.011237$), match results of the analytical solution precisely, verifying the correctness of the implementation.

In Fig. 17.6.11 the upper left and right diagrams show simulated concentration profiles of the individual CHC species versus results obtained by PHREEQC. Note that for the comparison with the PHREEQC simulation, kinetic reactions are not suppressed on the upstream model boundary. The lower diagram shows $\delta^{13}C$ isotope signatures. While concentrations of ^{12}PCE and ^{13}PCE decrease exponentially with distance from the source at the left hand side model boundary, isotopologues of TCE, DCE and VC show concentration peaks in different distances from the source. Eth isotopologues finally accumulate as the end products of the degradation chain and reach the source concentrations of ^{12}PCE and ^{13}PCE , respectively. Also, while TCE, DCE and VC isotope signatures increase almost linearly with travel distance, demonstrating the increasing enrichment of the heavy isotopologues, the Eth signature approaches the $\delta^{13}C$ of the source, i.e. PCE. For all isotopologue species, concentration profiles and isotope signatures show an excellent agreement with the PHREEQC simulation, verifying the numerical implementation also for sequential degradation reactions.

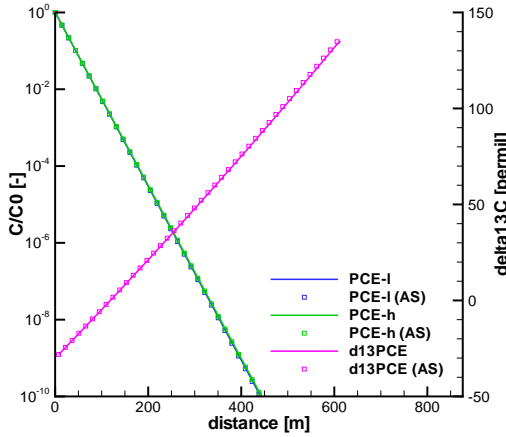


Figure 17.6.10: PCE isotopologue concentration profiles (left axis) and $\delta^{13}C$ isotope signature (right axis) versus transport distance along the 1D model. Lines represent GeoSys simulation results, symbols represent analytical solution results.

17.7 1D reactive transport: degradation of organic contaminants in a sand column experiment by five bacterial groups forming a degradation network

The Biogeochemical Reaction Network Simulator (BRNS, [170, 171]) is coupled to OpenGeoSys following a sequential non-iterative operator splitting scheme yielding the reactive transport model OpenGeoSys-BRNS. The technical coupling is sketched in Fig. 17.7.12.

17.7.1 Definition

An experimental study by von Gunten and Zobrist [172] has been used to validate the reactive transport models TBC [173] and the stand-alone 1D version of BRNS [174]. Both models could reproduce the experimental data set. Here, we use the same simulation scenario to validate GeoSysBRNS and compare simulation results to BRNS results.

In the example referred to as “Scenario 1” in [174], a sand column of 29 centimeters length is constantly flushed with water containing lactate as electron donor, and oxygen, nitrate, and sulfate as terminal electron acceptors (TEAs). Manganese and iron oxyhydroxides are bound to the sand matrix in solid phases

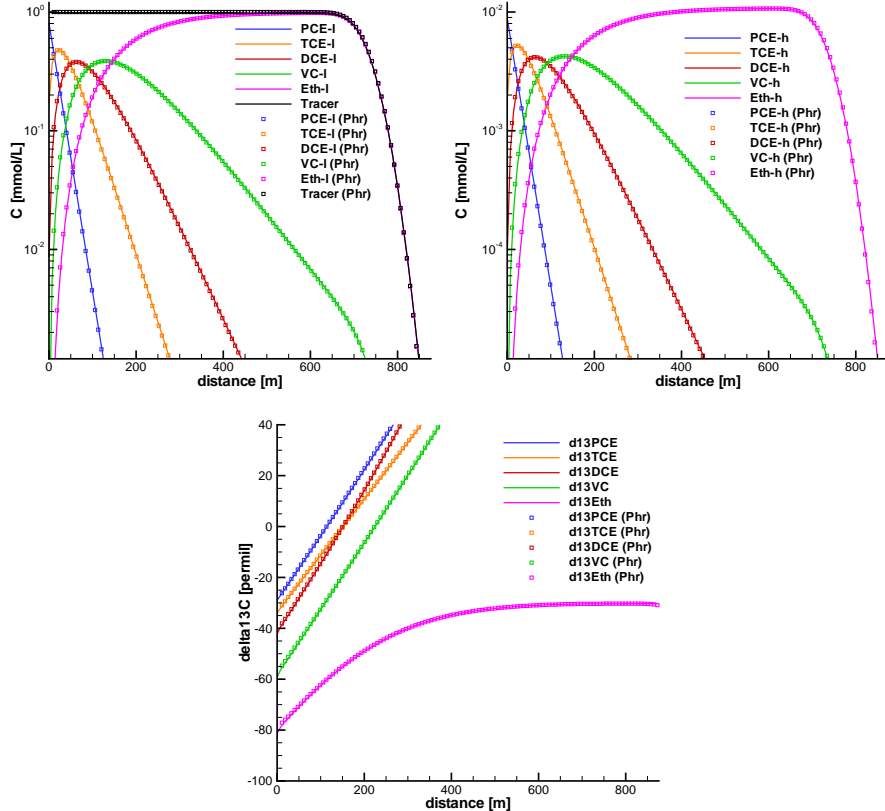


Figure 17.6.11: Light (upper left diagram), heavy (upper right diagram) isotopologue chlorinated hydrocarbon species profiles and $\delta^{13}\text{C}$ isotope signatures (lower diagram) versus transport distance along the 1D model. Full lines represent GeoSys simulation results, symbols represent PHREEQC simulation results.

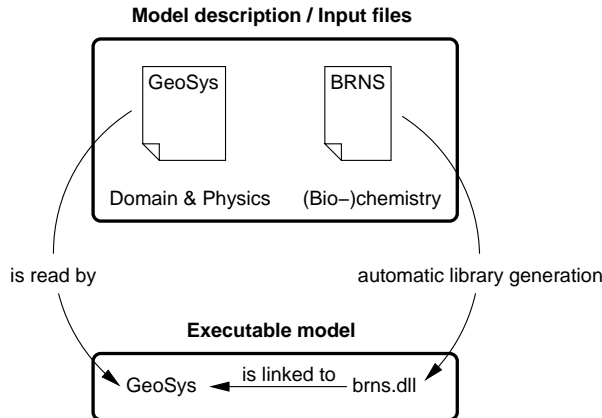


Figure 17.7.12: The setup of OpenGeoSys-BRNS. The model description is divided into two parts: the model domain definition, physical parameters, hydrogeological flow, and discretization parameters in OpenGeoSysformat, and the description of the coupled (bio-)chemical reaction processes in BRNS format. The latter is compiled into a problem specific library that is accessed by OpenGeoSysat runtime.

and act as two additional TEAs. Five distinct microbial groups, which catalyze the reduction of each TEA to sustain their growth, are considered in the model. The experimental results suggest that lactate is concomitantly mineralized into dissolved inorganic carbon (DIC) and fermented to acetate and propionate, with the latter being further oxidized into DIC. In addition to these microbial degradation pathways, reactive species concentrations are influenced by a set of abiotic reactions (Fig. 17.7.13). The complete reaction network of the model consists of 21 mobile and 18 immobile reactive species. The dynamics of the system is determined by 24 kinetically controlled chemical reactions and nine equilibrium reactions describing acid base dissociations.

The coupling of the BRNS to OpenGeoSysis shown to be correct by comparing simulation results of OpenGeoSys-BRNS to BRNS results [175].

17.7.2 Solution

We simulate the experiment with GeoSysBRNS using two spatial resolutions and three different temporal resolutions per spatial setting, ensuring Courant numbers smaller than 1.0 in all cases. As in previous studies [174, 173], we choose 48 days as the target time for comparing the results of the coupled model to those obtained with the BRNS model using the same set of spatio-temporal resolution settings. At this target time, the system is still in the transient state.

The simulation results of OpenGeoSys-BRNS and BRNS agree very well for all

- phase exchange (matrix, biophase, pore water)
- oxidation of sulfide by Fe(III)
- precipitation and dissolution of calcite and Fe(II) minerals
- acid-base reactions for carbonates, sulfides, lactate, propionate, acetate

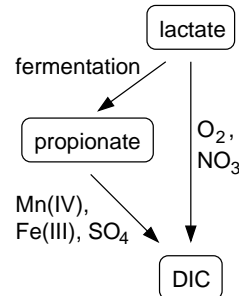


Figure 17.7.13: Modeling organic carbon degradation in a sand column experiment. Coupled abiotic processes considered in the model (left), and microbial degradation pathways with corresponding TAEs (right).

39 reactive species at the highest spatial and temporal resolution (see selected species in Figs. 17.7.14, 17.7.15). Decreasing the spatial resolution leads to slightly different results, with the coupled model generally staying closer to the high resolution result than the stand-alone version of BRNS (Figs. 17.7.14, 17.7.15).

When the time step size is increased, the numerical results of both models diverge from the high resolution result (Fig. 17.7.16). While increasing the time step from 4 s to 43.2 s does not lead to significant changes for both models and both spatial resolutions, a noticeable deviation is observed when the time step size is further increased to 108 s for the high, and to 216 s for the low spatial resolution. For these larger time step sizes, the results of OpenGeoSys-BRNS are again generally closer to the high resolution result than the BRNS solutions. The observed differences can be attributed to the different numerical schemes used by BRNS (finite differences) and OpenGeoSys-BRNS (finite elements). Further details of the OpenGeoSys-BRNS and its performance can be found in [175].

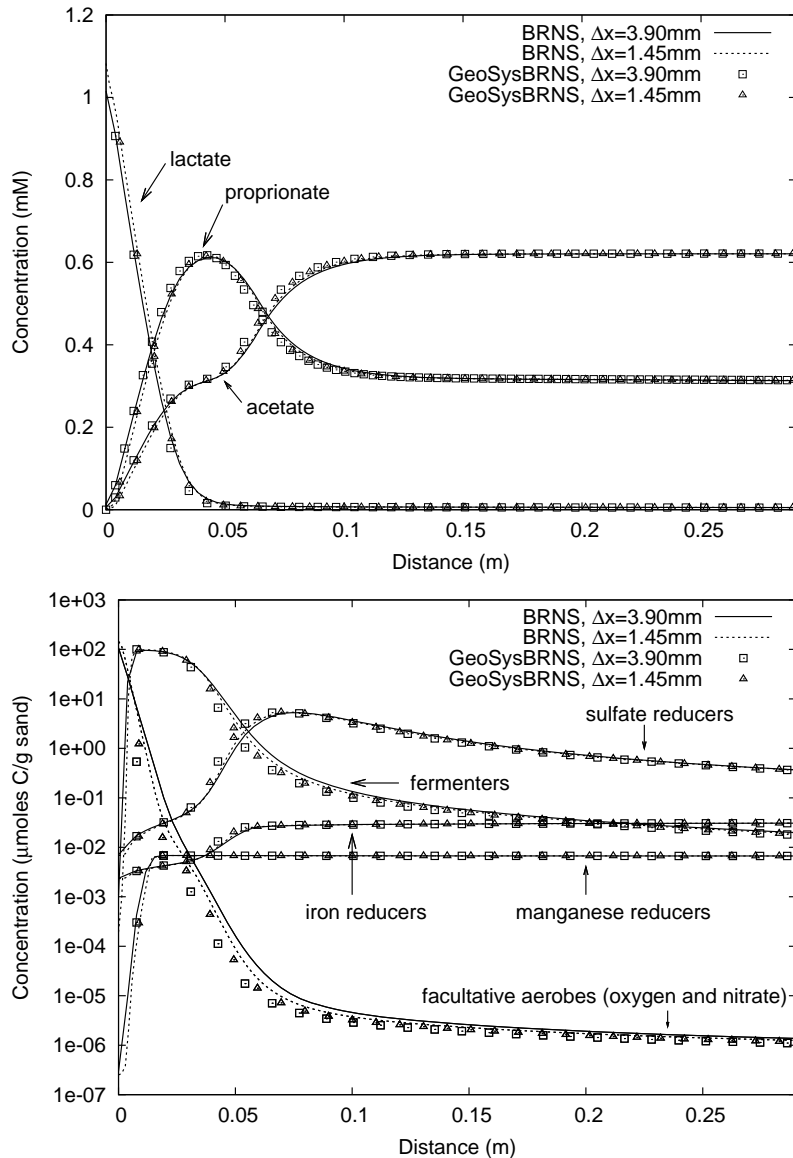


Figure 17.7.14: Comparison of simulation results obtained with BRNS (lines) and OpenGeoSys-BRNS (symbols): organic species (top) and all five bacterial groups (bottom) at day 48 using the highest temporal resolution ($\Delta t=4\text{ s}$) and two spatial resolutions.

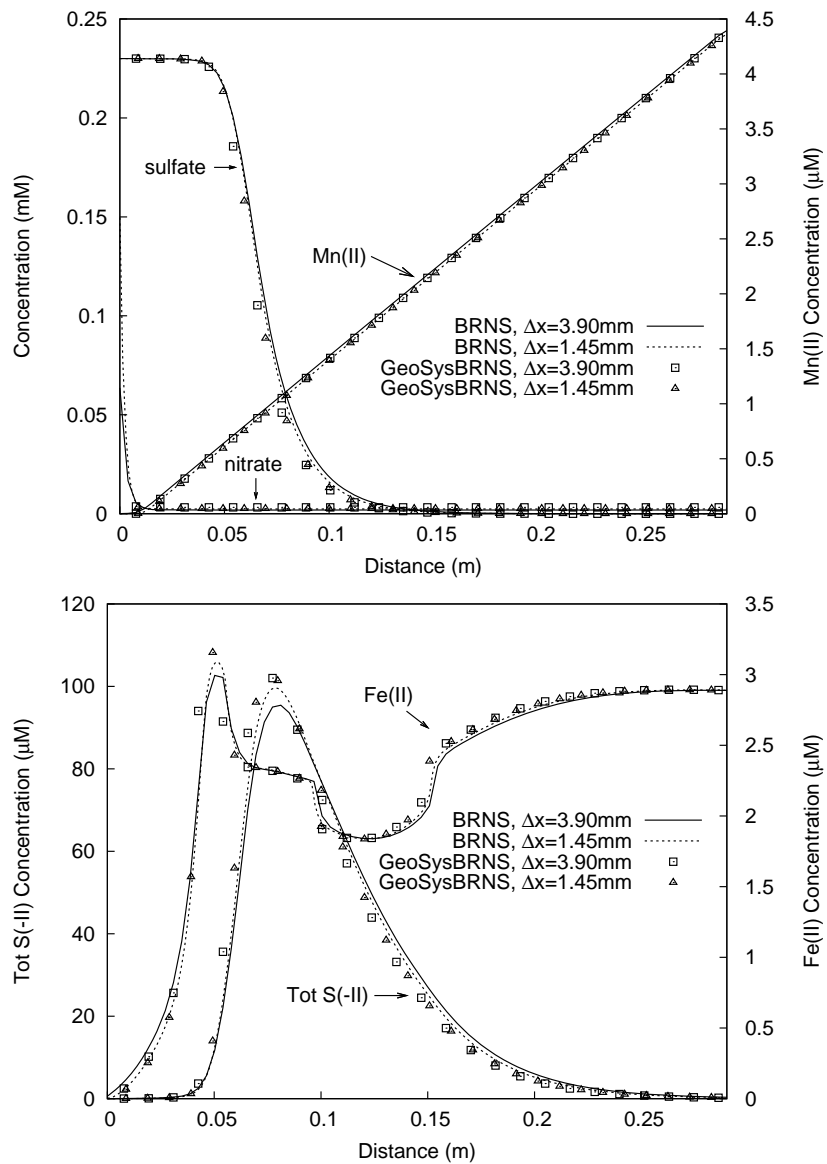


Figure 17.7.15: Comparison of simulation results obtained with BRNS (lines) and OpenGeoSys-BRNS (symbols): inorganic species at day 48 using the highest temporal resolution ($\Delta t=4\text{ s}$) and two spatial resolutions.

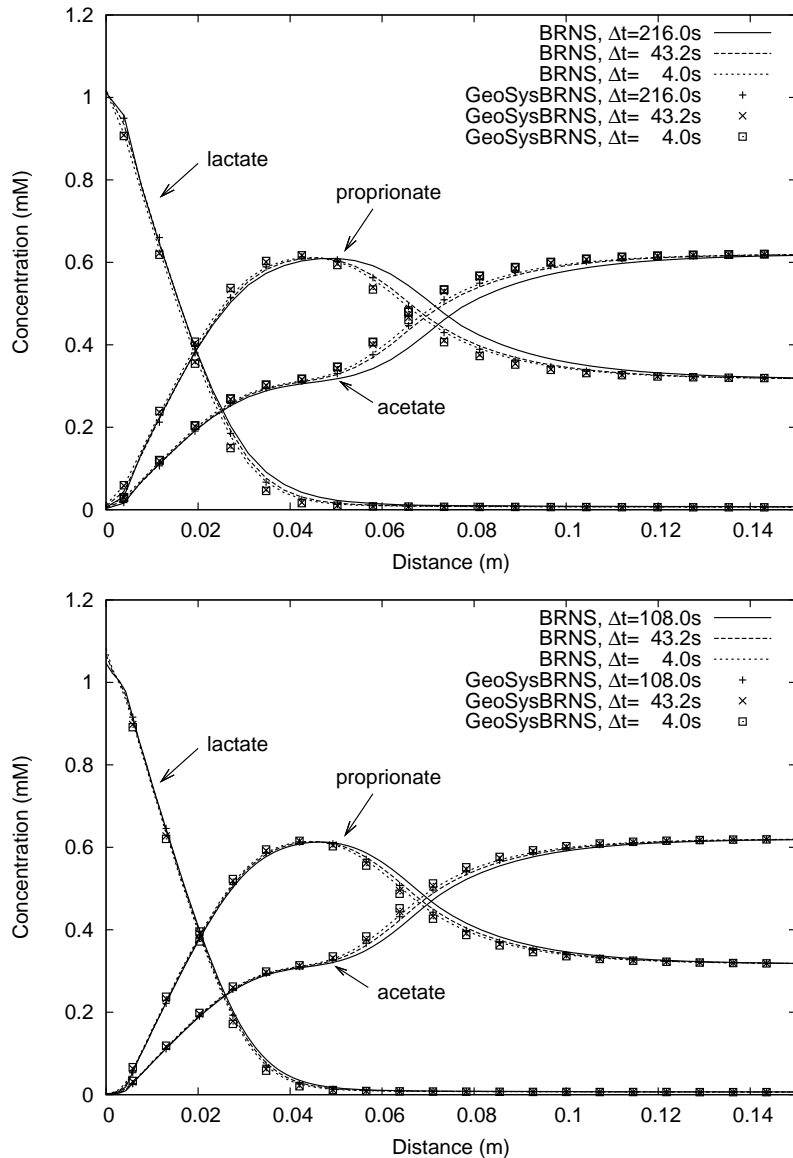


Figure 17.7.16: Comparison of simulation results obtained with BRNS (lines) and OpenGeoSys-BRNS (symbols) at day 48 using two spatial resolutions (top: $\Delta x=3.9\text{mm}$, bottom: $\Delta x=1.45\text{mm}$) and different time step sizes for lactate, propionate, and acetate.

17.8 1D reactive transport: Mixing Controlled Biodegradation (2D)

17.8.1 definition

For contaminated groundwater, the natural remediation process is usually limited by the availability of substrates acting as a carbon source for soil bacteria and the availability of electron acceptors. The transport of these chemical compounds is controlled by the dispersion length of the flow system. Recently, Cirpka and Valocchi [176] presented an analytical solution (revised in [177]; see also [178]) for the steady state of a two-dimensional scenario dominated by transversal mixing. This example serves as a first multidimensional benchmark to validate GeoSysBRNS. [176] and [177] provide analytical solutions for double-monod kinetics with first-order biomass decay. OpenGeoSys-BRNS is also compared to the KinReact module of OpenGeoSys(OpenGeoSys-KRC), which is able to solve the same problem.

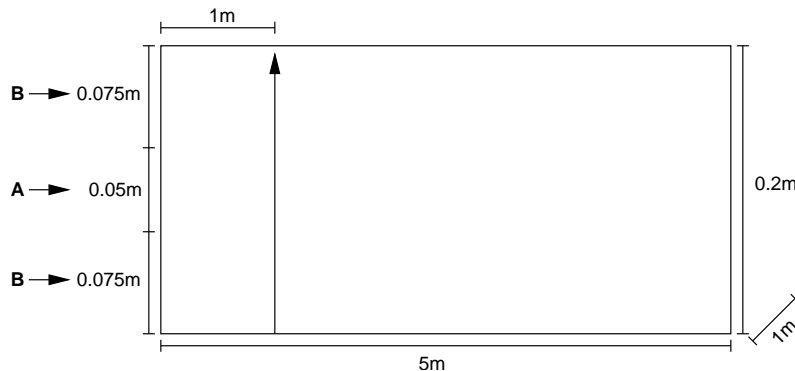


Figure 17.8.17: The simulation domain. Simulation results are compared using concentration profiles along a transect at a distance of one meter from the inflow boundary, indicated by the arrow.

In this scenario, bacterial growth is modeled using double-monod terms for the substrates. Biomass decays with a constant decay rate d . The overall dynamics is described by four differential equations, with the dynamics of species A, B, and C directly linked to the biomass growth r via yield factor Y :

$$\frac{\partial C_{bio}}{\partial t} = \underbrace{\frac{C_A}{K_A + C_A} \cdot \frac{C_B}{K_B + C_B} \cdot \mu_{max} \cdot C_{bio}}_r - d \cdot C_{bio} \quad (17.16)$$

$$\frac{\partial C_A}{\partial t} = -\frac{1}{Y} \cdot r \quad (17.17)$$

$$\frac{\partial C_B}{\partial t} = -\frac{1}{Y} \cdot r \quad (17.18)$$

$$\frac{\partial C_C}{\partial t} = +\frac{1}{Y} \cdot r. \quad (17.19)$$

The chemical parameters and their values are listed in Table 17.9.

Table 17.9: Reaction parameters and values.

Symbol	Parameter	Value	Unit
K_A	monod constant substrate A	8.33×10^{-5}	$\text{mol} \cdot \text{L}^{-1}$
K_B	monod constant substrate B	3.13×10^{-5}	$\text{mol} \cdot \text{L}^{-1}$
μ_{max}	maximum growth rate	1.0	d^{-1}
d	biomass death rate	0.1	d^{-1}
Y	yield coefficient	1.0	$\text{g} \cdot \text{mol}^{-1}$

Using OpenGeoSys-BRNS, here we simulate the case as a transient state groundwater flow process coupled with biodegradation. The numerical solutions are compared to the analytical steady state solutions and against the OpenGeoSys-KRC simulation.

The model domain is five meters long and 20 cm wide (see Figure 17.8.17). Groundwater flows from left to right. Transport velocity is 1 m/d. The transport parameters are listed in Table 17.10. Two substrates are continuously emitted at the left inflow boundary throughout the simulation period. Substrate A is centrally injected over a width of five centimeters with a concentration of 3.3×10^{-4} mol/l, while substrate B is emitted at the remaining part of the boundary with a concentration of 2.5×10^{-4} mol/l. Initially, the concentration in the whole simulation domain is zero for substrate A, 2.5×10^{-4} mol/l for substrate B, and 1.0×10^{-6} g/l for biomass. Biomass is considered to be immobile.

In the presence of both species A and B, with A representing a generic organic contaminant acting as a carbon source and B representing a generic electron acceptor, the biomass grows, and a waste product C is formed.

For the numerical simulation, a grid spacing of 2.5 cm in flow, and 0.4 cm transversal to the flow direction is used. Temporal discretization of 2min is employed. The OpenGeoSys-KRC simulation additionally verifies the functionality of three routines, which were implemented to enhance computational efficiency of the numerical simulation:

Table 17.10: Transport parameters and values.

Parameter	Value	Unit
v_a transport velocity	1.0	$\text{m}\cdot\text{d}^{-1}$
D_t transversal dispersion coefficient	2.5	$\text{cm}^2\cdot\text{d}^{-1}$
D_l longitudinal dispersion coefficient	0.0 ^a	$\text{cm}^2\cdot\text{d}^{-1}$

^aAs a zero value cannot be used in the numerical simulation, the value $2.5 \times 10^2 \text{cm}^2/\text{d}$ was used instead. When the numerical simulation reaches steady state, this difference can be neglected.

- The steady state flow field is computed only once (i.e. for the first time step) during the simulation. For later time steps, the velocities calculated for the first time step are reused for all transport processes. This modus is invoked by the flow process keyword

```
$TIM_TYPE
STEADY.
```

- Mass matrices for all transported (i.e. mobile) species are computed only once (i.e. for the first time step), stored and reused for later time steps. This modus is invoked by mass transport process keyword

```
$MEMORY_TYPE
1
```

- Source terms are defined as volumetric fluxes [$\text{m}^3 \cdot \text{s}^{-1}$]. The flux defined for a polyline is evenly distributed to all nodes of that polyline. This modus is invoked for a source term by the keyword

```
$DIS_TYPE
CONSTANT_GEO 2.31481E-06
```

where the number represents the volumetric flux assigned to a polyline.

In the OpenGeoSys-KRC simulation, the downgradient model boundary consists of two polylines with lengths of 0.15 and 0.05 m, respectively. In order to achieve a transport velocity (setting porosity $n = 0.5$) of $1 \text{ m}\cdot\text{d}^{-1}$ (or $1.15741 \times 10^{-6} \text{ m}\cdot\text{s}^{-1}$) with a given a total model cross section of 0.2 m^2 (i.e. assuming a unit width of the model), the volumetric fluxes assigned to the polylines are -8.75130×10^{-7} and $-2.822945 \times 10^{-7} [\text{m}^3 \cdot \text{s}^{-1}]$, respectively.

17.8.2 Solution

The concentrations of the conservative tracer (i.e. the mixing ratio X) fit well with the analytical solution, indicating that the flow field and conservative transport is properly simulated by both models, and all of the three routines tested

work correctly in the OpenGeoSys-KRC simulation, which allows a reduction of computation time by approximately 50 % for this test example. Also, both numerical simulations yield the same results for the reactive species. However, some small discrepancies are found between the numerical and the analytical solutions for the components A, B, C, and (most obvious) for the biomass concentration (see Figure 17.8.18). This is mainly due to the problem of exactly defining the transitions between boundary conditions of components A and B on the inflow boundary of the model: polylines defining inflow concentrations of A and B may not share nodes and hence the boundary condition polylines are separated by a distance of one element width (i.e. 0.005 m) which has to be overcome by transverse dispersion before A and B may react with each other, while in the analytical solution A and B are in direct contact right at the model boundary. This problem and hence differences between numerical and analytical solutions may be reduced by a local mesh refinement at the left hand side model boundary.

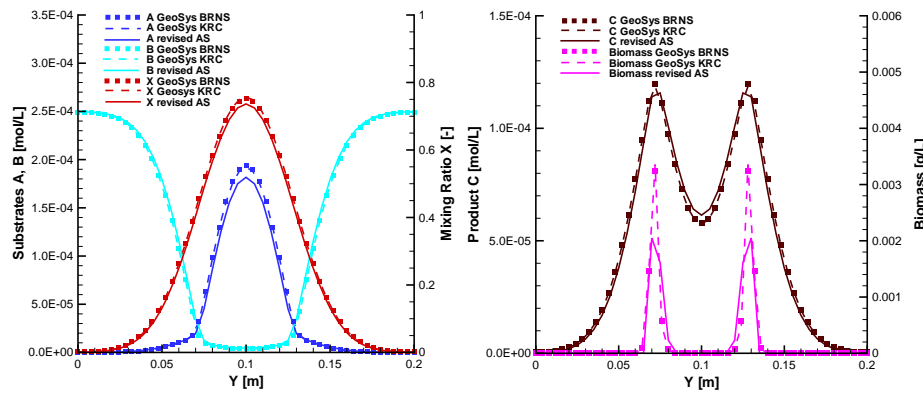


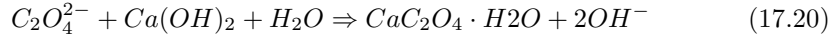
Figure 17.8.18: Simulation results for the transversal mixing model, using the kinetic approach and the finest temporal and spatial resolution. Analytical solution as solid lines, result of the numerical simulations with GeoSysBRNS as symbols and of GeoSysKRC as dashed lines.

17.9 2D reactive transport simulation of COMEDY clogging experiment

Clogging is a widely occurring phenomena in the porous media. The change of pore space structure normally leads to different behaviors of hydraulics. In such systems, flow and transport of solutes are strongly coupled with chemical reactions, imposing challenges to numerical simulations. The COMEDY experimental setup [179] was a 2D reactive transport scenario which involves clogging and perforation of an interface. Numerical models such as CRUNCH and HYTECH have been applied to simulate it. In this section, simulation results from OpenGeoSys-GEM are compared against those from other codes.

17.9.1 Definition

17.9.19 shows the geometry of the model domain. It is a chamber containing 3 regions. Two of them (Q1 and Q3) are made of chemically inert quartz and the central region (Q2) contains the reactant mineral portlandite. Oxalate ions were injected as a constant flux through Inlet 2, and sodium chloride solutions were introduced through Inlet 1. In Q2, the chemical reaction between the inlet solution and portlandite leads to the precipitation of calcium oxalate, as in the following.



The initial and boundary chemical was set up using the GEMS-PSI software package. It implements a Gibbs energy minimization algorithm in thermodynamic modeling of equilibrium in heterogeneous aquatic chemical systems. The oxalate ion was introduced as an independent component in the thermodynamic database. The reaction 17.20 was also introduced with equivalent logK values as in [179]. The detailed chemical set up for the different regions are given in 17.11. At some points, the system is in an undefined redox state. To avoid this, a small amount of dissolved O_2 was introduced in the initial bulk composition to keep the system in oxic condition. The value of porosity is obtained using the ratio $V_{Initial}/V_{Total}$.

The chamber is discretized with a finite element mesh of quadrilateral elements of 3.3 mm size. The domain contains 1849 nodes and 1764 elements. A variable time step scheme is used to calculate the maximal time step size, which influences the accuracy of simulation result.

The pressure at the outlet is set to 1 Bar.

The tortuosity is set different for Q2 region to mimic the initial effective diffusion coefficient, which is the same (1×10^{-09}) for the 3 regions in [179]. In this study diffusion and dispersion are assumed isotropic and D^* reduces to a scalar form, $D^* = \alpha \|\vec{U}\| + D$ where D is the effective diffusion coefficient. It is assumed

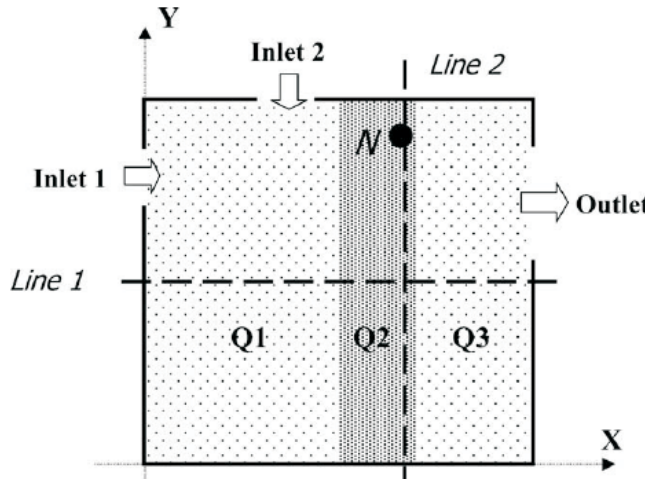


Figure 17.9.19: 2D model domain for the COMEDY experiment according to [179]. The setup is a square (14 cm of edge size). Lines labeled Line 1 ($y = 7.0$ cm) and Line 2 ($x = 9.5$ cm) (respectively node N ($x = 9.5$ cm; $y = 10.8$ cm)) are test lines/node on which specific profiles will be compared.

that all solutes have the same value. α (m) is the dispersivity of the porous medium and \vec{U} is the Darcy velocity vector. In this benchmark, advection and diffusion govern the transport process. The Archie's diffusion law $D_e = n^m \cdot D_p$ is applied in this model. The dissolution/precipitation reaction rate r_s (mol/s) is defined according to the following formula,

$$r_s = -A_s k_{rate} [1 - (Q_s/K)] \quad (17.21)$$

where k_{rate} is the dissolution and precipitation rate constant ($mol \cdot m^2 \cdot s^{-1}$). Q_s is the ion activity product. K is the equilibrium constant and A_s is the specific surface area ($m^2 \cdot mol^{-1}$). The values used here are $A_{bulk} = 1000 m_{solid}^2 / m_{porousmedium}^3$, $\log_{10} K_{Portlandite} = -5$ and $\log_{10} K_{CaOxa} = -5$.

17.9.2 Solution

For the flow part, 17.9.20 shows the Darcy velocities on Line 1, compared against the results given by HYTEC. The results obtained with OpenGeoSys are in good accordance quantitatively and qualitatively.

For the clogging process, porosity evolution profile 17.9.21 calculated by OpenGeoSys-GEM is compared against those from HYTEC and CRUNCH [179]. Qualitatively the results are in good accordance. Portlandite dissolves and calcium

Table 17.11: Equilibrium amount of independent components and phases for boundary and initial conditions

	Component	Q1(=Q3)	Q2	I1	I2
Amount of chemical species in aqueous phase (mol)	C	1.00e-5	5.50e-8	6.20e-8	5.51e-8
	Ca	1.00e-5	3.32	4.70e-8	3.00e-8
	Cl	1.20e-5	1.71e-12	0.02	4.25e-5
	H	33.2	27.7	33.2	33.3
	Na	1.71e-10	1.35e-3	0.02	0.8
	O	78.3	78.9	78.3	78.4
	Oxa	2.00e-8	1.00e-8	2.00e-8	0.40
	Si	30.9	30.9	30.9	30.9
	Zz	0	0	0	0
Amount of solid phases (mol)	Graphite	3.50e-8	3.50e-8	3.50e-8	3.50e-8
	Aragonite	1.00e-8	1.00e-8	1.70e-8	1.00e-8
	Calcite	1.00e-5	1.00e-8	1.00e-8	1.00e-8
	Portlandite	0	3.33	0	0
	Calcium Oxalate	1.00e-8	1.00e-8	1.00e-8	1.00e-8
	Quartz	30.87	30.87	30.87	30.87
	Amorph Silica	0	0	0	0
Equilibrium state	pH	7	12.5	7	7
	Liquid volume (L)	0.3	0.19	0.3	0.3
	Total volume (L)	1	1	1	1

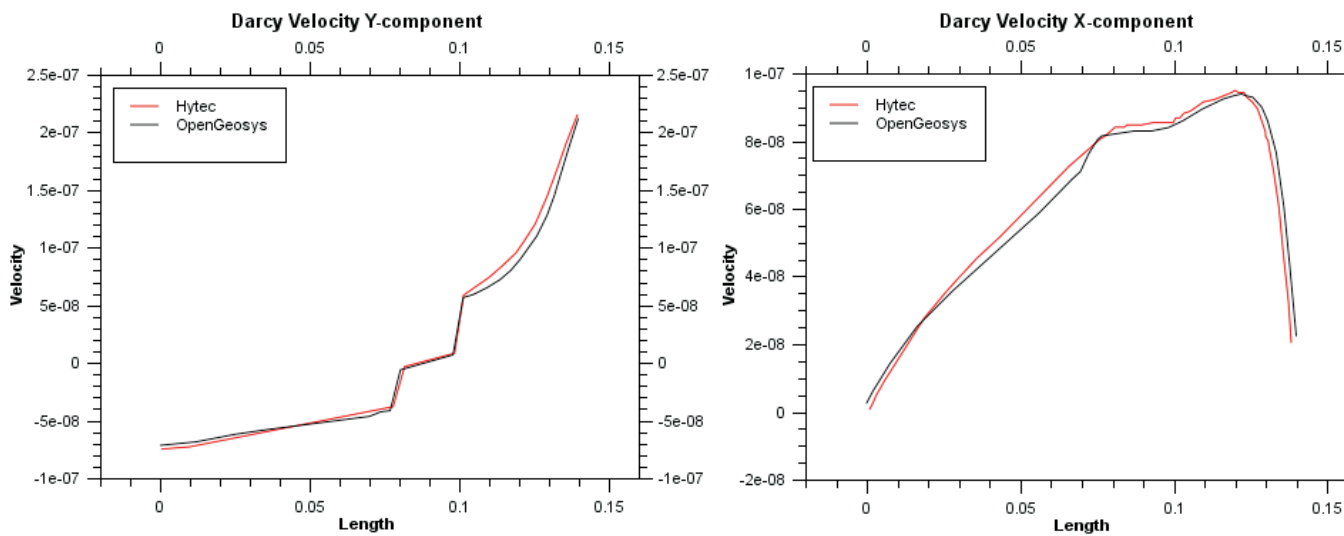


Figure 17.9.20: Darcy velocity profile on line 1 ($x=70$ cm)

Table 17.12: Hydraulic parameters of the model domain

Parameters	Q1	Q2	Q3
Hydraulic conductivity (m^2/s)	1.00e-5	1.64e-6	1.00e-5
Dispersivity (m)	2.00e-2	2.00e-2	2.00e-2
Diffusion coefficient (m^2/s)	3.33e-9	3.33e-9	3.33e-9
Tortuosity	1.0	1.58	1.0

Table 17.13: Model Setup for the inlets

Velocity (m/s)	Inlet 1	Inlet 2
x	5.7143e-10	0
y	0	11.429e-10

oxalate precipitates. After the calcium oxalate volume fraction reaches a maximum it dissolves. The porosity follows the opposite evolution of mineral volume fraction due to the decrease of 33mL per mol of reacted portlandite. When calcium oxalate starts to dissolve, the porosity increases until it reaches the maximal value of 0.3 due to inert quartz background in Q2.

Quantitatively, the results are different in several aspects. One of them is the evolution of porosity in time. With OpenGeosys, the portlandite dissolves much faster. It took 20 days in OGS whereas in CRUNCH and HYTEC the complete dissolution happens after 60 and 27 days respectively. The calcium oxalate is completely dissolved after 156 days in the OGS result, and took 60 and 90 days for CRUNCH and HYTEC. The porosity follows the same evolution in time. The dissolution time of calcium oxalate can slightly be reduced by increasing its precipitation/dissolution rate. Another difference is that with HYTEC and CRUNCH, portlandite volume ratio remain approximatively constant for the 20 days before dissolving. This difference can be explained by the fact that water in Q1 and Q3 is not in equilibrium with portlandite. When it diffuses into Q2, it starts to dissolve portlandite before oxalate ions reach the node N. Also noticed is, the hight of the maximum of calcium oxalate (20% vol. for Opengeosys, 28.1% vol. for Crunch, and 25.5% vol. for Hytec) makes the obstacle created with the OpenGeosys simulation more permeable. An increase in the hight of the maximum is observed when the precipitation/dissolution rate of calcium oxalate is increased.

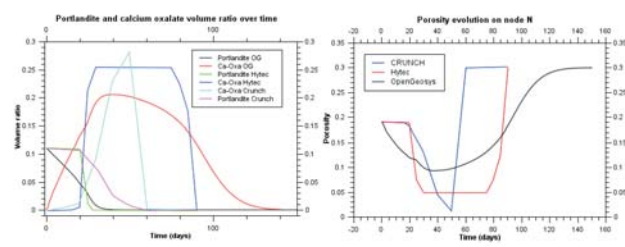


Figure 17.9.21: Solids volume ratio and porosity evolution on node N
($x=0.096\text{m}$; $y=0.11\text{m}$)

Appendix A

Software engineering

by Lars Bilke

The OpenGeoSys software development community is distributed all over the world and people with different backgrounds contribute code to a complex software system. The following points have to be addressed for a successful software development:

- Platform independent code
- A single build system
- A version control system
- A collaborative project web site
- Continuous builds and testing
- Providing binaries and documentation for end users

OpenGeoSys should run on a PC as well as on a computing cluster regardless of the operating system. Therefore the code should not include any platform specific feature or library. Instead open source and platform independent libraries like Qt¹ for the graphical user interface or VTK² for visualization algorithms are used. So developers can simply use the platform or tools they want.

Despite the use of platform independent code and libraries, in the end there must be platform specific build settings or project files for integrated development environments like Visual Studio or Eclipse. These are generated by the CMake³ build system which is configured using platform independent configuration files. Also, CMake enables so-called *out of source builds* which means that all the

¹Qt: <http://qt.nokia.com/products/>

²The Visualization Toolkit: <http://www.vtk.org>

³CMake: <http://www.cmake.org>

generated files are separated from the source code. This makes it easier to manage the source code in a version control system.

A source code management and version control system is a definite requirement for distributed software development. For this purpose Subversion⁴ is used which enables developers to work on separate versions (*branches*) of the software and to merge those versions at some point to the official one.

The version control system is integrated into an information and collaboration website based on a wiki⁵ system. The wiki is used for collecting informations such as tutorials, application examples and case studies. Discussions take place in the OpenGeoSys mailing list⁶.

To improve code stability and to verify code correctness a continuous build and testing system based on the Jenkins Continuous Integration Server⁷ has been established. This server is connected to the version control system and does the following on every code change:

- Compiles (*builds*) the code on every supported platform (Linux, Windows, MacOS)
- Runs a comprehensive test suite of over 120 benchmarks
- Verifies the test results
- Runs software development related metrics on the code (like compiler warnings, code complexity, static analysis tools)
- Generates source code documentation
- Provides binaries for end users
- Informs developers on errors

These points enhance the software development process considerably. The platform independence is maintained. Errors in the source code can be tracked down easily and at the time they were introduced. Developers get access to code analysis tools and an up-to-date source code documentation without the need to install it on their own machines.

Figure A.0.1 shows an overview of the software engineering workflow and concludes this section.

⁴Subversion: <http://subversion.tigris.org/>

⁵TracWiki: <http://trac.edgewall.org/wiki/TracWiki>

⁶OGS-Mailinglist: <http://groups.google.com/group/ogs6>

⁷Jenkins: <http://jenkins-ci.org/>

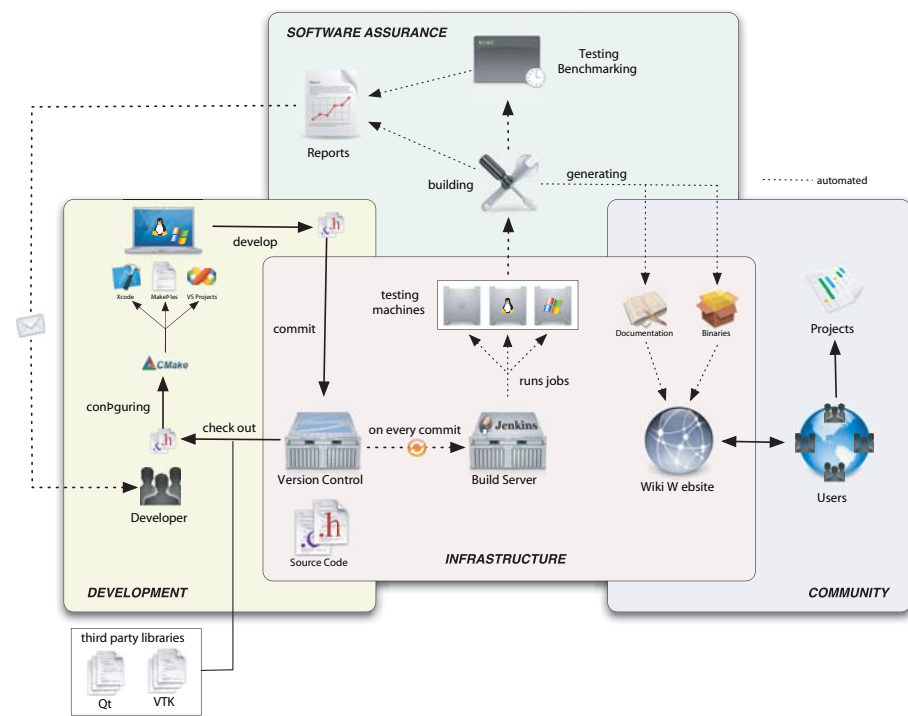


Figure A.0.1: Overview of the OpenGeoSys software engineering workflow.

Appendix B

Data processing

by Karsten Rink and Thomas Fischer

OpenGeoSys is a program for the simulation of (coupled) thermal, hydrological, mechanical and chemical processes that contains large amount of FEM-related functionality and numerical solvers. It is, however, a command line tool and therefore not intuitive to handle for first time users. Also, it is difficult to get a feeling for the data that is utilized by the program and simulation results cannot be directly verified without the help of other tools.

To address these issues, the OpenGeoSys Data Explorer has been developed as a graphical user interface (GUI) for OpenGeoSys (see fig. B.0.1). This allows for a 3D visualization of input and output data of process simulations and will thus convey a better understanding of the data as well as the simulations. As with the simulation software itself, the Data Explorer is platform independent due to the use of the open source application framework Qt and is tested under Windows- and Linux-based operating system as well as MacOS. It employs the same basic data structures as the command line tool and thus complements OpenGeoSys by giving users a way to visually assess their data sets.

An interactive 3D view (see fig. B.0.2) often enhances the understanding of the data and makes it easier to discuss certain aspects or problems with other scientists. Besides handling the native OpenGeoSys file formats, the Data Explorer also provides a large number of interfaces for the import of files created by established geoscientific software products such as the geographic information system ArcGIS, the groundwater modeling software GMS and – to a certain degree – software used in the mining or petroleum industry such as Petrel or Geocad. Non-spatial information such as time series data or borehole stratigraphies can be viewed in separate 2D windows. Furthermore, it is possible to import image data in popular formats such as JPEG or PNG. In addition to all these geoscientific input data formats, it is also possible to visualize FEM-related information like boundary conditions (see fig. B.0.3) and or 3D object structures

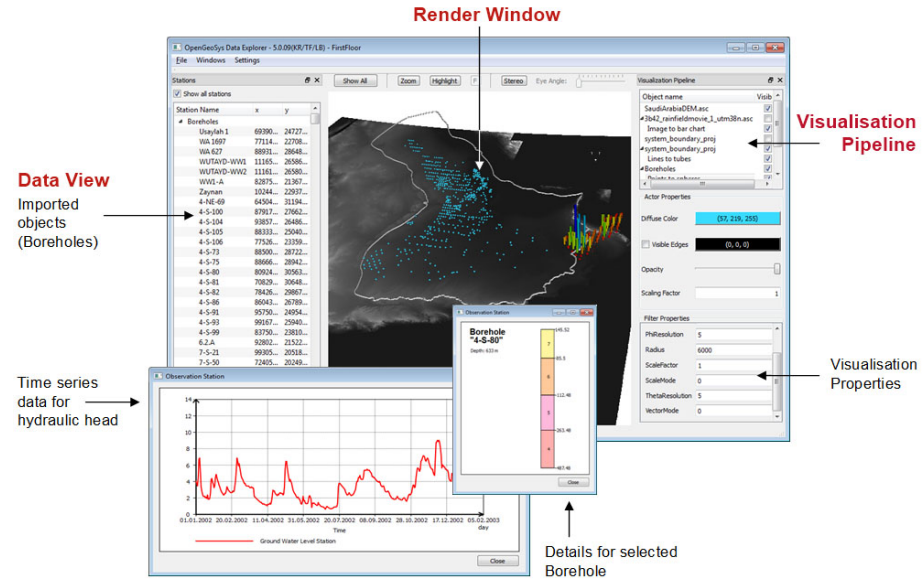


Figure B.0.1: The graphical user interface of the OpenGeoSys Data Explorer.

in the widespread VTK format. In particular, this format is used to store the time invariant results of process simulations calculated using OpenGeoSys .

The Data Explorer supports users when preparing simulations of processes by allowing them to see how various data sets complement or interact with each other. When data sets from various sources are used, it is not uncommon that inconsistencies between those data sets exist. Typical examples in the scope of hydrological data include the course of rivers not quite matching the underlying terrain model, subsurface layers penetrating each other or boreholes not starting at ground level but instead above or below the surface. The reasons for such inconsistencies are manifold and can be attributed to different data acquisition methods (such as remote sensing data scanned from orbit via satellites, bore-hole logs created manually using core samples, etc.), data conversion problems or human error. However, if models for the simulation of processes such as groundwater recharge are based on faulty or conflicting information they might produce erroneous or deceptive results. An interactive 3D view allows the user to assess the quality of the data and detect inconsistencies, artifacts or missing information.

A number of visualization options are available in the GUI to support users in this assessment process by allowing the adjustment of a number of visualization parameters for each data set. Examples include

- Super elevation of objects

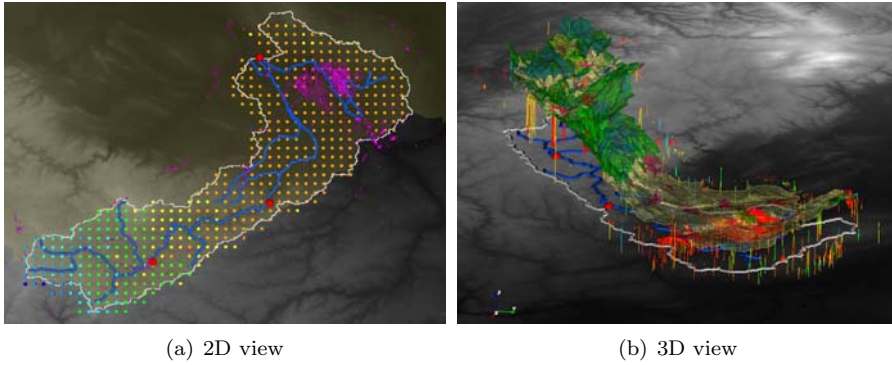


Figure B.0.2: Example for visualization of multiple data sets. Figure B.0.2(a) depicts geometrical information such as the boundary of the model region (white), the river network (blue), gauging stations (red) and boreholes (pink) in addition to a discrete precipitation map where the blue dots mark high precipitation and the red/orange dots low precipitation. Figure B.0.2(b) shows the same scene in 3D (although without the precipitation). Boreholes can now be seen as 3D structures. A semi-transparent surface mesh overlaid with land use classes have been added to the scene.

- Adjusting transparency, such that objects occupying the same space can be evaluated
- Application of user defined color tables (e.g. for borehole information)
- Selection of specific materials or stratigraphic layers (e.g. a specific set of lines or a certain subsurface layer) while blanking out the rest of the data set.
- Enlargement of selected features for better visibility

In addition, users can see the underlying data of visualized objects (such as point coordinates, mesh element information, etc.) in a separate menu and can even process geometric data to a certain degree (connecting polylines, triangulation of surfaces, etc.). Furthermore, it is possible to generate parameterized FEM meshes based on existing geometric data with a desired element density and optional mesh refinement towards selected features. For existing meshes it is possible to check the quality of all mesh elements with respect to certain well-established criteria such as the ratio of longest to shortest element edge, equi-angle skewness or global element area/volume and then analyze the results of such an analysis directly in the 3D view (see fig. B.0.4).

For more information on the topic of evaluation of 3D data sets the interested reader is referred to [180]. A comprehensive specification of the functionality of

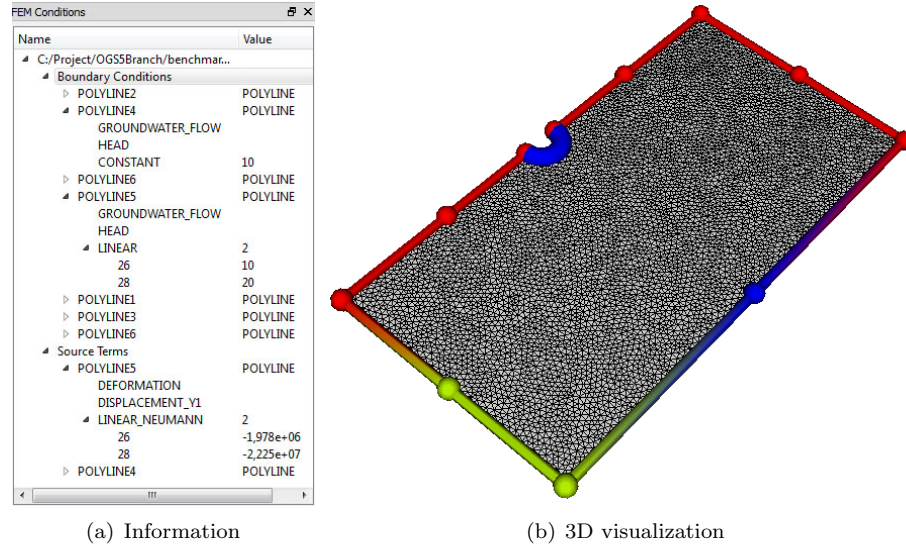


Figure B.0.3: Example for visualisation of FEM related data. Depicted are a number of boundary conditions for a FEM Mesh along with detailed information about their properties.

the OpenGeoSys Data Explorer can be found in [181].

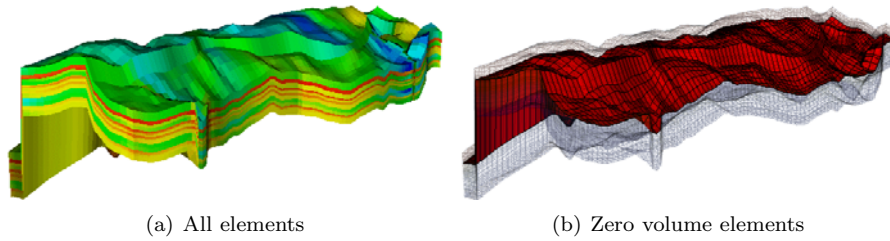


Figure B.0.4: Visualization of mesh element quality. Blue signifies good quality, red elements might cause problems during simulation. Figure B.0.4(b) depicts a layer containing zero volume elements blended into the transparent mesh.

Appendix C

Geometric Modelling, Gridding and Visualization

by Björn Zehner

Geometric modelling and 3D visualization are two aspects that are important for simulation. The first one is a preprocessing step in which a 3D description of the input model is set up which is later needed for generating the 3D grid on which the simulation is run and for setting the different parameters on the grid's cells and the initial and boundary conditions. The latter one is needed because the output of the simulation is usually a vast amount of numbers. Visualization (and Virtual Reality) deals with the question of how to represent these numbers in an intuitive and comprehensible way. Examples of this are the visualization of tensor fields from geomechanics [182] or of scalar fields with uncertainty [183].

Figure C.0.1 shows the overall processing workflow from data interpretation via modelling and simulation to visualization, as it is used in the geoscience domain. As a first step, a 3D model that describes the subsurface is constructed from the field data provided. While this 3D model construction can be done using CAD software for geotechnical and engineering applications, the more complicated and irregular geological structures require specialized software. One program that is commonly used by many universities, state agencies, oil companies and alike for this task is GOCAD¹ from Paradigm Ltd, another one is Petrel² from Schlumberger. The next necessary step is the generation of 3D simulation grids from the geometrical models. For reservoir simulation purposes, the use of hexahedral grids and finite difference simulation methods is more common and the construction of these grids works quite well in most modelling packages. However, to represent complicated 3D geological structures, such as fault systems,

¹GOCAD: <http://www.pdgm.com>

²Petrel: <http://www.slb.com>

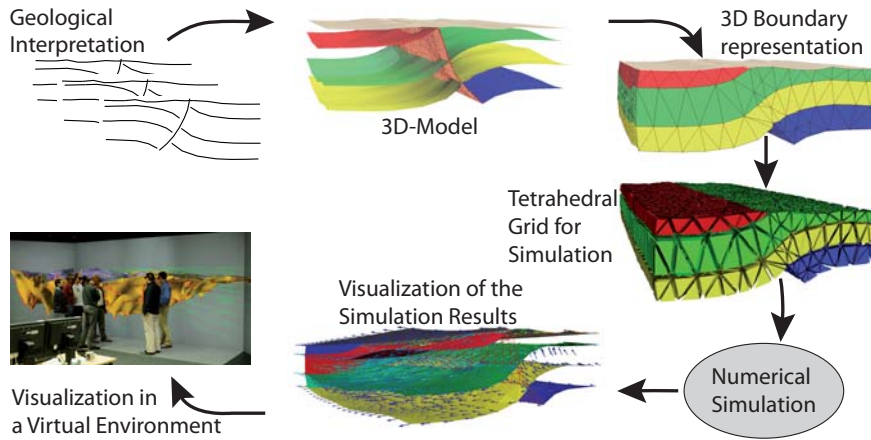


Figure C.0.1: Processing workflow from geological interpretation and geometrical modelling via simulation to visualization.

unstructured grids that use tetrahedra are more suitable. In order to generate these grids, the modelling software has to be used to construct a boundary representation of the 3D model from which the simulation grid can be generated using e.g. TetGen³, a software that is open source for research purposes. TetGen also recognizes if the volume is partitioned into subspaces and assigns corresponding identifiers to the generated tetrahedra. Further the geometries from the 3D Model can be used to set the initial and boundary conditions, for example a predefined flow on all vertices along a line.

After running the simulation the results need to be visualized. A very comprehensive C++ library that provides most of the standard algorithms for visualizing scientific data is the Visualization Toolkit (VTK)⁴ [184]. VTK is pipeline-oriented and provides different filters that each take an input data set, do some processing (such as isosurface extraction) and forward the result to the next filter or an object that visualizes it. In this way complicated pipelines can be constructed in order to assess the data. VTK also defines its own file formats and the finite element software OpenGeoSys (OGS) can output simulation results directly in this format. The VTK library can be used to implement a full visualization application. This has been done, for example, with the OGS Data Explorer (see chapter on data processing). Further the open source software Paraview⁵ is based on VTK and makes most of the filters available within a graphical user interface.

If synoptic views are created that visualize the simulation results together with

³TetGen: <http://tetgen.berlios.de/>

⁴VTK: <http://www.vtk.org>

⁵Paraview: <http://www.paraview.org>

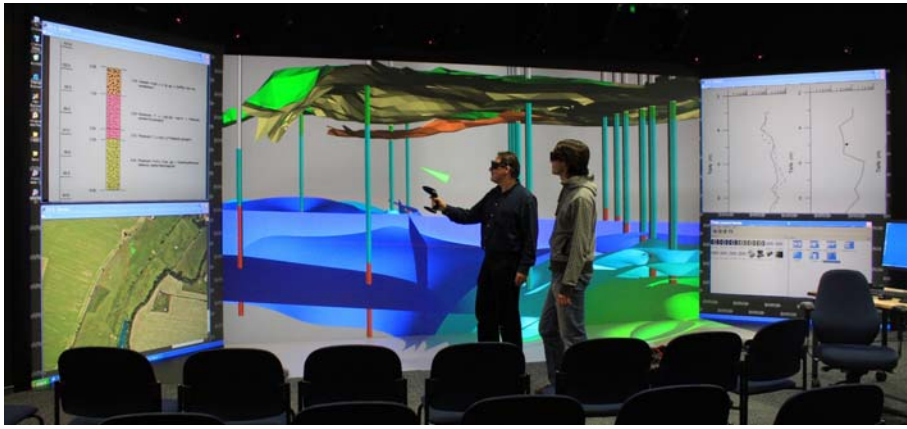


Figure C.0.2: Combined 2D and 3D visualization in the UFZ's visualization center as suggested in [185]. The rear screen and the floor are used to show the 3D model using head-tracked stereoscopic visualization. On the side screens additional information is shown, such as the stratigraphic profile of a borehole, graphs or a map on which the position of the user is indicated and the direction in which he or she is looking. 2D- and 3D-Views are coupled.

the geometrical model and with other data on which this model is based, the display quickly becomes cluttered and it becomes difficult for the viewers to grasp the spatial interrelationships of the data. Further simulation results are often discussed in small groups or are presented to stakeholders who are not familiar with the interpretation of the visualization shown to them, and for this reason have problems understanding it. Stereoscopic visualization on high resolution display walls can help to overcome these problems, as they provide a real 3D impression that is easier for the viewers to understand and can show much more detail. However, these display walls are usually more complicated to use as they involve several projectors that are run by a computer cluster and so require specialized software. The display at the UFZ-Helmholtz Centre for Environmental Research⁶, for example, uses 13 SXGA+ projectors in a theater-like configuration with a large rear screen, two side screens and a projection on the floor. It can be used either as an immersive VR display or as a display where the rear screen and the floor are used in VR mode, while the side screens show additional 2D information, such as maps, in order to help the users orient themselves in large-scale regional models or borehole data and logs (see Figure C.0.2). A full description of the system, its design concept and the use as visual information system can be found in [185].

⁶Homepage of UFZ's Visualization Center:<http://www.ufz.de/index.php?en=14171>

To run these kind of systems the open-source scenegraph OpenSG⁷ [186] can be used very well as it supports the distribution of the scenegraph. A visualization application runs on the master computer, assembles the scene and reacts on the user input. The scenegraph itself and the changes to it are always distributed to the remote computers on which OpenGL is used to render the scene. The scenegraph is relatively well documented and comes with examples that show different features, for example how to run a display wall with a computer cluster. The UFZ uses a commercial application, VRED from PI-VR GmbH⁸ that is based on OpenSG to run its visualization center. We have extended VRED using OpenSG and Nokia's Qt Toolkit for the graphical user interface. We also have extended VTK with a vtkOpenSGActor class so that content that has been created using a VTK pipeline can be easily converted on the fly into OpenSG format. In this way we have integrated some standard features, such as isosurface extraction from scalar fields or glyph rendering and streamline computation for vector fields, into VRED.

As we have seen, the whole workflow and data processing involves several software packages and libraries that are each specialized for a certain step of the workflow. For this reason the data have to be converted between these different formats and the information is distributed across several files that must be viewed with several software packages. We have experimented with using GOCAD as a tool for geometric modelling, data exchange with our project partners and model maintenance. GOCAD provides import and export functionality to different data formats, such as ArcGIS Shape files, and it can be extended, using C++ and a plugin mechanism, so that we can add our own algorithms, exporters and importers. In contrast to the often applied way to write data converters that read data in GOCAD ASCII format and output the desired file type, our chosen way of extending GOCAD has the advantage that we can make use of the topological information that GOCAD keeps track of internally but does not write to the files. Further we have access to the data that describe the appearance of the different objects in GOCAD (e.g. line width or colour of a surface), so that we can very easily create the same visualization using other formats. In order to provide an easier and more rapid data exchange we have added some modelling functionality and the necessary interfaces between GOCAD and Gmsh, TetGen, VTK, OpenSG and our finite element simulation software OpenGeoSys. In this way we support the processing of the data as is described in Figure C.0.3.

In order to generate the simulation grids, GOCAD already provides algorithms that generate a structured (hexahedral) grid which can be fitted to the geology that delineates the actual reservoir. However, as mentioned earlier, with regard to complicated reservoirs a (tetrahedral) mesh would be preferable. For many geometrical models, one critical step is the conversion from the surface- or boundary-based 3D model to the 3D grid, because this step requires the surface model to fulfil different constraints. In order to generate tetrahedral grids, the

⁷OpenSG: <http://www.opensg.org/>

⁸VRED: www.pi-vr.de

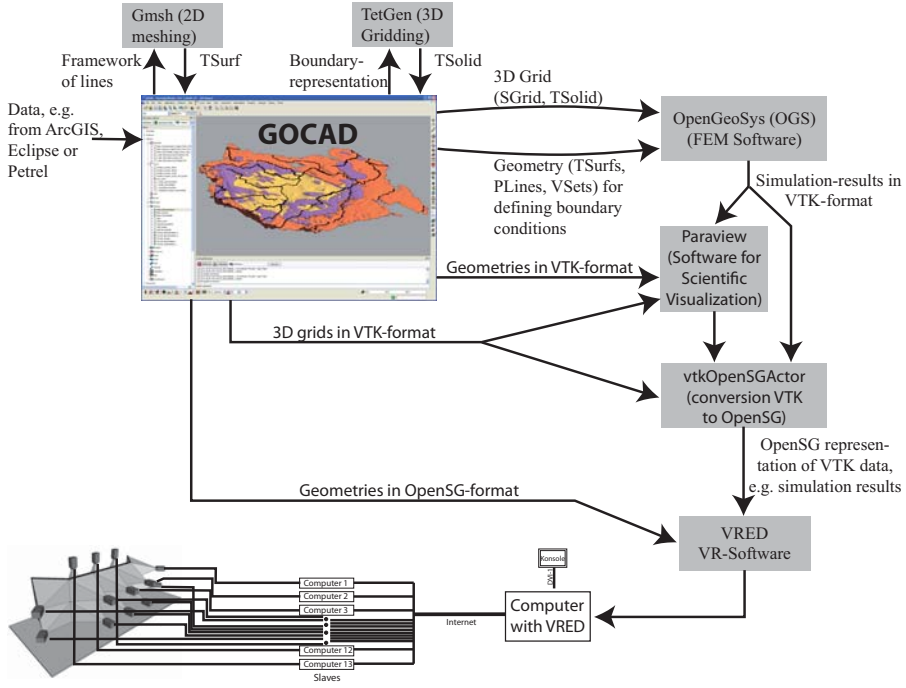


Figure C.0.3: Processing pipeline for the data from geometrical modelling through simulation to visualization.

quality of the triangular meshes must be higher than is normally required for illustration, communication and discussion purposes. The mesh should consist of triangles with not too large an aspect ratio (longest side length divided by shortest side length). The lines, where one surface intersects another one or is connected to it, for example at the contact of a stratigraphic layer and a fault, are also critical. As is shown in Figure C.0.4, it is essential that both surfaces share the same vertices and segments. Further the whole model should be represented by a boundary representation that has no holes and divides the space into volumes fully enclosed by surfaces.

There are several ways of generating or remeshing a model such that it can be used as a boundary representation model. We have extended GOCAD in order to use two of them which is described in more detail in [187]. One is more targeted at constructing complicated fault zones and requires a lot of individual work. The other is more suitable for the construction of large-scale regional models. Both of them make use of constrained delaunay triangulation by using the open source software Gmsh⁹.

⁹Gmsh: <http://www.geuz.org/gmsh/>

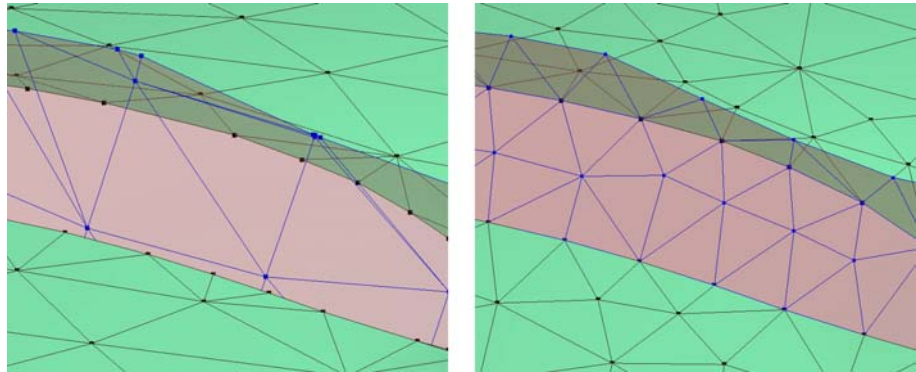


Figure C.0.4: The same part of a model of two surfaces (green) connected to a fault (reddish) shown twice. On the left side the three meshes do not share the segments and points where they are in contact. Further some of the triangles have a very bad aspect ratio. Before a tetrahedralization of this model would be possible it would have to be remeshed, so that it looks like the image on the right side.

In order to generate a complicated fault zone, the contact lines of the different horizons on the fault need to be constructed. This can be done by extracting the contact lines of the horizons on the fault from the existing model, using standard GOCAD commands, or by constructing from a series of geological cross sections from scratch. If the points on these lines are very irregularly spaced, they should be resampled using, for example, cubic spline interpolation. If the contact lines cross, the intersection must be calculated and a point inserted on both lines at this position. Further the outline of the fault must be constructed. The fault is now represented by a framework of lines (segments) that must be part of the fault's triangulation. To facilitate further processing, the best-fitting plane is calculated for the framework and the points are projected onto this plane. Then the framework is exported to the software Gmsh and Gmsh's constrained Delaunay algorithm is used to create a triangulation that contains all the points and segments of the framework. Subsequently this triangulation is loaded into GOCAD, the points that were part of the initial framework are transformed back to their original location and set as control nodes (which means that they are not allowed to move any more), and the mesh is smoothed using GOCAD's standard interpolation algorithm (DSI).

The way to construct a boundary representation for a large-scale regional model is shown in figure C.0.5 for a small part of the Thuringian basin in Germany. As a first step Gmsh is used to generate a triangulation of the whole region that accepts the different outlines of the stratigraphic units and other features, such as well locations and rivers as constraints (a). This triangulation is then later used in GOCAD as a template for the generation of the different horizons. The

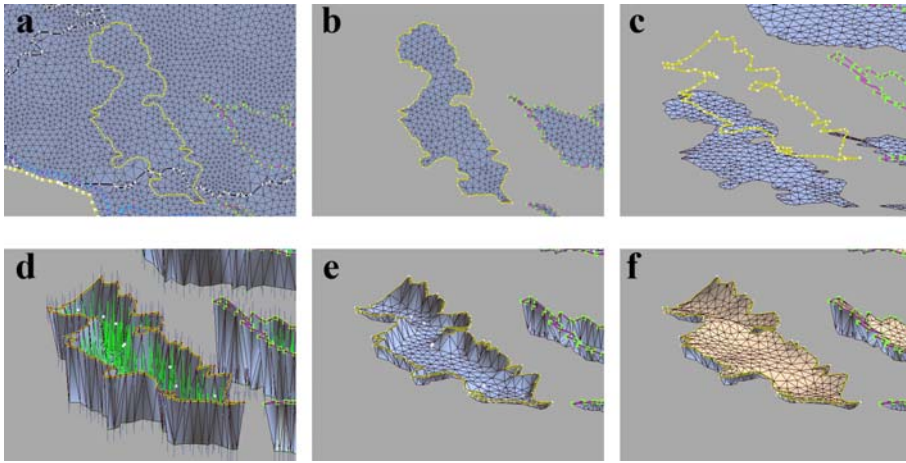


Figure C.0.5: Construction of a boundary representation for large scale regional models. See text for explanations.

triangles of the template that are outside the outline of a horizon are deleted (b). Then the vertices on the border of the triangulation are moved onto the line that represents the outline of the horizon on the terrain. Further they are set as control nodes so that they do not move any more during subsequent operations. For the other points different constraints are set, such as control points against which the surface should converge (step c-d). Using GOCAD's iterative standard interpolation algorithm (DSI) a smooth surface is generated (e). Applying the same sequence of operations for the top of the stratigraphic unit generates a cover as top that fits exactly over the first horizon, so that we get a closed volume (f).

A model that has been meshed or remeshed using the aforementioned methods has a boundary representation that can easily be gridded, using open source gridding software, such as TetGen to generate a tetrahedral grid. We have extended GOCAD by adding an exporter for TetGen input files and an importer for TetGen output files. The output of TetGen is read into GOCAD as a TSolid where the different subvolumes are represented as different parts. Another implemented exporter for GOCAD allows us to then write this grid directly in the format of our finite element simulation software OpenGeoSys. Further geometries, such as lines, points and surfaces can be exported from GOCAD in an XML format that is used by OpenGeoSys to define geometries that are used for setting boundary and initial conditions. In this way GOCAD can be used as a kind of preprocessor for OpenGeoSys.

The extensions to GOCAD described above have been tested and used within several projects at the UFZ. As part of the INFLUINS project, which deals with fluid flow in sedimentary basins, we have constructed a model of the Thuringian

basin, which has been partitioned into the stratigraphic units Bunter, Muschelkalk and Keuper. The corresponding simulation grid consisted of more than 600,000 tetrahedra and has been exported to OpenGeoSys to perform ground-water simulation. Further we have used the exporters to VTK and OpenSG for subsequent visualization of the model in our visualization center. Within the CO2MAN project we have used GOCAD to exchange data and the simulation grid with our project partners and to construct the necessary geometries for setting the boundary conditions.

Appendix D

Parallel computing

by Wenqing Wang and Thomas Kalbacher

Index

Bibliography

- [1] Nowak T, Kunz H, Dixon D, Wang W, G  rke U-J, and Kolditz O. Coupled 3-d thermo-hydro-mechanical analysis of geotechnical in situ tests. *Int. J. Numer. Anal. Meth. Geomech.*, 48(1):1–15, 2011.
- [2] G  rke U-J, Park C-H, Wang W, Singh AK, and Kolditz O. Numerical simulation of multiphase hydromechanical processes induced by co₂ injection into deep saline aquifers. *Oil and Gas Science and Technology – Rev. IFP Energies nouvelles*, 66(1):3446–118, 2011.
- [3] Watanabe N, McDermott C and Wang W, Taniguchi T, and Kolditz O. Uncertainty analysis of thermo-hydro-mechanical processes in heterogeneous porous media. *Computational Mechanics*, 45(4):263–280, 2010.
- [4] T. Kalbacher, C. Schneider, W. Wang, A. Hildebrandt, S. Attinger, and O. Kolditz. Parallelized modelling of soil-coupled 3d water uptake of multiple root systems with automatic adaptive time step control. *Vadose Zone Journal*, pages 1–11, 2010.
- [5] Wu Y, Toll M, Wang W, Sauter M, and Kolditz O. Development of a high-precision groundwater model with scarce data: The wadi kafrein area. *Environ Earth Sci*, 2011.
- [6] F. Sun, H. Shao, T. Kalbacher, W. Wang, Z. Yang, Z. Huang, T. Jiang, and O. Kolditz. Change of subsurface flow regime in the nankou area, beijing. *Environmental Earth Sciences*, pages 1–11, 2010.
- [7] Umbach E (ed). *Energie Forschung Zukunft*. Helmholtz Gemeinschaft Deutscher Forschungszentren, 2010.
- [8] Jacob Bear. *Dynamics of Fluids in Porous Media*. Elsevier, New York, 1972.
- [9] H.-J. G. Diersch. *Modellierung und numerische Simulation geohydrodynamischer Transportprozesse*. Habilitationsschrift, Akademie der Wissenschaften der DDR, Berlin, 1985.

- [10] W. Ehlers. Poröse Medien - ein kontinuumsmechanisches Modell auf der Basis der Mischungstheorie. Forschungsberichte aus dem Fachbereich Bauwesen, Uni Essen, 1989.
- [11] J. Bear and Y. Bachmat. *Introduction to modeling of transport phenomena in porous media*. Kluwer Academic Publishers, Dordrecht, 1990.
- [12] W. Kinzelbach. *Numerische Methoden zur Modellierung des Transports von Schadstoffen im Grundwasser*. R. Oldenburg Verlag, 1992.
- [13] Rainer Helmig. *Multiphase Flow and Transport Processes in the Subsurface*. Springer, Berlin, 1997.
- [14] R. W. Lewis and B. A. Schrefler. *The finite element method in the static and dynamic deformation and consolidation of porous media*. Wiley, 1998.
- [15] Reint de Boer. *Theory of Porous Media*. Springer, Berlin, 2000.
- [16] O. Kolditz. *Computational methods in environmental fluid mechanics*. Graduate Text Book, Springer Science Publisher, Berlin, 2002.
- [17] P. Haupt. *Continuum mechanics and theory of materials*. Springer, 2002.
- [18] Bowen R.M. *Theory of mixture*, volume III of *Continuum Physics*. Academic Press, New York, 1976. Eringen, A.C. (Ed.).
- [19] Truesdell C. and Toupin R.A. *The classical field theories*, volume III/1 of *Handbuch der Physik*. Springer, Berlin, 1960. Flügge, S. (Ed.).
- [20] Bowen R.M. Incompressible porous media models by use of the theory of mixtures. *Int. J. Eng. Sci.*, 18:1129–1148, 1980.
- [21] de Boer R. and Ehlers W. On the problem of fluid- and gas-filled elasto-plastic solids. *Int. J. Sol. Struct.*, 22:1231–1242, 1986.
- [22] Prevost P. Mechanics of continuous porous media. *Int. J. Eng. Sci.*, 18:787–800, 1980.
- [23] Ehlers W. and Bluhm J. *Porous media: Theory, experiments and numerical applications*. Springer, Berlin, 2002.
- [24] Görke U.-J., Wimmer M.A., Alini M., Schneider E., and Günther H. Multiscale finite element modeling in tissue engineering of articular cartilage. *Eur. Cells Mater.*, 12(1):19, 2006.
- [25] H. Lamb. *Hydrodynamics*. Cambridge University Press, 1932.
- [26] P. Forchheimer. *Hydraulik*. Teubner, Berlin, 1914.
- [27] H. Darcy. *Les Fontaines Publiques de la Ville de Dijon*. Dalmont, Paris, 1856.

- [28] A.E. Scheidegger. *The physics of flow through porous media*. University of Toronto Press, 3rd edition, 1974.
- [29] F.A. Dullien. *Porous media: fluid transport and pore structure*. Academic Press, 1979.
- [30] Rutqvist J, Börgesson L, Chijimatsu M, Kobayashi A, Jing L, Nguyen TS, Noorishad J, and Tsang C.-F. Thermohydromechanics of partially saturated geological media: governing equations and formulation of four finite element models. *Int. J. Rock Mech. Min. Sci.*, 38:105–127, 2001.
- [31] Bishop AW and Blight GE. Some aspects of effective stress in saturation and partly saturated soil. *Geotéchnique*, 13:177–197, 1963.
- [32] Otto Redlich and J. N. S. Kwong. On the Thermodynamics of Solutions. v. An Equation of State. Fugacities of Gaseous Solutions. *Chemical Reviews*, 44:233–244, 1949.
- [33] D.Y. Peng and D.B. Robinson. A new two-constant equation of state. *Ind. Eng. Chem. Fundam.*, 15:59–64, 1974.
- [34] D. G. Friend, J. F. Ely, and H. H. Ingham. Thermophysical properties of methane. *Journal of Physical and Chemical Reference Data*, 18(2), 1989.
- [35] Ulrich Setzmann and Wolfgang Wagner. A new equation of state and tables of thermodynamic properties for methane covering the range from the melting line to 625 K at pressures up to 1000 MPa. *J. Phys. Chem. Ref. Data*, 20:1061–1155, 1991.
- [36] A. Fenghour, W.A. Wakeham, and V. Vesovic. The Viscosity of Carbon Dioxide. *Journal of Physical and Chemical Reference Data*, 27:31–44, 1998.
- [37] R. Span and W. Wagner. A new Equation of State for Carbon Dioxide Covering the Fluid Region from the Triple-Point Temperature to 1100 K at Pressures up to 800 MPa. *Journal of Physical and Chemical Reference Data*, 25(6):1509–1596, 1996.
- [38] International Association for the Properties of Water and Steam. *Release on the IAPWS Formulation 2008 for the Viscosity of Ordinary Water Substance*, 2008.
- [39] W. Wagner and A. Pruss. The IAPWS formulation 1995 for the thermodynamic properties of ordinary water substance for general and scientific use. *Journal of Physical and Chemical Reference Data*, 31(2), 2002.
- [40] K. Stephan, R. Krauss, and A. Laesecke. Viscosity and thermal conductivity of nitrogen for a wide range of fluid states. *Journal of Physical and Chemical Reference Data*, 16(4), 1987.

- [41] R. Span, E.W. Lemmon, R.T. Jacobsen, W. Wagner, and A.Yokozeki. A Reference Equation of State for the Thermodynamic Properties of Nitrogen for Temperatures from 63.151 to 1000K and Pressures to 2200MPa. *J. Phys. Chem. Ref. Data*, 29:1361–1431, 2000.
- [42] Johannes Diderik van der Waals. *Over de Continuiteit van den gas- en vloeistoftoestand*. Sijthoff, Leiden, 1873.
- [43] Roland Span. *Eine neue Fundamentalgleichung für das fluide Zustandsgebiet von Kohlendioxid bei Temperaturen bis zu 1100 K und Drücken bis zu 800 MPa*. VDI Verlag, Düsseldorf, 1993.
- [44] Andreas Prüß and Wolfgang Wagner. *Eine neue Fundamentalgleichung für das fluide Zustandsgebiet von Wasser für Temperaturen von der Schmelzlinie bis zu 1273 K bei Drücken bis zu 1000 MPa*. VDI Verlag, Düsseldorf, 1995.
- [45] D. Bücker and W. Wagner. A reference equation of state for the thermodynamic properties of ethane for temperatures from the melting line to 675 K and pressures up to 900 MPa. *J. Phys. Chem. Ref. Data*, 35:205–266, 2006.
- [46] D. G. Friend, H. Ingham, and J. F. Ely. Thermophysical properties of ethane. *Journal of Physical and Chemical Reference Data*, 20(2), 1991.
- [47] V. Vesovic and W.A. Wakeham. The transport properties of carbon dioxide. *Journal of Physical and Chemical Reference Data*, 19(3):763–807, 1990.
- [48] B. A. Younglove and J. F. Ely. Thermophysical properties of fluids. ii. methane, ethane, propane, isobutane, and normal butane. *Journal of Physical and Chemical Reference Data*, 16(4), 1987.
- [49] International Association for the Properties of Water and Steam. *Revised Release on the IAPWS Formulation 1985 for the Thermal Conductivity of Ordinary Water Substance*, 2008.
- [50] Jaeger J.C., Cook N.G.W., and Zimmermann R.W. *Fundamentals of rock mechanics*. Blackwell Publishing, 4 edition, 2007.
- [51] R. N. Brooks and A. T. Corey. Properties of porous media affecting fluid flow. *J. Irrig. Drain. Div. ASCE*, 92:61–68, 1964.
- [52] Brooks RH and Corey AT. Hydraulic properties of porous media. Technical report, Colorado State University, Fort Collins, 1964. Hydrology Paper No. 3.
- [53] M. T. Van Genuchten. A closed-form equation for predicting the hydraulic conductivity of unsaturated soils. *Soil Sci. Soc. Am. J.*, 44:892–898, 1980.

- [54] Yechezkel Mualem. A new model for predicting the hydraulic conductivity of unsaturated porous media. *Water Resources Research*, 12:513–522, 1976.
- [55] R. Haverkamp, M. Vauclin, J. Touma, P. J. Wierenga, and G. Vachaud. A comparison of numerical simulation models for one-dimensional infiltration. *J. Soil Science Society of America*, 41:284–294, 1977.
- [56] R. W. Lewis and B. A. Schrefler. *The Finite Element Method in the Static and Dynamic Deformation and Consolidation of Porous Media (Second Edition)*. Wiley, 1998.
- [57] R. de Boer. *Theory of Porous Media: Highlights in Historical Development and Current State*. Springer-Verlag, Heidelberg, 2002.
- [58] R. de Boer. *Trends in Continuum Mechanics of Porous Media: Theory and Applications of Transport in Porous Media*. Springer-Verlag, Heidelberg, 2005.
- [59] *Proceedings of the GeoProc International Conference on Coupled T-H-M-C Process in Geo-Systems*, The Royal Institute of Technology, Stockholm, Sweden, 2003.
- [60] W. Ehlers and J. Bluhm. *Porous Media: Theory, Experiments and Numerical Applications*. Springer-Verlag, 2002.
- [61] O. Kolditz, W. Wang, J. de Jonge, M. Xie, and S. Bauer. A process-oriented approach to compute thm problems in porous media - part 1: Theoretical and informatics background. In T. Schanz, editor, *Unsaturated Soils: Numerical and Theoretical Approaches*, pages 53–66. Springer, 2004.
- [62] O. Kolditz and J. De Jonge. Non-isothermal two-phase flow in low-permeable porous media. *Computational Mechanics*, 33(5):345–364, 2004.
- [63] B. Stroustrup. *The C++ Programming Language (Third Edition)*. Addison-Wesley, 2000.
- [64] T. Budd. *An Introduction to Object-Oriented Programming*. Addison Wesley, Third edition, 2001.
- [65] G. L. Fenvesm. Object-oriented programming for engineering software development. *Engineering With Computers*, 6(Winter):1–15, 1990.
- [66] B. Forde, R. O. Foschi, and S. F. Stiemer. Object-oriented finite element analysis. *Computers & Structures*, 34(3):355–374, 1990.
- [67] J. Filho and P. Devloo. Object-oriented programming in scientific computations: The beginning of a new era. *Engineering Computations*, 8:81–87, 1991.

- [68] R. I. Mackie. Object-oriented programming of the finite element method. *International Journal for Numerical and Analytical Methods in Geomechanics*, 35(2):425–436, 1992.
- [69] T. Zimmermann, Y. Duboispelein, and P. Bomme. Object-oriented finite element programming: I: governing principles. *Computer Methods in Applied Mechanics and Engineering*, 98(2):291–303, 1992.
- [70] Y. Duboispelein, T. Zimmermann, and P. Bomme. Object-oriented finite element in programming: II: a prototype program in smalltalk. *Computer Methods in Applied Mechanics and Engineering*, 98(3):361–397, 1992.
- [71] Y. Duboispelein and T. Zimmermann. Object-oriented finite element in programming: II: an efficient implementation in c++. *Computer Methods in Applied Mechanics and Engineering*, 108(1-2):165–183, 1993.
- [72] R. M. V. Pidaparti and A. V. Hudli. Dynamic analysis of structures using object-oriented techniques. *Computers & Structures*, 49(1):149–156, 1993.
- [73] B. Raphael and C. S. Krishnamoorthy. Automating finite element development using object-oriented techniques. *Engineering Computations*, 10:267–278, 1993.
- [74] K. G. Budge and J. S. Peery. RHALE – A MMALE shock physics code written in c++. *International Journal of Impact Engineering*, 14:107–120, 1993.
- [75] A. V. Pidaparti, R. V. M. and Hudli. Dynamic analysis of structures using object-oriented techniques. *Computers & Structures*, 49(1):149–156, 1993.
- [76] P. Mentrey and T. Zimmermann. Object-oriented non-linear finite element analysis: application to j2 plasticity. *Computers & Structures*, 49(5):767–773, 1993.
- [77] G. Yu and H. Adeli. An integrated computing environment for solution of complex engineering problems using the object-oriented programming paradigm and a blackboard architecture. *Journal Of Structural Engineering-ASCE*, 119(9):2763–281, 1993.
- [78] H. Adeli and G. Yu. An integrated computing environment for solution of complex engineering problems using the object-oriented programming paradigm and a blackboard architecture. *Computers & Structures*, 54(2):255–265, 1995.
- [79] E. J. Silva, P. Mesquita, R. R. Saldanha, and P. F. M. Palmeira. An object-oriented finite element program for electromagnetic field computation. *IEEE transactions on magnetics*, 30:3618–3621, 1994.

- [80] R. Sampath and N. Zabaras. An object oriented implementation of a front tracking finite element method for directional solidification process. *International Journal for Numerical Methods in Engineering*, 44:1227–1265, 1999.
- [81] C. Rihaczek and B. Kroplin. Object-oriented design of finite element software for transient, non-linear coupling problems. In ASCE, editor, *Second Congress on Computing in Civil Engineering*, 1994.
- [82] O. Kolditz and S. Bauer. A process-orientated approach to compute multi-field problems in porous media. *Int. Journal of Hydroinformatics*, 6:225–244, 2004.
- [83] S. P. Scholz. Elements of an object-oriented fem++ program in c++. *Computers & Structures*, 43(3):517–529, 1992.
- [84] G. W. Zeglinski, R. P. S. Han, and P. Aitchison. Object-oriented matrix classes for use in a finite element code using c++. *International Journal for Numerical and Analytical Methods in Geomechanics*, 37(22):3921–3937, 1994.
- [85] J. Lu, D. W. White, W. F. Chen, and H. E. Dunsmore. A matrix class library in c++ for structural engineering. *Computers & Structures*, 55(1):95–111, 1995.
- [86] Th Zimmermann and D Eyheramendy. Object-oriented finite elements : I. principles of symbolic derivation and automatic programming. *Computer Methods in Applied Mechanics and Engineering*, 132(3–4):259–276, 1996.
- [87] D Eyheramendy and Th Zimmermann. Object-oriented finite elements ii. a symbolic environment for automatic programming. *Computer Methods in Applied Mechanics and Engineering*, 132(3–4):277–304, 1996.
- [88] D Eyheramendy and Th Zimmermann. Object-oriented finite elements iii. theory and application of automatic programming. *Computer Methods in Applied Mechanics and Engineering*, 154(1–2):41–68, 1998.
- [89] D Eyheramendy and Th Zimmermann. Object-oriented finite elements. iv. symbolic derivations and automatic programming of nonlinear formulations. *Computer Methods in Applied Mechanics and Engineering*, 190(22–23):2729–2751, 2001.
- [90] O. Kolditz, M. Beinhorn, M. Xie, T. Kalbacher, S. Bauer, W. Wang, C. McDermott, C. Chen, C. Beyer, J. Gronewold, D. Kemmler, R. Walsh, C.H. Park, and Y. Du. GeoSys Rockflow, Open Source Software Design. Technical Report, GeoSys-Preprint [2004-25] <http://www.uni-tuebingen.de/zag/geohydrology>. Technical report, Center for Applied Geosciences, University of Tuebingen, 2004.

- [91] O. Kolditz, M. Beinhorn, and R. Liedl. An object-oriented groundwater/river model. *IAHS Publ.*, 297:531–539, 2005.
- [92] M. Beinhorn. *Contributions to computational hydrology: Non-linear flow processes in subsurface and surface hydrosystems*. PhD thesis, GeoHydrology and HydroInformatics, Center for Applied Geosciences, Tübingen University, 2005.
- [93] Frieder Häfner, Dietrich Sames, and Hans-Dieter Voigt. *Wärme- und Stofftransport: Mathematische Methoden*. Springer, Berlin, 1992.
- [94] A. Ogata and R. B. Banks. A solution of the differential equation of longitudinal dispersion in porous media. Technical report, U.S. Geological Survey, Washington, D.C., 1961.
- [95] O. Kolditz. *Strömung, Stoff- und Wärmetransport im Kluftgestein*. Borntraeger-Verlag, Berlin-Stuttgart, 1997.
- [96] O. Gunduz and M. M. Aral. River networks and groundwater flow: a simultaneous solution of a coupled system. *Journal of Hydrology*, 301(1-4):216 – 234, 2005.
- [97] R. E. Glover. *Transient Ground Water Hydraulics*. Water Resources Publications, 1978.
- [98] Rajesh Srivastava and Amado Guzman-Guzman. Practical approximations of the well function. *Ground Water*, 36(5):844–848, 1998.
- [99] O.D.L. Strack. Assessment of effectiveness of geologic isolation systems. analytic modeling of flow in a permeable fissured medium. Technical report, Pacific Northwest Lab., Richland, WA., 1982.
- [100] R E Horton. An approach toward physical interpretation of infiltration capacity. *Soil Science Society of America*, 5:399–417, 1940.
- [101] S Ferrari and F Saleri. A new two-dimensional shallow water model including pressure effects and slow varying bottom topography. *Math. Modell. Numer. Anal.*, 38(2):211–234, 2004.
- [102] R S Govindaraju, S E Jones, and M L Kavvas. On the diffusion wave model for overland flow 1. Solution for steep slopes. *Water Resour. Res.*, 24(5):734–744, 1998.
- [103] E Miglio. *Mathematical and Numerical Modeling for Environmental Applications*. PhD thesis, Modeling and Scientific Computation Laboratory, Polytechnic University of Milan, 2000.
- [104] W H Green and G A Ampt. Studies on soil physics: 1. Flow of air and water through soils. *J. Agric. Sci.*, 4:1–24, 1911.

- [105] R. S. Govindaraju, S. E. Jones, and M.L. Kavvas. On the diffusion wave model for overland flow 1. solution for steep slopes. *Water Resources Research*, 24(5):734–744, 1988.
- [106] P Di Giacomo, P E Todini, and P Lamberti. A conservative finite elements approach to overland flow: The control volume finite element formulation. *Journal of Hydrology*, 175:267–291, 1996.
- [107] R E Smith and D A Woolhiser. Overland flow on an infiltrating surface. *Water Resources Research*, 7(4):899–913, 1971.
- [108] H D Voigt and M Lauterbach. Druckaufbaumessungen an Gas-Sonden. Technical report, Zentrales Geologisches Institut, Berlin, 1985. Haefner et al. Geohydrodynamische Erkundung von Erdöl-, Ergas- und Grundwasserlagerstätten.
- [109] M Muskat. *The flow of homogenous fluids through porous media*. J.W. Edwards Inc., Ann Arbor, Michigan, 1nd edition, 1937.
- [110] I.S. Leibenzon. *The flow of natural fluids in porous media (in Russian)*. Gostekizdat, 1947.
- [111] V.I. Aravin and S. N. Numerov. *Theory of fluid flow in undeformable porous media*. Israel Program for Scientific Translations, 1965.
- [112] C I McDermott, A L Randriamananjato, H Tenzer, and O Kolditz. Simulation of heat extraction from crystalline rocks: The influence of coupled processes on differential reservoir cooling. *Geothermics*, 35(3):321–344, 2006.
- [113] R C Reid, J M Prausnitz, and B E Poling. *The properties of liquids and gases*. McGraw-Hill, 1988.
- [114] A I Zografos, W A Martin, and J E Sunderland. Equations of properties as a function of temperature for seven fluids. *Computer Methods in Applied Mechanics and Engineering*, 61:177–187, 1987.
- [115] N B Vargaftik, J K Vinogradov, and V S Jargin. *Handbook of physical properties of liquids and gases: Pure substances and mixtures*. Begell House, Redding, 1996.
- [116] W. Wang and O. Kolditz. Object-oriented finite element analysis of thermo-hydro-mechanical (thm) problems in porous media. *Int. J. Numerical Methods in Engineering*, 69(1):162–201, 2007.
- [117] K.-H. Lux. *Gebirgsmechanischer Entwurf und Felderfahrungen im Salzkavernenbau: Ein Beitrag zur Entwicklung von Prognosemodellen für den Hohlraumbau im duktilen Salzgebirge*. Ferdinand Enke Verlag, Stuttgart, 1984.

- [118] J. Schröder. Theoretische und algorithmische Konzepte zur phänomenologischen Beschreibung anisotropen Materialverhaltens. Dissertation, Universität Hannover, 1996.
- [119] M. Kohlmeier. Coupling of thermal, hydraulic and mechanical processes for geotechnical simulations of partially saturated porous media. Dissertation, Universität Hannover, 2006.
- [120] M. Fiolka. Theorie und Numerik volumetrischer Schalenelemente zur Delaminationsanalyse von Faserverbundlaminaten. Dissertation, Berichte des Instituts für Mechanik 2008/2, 2008.
- [121] E. Ramm, E. Rank, R. Rannacher, K. Schweizerhol, E. Stein, W. Wendland, G. Wittum, P. Wriggers, and W. Wunderlich. *Error-controlled Adaptive Finite Elements in Solid Mechanics*. Wiley, England, 2003.
- [122] I.S. Sandler and J.P. Wright. Strain softening. In S. Nemat, R. Asaro, and G. Hegemier, editors, *Theoretical foundations for Large Scale Computations of Nonlinear Behavior*, pages 285–315. Martinus Nijhoff, Netherlands, 1984.
- [123] R. I. Borja. A finite element model for strain localization analysis of strongly discontinuous fields based on standard Galerkin approximation. *Computer Methods in Applied Mechanics and Engineering*, 190:1529–1549, 2000.
- [124] D. Sheng, S. W. Sloan, and H. S. Yu. Aspects of finite element implementation of critical state models. *Computational Mechanis*, 26:185–196, 2000.
- [125] Z. Hou. Untersuchungen zum Nachweis der Standsicherheit für Untertagedeponien im Salzgebirge. Dissertation, Technische Universität Clausthal, 1997.
- [126] Z. Hou. Geomechanische Planungskonzepte für untertägige Tragwerke mit besonderer Berücksichtigung von Gefügeschädigung, Verheilung und hydromechanischer Kopplung. Habilitation, Technische Universität Clausthal, 2002.
- [127] Z. Hou and K.-H. Lux. Ein neues Stoffmodell für duktile Salzgesteine mit Einbeziehung von Gefügeschädigung und tertiärem Kriechen auf der Grundlage der Continuum-Damage-Mechanik. *Geotechnik*, 21(3):259–263, 1998.
- [128] U. Hunsche and O. Schulze. Das kriechverhalten von steinsalz. *Kali und Steinsalz*, 11:238–255, 1994.
- [129] U. Gabbert, A. Honecker, H. Köppe, and H. Nipp. Numerical analysis of large geomechanical systems in civil engineering by the dynamic relaxation technique. In P.J. Pahl and H. Werner, editors, *Computing in Civil*

- and Building Engineering*, pages 1275–1281. A.A. Balkema Publishers, Rotterdam, 1995.
- [130] A. Habbar. Direkte und inverse Modellierung reaktiver Transportprozesse in klüftig-porösen medien. Dissertation, Bericht Nr. 65, Institut für Strömungsmechanik und Elektronisches Rechnen im Bauwesen, 2001.
 - [131] G. Kosakowski and P. Smith. Modelling the transport of solutes and colloids in the grimsel migration shear zone. Technical Report 05-03, Paul Scherrer Institut, Villigen, Switzerland, 2005.
 - [132] J. Bear. *Hydraulics of groundwater*. McGraw-Hill, New York, 1979.
 - [133] K. Ito. On stochastical differential equations. *American Mathematical Society*, 4:289–302, 1951.
 - [134] W. Kinzelbach. *Groundwater Modelling*. Elsevier, Amsterdam, 1986.
 - [135] A F B Tompson and L W Gelhar. Numerical simulation of solute transport in three-dimensional randomly heterogeneous porous media. *Water Resources Research*, 26(10):2451–2562, 1990.
 - [136] E. M. LaBolle, G. E. Fogg, and A. F. B. Tompson. Random-walk simulation of transport in heterogeneous porous media: Local mass-conservation problem and implementation methods. *Water Resources Research*, 32(3):583–593, 1996.
 - [137] W. Kinzelbach. The random-walk method in pollutant transport simulation. *NATO ASI Ser, Ser.(C224)*:227–246, 1988.
 - [138] H. Hoteit, R. Mose, A. Younes, F. Lehmann, and Ph. Ackerer. Three-dimensional modeling of mass transfer in porous media using the mixed hybrid finite elements and the random-walk methods. *Mathe. Geology*, 34(4):435–456, 2002.
 - [139] T. Harter and S. Wagner. Colloid transport and filtration of *Cryptosporidium parvum* in sandy soils and aquifer sediments. *Environ. Sci. Technol.*, 34:62–70, 2000.
 - [140] W. P. Johnson, K. A. Blue, and B. E. Logan. Modeling bacterial detachment during transport through porous media as a residence-time-dependent process. *Water Resour. Res.*, 31:2649–2658, 1995.
 - [141] A E Hassan and M M Mohamed. On using particle tracking methods to simulate transport in single-continuum and dual continua porous media. *Journal of Hydrology*, 275(3-4):242–260, 2003.
 - [142] A.R. Piggott and D. Elsworth. Laboratory assessment of the equivalent apertures of a rock fracture. *Geophysical Research Letters*, 20(13):1387–1390, 1993.

- [143] R. R. Goswami and T. P. Clement. Laboratory-scale investigation of saltwater intrusion dynamics. *Water Resour. Res.*, 43, 2007.
- [144] H. R. Henry. *Salt intrusion into coastal aquifers*. PhD thesis, Columbia University, New York, USA, 1960.
- [145] L. A. Richards. Capillary conduction of liquids through porous mediums. *Physics A-J Gen. Appl. Phys.*, 1(1):318–333, 1931.
- [146] S. Sugio and C. S. Desai. Residual flow procedure for sea water intrusion in unconfined aquifers. *Int J Num Meth Engng*, 24(8):1439–1450, 1987.
- [147] R. R. Goswami, B. Ambale, and T. P. Clement. Estimating errors in concentration measurements obtained from image analysis. *Vadose Zone Journal*, 8(1):108–118, 2009.
- [148] R. A. Schincariol, F. W. Schwartz, and C. A. Mendoza. On the generation of instabilities in variable density flow. *Water Resources Research*, 30(4):913–927, 1994.
- [149] Jude L. Musuuza, Sabine Attinger, and Florin A. Radu. An extended stability criterion for density-driven flows in homogeneous porous media. *Advances in Water Resources*, 32:796–808, 2009. doi:10.1016/j.advwatres.2009.01.012.
- [150] R. A. Schincariol, F. W. Schwartz, and C. A. Mendoza. Instabilities in variable density flows: Stability and sensitivity analyses for homogeneous and heterogeneous media. *Water Resources Research*, 33(1):31–41, 1997.
- [151] L. Sanavia, F. Pesavento, and B. A. Schrefler. Finite element analysis of non-isothermal multiphase geomaterials with application to strain localization simulation. *Trans. Amer. Math. Soc.*, 37(4):331–348, 2006.
- [152] A. Liakopoulos. Retention and distribution of moisture in soils after infiltration has ceased. *Bull. Intern. Assoc. Scientific Hydrology*, 10:58–69, 1965.
- [153] S. E. Buckley and M. C. Leverett. Mechanism of fluid displacements in sands. *Transactions American Institute of Mining and Metallurgical Engineers (TAIME)*, 146:107–116, 1941.
- [154] N. Khalili and P. S. Selvadurai. A fully coupled constitutive model for thermo-hydro-mechanical analysis in elastic media with double porosity. *Geophysical Research Letters*, 30(24):5, 2003.
- [155] J. Rutqvist, L. Börgesson, M. Chijimatsu, A. Kobayashi, L. Jing, T. S. Nguyen, J. Noorishad, and C.-F. Tsang. Thermohydromechanics of partially saturated geologic media: governing equations and formulation of four finite element models. *International Journal of Rock Mechanics & Mining Sciences*, 38:105–127, 2001.

- [156] H. F. Wang. *Theory of Linear Poroelasticity*. Princeton University Press, Princeton, 2000.
- [157] E. Detournay and H.-D. Cheng. Fundamentals of poroelasticity. In J. A. Hudson, editor, *Comprehensive rock engineering*, pages 113–171. Pergamon, New York, 1993.
- [158] J. Birkholzer, J. Rutqvist, E. Sonnenthal, and D. Barr. Decovalex-thmc project, task d: Long-term permeability/porosity changes in the edz and near field due to thm and thc processes in volcanic and crystalline-bentonite systems. Technical Report 2008:45, SKI, Stockholm, 2008.
- [159] J. Rutqvist. Coupling thermal-hydrological-mechanical analysis within the framework of (decovalex-thmc), task d_thm, step 1: Model inception. Technical report, Earth Sciences Division, Lawrence Berkeley National Laboratory, USA, 2005.
- [160] H. S. Carslaw and J. C. Jaeger. *Conduction of heat in solids*. Oxford University Press, Oxford, 2nd edition, 1959.
- [161] A. M. Wijesinghe. An exact similarity solution for coupled deformation and fluid flow in discrete fractures. Technical Report UCID-20675, Lawrence Livermore National Laboratory, Livermore, CA, February 1986.
- [162] J. Noorishad, C.F. Tsang, and P.A. Witherspoon. Theoretical and field studies of coupled hydromechanical behaviour of fractured rocks—1. development and verification of a numerical simulator. *International Journal of Rock Mechanics and Mining Sciences & Geomechanics Abstracts*, 29(4):401–409, July 1992.
- [163] D. Swenson, R. DuTeau, and T. Sprecker. Modeling flow in a jointed geothermal reservoir. In *World Geothermal Congress 1995, Florence, Italy*, 1995.
- [164] K.M. Bower and G. Zyvoloski. A numerical model for thermo-hydro-mechanical coupling in fractured rock. *International Journal of Rock Mechanics and Mining Sciences*, 34(8):1201–1211, 1997.
- [165] W. Hummel, U. Berner, E. Curti, F.J. Pearson, and T. Troenen. *The Nagra/PSI Chemical Thermodynamic Data Base 01/01*. Universal Publishers, 2002.
- [166] D.L. Parkhurst and C. A. J. Appelo. User's guide to phreeqc (version 2) - a computer program for speciation, batch-reaction, one-dimensional transport, and inverse geochemical calculations, 1999.
- [167] T. P. Clement Sun Y., J. N. Petersen and R. S. Skeen. Development of analytical solutions for multispecies transport with serial and parallel reactions. *Water Resources Research*, 35(1):185–190, 1999.

- [168] Ralf Köber Dirk Schäfer and Andreas Dahmke. Competing tce- and cis-dce-degradation kinetics by zero-valent iron - experimental results and numerical simulation. *Journal of Contaminant Hydrology*, 65:183–202, 2003.
- [169] B.V. Van Breukelen, D. Hunkeler, and F. Volkering. Quantification of sequential chlorinated ethene degradation by use of a reactive transport model incorporating isotope fractionation. *Environ. Sci. Technol.*, 39(11):4189–4197, 2005.
- [170] D.R. Aguilera, P. Jourabchi, C. Spiteri, and P. Regnier. A knowledge-based reactive transport approach for the simulation of biogeochemical dynamics in earth systems. *Geochemistry, Geophysics, Geosystems*, 6:Q07012, 2005.
- [171] P. Regnier, J.P. O’Kane, C.I. Steefel, and J.P. Vanderborgh. Modeling complex multi-component reactive-transport systems: towards a simulation environment based on the concept of a knowledge base. *Applied Mathematical Modelling*, 26:913–927, 2002.
- [172] Urs von Gunten and Jürg Zobrist. Biogeochemical changes in groundwater-infiltration systems: Column studies. *Geochimica et Cosmochimica Acta*, 57:3895–3906, 1993.
- [173] Dirk Schäfer, Wolfgang Schäfer, and Wolfgang Kinzelbach. Simulation of reactive processes related to biodegradation in aquifers. 2. model application to a column study on organic carbon degradation. *Journal of Contaminant Hydrology*, 31:187–209, 1998.
- [174] Martin Thullner, Philippe Van Cappellen, and Pierre Regnier. Modeling the impact of microbial activity on redox dynamics in porous media. *Geochimica et Cosmochimica Acta*, 69(21):5005–5019, 2005.
- [175] Florian Centler, Haibing Shao, Cecilia de Bias, Chan-Hee Park, Pierre Regnier, Olaf Kolditz, and Martin Thullner. Geosysbrns - a flexible multidimensional reactive transport model for simulating biogeochemical subsurface processes. *submitted to Computers & Geosciences*, 00:0000, 2009.
- [176] Olaf A. Cirpka and Albert J. Valocchi. Two-dimensional concentration distribution for mixing-controlled bioreactive transport in steady state. *Adv Water Resour*, 30:1668–1679, 2007.
- [177] Olaf A. Cirpka and Albert J. Valocchi. Reply to comments on two-dimensional concentration distribution for mixing-controlled bioreactive transport in steady state by h. shao et al. *Adv Water Resour*, 32:298–301, 2009.
- [178] Haibing Shao, Florian Centler, Cecilia de Bias, Martin Thullner, and Olaf Kolditz. Comments on "two-dimensional concentration distribution for

- mixing-controlled bioreactive transport in steady state" by o. a. cirpka and a. j. valocchi. *Adv Water Resour*, 32:293–297, 2009.
- [179] B Cochebin, L Trotignon, O Bildstein, Carl I Steefel, V Lagneau, and J Vanderlee. Approaches to modelling coupled flow and reaction in a 2d cementation experiment. *Advances in Water Resources*, 31(12):1540–1551, 2008.
- [180] Rink K, Fischer T, and Kolditz O. Data visualisation and validation for hydrological models. In *Proc of Int Conf on Computer Graphics, Visualization, Computer Vision and Image Processing (CGVCVIP)*, 2011.
- [181] Rink K. The opengeosys data explorer manual. Technical report, Department of Environmental Informatics, Helmholtz Centre for Environmental Research - UFZ, Leipzig, Germany, 2011.
- [182] B. Zehner. Interactive exploration of tensor fields in geosciences using volume rendering. *Computers & Geosciences*, 32:73–84, 2006.
- [183] B. Zehner, N. Watanabe, and O. Kolditz. Visualization of gridded scalar data with uncertainty in geosciences. *Computers & Geosciences*, 36:1268–1275, 2010.
- [184] W. Schroeder, K. Martin, and B. Lorensen. *The Visualization Toolkit, An Object-Oriented Approach to 3D Graphics*. Prentice-Hall Inc., 1996.
- [185] B. Zehner. Mixing Virtual Reality and 2D Visualization - Using Virtual Environments as Visual 3D Information Systems for Discussion of Data from Geo- and Environmental Sciences. In *Proceedings of the International Conference on Computer Graphics Theory and Applications (GRAPP2010)*, pages 364–369, 2010. Available from: <http://www.ufz.de/index.php?en=19329>.
- [186] D. Reiners, G. Voss, and J. Behr. Opensg: Basic concepts. In *OpenSG Symposium 2002*, 2002.
- [187] B. Zehner. Constructing Models for Finite Element Simulation Using Gocad. In *Proceedings of the 31st Gocad Meeting, June 2011, Nancy*, 2011. CD-ROM.